STUDY OF THE VERY HIGH ENERGY GAMMA-RAY EMISSION FROM SUPERNOVA REMNANTS WITH VERITAS. TWO TEST CASES: CASSIOPEIA A AND IC 443

by

Sajan Kumar

A dissertation submitted to the Faculty of the University of Delaware in partial fulfillment of the requirements for the degree of Doctor of Philosophy in Physics

Spring 2018

STUDY OF THE VERY HIGH ENERGY GAMMA-RAY EMISSION FROM SUPERNOVA REMNANTS WITH VERITAS. TWO TEST CASES: CASSIOPEIA A AND IC 443

by

Sajan Kumar

Approved: _____

Edmund R. Nowak, Ph.D.
Chair of the Department of Physics and Astronomy

Approved: _____

George H. Watson, Ph.D.
Dean of the College of Arts and sciences

Approved: _____

Ann L. Ardis, Ph.D.
Senior Vice Provost for Graduate and Professional Education

I certify that I have read this dissertation and that in my opinion it meets the academic and professional standard required by the University as a dissertation for the degree of Doctor of Philosophy.

Signed: _____

Jamie Holder, Ph.D.
Professor in charge of dissertation

I certify that I have read this dissertation and that in my opinion it meets the academic and professional standard required by the University as a dissertation for the degree of Doctor of Philosophy.

Signed: _____

Brian Humensky, Ph.D.
Member of dissertation committee

I certify that I have read this dissertation and that in my opinion it meets the academic and professional standard required by the University as a dissertation for the degree of Doctor of Philosophy.

Signed: _____

Thomas K. Gaisser, Ph.D.
Member of dissertation committee

I certify that I have read this dissertation and that in my opinion it meets the academic and professional standard required by the University as a dissertation for the degree of Doctor of Philosophy.

Signed: _____

James MacDonald, Ph.D.
Member of dissertation committee

ACKNOWLEDGEMENTS

First and foremost, I would like to thank Dr. Jamie Holder for his constant support and encouragements throughout the period of my Ph.D. research. Without his help and feedback, I could not imagine myself finishing this dissertation work. I would also like to thank my thesis committee members, Thomas Gaisser, James McDonald, Brian Humensky for their valuable comments on the writing part. I would also like to thank Maura Perkins and Kim for all their help in the administrative work throughout my Ph.D. period.

I am also indebted to all the members of the VERITAS collaboration, which have contributed to this work either by building the VERITAS array or writing the software packages used for data analysis. In particular, I would like to thank Brian Humensky, Gernot Maier, Alina Wilhelm, Martin Pohl, Nahee Park, Henrike Fleischhack, Sean Griffin, Dana Saxon, Karsten Berger, Pascal Fortis, Micheal Daniel, Gareth Hughes, Jack and George.

I also extend sincere gratitude to small circle of my friends Rahul, Tulasi, Asif, Gurbir, Nikhil, Priyanka, Rajiv and Avtar. These people may not have helped me in the research directly but they made my PhD duration very pleasant in USA. These are people with whom I share lot of my experiences and problems. I would also like to thank you Sumita and Aman aunty, who fed me with tasty foods for almost five years.

I would like to express my thanks and love for my wife, Khushboo verma, for her unstinted support and belief in me. She is not only my partner in life but also partner in thoughts.

I would like to thank my brothers (Rajan and Kamal) and Pali Uncle who always listen to me and understands me.

As the foundation is always at the bottom, I remain grateful to my parents for their incredible support and encouragement throughout my life.

I apologies to all the other people in my life who I forgot to mention.

DEDICATION

I dedicate this work to the memory of my taya ji (Mela Ram Saraf), who passed away on July 21, 2017. His life of honor, courage and sacrifice will always remain an inspiration for me.

"be-qarari si be-qarari hai
us se kahiyo ki dil ki galiyon mein
raat din teri intizari hai"
-by Jaun Elia

TABLE OF CONTENTS

LIST OF TABLES

LIST OF FIGURES

ABSTRACT

The research in this thesis is concerned with the study of gamma-ray emission from supernova remnants (SNRs). In particular, I have performed an analysis of the data accumulated from VERITAS observations of two SNRs: Cassiopeia A and IC 443. VERITAS is an array of four 12 m telescopes located in Arizona at an altitude of 1268 m. The current configuration of the VERITAS observatory is sensitive to gamma-ray photons with energies from 85 GeV to 30 TeV. I have also performed data analysis in the high-energy (HE) gamma-ray domain using publicly available Fermi-LAT data on Cassiopeia A. The HE/VHE emission from supernova remnants arises from the interaction between high energy cosmic ray particles accelerated at the SNR shocks and the surrounding medium. Therefore, gamma-ray emission can be used as a powerful probe for testing SNRs as a potential source of Galactic cosmic rays.

Chapter 1 of this thesis gives an introduction to gamma-ray astronomy and the instruments used for detecting HE/VHE gamma rays. This chapter also summarizes the population of very high-energy (VHE) gamma-ray sources which have been detected so far. Chapter 2 discusses the general imaging atmospheric Cherenkov technique for detecting VHE gamma-ray showers from the ground. This is followed by Chapter 3, in which a comprehensive description of VERITAS observatory is presented. Chapter 4 describes the analysis techniques used for analyzing the data from the VERITAS array. Chapter 5 includes a broad description of SNRs in the HE/VHE gamma-ray domain. In this chapter, a general classification of SN explosions and their dynamical evolution is discussed. A simplified mathematical treatment of diffusive shock acceleration theory is presented, followed by a description of gamma-ray production mechanisms at HE/VHE energies. The final part of Chapter 5 discusses the gamma-ray emission from young and middle-aged SNRs.

Chapter 6 provides a detailed description of the results from Cassiopeia A obtained by analyzing data from Fermi-LAT and VERITAS. The second part of Chapter 6 discusses the interpretation of the HE/VHE gamma-ray emission result in the context of multi-wavelength data. The final Chapter of the thesis presents the detection of extended gamma-ray emission from a middle-aged SNR, IC 443. This SNR is interacting with molecular clouds and evolving in a very heterogeneous environment. To understand the possible origin of gamma-ray emission from IC 443, I present the results of some modelling of the system.

Chapter 1

INTRODUCTION TO GAMMA RAY ASTROPHYSICS

In the early days of astronomy, visible light was the only means to explore the Universe. Thomas Harriot, an English astronomer, was considered as the first person to make drawing of moon through an optical telescope on 26 July, 1609 [44]. For the next $\sim$ 320 years, astronomers observed the Universe only in optical wavelengths, thus revealing more and more of the thermal Universe. A new impetus to observational astronomy was given in the twentieth century when scientists began to explore the Universe at other wavelengths, such as radio, X-rays and gamma (γ) rays. In particular, the detection of γ-radiation from a large variety of astrophysical sources, including supernova remnants, pulsars, and active galactic nuclei, indicates that non-thermal emission processes, involving relativistic protons and electrons, provide a complementary way to study the Universe.

1.1 Gamma rays: Messengers of Cosmic rays

In the year 1912, the Austrian physicist Victor Hess undertook a balloon flight to an altitude of around 5300 meters and discovered that a mysterious high energy radiation is constantly bombarding the Earth from space [45]. This radiation was later named "cosmic rays". Cosmic rays (CRs) are energetic charged particles that consist mainly of protons ($\sim$ 89%), alpha particles ($\sim$ 10%), nuclei of heavy particles ($\sim$ 1%) and electrons/positrons ($\sim$ 1%). Figure 1.1 shows the energy spectrum of the flux of cosmic ray particles measured from different experiments. The most striking feature of the energy spectrum is the fact that it extends over 13 orders of magnitude in energy and over 32 orders of magnitude in intensity. Above an energy of $\sim 10^{10}$ eV, where the effect of the solar wind is minimum, the differential flux of cosmic rays can

be divided into four regions. Each region can be described by a power law with a negative spectral index. From 10^{10} eV to 10^{15} eV, the differential spectral index is $\alpha = -2.7$. The region around an energy of $\sim 10^{15}$ eV is called the "knee" of the cosmic ray spectrum. It is believed that the cosmic ray particles up to the knee energy are produced in our Galaxy. From 10^{15} eV to 10^{18} eV, the spectral index steepens from $\alpha = -2.7$ to -3.1. The particles between the "knee" ($\sim 10^{15}$ eV) and "ankle" ($\sim 10^{18}$ eV) energies are generally considered as originating outside of our Galaxy. Above 10^{19} eV, the spectrum again flattens to a spectral index of ~ -2.6. In the energy range above $\sim 10^{20}$ eV, the CR spectrum shows a cutoff, also known as GZK (GZK stands for Greisen-Zatsepin-Kuzmin) cutoff [46]. This cutoff puts a theoretical upper limit on the energy of cosmic ray particles. Cosmic ray particles beyond an energy of 10^{20} eV, when moving through intergalactic space, interact with the photons of Cosmic Microwave Background (CMB) radiation and decay into relativistic particles having energy less than GZK limit.

A fundamental problem with cosmic rays is that it is impossible to localize CR sources except for ultra high energy cosmic rays reaching energy of $\sim 10^{20}$ eV. CRs are charged particles, and so their trajectories are deflected by the presence of Galactic and intergalactic magnetic fields. This implies that information about their direction of origin is lost when they traverse from their source of origin to a detector on Earth. Therefore, the only way to have information about the CR sources is to find neutral messengers, such as γ-rays or neutrinos, produced by the interaction of CRs with interstellar medium near the acceleration sites.

Gamma rays are the highest energy form of electromagnetic radiation and cover a broad energy range from 10^5 eV to 10^{20} eV (See Figure 1.2). Different techniques are employed for their detection and every technique has its applicability to a different energy band. In particular, we can divide the 15 decades of the energy range into four bands: low/medium(LE or MeV), high (HE or GeV), very high (VHE or TeV) and ultra-high (UHE $>$ 100 TeV). For the LE/HE bands, space-based detectors are used, while for VHE/UHE, ground-based detector are most sensitive. The majority of the

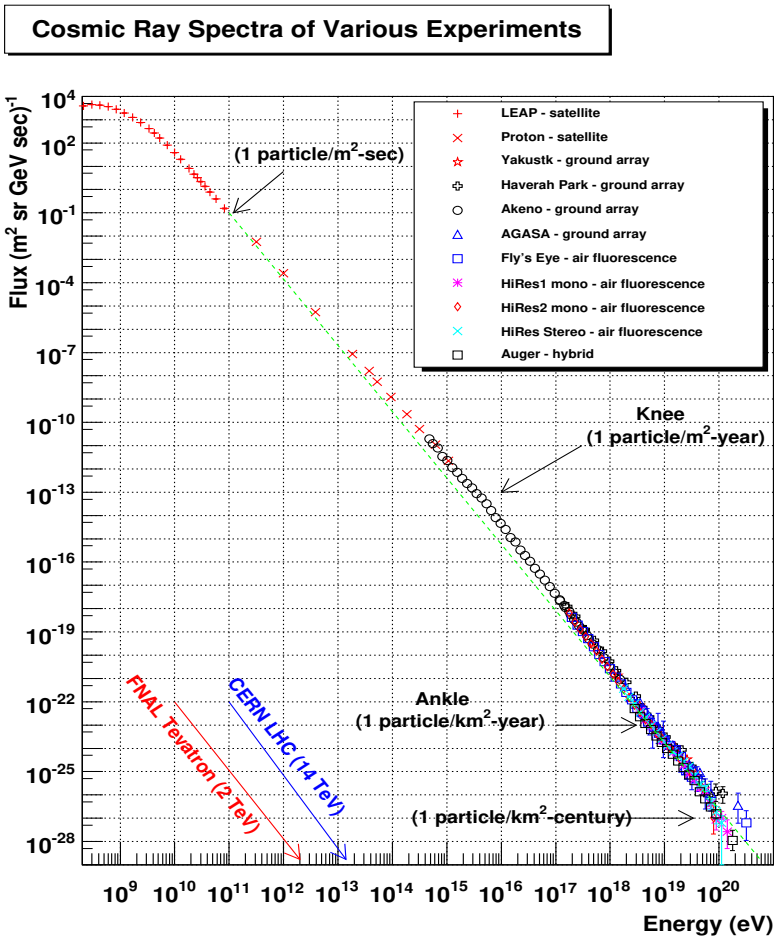

Figure 1.1: Cosmic ray spectrum obtained by combining data from various instruments, available at www.physics.utah.edu/~whanlon/spectrum.html

work in this thesis is related to two of these energy bands: HE and VHE. We will, therefore, give a brief overview of HE and VHE astronomy.

1.2 High Energy gamma-ray astronomy (GeV sky)

The atmosphere of the Earth is opaque to high-energy photons, therefore, the direct detection of these photons requires space-based experiments. In the last decade or so, space-based instruments, particularly in the energy range from $\sim$ 100 MeV to $\sim$ 100 GeV, have greatly advanced our understanding of the non-thermal Universe. The detection of γ-ray emission from several categories of objects reveals the presence

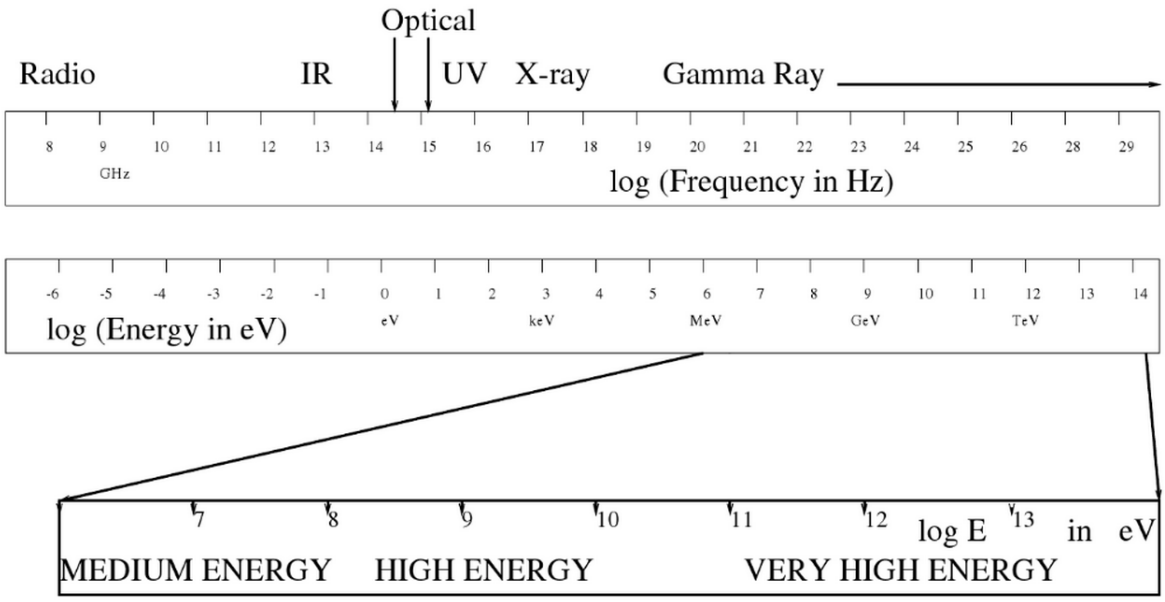

Figure 1.2: Figure 1.1 taken from [1] showing the full extent of Electromagnetic spectrum and the part covered by generic term γ rays.

of strong shocks associated with stellar explosions or compact objects such as neutron stars or black holes.

Historically speaking, Explorer 11 was the first γ-ray satellite detector [47] launched in 1961. It was designed to detect γ-rays above 50 MeV. During its short lifespan of less than 5 months, it detected 22 γ-ray events appearing to come from every direction in the sky. Although the detection suffered from heavy backgrounds of cosmic radiation, it still opened an era of γ-ray detection from space. Similar attempts were made again in 1967 using improved detectors on board the OSO-3 satellite [48]. OSO-3 detected 621 γ-ray events ($>$ 50 MeV) over a 16-month period. It also revealed that the distribution of γ-rays is highly anisotropic, with a higher concentration along the Galactic plane. Following that, pulsed γ-ray emission was detected from the Crab pulsar using a balloon experiment [49]. In 1972, the Small Astronomy Satellite 2 (SAS 2) experiment was launched to detect γ-rays in the energy range from 20 MeV

to 1 GeV [50]. During the $\sim$ 6 months of operation, SAS-2 mapped the Galactic plane and found a second γ-ray pulsar, known as the Vela pulsar [51]. The first catalogue of 25 γ-ray sources at an energy above 300 MeV was produced by the COS-B satellite [52], launched by the European space agency in 1975. The COS-B mission operated for six and half years and produced detailed maps of the γ-ray sky. Besides confirming and expanding the results from SAS-2, it also found the first high-energy extra-galactic γ-ray source, 3C 273 [52].

A great leap in the field of γ-ray astronomy came with the Compton Gamma-Ray Observatory (CGRO), launched in 1991 [53]. The CGRO carried four instruments; Burst and Transient Source Experiment (BATSE), Oriented Scintillation Spectrometer Experiment (OSSE), Compton Telescope (COMPTEL), and Energetic Gamma Ray Experiment Telescope (EGRET). Together, these four instruments provided a comprehensive view of the γ-ray sky from 15 keV to more than 30 GeV. In particular, the high energy instrument EGRET produced the first detailed map of the entire sky in γ-rays, covering the energy range from 20 MeV to 30 GeV. EGRET had a field of view of about $\sim$ 0.5 sr, with an angular resolution of 6° at an energy of 100 MeV (increasing to 0.5° at 5 GeV) [54, 55, 56]. During its lifetime, of 9 years, it detected 271 sources. 60% of these sources had no counterpart in other wavelengths and were labelled as unidentified sources. The second largest class of objects were active galactic nuclei of the blazar class ($\sim$ 35%). Five sources were associated with known Galactic pulsars (See EGRET catalogue 3 for more details [57]). A revised catalogue of EGRET sources was published in 2008 using a different background emission model. This analysis reduced the number of sources from 270 to 188, thus shows that large fraction of original EGRET sources, especially unidentified sources, were not real, probably due to poorly modelled regions of diffuse background [58].

After the success story of the CGRO observatory and following substantial advancement in the field of detector technology, a follow-up mission was developed by NASA. This led to the launch of the Fermi γ-ray satellite in 2008, which brought a breakthrough in our understanding of high energy astrophysics.

1.2.1 The Fermi Gamma-ray Space Telescope

The Fermi Gamma-ray Space Telescope is an observatory to study γ-ray emission from astrophysical sources. Fermi has two main instruments: (1) the Large Area Telescope (LAT) and (2) the Gamma Ray Burst Monitor (GBM). The LAT is a γ-ray imaging detector sensitive in the energy range from 20 MeV to more than 300 GeV. It is a wide field of view detector (~ 2 sr) with an effective collection area of ~ 6500 cm^2 for normal incidence at 1 GeV. The key improvement of the LAT detector over EGRET is that it uses solid state detectors instead of a spark chamber for particle tracking. This leads to better angular and energy resolution for detecting γ-ray photons.

The basic detection principal of the LAT detector is shown in Figure 1.3. The two main challenges for any such detector are: (1) the identification of γ-ray photons against a huge background of charged cosmic rays; (2) to measure the properties of the incoming photons, such as arrival direction, arrival time and energy. In order to achieve the objective of rejecting background CRs, the LAT is surrounded by an anti-coincidence detector (ACD) made of plastic scintillators. ACD is a very common technique used in high energy physics detectors for rejecting background events in real time.

In the energy above 100 MeV, photons interact exclusively through the process of electron-positron pair production ($\gamma \rightarrow e^+ + e^-$). In the LAT, thin tungsten foils are used for converting a photon into an electron/positron pair. The arrival direction of the incident photon can be derived indirectly from the reconstruction of electron/positron tracks using a particle tracking detector (silicon strip detectors). The charged particles undergo multiple Coulomb scattering as they transverse through the detector material, which degrades the ability of the detector to measure the arrival direction with great accuracy. Since the multiple Coulomb scattering reduces as the energy increases, the angular resolution improves with increasing energy of incident photon, with a typical angular resolution of approximately 1° at 1 GeV. Finally the particles are stopped by a calorimeter (cesium iodide) which measures the total energy deposited. The typical resolution for energy estimation is estimated at about $15 - 20\%$. For a detailed

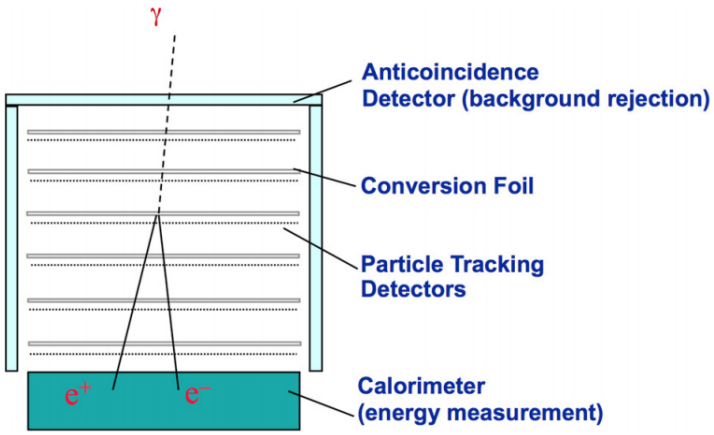

Figure 1.3: Basic space based γ-ray detector.

description of the LAT and its performance, see [59].

Over the last 9 years, *Fermi*-LAT has significantly improved our understanding of the MeV to GeV γ-ray sky. Based on the first four years of science data, the third source catalogue (3FGL), in the energy range from 100 MeV to 300 GeV, was published [60]. The 3FGL catalogue contains 3033 sources detected above 4σ, including γ-ray emitting pulsars, AGN, supernova remnants and many more. For 1010 sources there is no association at other wavelengths.

AGILE (light imaging detector for γ-ray astronomy) is an another space mission launched by Italian groups in 2003. It carried two instruments, one for γ rays and another for hard X-ray detection. This instrument has also made contributions to the understanding of the γ-ray sky ,and is sensitive in the energy range from 30 MeV to 50 GeV) [61].

1.3 Very High Energy gamma-ray astronomy (TeV sky)

Very High Energy (VHE) γ-ray astronomy is concerned with detecting γ-ray photons of energies between $\sim$ 100 GeV and $\sim$ 100 TeV. This energy range will be pushed further up to $\sim$ 300 TeV, with the development of the next generation of

ground-based observatory, the Cherenkov Telescope Array (CTA) [62]. The detection of γ-ray photons in this energy range lies outside the capability of space based instruments, due to the rapidly decreasing photon flux with increasing energy, and the small area ($\sim$ 1 m^2) of space-based detectors. For example, the flux of photons above 1 TeV from the Crab Nebula, one of the strongest source of γ-ray photons, is 2.2×10^{-7} m^{-2} s^{-1} [63]. Therefore, a detector area of the order of 10^4 m^2 is required to detect a few photons in an hour. Such large detectors cannot be placed in space, and are required to be installed on the Earth. Ground-based techniques are typically divided into two categories; Imaging Atmospheric Cherenkov experiments, and air shower arrays.

1.3.1 Imaging Atmospheric Cherenkov telescopes

The technique of Imaging Atmopsheric Cherenkov telescopes (IACTs) is a very successful tool to detect γ-ray photons in the energy range beyond 50 GeV [64, 65]. The window of VHE γ-ray astronomy was opened in 1989 by the Whipple observatory with the successful detection of VHE emission from the Crab Nebula [66]. The Whipple observatory consisted of a single 10 m telescope, originally equipped with a 37-pixel imaging camera. Currently, three major IACT observatories are in operation. Two of them, MAGIC [67, 68] and VERITAS [69, 70], are located in the northern hemisphere, whereas the third one, H.E.S.S. [71, 72], is located in the southern hemisphere. All of the current generation of observatories use multiple telescopes, at a typical spacing of $\sim$ 100 m, to observe the γ-ray sky. For a detailed description of the IACT technique, see Chapter 2.

The High Energy Stereoscopic System (H.E.S.S.) Observatory is a system of five IACTs located in Namibia at an altitude of 1800 m in the southern hemisphere. In phase I, completed in 2004, four telescopes, each with a mirror area of 107 m^2 and focal length of 15 m, were built and arranged on four corners of a square having a side length of 120 m. The Cherenkov light from the air shower is imaged using a pixellated camera having a field of view of $\sim 5^\circ$. In phase II, completed in 2012, a larger telescope, of

mirror area 600 m^2, was added at the center of the array. This improves the sensitivity of the array for low energy showers [63, 73].

The Major Atmospheric Gamma-ray Imaging Cherenkov (MAGIC) system consists of two very large telescopes, each having a dish area of about 236 m^2. It is located on the Canary island of La Palma at an altitude of 2400 m. Due to its large mirror area, MAGIC is sensitive to detecting γ-rays between 50 GeV and 30 TeV. The field of view of the MAGIC telescopes is 3° diameter [74].

The Very Energetic Radiation Imaging Telescope Array System (VERITAS) is operating at the Fred Lawrence Whipple Observatory in the southern Arizona, USA, at an altitude of 1268 m. It consists of four telescopes each with a mirror area of 106 m^2, and a camera of field of view of $\sim 3.5°$. The energy threshold of the VERITAS array for detecting γ rays is about 85 GeV, which is somewhat higher than the MAGIC and H.E.S.S. array [75]. However, the angular resolution and energy resolution of VERITAS is better than MAGIC telescope, due to the number of telescopes in the array. For a detailed description of the VERITAS array, see Chapter 3.

1.3.2 Air Shower Arrays

An alternative technique to detect γ-rays and cosmic rays from the ground is based on a dense array of detectors distributed over a large area. The feasibility of detecting very high energy γ-rays from the ground has been demonstrated by the Milagro [76], HAWC [77], ARGO-YBJ [78] and Tibet ASγ [79] detectors. This technique requires the shower particles, which are produced through the interaction of primary γ-rays with the atmosphere, to reach ground level. As high energy showers are more penetrating, and produce charged particles at lower altitudes than lower energy showers, the air shower arrays have a higher energy threshold compared to IACTs. The arrival direction of the primary γ-ray is estimated from the arrival times of shower particles in different detectors, while the energy is estimated from the total number of detected particles on the ground. Unlike the imaging atmospheric Cherenkov telescopes, the design of air shower arrays allows the detectors to operate even during

Figure 1.4: (upper) The VERITAS γ-ray observatory located at Mt. Hopkins, Arizona. (lower left) Two large telescopes of the MAGIC Observatory located on the Canary island of La Palma. (lower right) Five H.E.S.S. telescopes in Namibia.

the daytime, thus providing a high duty cycle. In addition to the high duty cycle, this technique has the advantage of a large field of view, compared to the few degrees ($\sim 4^{\circ}$) provided by the IACTs. However, for point sources of γ rays, the IACTs, due to their better background rejection($> 99\%$), are more sensitive than the air shower arrays, particularly below an energy of a few TeV.

The High Altitude Water Cherenkov Observatory (HAWC) is located at a height of 4100 m above sea level in Sierra Negra, Mexico (see left Figure 1.5) [77]. It consists of an array of 300 water Cherenkov detectors (WCD), covering an area of 22000 m^2, and is sensitive to γ-rays in the energy range of 100 GeV to 100 TeV. Each WCD is a cylindrical tank with a 7.3 m diameter and 4.5 m depth, inside of which $\approx$ 200000 liters of pure water is filled. The readout of each WCD is performed by four, upward facing photomultiplier tubes (PMTs). All of the four PMTs are positioned at the bottom of each tank, which is then covered with a light-tight material. Three of the four photomultiplier tubes are 8-inch Hamamatsu R5912 PMTs used previously in the Milagro experiment, and arranged on an equilateral triangle with a side length of 3.2 m. The fourth, 10-inch Hamamatsu R7081 PMT, is placed at the center of each tank and is designed to increase the efficiency of the observatory for low-energy showers (< 1 TeV). These PMTs observe the Cherenkov light flashes produced by shower particles when they pass through the WCDs (see right Figure 1.5). Currently, a source having an integral flux equal to $\sim 5 - 10\%$ of the flux of Crab Nebula, can be detected in a one year period with HAWC detector [80].

1.4 TeV source Catalog

In the past 15 years, a lot of progress has been made in the field of very high energy γ-ray astronomy. The known TeV source catalog has been increased from 10, in 2003, to more than 200 in 2018. This progress was made possible through the success of current generation of ground-based γ-ray telescopes: VERITAS, H.E.S.S., MAGIC and HAWC. Currently, as of January 2018, 208 VHE γ-ray emitting sources exist in the TeV catalogue, as shown in Fig 1.6. Each source is shown with a different symbol and

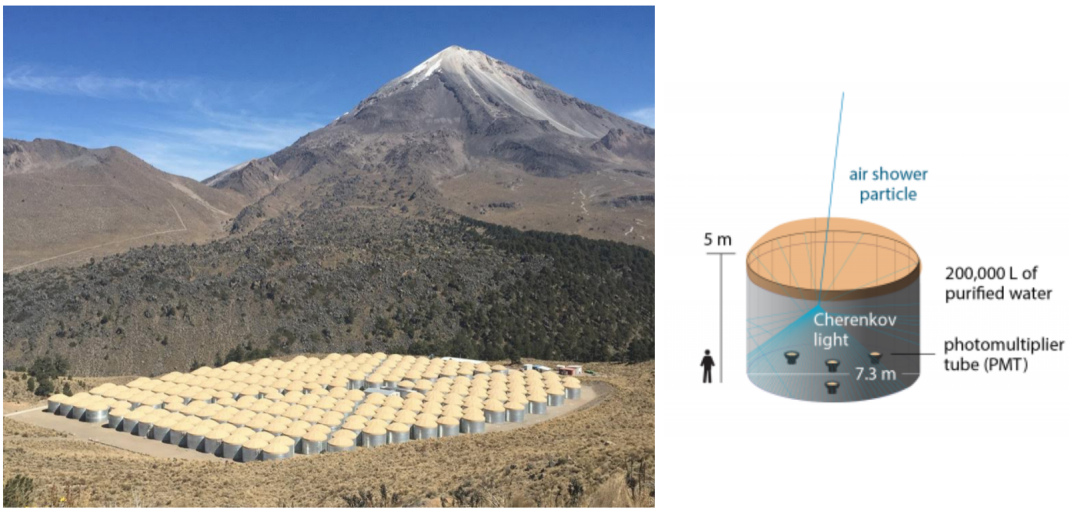

Figure 1.5: (left) The HAWC observatory on the Pico de Orizaba, with 300 water tanks installed (right) A sketch of water Cherenkov detector principle.

summarized broadly into two different categories; Galactic and extra-galactic sources. It should be noted that about 25% of all the detected TeV sources are classified as unidentified objects; i.e., these objects have not been firmly associated with a known object at other wavelengths. For the most recent status update on the detected sources with ground-based γ-ray observations, see the presentation by one of our collaborator Nahee Park [1] at 35th International Cosmic Ray Conference (ICRC). Here, we provide a brief overview of the Galactic and extragalactic TeV sky. The details of sources relevant for the research work in this dissertation are described in subsequent chapters.

1.4.1 Galactic sources

Table 1.1 shows a list of the 72 Galactic sources detected so far, including pulsars, pulsar wind nebulae (PWNe), supernova remnants (SNRs) and binaries. PWNe and SNRs are the two main classes that dominate the population of Galactic sources. For a detailed description of SNRs, see Chapter 5.

[1] https://pos.sissa.it/301/1116/pdf

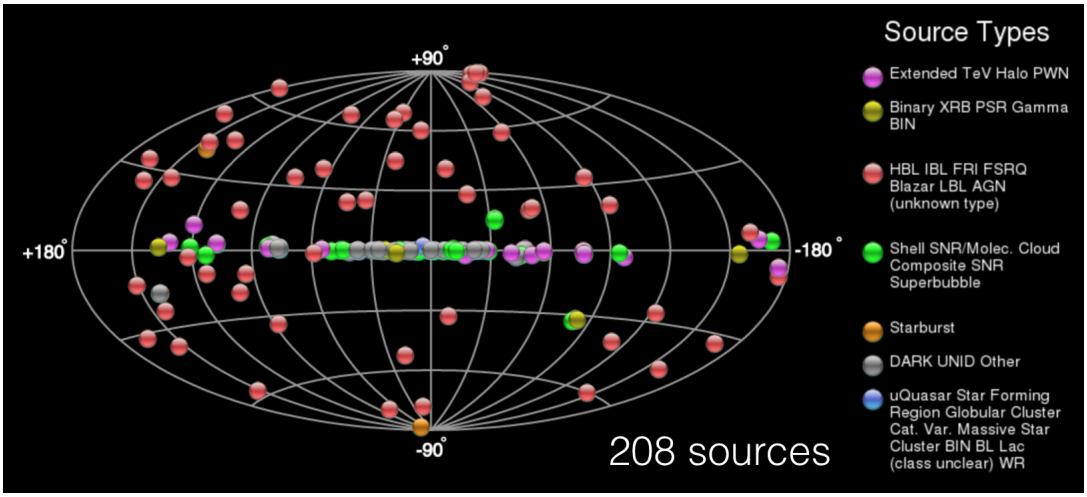

Figure 1.6: The TeV catalogue of all the detected sources in Galactic coordinates as of January 2018. It is retrieved from the online TeV catalog http://tevcat.uchicago.edu/ [2].

In PWNe, the TeV emission is powered by a fast rotating neutron star, produced in a supernova explosion of a massive star. The neutron star loses its rotational energy mainly through a wind of electrons and positrons, also known as a pulsar wind. When this strong wind interacts with the slow moving supernova ejecta, it creates a termination shock. The relativistic plasma between the termination shock and the supernova ejecta is called a pulsar wind nebula. The electrons are accelerated up to an energy of > 100 TeV at the termination shocks. When these high energy electrons interact with the diffuse radiation field, by inverse Compton scattering, they produce γ rays in the TeV range. In this class, the Crab Nebula was the first source discovered in TeV energies by the Whipple collaboration [66]. As of now, 34 PWNe have been discovered by different ground-based telescopes.

Another interesting class of Galactic sources are binary systems. A binary system consists of massive star and a compact object (neutron star or black hole) orbiting around common center of mass. The period of known VHE γ-ray binaries can range from days to decades. Although the particle acceleration and subsequent γ-ray emission process is not well-known in these system, two scenarios are generally

proposed. In the first case, the compact object accretes mass from the companion star. The accretion onto the compact object produces jets similar to those observed in active galactic nuclei (AGNs). The shocks associated with such jets provide a potential site for particle acceleration (microquasar scenario). The second scenario by which particle acceleration can happen, is the collision of the stellar wind with the pulsar wind (wind-wind scenario), similar to the situation in PWNe. Moreover, variability in the VHE γ-ray emission from binaries is also seen, caused by changing environmental conditions at different orbital phases. Until now, 8 VHE γ-ray emitting binary systems, including PSR B1259-63 [81], LS 5039 [82], LS I+61 303 [83, 84] and HESS J0632+057 [85], have been reported. The most recent addition to this class is PSR J2032+4127 [86] having an orbital period of 40-50 years. It reached periastron in November 2017, thus giving a unique opportunity to perform a multi-wavelength observing campaign on this source. Both VERITAS and MAGIC reported a detection of an enhanced TeV flux from PSR J2032+4127, which is expected from a binary system when the orbital phase lies between periastron and superior conjunction [87].

Table 1.1: Number and type of Galactic sources in the TeVCat as of winter 2018

Type	**Objects**	**Representatives**
Pulsar	2	Crab, Vela
Pulsar Wind Nebula	34	Crab, Geminga, Vela X
Supernova remnant with shell	14	RX J1713.7-3946, Cassiopeia A, Tycho
Supernova remnant interacting with molecular clouds	10	IC 443, W28, W44
Binary systems	8	PSR B1259-63, LSI +61 303, PSR J2032+4127
Galactic centre	-	Unidentified
Massive star clusters	3	HESS J1848-018
Globular cluster	1	Terzan 5

1.4.2 Extragalactic sources

As of winter 2018, 71 extragalactic sources have been discovered in the TeV band (see Table 1.2). The largest fraction of the extragalactic sources is given by the active galactic nuclei class. AGNs are compact objects located at the center of host galaxies. The compact object is a black hole whose mass can vary from a few million solar masses to a few billion solar masses. As the matter falls onto the black hole, gravitational energy is released, some of which is used to produce well-collimated relativistic jets of plasma [88]. Particles can be accelerated in these jets, through the Fermi mechanism or magnetic reconnection, and produce broadband electromagnetic radiation, from radio to TeV γ-rays. For a detailed review of γ-ray emission in AGNs, see this review [89].

AGNs can be further classified into two categories; blazars and radio galaxies. This classification is based upon the viewing angle of the jets with respect to the line of sight, as discussed in the well-known unification scheme of Urry & Padovani [90]. For the blazars, the jets point directly towards the observer, whereas for radio galaxies the angle between the line of sight and the direction of the jets is large. There are only four radio galaxies detected so far in the TeV regime, whereas the rest of the 65 objects belong to the blazar class. Blazars, depending upon the emission properties, can be divided into BL Lacertae (BL Lac) objects and flat spectrum radio quasars (FSRQs). The main differences between BL Lacs and FSRQs is that FSRQs are more distant and show strong emission lines. Only 7 FSRQs have been detected so far at TeV energies. The BL Lac objects are further divided into three categories: low-frequency peaked BL Lacs (LBL), intermediate-frequency peaked BL Lacs (IBL) and high-frequency peaked BL Lacs (HBL). This distinction is derived from position of the peak of synchrotron emission spectrum in a νF_ν spectral energy distribution.

Apart from AGNs, two starburst galaxies, M 82 [91] and NGC 253 [92], have also been discovered in the VHE γ-ray band. Starburst galaxies are galaxies associated with regions of high star formation, enhanced gas density, and also a high rate of supernova explosions. If the supernova remnant paradigm of cosmic ray acceleration

is true, then these regions are expected to produce an intense flux of cosmic rays by diffusive shock acceleration. Because of the dense medium, the high rate of cosmic rays produces γ-ray emission, which can be detected with ground-based and space-based γ-ray observatories.

Table 1.2: Number and type of Extragalactic sources in the TeVCat as of winter 2018

Type	**Objects**	**Representatives**
HBL Lac type of blazar	48	Mrk 421, Markarian 501, PG 1553+113
IBL Lac type of blazar	8	W Comae, BL Lacertae
LBL Lac type of blazar	2	OT 081, AP Librae
FSRQ type of blazar	7	3C 279, PKS 1441+25
Radio galaxy	4	NGC 1275, Centaurus A
Starburst galaxy	2	NGC 253 , M82

Chapter 2

DETECTION METHODS FOR VERY HIGH ENERGY GAMMA-RADIATION

Unlike in optical and X-ray astronomy, where the photons are detected directly, detection in γ-ray astronomy is done by indirect means. In order to be detected, a γ-ray photon needs to interact with matter and produce secondary particles. In the ground based γ-ray detection technique, the atmosphere itself becomes the target matter. When a γ-ray photon interacts with the atmosphere, it initiates an extensive air shower (EAS). If the energy of the primary γ-ray photon is high enough (> 50 TeV), then a sufficient number of secondary particles reach ground level to make it possible to reconstruct the properties of the primary photon. This technique is used by the HAWC collaboration [93]. However, at lower energies (100 GeV to 50 TeV), only a very small number of secondary particles can make it to ground level, which makes the measurement of photon properties very difficult. This difficulty was overcome by Galbraith and Jelley in the 1950 by detecting the Cherenkov light from the air showers [94], as proposed by Blackett in 1948 [95]. Detection of this air Cherenkov light at the ground provides very useful information for reconstructing the properties of γ-ray photons. With time this technique has become very sensitive and at present, about 200 known VHE gamma-ray sources have been successfully detected by different observatories [2].

In this chapter, the production of extensive air showers is explained, which are the starting point for the detection of γ rays from the ground. This is followed by the description of Cherenkov light emission from air showers. In the final section, the Imaging Atmospheric Cherenkov Technique (IACT) will be presented.

2.1 Extensive air showers (EAS)

When cosmic rays (CRs) hit the Earth's atmosphere, they interact with the atmospheric nuclei and produce secondary particles. If the energy is sufficiently high, then these secondary particles further interact with the atmosphere and create more and more particles, leading to an extensive air shower. Depending upon the type of first interaction between primary particle and atmospheric nuclei, the development of air showers differs. For example, if it is initiated by strong interactions then it is called a hadronic shower and if it is initiated by electromagnetic interactions, it is called an electromagnetic shower.

2.1.1 Electromagnetic showers

When a γ-ray photon enters the Earth's atmosphere, it creates an electron-positron pair in the Coulomb field of an atmospheric nucleus. This process is called pair production ($\gamma \rightarrow e^+ + e^-$). Following this, the electron and positron interact by the bremsstrahlung process ($e^\pm \rightarrow \gamma + e^\pm$), where the electron (or positron) path is deflected in the electric field of atomic nuclei and produces an electron (or positron) and photon. If the energy of the photon produced through the bremsstrahlung process is high enough, it again converts itself into electron-positron pair which in turn produces photons again through bremsstrahlung, and so on, thus producing a cascade of photons, electrons and positrons as a function of atmospheric depth. This leads to the formation of an extensive air shower which is electromagnetic in nature, because the energy loss processes involved are electromagnetic. The particle number keeps on increasing until the secondary particle energy becomes less than the critical energy (in air $E_C =$ 85 MeV [96]), after which energy loss of electrons by ionisation becomes dominant over bremsstrahlung. A gamma-ray induced shower according to the simplified model of Heitler [3] is shown in Figure 2.1.

There are two dominant processes, pair production and bremsstrahlung, which contribute to the development of the EAS, and both have a very similar characteristic

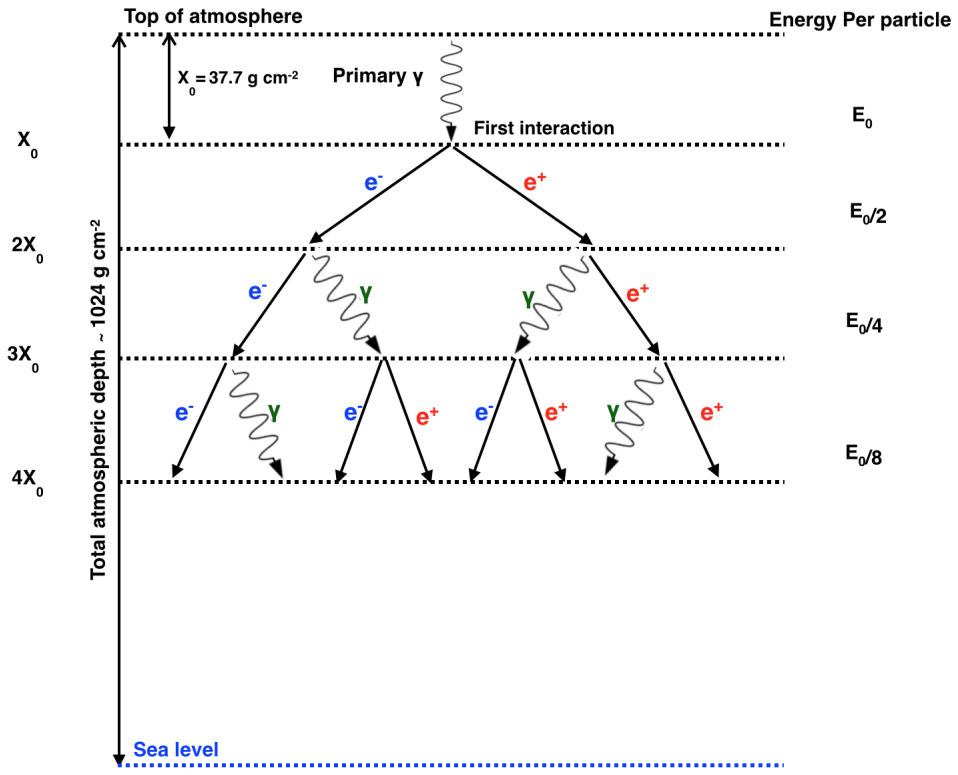

Figure 2.1: Simplified toy model evolution of electromagnetic shower proposed by Heitler [3]. At each step of the evolution, number of particles get doubled, through either pair creation or bremsstrahlung. Also, at each step energy gets equally divided between particles.

radiation length[1], X_0. The typical value of this radiation length in air is equal to 37.7 g cm^{-2} and the total atmospheric depth is approximately equal to 1024 g cm^{-2}. After the first interaction that occurs high in the atmosphere, the number of shower particles increases and the energy per particle decreases as the particles penetrate deeper and deeper into the atmosphere. As a result of this, the total number of

[1] A radiation length is defined as the characteristic amount of matter (measured in gcm^{-2}) traversed by a particle after which the energy reduces to $1/e$ of its original energy.

particles in the shower after n radiation lengths is

$$N = 2^n \tag{2.1}$$

and, due to the equal distribution of energy between particles, the energy of shower particles after n radiation lengths is

$$E = E_0 2^{-n} \tag{2.2}$$

This is shown in Figure 2.1. If we assume that n_{max} is the number of radiation lengths after which the energy falls below the critical energy (E_C), then the maximum number of radiation lengths is given by:

$$n_{max} = (\ln 2)^{-1} \ln \left(\frac{E_0}{E_C}\right) \tag{2.3}$$

From this, the maximum number of shower particles can be calculated as

$$N_{max} = 2^{n_{max}} = E_0/E_C \tag{2.4}$$

All of the above relations are based on a very simple model given by Heitler [3]. However, the detailed model for the longitudinal development of the shower is calculated by Hillas [97]. It calculates the total number of secondary electrons and positrons as a function of atmospheric depth t expressed in radiation lengths and the primary energy E_0 as

$$N_e(t, E_0) = \frac{0.31}{\sqrt{\ln(E_0/E_C)}} \exp[t(1 - 1.5 \ln s)] \tag{2.5}$$

where s is a dimensionless quantity defined as $s = 3t/(t + 2\ln(E_0/E_C))$ and is called the shower age. Figure 2.2 shows the relation of number of particles to the atmospheric depth for showers with different primary photon energy.

Although the electromagnetic cascade is beamed along the direction of the primary photon due to small transverse momentum, there is also a lateral spread of the

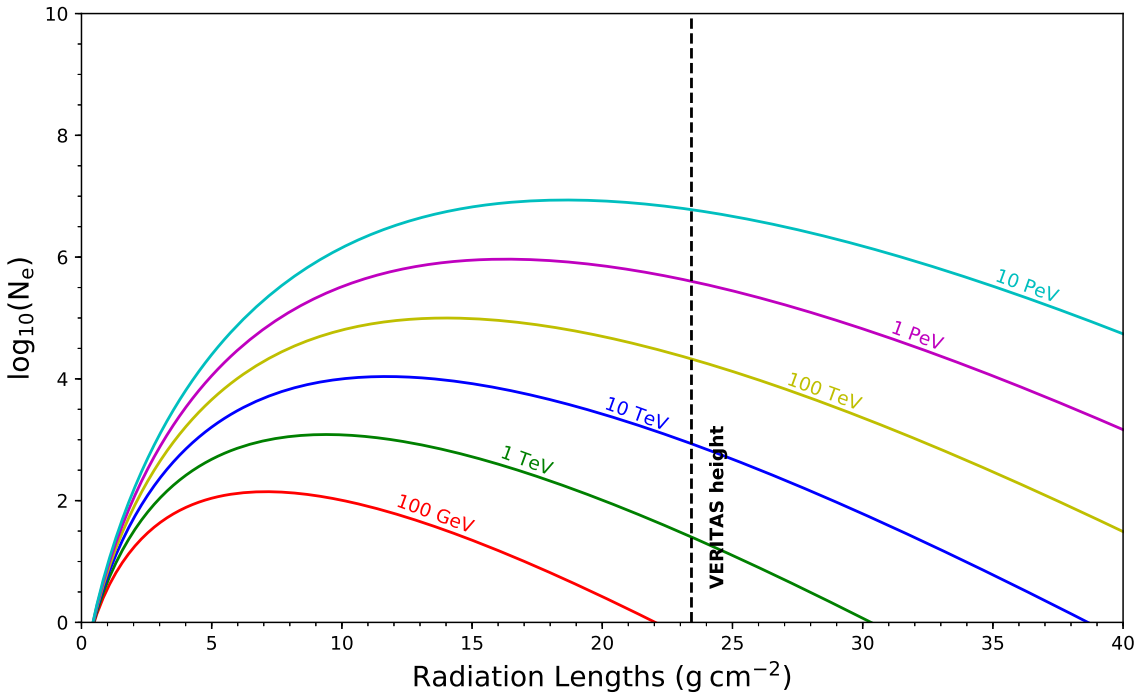

Figure 2.2: The longitudinal development of extensive air showers as a function of atmospheric depth [4].

shower. Multiple Coulomb scattering of electrons in air is the predominant process which determines the lateral spread of the shower. This broadening for electromagnetic (EM) showers scales with a quantity known as the Molière radius [98] and is given by:

$$R_{mol} = x_{mol}/\rho_{air} \tag{2.6}$$

where $x_{mol} = X_0 E_s/E_C$, with $E_s = 21$ MeV. The ρ_{air} is the density of air, given by $\rho_{air} = \rho_0 \exp(-z/h)$, where z is the height above the sea level, $h = 8.5$ km is the scale height of the atmosphere, and $\rho_0 = 1.205 \times 10^{-3}$ g cm^{-3} is the atmospheric density at the sea level. This results in $R_{mol} = 80$ m at the sea level. The physical significance of

this Moliere radius is that it is the radius of a cylinder that contains roughly 90% of the shower energy.

2.1.2 Hadronic showers

When cosmic-ray particles, which are mostly protons (with a small fraction of heavier nuclei from helium to iron), hit the atmosphere and undergo nuclear interactions, they initiate a hadronic air shower. The mean free path for the interaction of a proton of energy 1 TeV through the Earth's atmosphere is equal to $\sim$ 85 g cm^{-2} [9], which is twice as large as the electromagnetic radiation length. Therefore, the hadronic showers penetrate deeper in the atmosphere than pure electromagnetic showers. Furthermore, since the hadronic interactions create secondary particles with larger transverse momentum, the lateral spread of hadronic showers is larger than the electromagnetic showers [99, 9].

The hadronic shower consists mainly of two components: a nuclear core and pions (π^+, π^-, π^0), as shown in Figure 2.3. The neutral pions (π^0) have a short lifetimes of 1.78×10^{-16} s. They decay into two γ-photons which initiate electromagnetic showers. On the other hand, charged pions, with a relatively longer decay time of 2.55×10^{-8} s, decay into charged muons according to $\pi^{\pm} \rightarrow \mu^{\pm} + \nu_{\mu}$. The lifetime of muons, before they decay, in their rest frame of reference is equal to 2.2×10^{-6} s. The muons which are created at higher altitude in atmosphere (close to 10 km) have very high energy ($\gamma \geq 15$, where γ is the Lorentz factor and equal to $(1 - \frac{v^2}{c^2})^{-1/2}$. To an observer on the ground level, due to relativistic time dilation, the mean decay time of muons become $2.2 \times 10^{-6}\gamma$ s. These muons can be observed at the ground level and consitute the muonic component of the shower. However, there are some low energy muons which decay as $\mu^{\pm} \rightarrow e^{\pm} + \nu_{\mu} + \nu_{e}$. The electrons/positrons produced through the decay of low energy muons can either start a electromangetic sub-showers or can be absorbed in the atmosphere before reaching the ground level.

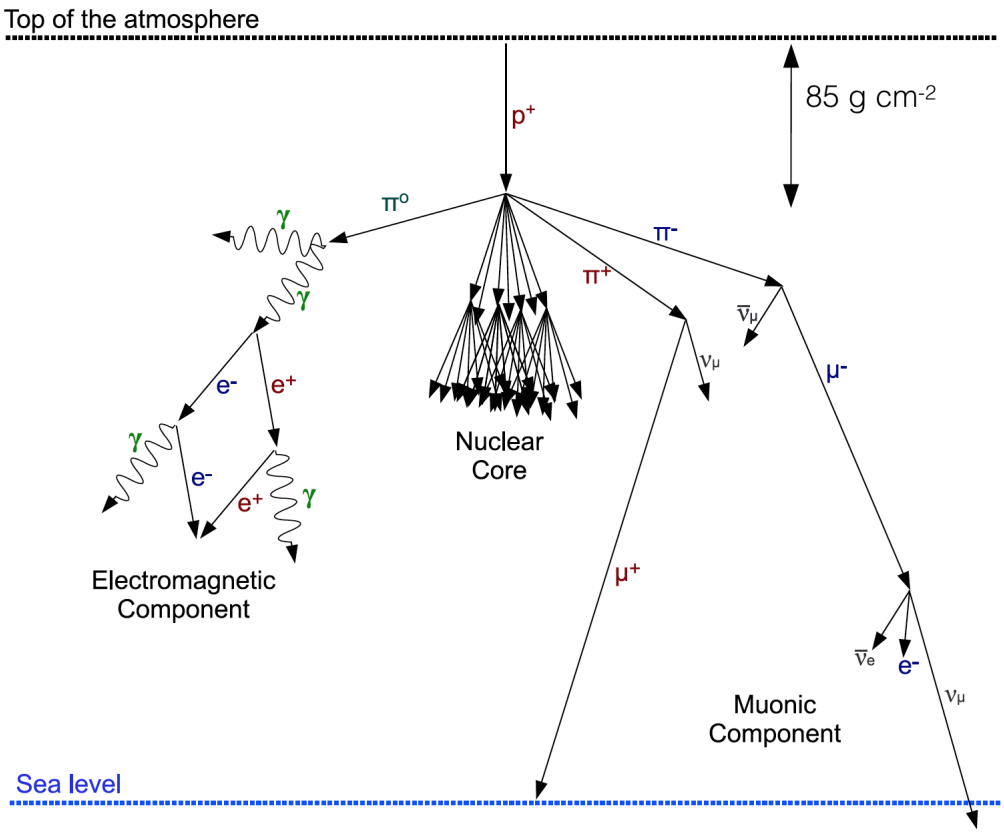

Figure 2.3: Figure 3.5 taken from [5] with permission. Schematic of evolution of hadronic shower produced by the interaction of a cosmic-ray proton with the Earths atmosphere. The shower forms through hadronic and electromagnetic processes.

2.2 Cherenkov Radiation in EAS

When a charged particle moves through a transparent medium with a velocity greater than the local speed of light in that medium, it produces a faint bluish-white light, called Cherenkov radiation. This radiation was predicted by Heavyside in 1889 [100] and later discovered experimentally by P.A Cherenkov in 1934 [101]. The theoretical explanation for this radiation was given by I.E. Tamm and I.M. Frank in 1937 [102]. A qualitative description of this effect is illustrated in Figure 2.4 (a & b), in which the electromagnetic field of a charged particle polarizes the medium when it

moves through it. When the speed of the particle is slow (Figure 2.4 (a)), the polarization field is symmetric both azimuthally and along the axis, resulting in no radiation field at large distance. However, as the speed of the charged particle becomes fast (Figure 2.4 (b)), there is a loss of symmetry along the axis and thus a net dipole field from each element along the track of the charged particle. In general, the dipole field from each element along the track of the charged particle interferes destructively, which means at large distance, the resultant field is still zero. However, as the speed of the particle becomes higher than the speed of light in the medium, a net radiation field is produced at a particular angle, called the Cherenkov angle (θ_C). For example, as shown in Figure 2.4 (c), the electromagnetic waves from three points T1, T2 and T3 on the particle track interfere coherently and form a plane wavefront BC. This coherence takes place when the time taken by a particle to move from A to B is same as the time taken by light to move from A to C. If n is the refractive index of the medium and βc is the velocity of particle, then the Cherenkov angle is given by

$$\cos(\theta_C) = \frac{AC}{AB} = \frac{1}{\beta.n} \tag{2.7}$$

This implies that light emission can only take place if $\beta \geq 1/n$.

The refractive index of the atmosphere changes with altitude according to the formula:

$$n = 1 + \eta_0 e^{-h/h_0} \tag{2.8}$$

where $\eta_0 = 2.9\times10^{-4}$ and $h_0 = 7250$ m. If we substitute the value of the refractive index n in equation 2.7, one can calculate the dependence of the Cherenkov angle on altitude. Figure 2.5 (a) shows that, as one goes lower and lower in the atmosphere, the Cherenkov angle increases. At sea level, the angle becomes close to 1.4°. Since the Cherenkov light is emitted in a narrow cone around the particle trajectory with an opening angle of $2\theta_C$, it forms a circular ring with a radius of R_C given by $R_C = (h - h_{obs}) \tan\theta_C$ (See Figure 2.5 (b)). At the VERITAS site ($h_{obs} = 1.26$ km), the radius of circular ring

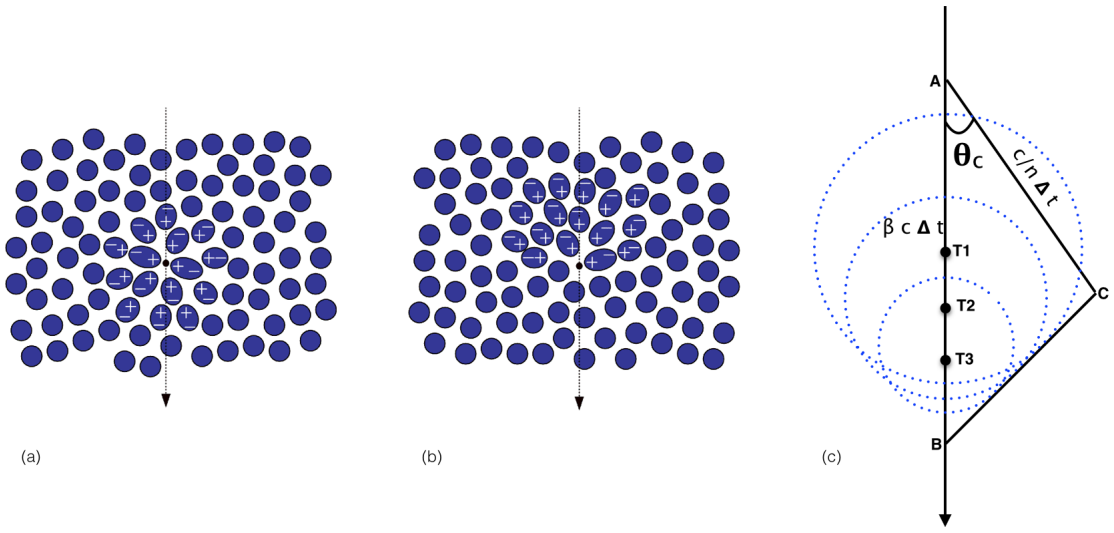

Figure 2.4: Adapted from Figure 4.4 in [6]. "Polarization produced in a dielectric medium by a charged particle: a) $\beta < 1$ and b) $\beta \sim 1$. c) shows the propagation of Cherenkov light derived from Huygens principle."

formed on ground for an emission height of 10 km is $\sim$ 100 m. Figure 2.5 (c) shows the radius of Cherenkov light cones at ground for different altitudes. This Cherenkov light from different altitude arrives within a time interval of few nanoseconds ($\sim$ 2 ns to 5 ns) and is superimposed to give a homogenous light distribution at the observation level in a circle with radius between 50 m to 120 m. A bump in the light intensity is also seen at a radius of $\sim$ 130 m (for a typical gamma-ray shower) due to focussing effect resulting from the superposition of Cherenkov emission from different altitudes.

There is also a minimum energy required to emit the Cherenkov radiation in a medium of refractive index n, given by:

$$E_{min} = \frac{mc^2}{\sqrt{1-\beta^2}} = \frac{mc^2}{\sqrt{1-n^{-2}}} \tag{2.9}$$

Since the minimum energy depends upon the mass of the particle, light particles such as electrons and positrons dominate the Cherenkov emission in air showers. Above this

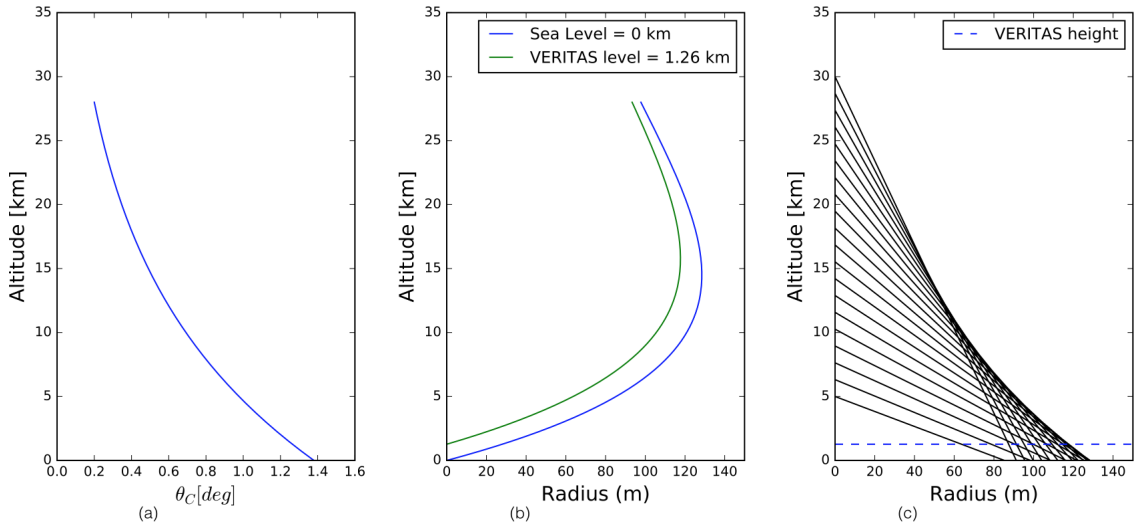

Figure 2.5: Adapted from Figure 4.5 in [6]. "Shown in a) and b) are the dependencies of the Cherenkov emission half angle θ_C and the radius (in km) of the light cone on the emission height, respectively. Radius is shown for two different observation levels: at sea level and at 1.26 km above sea level, approximately the altitude in which the VERITAS Telescope is located. c) is a comprehensive scheme of the geometry of the Cherenkov light cones emitted in different heights."

energy threshold, the number of Cherenkov photons emitted is given by the Franck-Tamm relation:

$$\frac{d^2N_{ph}}{dxd\lambda} = \frac{2\pi\alpha}{\lambda^2}\sin^2(\theta_C) \tag{2.10}$$

This gives the differential number of Cherenkov photons emitted per unit wavelength interval and per unit path length at the Cherenkov angle θ_C ($\alpha \approx 1/137$ is the fine structure constant). Since the number of photons emitted is inversely proportional to λ^2, the Cherenkov light distribution is strongly peaked at short wavelengths (UV-blue). The observed spectrum of Cherenkov photons traveling through the atmosphere and arriving on Earth is strongly modified due to scattering and absorption in the atmosphere. This implies that the number density of photons reaching the observation level is relatively small *i.e.* for a 300 GeV gamma-ray shower, ~ 70 photons/m^2 arrive

at observation level of VERITAS, with a radial extent of $\sim$ 130 m (See Figure 2.6).

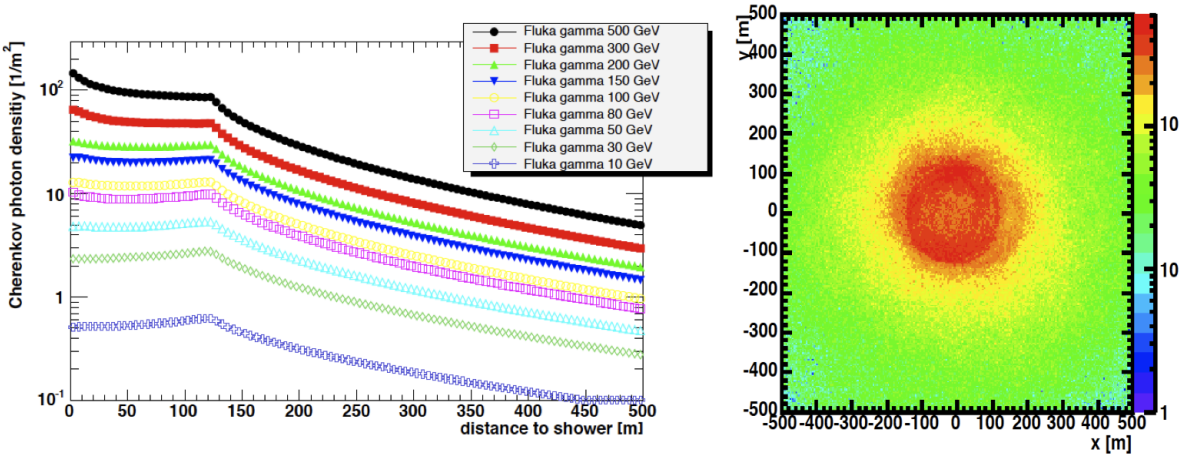

Figure 2.6: Figure 4.4 taken from [7]. "Monte Carlo simulations of the distribution of Cherenkov photons on the ground for gamma-ray initiated air showers. The left plot shows the Cherenkov photon density as a function of radial distance from the shower core for primaries with a range of energies, the right shows the two-dimensional photon density on the ground for a shower with a 300 GeV primary. Figure courtesy of G. Maier."

2.2.1 Distinction between Electromagnetic and Hadronic showers

The major interest of doing γ-ray astronomy is to detect a γ-ray and then find its point of origin (i.e. the source of γ rays in the sky), its energy and its time of arrival. However, the main difficulty for this detection comes from the troublesome background of cosmic ray ions, mainly protons. For example, the cosmic ray flux above 100 GeV is $\Phi(> 100 \text{ GeV}) = 2 \times 10^{-3}$ particles cm^{-2} s^{-1} sr^{-1} [9]. This is equivalent to an event rate of:

$$R_{CR} = \Phi(> 100 \text{ GeV}) \times A \times \Delta\Omega = 2400 \text{ s}^{-1} \tag{2.11}$$

where $A \simeq 3 \times 10^8$ cm^2 corresponds to the area of the Cherenkov light pool on ground, and $\Delta\Omega \sim 4 \times 10^{-3}$ sr is the solid angle corresponding to the field of view of the Cherenkov telescope ($\sim 4°$).

On the other hand the event rate from a typical γ-ray source above 100 GeV is equal to 0.01 s^{-1}, which is five order of magnitude less than the cosmic ray background rate. Therefore, for a successful detection of a γ-ray source, it becomes imperative to reject the numerous background of cosmic rays. This rejection is mainly connected with the difference in the properties of electromagnetic and hadronic showers that is revealed subsequently in the distribution of Cherenkov photons produced by these showers at the observation level. For example, the Cherenkov photon density is irregular and heterogenous in the case of hadronic showers due to significant contributions of Cherenkov photons from the muons, whereas electromagnetic showers are more compact and their photon density is uniform to a distance of $\sim$ 120 m, beyond which it falls off rapidly. This can be seen from Figure 2.7 which shows Cherenkov light distribution on ground, simulated using the CORSIKA software package [8], from a 300 GeV gamma-ray induced shower and a 500 GeV proton induced shower. Also, the arrival time of photons in the hadronic shower is wider ($10-15$ ns) than in the electromagnetic shower ($2-5$ ns) due to the larger transverse momentum and combination of many EM and hadronic sub showers in the hadronic case. Both of these differences can be employed to distinguish between electromagnetic and hadronic showers.

2.3 Imaging atmospheric Cherenkov technique

Historically speaking, the first experimental evidence for the detection of Cherenkov photons from air showers is attributed to Galbraith and Jelley. They used a very simple experimental setup consisting of a 25 cm diameter concave mirror and a 5 cm diameter photo-multiplier tube (PMT) at the focus of the mirror [94], where PMT is a very sensitive detector of light (for more details on PMTs, see section 3.2.1). The output from the PMT was coupled to an amplifier and displayed on the oscilloscope. With this setup, they managed to detect Cherenkov light pulses of short duration above the night sky background every 2 to 3 minutes. In spite of this detection of Cherenkov pulses from the air showers, it was not possible to identify point sources of γ rays with this simple setup, mainly because of the cosmic ray background.

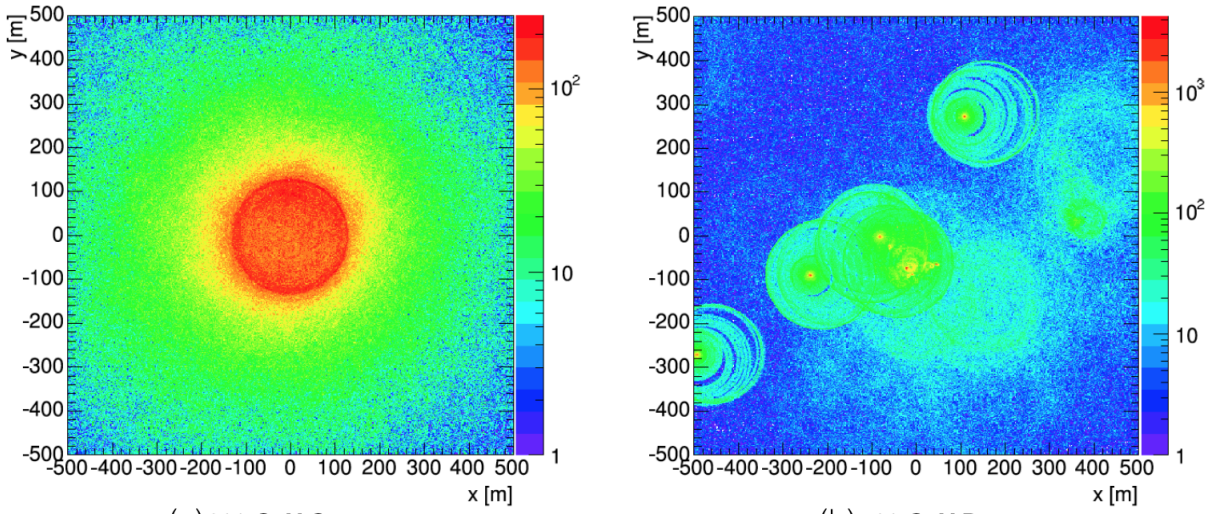

Figure 2.7: Figure 3.7 taken from [5]. "Plots of the Cherenkov photon density on the ground plane from air showers simulated with the CORSIKA software package [8]. Panel (a) shows the relatively uniform photon yield from a single gamma-ray initiated shower with the bulk of the photons falling in a circular region with a radius of 120 m. Panels (b) show photon densities from cosmic-ray showers. Evident is the non-uniform spread of the photons. Plots provided by Dr. Gernot Maier."

With the advent of the imaging atmospheric Cherenkov technique (IACT), a single PMT at the focal plane is replaced with an array of PMTs, which allows the camera to take an image of the Cherenkov light emitted from air showers. The original gamma-ray photon disappears on entering the atmosphere and initiates an extensive air shower (EAS) (see section 2.1). The particles in the EAS then produce Cherenkov photons (see section 2.2), whose total number depends upon the energy of the incident γ-ray photon. For example, the total number of Cherenkov photons emitted from a 1 TeV γ-ray shower is roughly equal to 5×10^6. The radius of the Cherenkov light pool on ground is ~ 120 m, resulting in a shower detection area of $\sim 5 \times 10^4$ m^2. A detector placed anywhere within this light pool will be able to record the shower image. This means that the effective collection area depends upon the size of Cherenkov light pool, not the size of the telescope mirror.

Since the Cerenkov light from an air shower lasts only for a few nanoseconds, high speed detectors (photo-multiplier tubes) and electronics are required to detect faint flashes of Cherenkov light against the night-sky background (NSB) light. The flux of NSB photons is large, $\sim 10^{12}$ photons $\mathrm{m}^{-2}\,\mathrm{s}^{-1}\,\mathrm{sr}^{-1}$. Therefore, to increase signal to noise ratio, one has to reduce the amount of night sky background light collected. If τ is the integration time of the photo-multiplier tubes, which is greater than the duration of the Cherenkov light pulse ($3-5$ ns), then the signal is given by:

$$S = \int_{\lambda_1}^{\lambda_2} C(\lambda)\eta(\lambda)A d\lambda \tag{2.12}$$

where $C(\lambda)$ is the Cherenkov photon flux, $\eta(\lambda)$ is the quantum efficiency of the PMT, λ_1 and λ_2 are the minimum and maximum wavelengths between which PMT responds and A is the area of telescope mirror.

Similarly, the night sky noise in the time duration of τ is given by

$$B = \int_{\lambda_1}^{\lambda_2} F(\lambda)\eta(\lambda)A\tau\Omega d\lambda \tag{2.13}$$

where $F(\lambda)$ is the night sky background flux, Ω is the field of view of the telescope (solid angle). The ratio of Cherenkov signal S from air showers, to the noise N due to night sky background, can then be written as

$$\frac{S}{N} = \frac{S}{\sqrt{B}} = \int_{\lambda_1}^{\lambda_2} C(\lambda)\sqrt{\frac{\eta(\lambda)A}{F(\lambda)\tau\Omega}}d\lambda \tag{2.14}$$

Also, the inverse of the signal to noise ratio gives the minimum detectable energy (i.e. energy threshold) of gamma-ray photon:

$$E_t \propto \frac{1}{C(\lambda)}\sqrt{\frac{F(\lambda)\tau\Omega}{\eta(\lambda)A}} \tag{2.15}$$

To put things in context, if we choose an integration time window of 5 ns, then the number of background photons becomes $\sim 5\times 10^3$ photons $\mathrm{m}^{-2}\,\mathrm{sr}^{-1}$. The other factor which can be helpful in reducing the number of background photons is

the field of view. For a typical ground based gamma-ray telescope, the field of view is $\sim 4^{\circ}$ (solid angle of 4×10^{-3} sr), which means the night sky background becomes $\sim$ 20 photons m^{-2}. These calculations clearly show that for a typical gamma-ray shower, the Cherenkov signal from an air shower is not lost in the background noise, and thus the detection of Cherenkov light above the background is practically possible.

Using the imaging technique, the first success is achieved by the Whipple collaboration in 1989, when they detected the Crab Nebula as a source of γ rays [66]. For this detection, the Whipple collaboration employed a 10 m optical reflector to collect the Cherenkov light from air showers. The shower image was taken with a 37-pixel imaging camera that allow the efficient discrimination of gamma/hadron showers, based on Hillas methods [103]. They reported a 9σ detection from the Crab Nebula using 80 hours of data. However, with modern IACTs telescopes in operation, the same significance can be achieved with only 5 minutes of data taken on the Crab Nebula.

2.3.1 Modern day Cherenkov telescopes

Instead of just one telescope, modern day IACTs, such as VERITAS, HESS and MAGIC, consist of multiple telescopes, where each telescope has a reflector size of about 10 m in diameter. The telescopes are operated mostly in total darkness under clear sky, resulting in a small duty cycle, typically 10-15% of the total number of hours in a year. Two or more telescopes with separations of about 100 m provide a stereoscopic image of an air shower (see Figure 2.8). This technique was first used successfully by the HEGRA collaboration using a 5-telescope array [104]. The advantage of stereoscopic observations is to reduce the energy threshold for the detection. In principal, the energy threshold is inversely proportional to the square root of the mirror area as shown in the Equation 2.15. But this theoretical energy threshold calculated from mirror area is not achievable with a single telescope, mainly due to the background from local muons. Below $\sim$ 300 GeV, Cherenkov light image from local muons is very similar to the γ-ray showers, which makes it hard to discriminate between muon showers and a gamma-ray shower in the camera, based on Hillas parametrization. These muons, thus,

become the irreducible background at low energies. This prevents the single telescope from reaching a energy threshold below 300 GeV. However, the use of coincident trigger between multiple telescopes eliminates this muon background and thus allows the study of low energy gamma-ray showers in the energy range from 50 GeV to 50 TeV.

Also, when the same shower is seen from different directions using multiple telescopes, shower position on the sky can be determined unambiguously by superimposing multiple images. This leads to a better angular resolution. The angular resolution of the current generation IACTs is approximately 0.1°. Similarly, the core position of the shower on the ground can be determined within $\sim$ 10 m. This helps in improving the energy resolution (which is around 15%). The sensitivity of modern day IACT arrays is such that it takes only one minute to detect the Crab Nebula, and about 25 h to detect a source with a flux equal to 1% of the Crab Nebula flux [75].

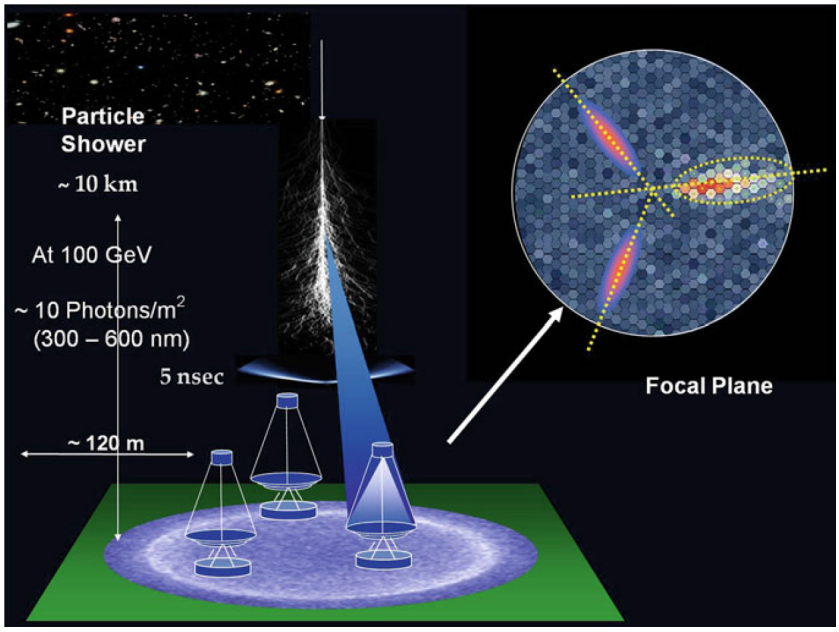

Figure 2.8: Figure 9.1 taken from [9]. Sketch of the Imaging Atmospheric Cherenkov technique using multiple telescopes. The Cherenkov light from an air shower is focused onto a high-speed multi-PMT camera on each telescope. The projected images from different telescopes allow the geometrical reconstruction of shower direction and impact distance.

Chapter 3

THE VERITAS OBSERVATORY

The Very Energetic Radiation Imaging Telescope Array System (VERITAS) is a ground-based observatory designed to detect γ-ray photons in the energy range from 85 GeV to 30 TeV. It is located at the Fred Lawrence Whipple Observatory in southern Arizona (latitude 111° W and longitude 32° N) at an elevation of 1270 m above sea level. The layout of the array is shown in Figure 3.1. It consists of an array of four 12 m telescopes separated on average 100 m from each other. Each telescope has a field of view of 3.5°. The reflector of each telescope is constructed from 350 hexagonal mirrors placed according to Davies-Cotton design and the camera is made using 499 photo-multiplier tubes (PMTs). VERITAS has been fully operational since 2007 and underwent two major upgrades; first, in 2009, when the prototype telescope T1 was relocated to a new location and second in 2012 when the camera old photo-multiplier tubes (PMTs) were replaced with new higher quantum efficiency PMTs. The combined effect of these upgrades results in an improved performance for the VERITAS detector. The sensitivity of the detector is such that a γ-ray point source with a flux of 1% the Crab Nebula can be detected within 25 h [75].

Since September 2007, the observations with the VERITAS have been carried out at night throughout the year, except in July and August when the operations remain closed due to monsoon. To take these observations, a team of about 60 observers signup each year, where each observer spends about 2 weeks per year at the observing site in Arizona. Every year about 1200 hours of good weather data is recorded under conditions of dark and low illumination moonlight (illumination less than 35%). In 2012, VERITAS began to start taking data under bright moonlight conditions (illumination $35 - 65\%$), which in turn adds an additional 200 hours of data in the annual

yield of VERITAS observations. Data under bright moon conditions is acquired by operating the PMTs in the camera with reduced high voltages (RHV); a PMT is operated with a voltage value equal to 81% of the voltage used under normal dark mode observations.

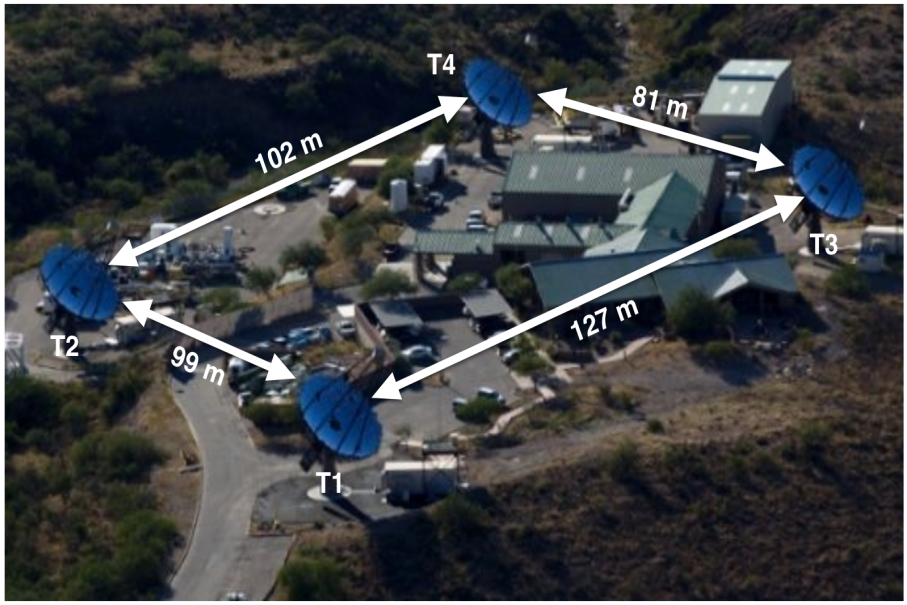

Figure 3.1: Array Layout of VERITAS Observatory

3.1 The Telescope Description

3.1.1 Mechanical assembly

The mechanical assembly of each VERITAS telescope consists of a commercial altitude-azimuth positioner, a steel optical support structure (OSS), a quadra-pod arm structure that supports the camera, and counter-weights (see Figure 3.2). Based on the Davies and Cotton design [105], hexagonal mirrors are mounted on the OSS, providing a 12 m diameter telescope reflector. The camera, whose load is balanced by weights located at the back of the OSS, is mounted on a quadra-pod arm structure at a focal distance of 12 m. This makes the telescope an f/1 system. The positioner unit is manufactured by RPM-PSI Rotating Precision Mechanisms Inc. and is capable of a

pointing accuracy of $\pm 0.01^{\circ}$ [106]. The positioner is designed to slew at a rate of 1° s^{-1} around the elevation and azimuth axes [106]. However, due to safety reasons, during normal operation the slew rate is around $0.3 - 0.5^{\circ}$ s^{-1}. The motion of each telescope is controlled remotely by the tracking software through an Ethernet interface and telescope pointing information is logged into the VERITAS database at a rate of ≈ 4 Hz during the data-taking process.

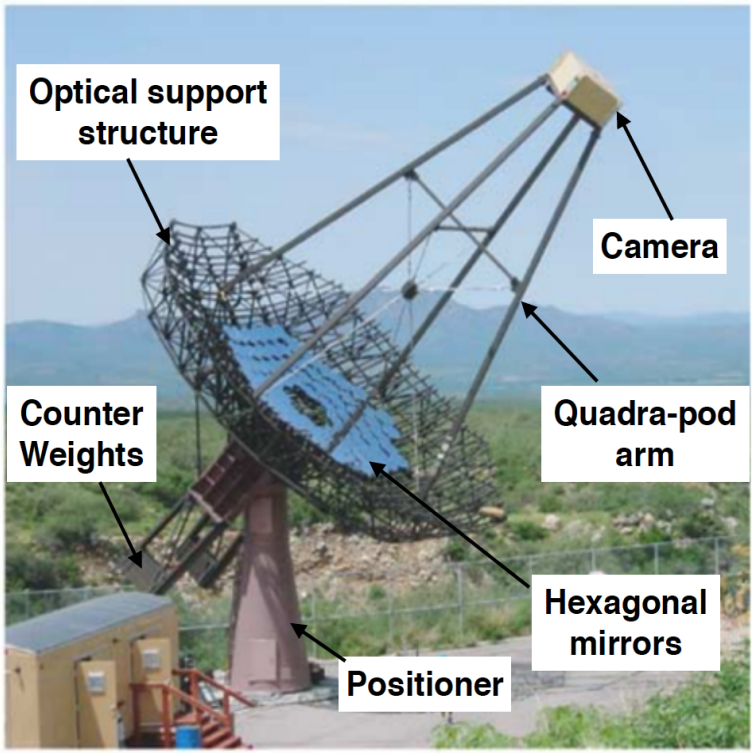

Figure 3.2: Figure 2(b) from [10]. Mechanical assembly of the first VERITAS telescope during construction before completion.

3.1.2 The Reflector

The reflector of ground based γ-ray telescopes generally follows either a spherical Davies-Cotton (followed by VERITAS [107] and H.E.S.S. [108]) or parabolic design layout (followed by MAGIC [109]). In terms of design and construction, Davies and Cotton reflectors offer many advantages; identical focal length mirrors are relatively

inexpensive to build, unlike the mirrors for parabolic reflectors in which the focal length of each mirror varies according to its distance from the optical axis. The Davies-Cotton design offers smaller off-axis aberration than parabolic design, thus provides better quality images at large off-axis angles. The main disadvantage of Davies and Cotton reflector is that it introduces a time dispersion of few nanoseconds in the arrival time of photons at the telescope camera [10]. This spread is acceptable as long as it is less than the intrinsic time spread of the Cherenkov light pulse, and which holds true if the dish size is less than < 15 m. For large dish size, such as the one used in MAGIC telescope (dish size 17 m), parabolic design is preferred to minimize the time spread.

In the case of VERITAS, the Davies and Cotton layout is employed, in which each telescope reflector is segmented and constructed using 350 identical hexagonal mirror facets (see Figure 3.3(b)). All mirror facets have same focal length f, identical to the focal length of the spherical optical support structure (OSS) on which they are mounted. Each mirror facet has a surface area of 0.322 m^2 providing a total mirror area of ~ 110 m^2. A hexagonal shape is employed over a circular shape as it allows close packing of mirrors, thus maximizing the total area of the reflector dish. Mirrors are mounted on the optical support structure using a triangular frame (see Figure 3.3(a)) which isolates the mirrors from the OSS flexure. Adjustable screws on the mount are used to align the mirror manually so that a relatively small point spread function (PSF) can be achieved, where the PSF describes the response of the imaging device to a point source at infinity. Once the mirrors are aligned, the 80% containment radius of the optical PSF of a VERITAS telescope is $\sim 0.05^\circ$ which is substantially less than the pixel size in the camera ($\sim 0.15^\circ$) [12].

Every mirror facet is made from slumped glass which is later cleaned, aluminized and anodized at an on-site facility at the FLWO. The reflectivity curve for all four telescopes is shown in figure 3.3(c) and is taken from [11]. The peak of the reflectively is coincident with the peak in the Cherenkov light spectrum from air showers i.e. more than 90% at 320 nm. Since every facet is exposed continuously to dust and sand of the Arizona desert, it becomes necessary to recoat the mirror facets periodically in order

(a)

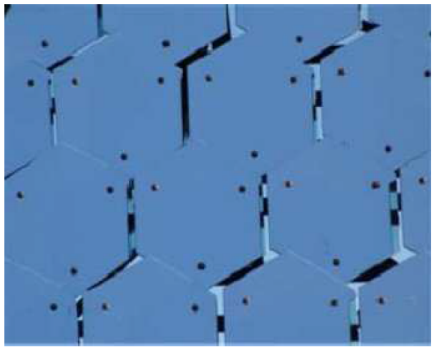

(b)

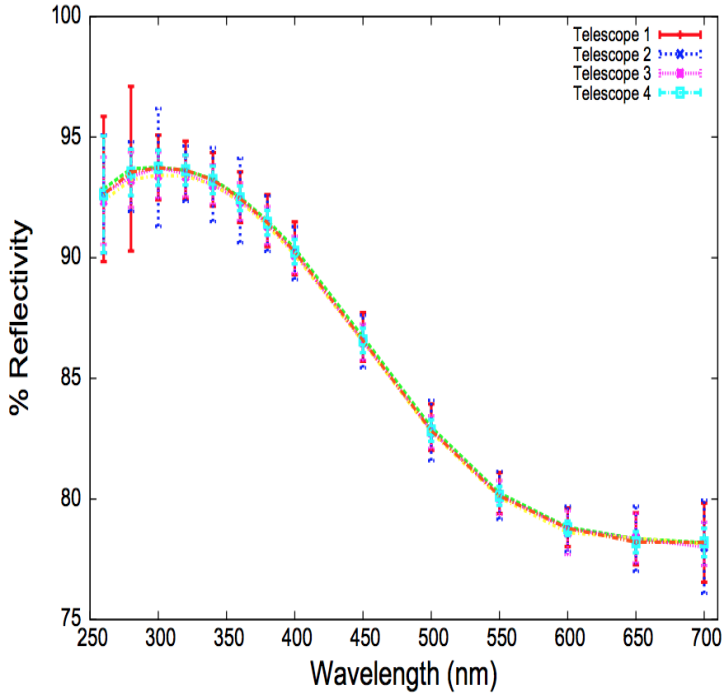

(c)

Figure 3.3: (a) Triangular three-point suspension mirror mount, (b) A close-up view of the hexagonal VERITAS mirror facets, (c) Figure 2 from [11]. "VERITAS telescope mirror reflectivity versus wavelength broken down by telescope. The design specified reflectivties of 90% at 320 nm and $\geq$ 85% between 280 nm and 450 nm."

to maintain the peak mirror reflectively above 90% [11].

3.2 The Cameras

The camera of each of the four VERITAS telescopes is placed at a distance of 12 m from the mirrors of the telescope. The primary component of the camera consists of an array of 499 photomultiplier tubes (see Figure 3.4(a)). The angular field of view of each PMT is 0.15°, resulting in a total field of view of 3.5° per camera. A light concentrator plate consisting of 499 plastic cones glued together is placed in front of the camera to reduce the dead spacing between the PMTs. Each cone has a hybrid design, in which light passes through a large hexagonal entrace window and exits through a smaller window (Winston cones). This results in the concentration of light on the active region of the PMT photo-cathode (see Figure 3.4(b)). During operations, each PMT is supplied with a voltage of $\sim$ 1000 V, which yields a gain of $\sim 2 \times 10^5$. The voltage is provided by a commercially built multi-channel power supply that allows to set the voltage of each pixel channel individually over a certain range. At the base of each PMT, a custom-built preapmlifier with a bandwidth of 300 MHz is connected. The preamplifier provides an extra gain of 6.6 to the PMT signal. This boosted signal then travelled through long cable wires (length $\sim$ 150 ft) to the readout electronics. The various components such as a PMT, high voltage connector and a preamplifier are placed inside a cylindrical aluminimum casing. A spring is also attached at the end of the casing to provide connective compression. This whole assembly constitutes a single VERITAS pixel (see Figure 3.5).

To monitor the current in each PMT during operations, a current monitor board is integrated inside the camera. The current boards report the anode current to the observer and to the high voltage (HV) program. If the current exceeds the tolerance limit of a PMT, the HV program automatically switched off the HV power supply to that pixel. This is an important safety measure to protect the PMTs from transient bright light sources moving through the field of view of the tubes during data taking. During astronomical observations, typical average PMT currents lie between 4 and 8 μA. To provide an another safety measure, temperature and humidity sensors are also installed inside the camera box to monitor the safe environmental conditions during

telescope operations.

All of the components of the camera are housed inside a water-tight and light tight box. In order to protect the PMTs from sunlight, the camera is equipped with a garage style shutter which is closed during the daytime.

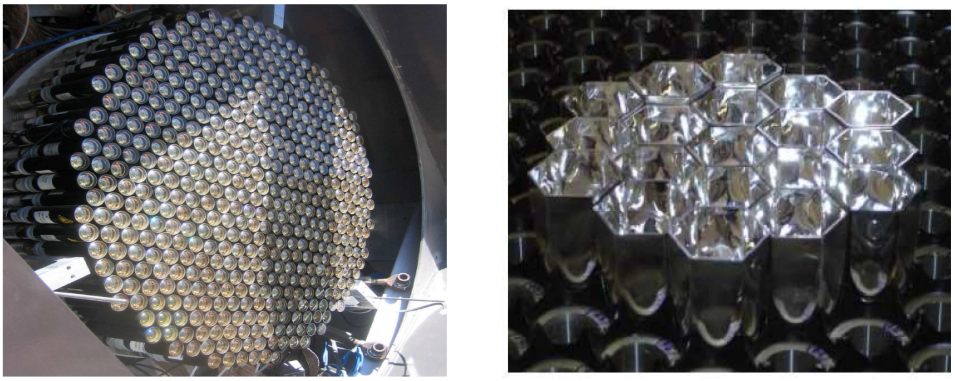

(a) (b)

Figure 3.4: Figure taken from [12]. (a) VERITAS camera, (b) Light concentrator ("Winston cones")."

3.2.1 Photo Multiplier Tubes (PMT)

Ground-based γ-ray telescopes use large optical reflectors to collect the Cherenkov light and focus this light on to a multi PMT based camera. Since the Cherenkov light signal lasts only for a few nanoseconds, a high gain ($\sim 2 \times 10^5$) and fast-response photon detector (rise time ≤ 2.5 ns) is required to capture the Cherenkov flashes. To meet these requirements, PMTs have proved to be the most efficient photon detectors, and are therefore used by most of the ground based γ-ray telescopes. A photomultiplier tube consists of an input glass window, photocathode, focussing electrodes, series of electron multipliers (dynodes) and an anode in a vacuum tube (see Figure 3.6(a)). An incoming photon enters the glass window of the tube and strikes the photocathode. This results in the release of photo electrons from the photocathode due to the photoelectric effect. The released photoelectrons are focused by the focusing electrodes towards the electron multiplier where electrons are multiplied by process of secondary

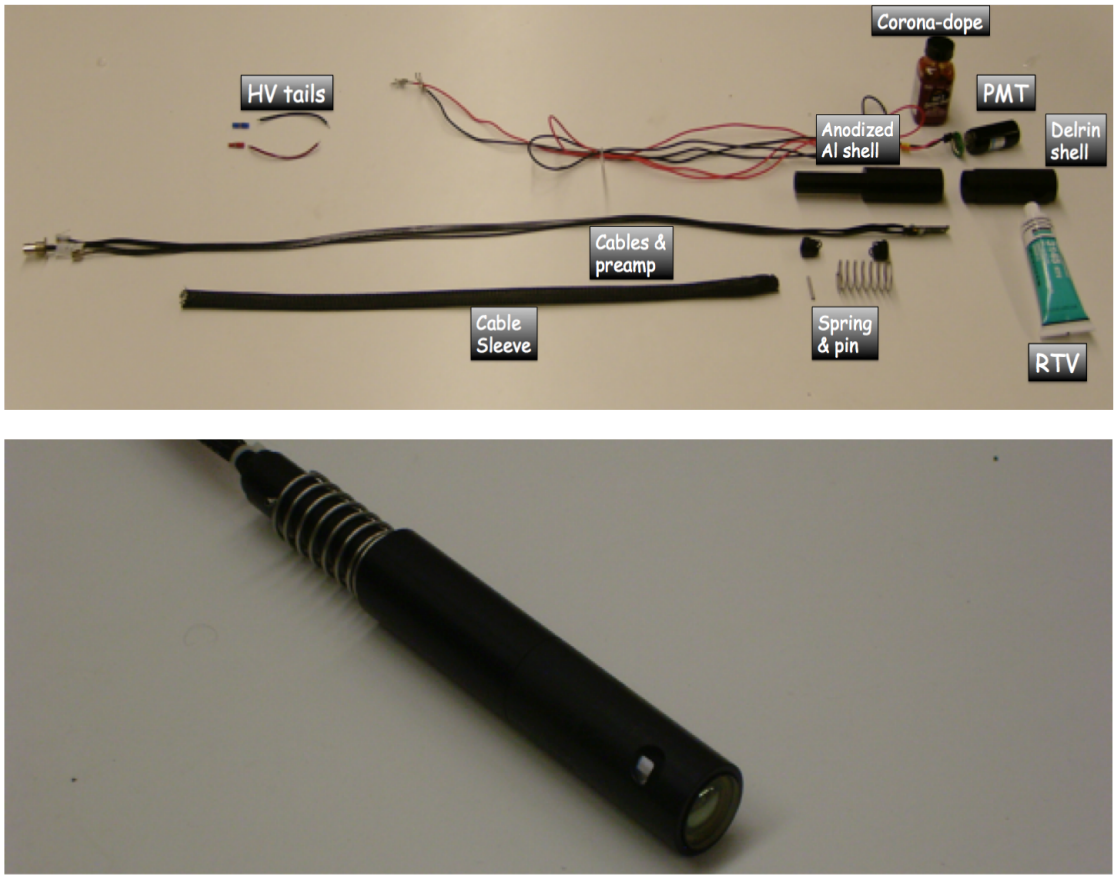

Figure 3.5: Upper image shows all the components from which a camera pixel is made up, and lower picture shows the pixel in its final stage that is used in the camera

electron emission. The number of electrons released depends upon the material of the dynodes and the applied potential at each dynode stage. This defines the gain of the PMT i.e. the average number of electrons produced at the final dynode by a single photoelectron. At the final stage, these electrons are collected by the anode to produce a output signal.

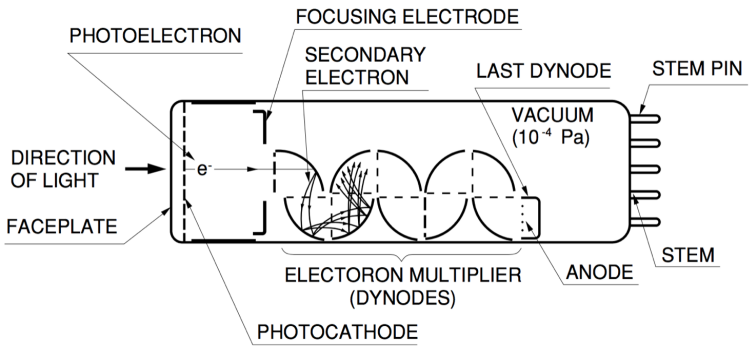

(a)

(b)

Figure 3.6: (a) PMT sketch; Figure 2-1 from https://www.hamamatsu.com/resources/pdf/etd/High_energy_PMT_TPMO0007E.pdf, (b) Figure 1 from [13].The PMT model shown in back is photonis XP2970, which was replaced in the VERITAS cameras with Hamamatsu R10560-100-20 model, shown in the front.

For the VERITAS cameras, from commissioning of the array in 2007 until summer 2012, the Photonis XP2970/02 model PMT, with a 28 mm diameter and bi-alkali

photocathode, was used. This PMT had 10 gain stages and was sensitive in the UV/blue part of the electromagnetic spectrum. In summer 2012, every PMT in all four cameras of the VERITAS telescopes was replaced with 25.4 mm diameter Hamamatsu R10560 model phototubes (see Figure 3.6(b)). These PMTs contain superbialkili photocathodes, which have higher quantum efficiency (32-34 %) than the previous bialkali photcathodes (18-22 %) at wavelengths most relevant for Cherenkov radiation ($\sim$ 320 nm). The quantum efficiency (QE) is an important parameter characterizing a PMT which is a measure of the probability of a photo-electron being released if the photo-cathode is struck by a photon. It depends upon the material used for the photocathode and the wavelength of the incident photon. Another advantage of R10560 model is its photoelectron collection efficiency of 90%, which is better than 75% collection efficiency of the old model Xp2970/02. The combination of higher QE with higher collection efficiency for R10560 model results in higher photon detection efficiency (PDE) for R10560 (see Figure 3.7(a)). When the PDE mesurements are folded with the Cherenkov light spectrum in the focal plane of a VERITAS telescope, 23% of the Cherenkov photons will be detected with R10560 PMT model, which is a 35% higher light yield than the older Photonis XP2970/02 PMT. The advantage of higher light yield results in lowering the energy threshold of VERITAS from 100 GeV to 70 GeV [13].

In addition, the pulse shape has a full width at half maximum (FWHM) of 4.2 ns in the new model of PMTs (see Figure 3.7(b)), which is 40% less than the old model PMTs (6.2 ns). The narrower pulse shape allows a better discrimination of the Cherenkov signal against the background noise photons.

3.3 The Trigger System

In VERITAS, the trigger is a system that helps to record only those events which are interesting for later analysis. The necessity of such a trigger arises to maintain a minimum possible dead-time without losing the sensitivity for low energy γ-ray showers. The dead-time scales linearly with array trigger rate. At the present moment, the

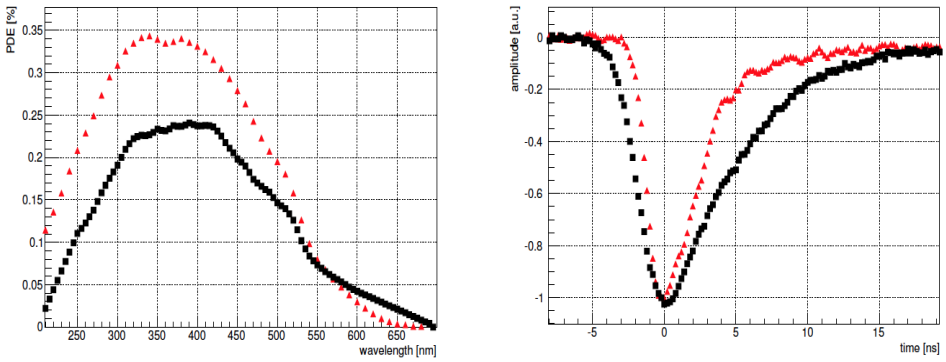

(a) (b)

Figure 3.7: Figure taken from [14], black squares are before the upgrade (XP2970), red triangles are after the upgrade (R10560) (a) Photon detection efficiency as a function of wavelength. Curves are obtained from measurements performed at UCSC and WashU (VERITAS Collaboration), (b) Pulse shape produced by a single photo-electron.

trigger rate of VERITAS array is close to 450 Hz, which gives a dead-time of $\sim 15\%$. Secondly, rejecting the background events at the trigger level helps to reduce the load on the data storage and computing power. At the lower end of the energy range, the trigger rate is dominated mainly by the fluctuations in the night sky background and by single muons from the cosmic ray background showers. Both of these effects are suppressed with the help of a 3-level trigger system.

3.3.1 Pixel Trigger ("Level 1")

The pixel trigger is comprised of a constant fraction discriminator (CFD) for each PMT pixel in a telescope camera. The working of the Level 1 trigger is explained in detail in [110]. It consists of three components: a threshold discriminator, a zero-crossing discriminator and a rate feed-back mechanism (see Figure 3.8). It works by splitting the output signal from each PMT into three copies. The first copy goes directly into a simple threshold discriminator that fires when the PMT signal amplitude rises above some threshold voltage (typically set to 45 mV). The other two copies of signal, one attenuated by some factor f, the other inverted and delayed, are fed into a

zero-crossing discriminator. The zero-crossing discriminator combines these two pulses and fires at a time when the summed signal crosses zero. This ensures that the zero-crossing discriminator will trigger at the same time, irrespective of the input PMT pulse amplitude. The combination of a threshold discriminator and a zero-crossing discriminator is called a constant fraction discriminator, and this helps to keep the timing jitter between pulses of different amplitude to a minimum. To prevent the effect of varying night sky noise level on Level 1 trigger rate, another circuit rate feedback mechanism, is incorporated. This automatically adjusts the effective threshold of the CFD when the night sky noise level rises, which in turn regulates the trigger rate.

In order to account for the timing difference between PMT signals due to differences in the cable lengths, a programmable delay, up to ~ 6 ns, is used in the Level 1 trigger. The typical operational Level 1 trigger rate of the VERITAS under dark conditions ranges from $\sim$ 3 kHz to $\sim$ 3 MHz. The output of the Level 1 trigger is given to the "Level 2" trigger system in the form of emitter coupled logic pulses having a width of 13 ns.

3.3.2 Pattern Trigger ("Level 2")

The Pattern trigger is a camera-level trigger. It is designed in such a way that it fires only when the neighboring pixels in a telescope camera, usually 3, pass the Level 1 trigger within a coincidence time window of about 6 ns. This allows us to maintain a manageable trigger rate even with a lower CFD threshold value. When the CFD threshold value is low, the number of Level 1 triggers will rise due to random NSB events. However, it is very unlikely that these random events occur in three or four adjacent pixels within the coincidence time window. The Level 2 trigger therefore reduces the number of triggers produced from random night sky background events. The block diagram of the Level 2 trigger is shown in Figure 3.9. The Level 2 trigger works by combining the Level 1 signals from the camera into 19 overlapping patches, where each patch contains about 59 channels. Every Level 1 channel is a part of 3 to 5 of these 19 patches. The signal from the 59 pixels in a patch are connected

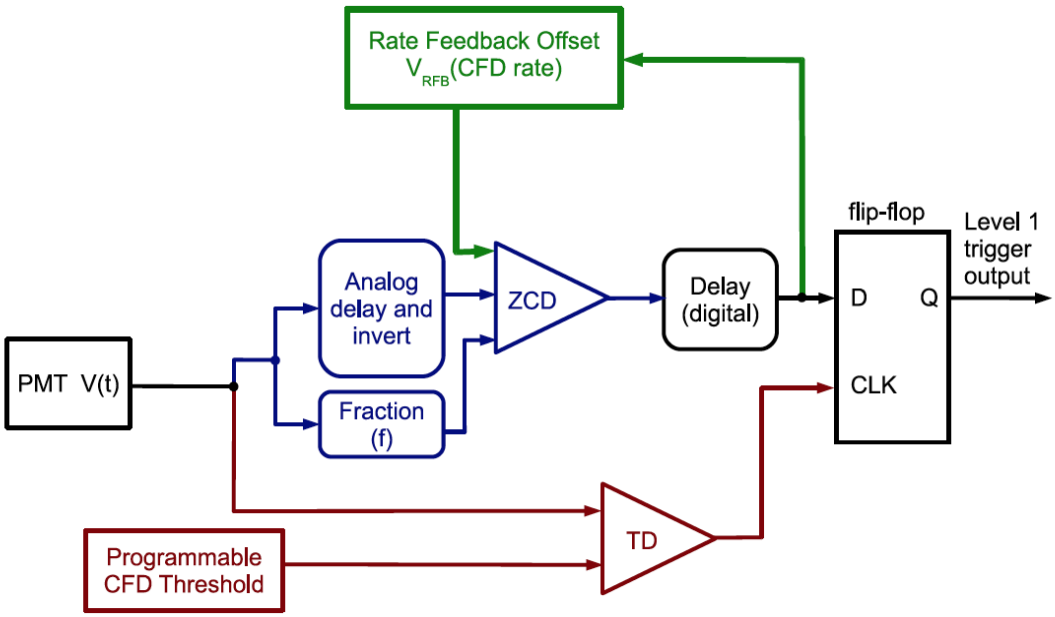

Figure 3.8: Figure 3-15, taken from [5]. Block diagram of Level 1 trigger

to pattern selection trigger modules (PST). The patterns from the Level 1 triggers are then compared with the pre-chosen patterns loaded into the memory of the PST module, and if the pattern matches, the PST module gives a positive signal. The outputs from all of the PST modules are connected with an OR circuit that gives a Level 2 trigger if any of the 19 PST modules gives a positive signal. This trigger worked until 2011, when a new Level 2 trigger was installed in the VERITAS telescopes [111]. The upgraded trigger uses a fast field-programmable gate array (FPGAs) integrated circuit, which allows more accurate pixel to pixel alignment and narrower coincidence timing windows ($\sim$ 5 ns) between adjacent pixels compared to the old Level 2 trigger.

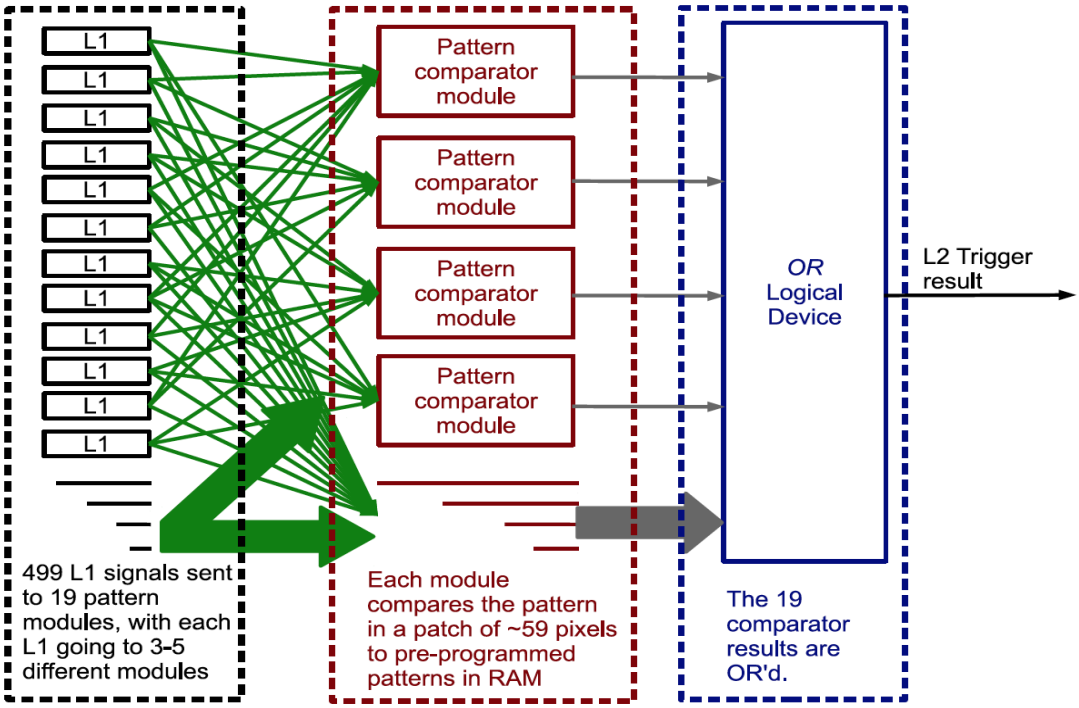

Figure 3.9: Figure 3-17, taken from [5]. Block diagram of Level 2 trigger

3.3.3 Array Trigger ("Level 3")

The array trigger operates at the multi-telescope level and is designed to fire when Level 2 signals from multiple telescopes arrive within some coincidence timing

window. The Level 2 triggers from each telescope are transmitted to the centrally located Level 3 system via high-speed optical fibre cables. Owing to the physical geometry of the array, different cable lengths are required to transmit the Level 2 signal from each telescope. This introduces a known time delay between the Level 2 triggers. In addition to this delay, the wavefront of Cherenkov light emitted by γ-ray/cosmic-ray showers does not reach each telescope at the same time, which leads to another type of delay in the Level 2 signal. These delays are corrected by a pulse delay module (PDM) before sending the signals to a sub-array trigger (SAT) board. The SAT module then determines if the delayed corrected Level 2 signal from multiple telescopes (generally 2) arrives within a certain coincidence window ($\sim$ 50 ns). If the condition is met, then it issues a Level 3 trigger to the data acquisition (DAQ) system to record that particular event.

Although the triggers due to NSB events can be removed at the Level 2 level, local muons, which penetrate deeper in the atmosphere, still become the irreducible background at a single telescope level. The reason being the similarity between the images produced by local muons and γ-ray showers in telescope camera. Using two or more telescopes in coincidence enables us to reduce the background due to local muons which results in higher sensitivity for detecting gamma-ray showers.

3.3.4 Bias Curve

In order to obtain the best sensitivity of the VERITAS array for low energy showers, while maintaining a stable trigger condition, optimal trigger parameters are required. For estimating these parameters, special runs, called bias curves, are taken, where telescope trigger rate (Level 2) and array trigger rate (Level 3) are recorded by the system as a function of CFD threshold. The optimal value of the CFD threshold corresponds to a value below which the rates are dominated by the night sky background photons and above which rates are dominated by the cosmic ray showers. For dark sky conditions, the optimal CFD threshold for each pixel is set at 45 mV, which corresponds to approximately 4-5 photoelectrons (see Figure 3.10).

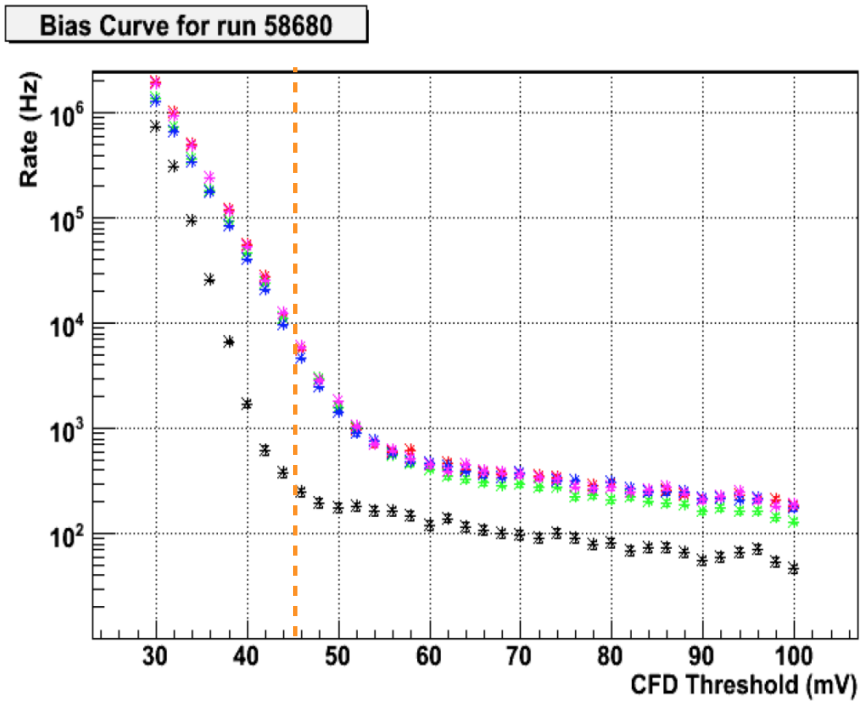

Figure 3.10: Bias curve taken under dark sky conditions. Black crosses show the Level 3 trigger rate, while the coloured crosses show Level 2 trigger rate for different telescopes. (T1: red, T2: green, T3: blue, T4:magenta). Brown dotted line shows the CFD threshold chosen to achieve low energy threshold without being falsely triggered by the noise.

3.4 Data Acquisition System

Every telescope in the VERITAS array is equipped with a photo-multiplier tube camera. When the light reflected from the telescope mirror hits a PMT, it produces an analog electrical signal. In order for this analog signal to be handled properly by computers for later analysis, it needs to be digitized. To do the digitization, the output signal from each PMT is connected to a channel on a Flash Analog-to-digital (FADC) converter board. Each board has 10 channels and in total there are 50 boards to take care of all the 499 pixels in a camera. All of the FADC boards are placed inside four Virtual Machine Environment (VME) crates that provide power to all the boards. Each crate has a computer board that is used to configure the setting on the FADC boards, such as the size of FADC buffers to be recorded, the look-back time, CFD threshold and output pulse width. There is one extra VME crate, called auxiliary crate, which holds the master clock trigger board (CTB) and the Global Positioning System (GPS) clock.

The FADC samples the signal with a 8-bit resolution at a rate of 500 MHz (2 ns). Two modes are available on each FADC channel; high gain and low gain. It generally operates in high gain mode unless the pulse amplitude exceeds the range provided by the high gain mode. In that case the signal is passed through the low gain channel where the gain is reduced by a factor of 6. The digitized signal is stored continuously to the FADC circular memory buffer which has a maximum depth of 64 μs. When the array level trigger (Level 3) is received by the FADC system, the buffering process stops. The busy signal is set on the crates, making them incapable of receiving further Level 3 triggers. Then, a segment of the FADC memory buffer is readout by the VME data acquisition system. The length of this segment (readout window; 16 samples or 32 ns) is configurable and is set such that the entire length of the pulse relevant for the event is read and stored in the VME data acquisition memory buffer (size of 8 MB). Once the readout is complete, the busy signal on the VME crates is unset and the telescope becomes ready to receive the next Level 3 trigger.

When the VME memory buffer becomes full by reading multiple events, the

VME system transfers the information of all events to a computer called "event builder" through the Scalable Coherent Interface (SCI). In addition to the FADC data, event builder also receives time stamp information from the auxiliary crate. It assembles these data to form a telescope event file and writes it to disk. The same process happens in all four telescopes at the same time. The telescope event file from each event builder is then sent to an another computer called Harvester. At the harvester, the telescope event files from all the four telescopes are combined to form an array file. This array file is of the custom VERITAS Bank Format (VBF), which has a size of about $\sim$ 12 GB for a typical 30 min run having steady Level 3 trigger rate of $\sim$ 425 Hz. At the end of the night, the harvester data are transferred to an archive where members of VERITAS can access them for off-line analysis. See Figure 3.11 for graphical illustration of the trigger system and data acquisition system.

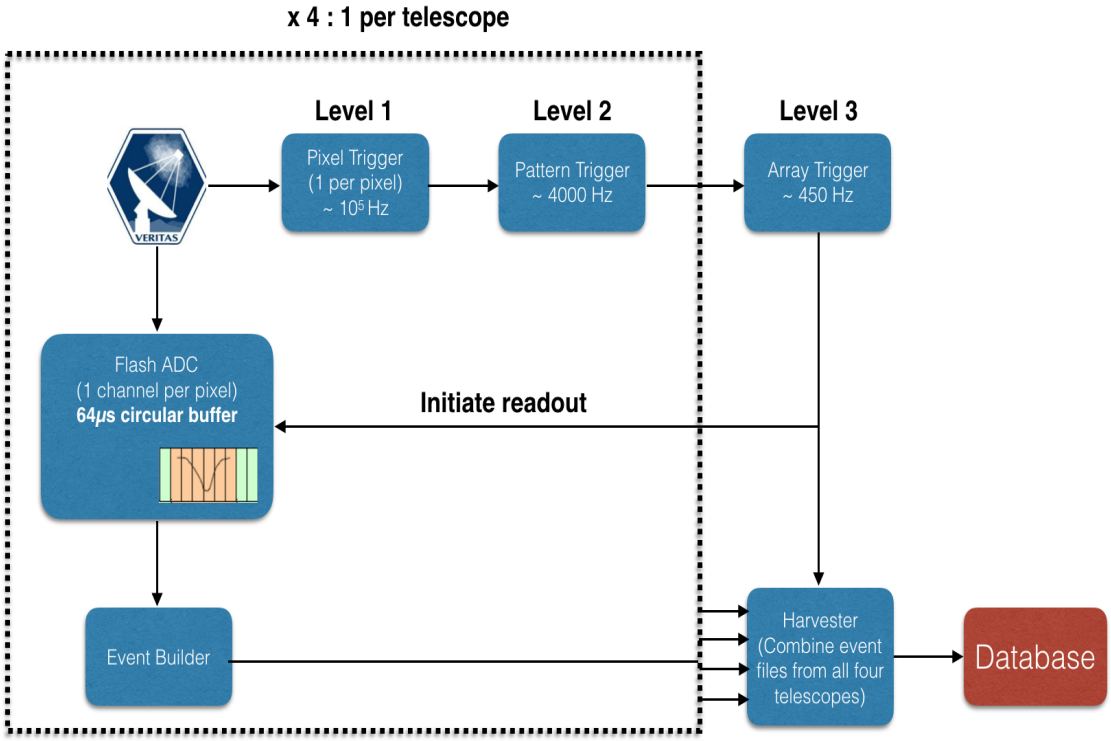

Figure 3.11: A simplified flowchart of the VERITAS trigger system and the data acquisition system.

Chapter 4

DATA ANALYSIS PROCEDURE FOR THE VERITAS ARRAY

The vast majority of events (more than 99.95%) which trigger the VERITAS telescopes consist of the isotropic flux of hadronic cosmic rays. The suppression of this huge cosmic-ray flux is required in order to successfully detect sources of γ rays. In VERITAS, this task is achieved with a multi-step data analysis procedure. The first step in the data analysis chain is the selection of good quality data, followed by the calibration of the dataset. After the calibration, an image cleaning step is required in order to select only those pixels which contain the Cherenkov light in an image. All other pixels containing night sky background light are removed from the image analysis. Cleaned images are parametrised using a second moment analysis to determine the shape and orientation of the image in each camera. The information from all of the camera images is then combined stereoscopically to reconstruct the shower direction on the sky and its core position on the ground. The next step is to suppresses the flux of cosmic rays using cuts on the shape and orientation parameters of the Cherenkov images. Although this step suppress most of the cosmic-ray induced events, there are still some irreducible gamma-like cosmic-ray events, whose directions are reconstructed close to the gamma-ray source direction. In order to estimate the number of these background events at the source position, various background estimation methods are used. Finally the significance of the source is established. If the source is statistically significant (generally above or equal to 5σ), its flux, spectral properties and morphology are determined. Otherwise an upper limit is set on the source flux.

For the analysis of data which constitute my work in this thesis, the Event-Display software package [112] is used, and all the results are cross-checked with an

independent software, VEGAS [113]. This chapter will describe the details of all the data analysis steps.

4.1 Data Selection

In order to minimise the effect of systematic errors on the final results, the selection of good quality data is a necessary first step. After making a decision on analyzing a particular source of interest (for example, Cassiopeia A & IC 443 for my thesis work), a list of all the observations of the source are compiled. During standard operations, each observation run has a time duration of 30 minutes. Previously, it was 20 minutes per run. This was changed to 30 minutes since 2009, in order to reduce the telescope slew time. A number of flags are assigned to each data run that tell the quality of the data and the conditions under which the data were taken. For example, the observers assign a grade letter (A-F) to the weather conditions during a particular run, where A means perfect weather and F means very bad weather. The flag on the weather condition is based on the observers assessment, supplemented by information from a system of three far infrared (FIR) cameras that monitor cloud cover via changes in temperature conditions. Two of these FIRs have a 2.7 degree field of view and are attached directly with the Telescope 2 and 3. The third static FIR has a wider field of view and points directly towards the zenith. In addition to that, one Light Detection And Ranging (LIDAR) system is also installed that not only monitors the presence of clouds, but also their vertical distribution. The presence of clouds can lead to absorption of Cherenkov light from the air showers and thus make the trigger rate unstable. Figure 4.1 shows the trigger rates as a function of time for two data runs; one where the sky was clear (left Figure 4.1) and the other where clouds are present (right Figure 4.1).

The quality of data can also be affected by the technical performance of the telescope system. Technical issues affecting the data mainly come from faulty camera pixels (photo-multiplier tubes), telescope tracking errors, and non-participation of one or more telescopes during the data taking process. Data taken with only two telescopes

is usually not considered as good quality data due to the poor reconstruction ability of two telescopes for air showers.

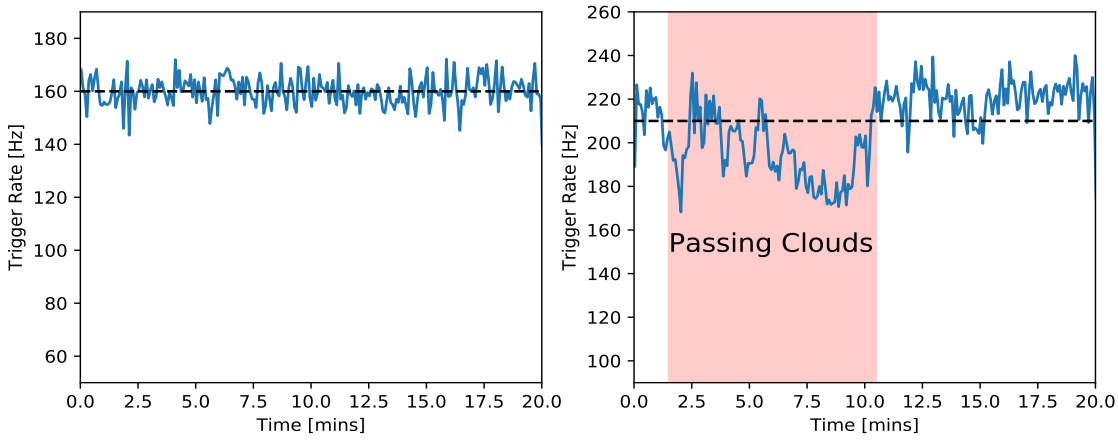

Figure 4.1: (left) The trigger rate vs time when sky is clear, (right) The trigger rate vs time when the clouds moved through the field of view of telescope.

4.2 Data Calibration

The data calibration for the VERITAS is divided into two parts; absolute calibration and relative calibration. The absolute calibration estimates the signal size in a photo-multiplier tube (PMT) that results from a single incident photon. The absolute calibration is an important input parameter for detector simulations to properly model the detector response and energy scale. The relative calibration, on the other hand, is concerned with a uniform response of the telescope. If relative calibration is not done, then a uniform light impinging on each camera pixel can result in a different output response because of different gains and timing offsets for each pixel.

There are several calibration parameters; pedestal level, relative timing alignments, relative gain corrections, and absolute gain of a pixel. These parameters are measured with the help of custom built flasher system installed on each telescope [114]. Each flasher unit contains seven ultraviolet light-emitting-diodes (LEDs). In front of each flasher, a 50 mm opal diffuser is placed, which spreads the light to illuminate the PMT camera with uniform intensity. In order to scan over a wide range of PMT and

FADC responses, the number of illuminated LEDs is continuously changed from zero to seven so that light intensity from zero to maximum can be achieved repeatedly.

4.2.1 Pedestal Calculation

Even in the absence of any Cherenkov light, positive and negative fluctuations are present in the PMT signal due to night sky background (NSB). The PMT output is connected to the AC-coupled preamplifier, which removes the steady component of the NSB and sets the baseline to zero volts. After this, the signal is sent to the FADC system for digitization. Since the FADC's cannot digitize a signal of positive polarity, it is not possible to record any positive fluctuations from NSB. To overcome this problem, a negative voltage offset, equivalent to roughly 16 digital counts (also called the "pedestal") is artificially added to the signal before digitization, such that the night sky background fluctuates around this offset voltage in the absence of Cherenkov light. Figure 4.2(a) shows the FADC trace of a single PMT recorded during an event when there is only NSB present. This event is called a pedestal event. During the data taking process, many of these pedestal events are recorded, at a constant rate of 1 Hz, by sending a forced trigger to all of the telescopes. During the offline analysis of all the recorded pedestal events, the contribution of the injected pedestal and the fluctuation around that pedestal due to NSB is estimated. The amount of charge deposited in each camera pixel by the pedestal event is calculated by integrating the FADC trace over a certain duration (I used window length of 12 ns during my analysis) and histogram is plotted. From the histogram (see Figure 4.2(b)), the mean pedestal value and the standard deviation (called "pedvar") is calculated for every pixel of each camera.

4.2.2 Relative timing calibration

In order to use the correct integration window on a FADC trace, the arrival time of the signal pulse, irrespective of any hardware delays, needs to be accurately determined. The arrival time of a signal pulse, referred to as T_{zero}, is measured from the FADC trace after subtracting the pedestal value (see Figure 4.7). It is defined as the

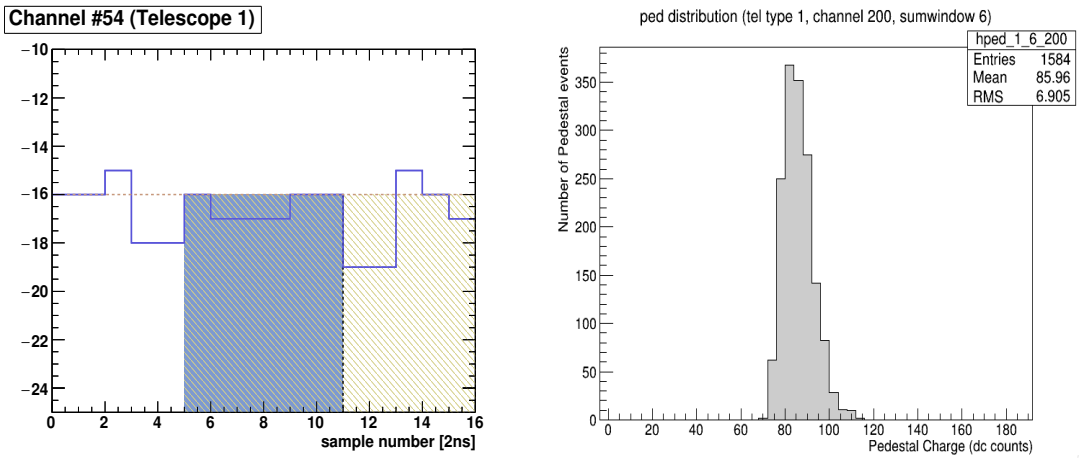

(a) (b)

Figure 4.2: (a) An example of Flash analog to digital converter (FADC) trace for a pedestal event from a single PMT. The y-axis denotes the number of digital counts. Blue region denotes the size of the window for trace integration (6 samples or 12 ns). (b) Histogram of distribution of pedestal charge for an integration window of 6 samples is plotted for telescope 1. The mean of the pedestal value is 85.96 for channel 200 and pedestal variance is 6.905.

time on the falling edge at which trace reaches half of its maximum value. Each FADC trace has a different value for T_{zero} even if a flash of light illuminates all the camera pixels at the same time. This time shift is introduced because of small differences in cable lengths from the pixels to the FADC boards, in the high voltage supplies to each pixel and other electronic delays. In order to account for these time shifts, a dedicated flasher run is taken every night which measures relative timing offsets between pixels. The timing offset for a particular pixel, also called T_{offset}, is defined as the average over all of the events, of the difference between start of the pulse on that pixel and arrival time of the event. The arrival time of each event is defined as the average over all pixels of the arrival time of the signal (T_{zero}) for all the pixels in a camera and can be written as:

$$T_{event} = \frac{1}{N}\sum_{i=1}^{N}(T_{zero})_i \tag{4.1}$$

where N is number of pixels in a camera (499 pixels in each VERITAS camera).

The time difference between the arrival time of the signal at a channel i and the arrival time of the event is defined as:

$$\Delta t_i = (T_{zero})_i - T_{event} \tag{4.2}$$

$(T_{offset})_i$ for a particular pixel is then obtained from the mean of the Δt_i distribution for a large number of events E, recorded during a laser run, as:

$$(T_{offset})_i = \frac{1}{E} \sum_{event=1}^{E} (\Delta t_i)_{event} \tag{4.3}$$

Once the timing offset for a single pixel is calculated, the relative timing offsets between all the pixels are measured. Figure 4.3(a) shows the plot of relative timing between all the pixels on telescope 3, calculated using a laser run taken during the night of 12/23/2014. It can be seen that the relative timing difference between pixels is not more than ± 2 ns for 99% of the channels.

4.2.3 Relative gain calibration

The relative gain measures the response of different pixels when they are exposed to same intensity of light. This response is a product of three factors; (1) Quantum efficiency which is defined as the number of photoelectrons emitted from the photocathode divided by the number of incident photons. (2) Collection efficiency of photoelectrons by first dynode, and (3) Multiplication of electrons in the subsequent dynode stages, called absolute gain. The first two factors are probabilistic in nature and difficult to manipulate, whereas the third factor is a function of high voltage (HV). Therefore, during every observing season, the PMT voltages are set so that the gain is adjusted in such a way as to get a uniform response from the camera. However, PMT aging, dirt accumulation on the PMT face or any other electronic factor can change the PMT response on night by night basis. This effect needs to be corrected with the help of flasher events which illuminate each pixel of the camera with equal intensity of light

photons. The average of the integrated number of digital counts from a FADC trace over all the pixels during an event is calculated as:

$$\langle DC_{event} \rangle = \frac{1}{N} \sum_{i=1}^{N} DC_i \tag{4.4}$$

where N is number of pixels in a camera (499 pixels in each VERITAS camera).

From the above equation, the relative digital counts for each pixel during an event is calculated as:

$$Rel(DC_i) = \frac{DC_i}{\langle DC_{event} \rangle} \tag{4.5}$$

The relative gain for each pixel is calculated using large number of flasher events as follows:

$$Rel.Gain_i = \frac{1}{M} \sum_{event=1}^{M} (Rel(DC_i))_{event} \tag{4.6}$$

Figure 4.3(b) shows the relative gain of all the pixels for telescope 1, using the laser run 75724 taken during the night of 12/23/2014.

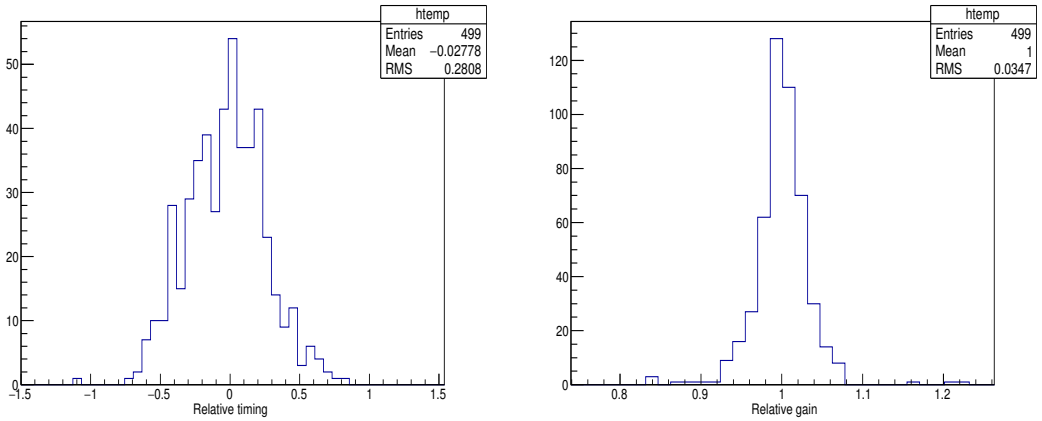

(a) (b)

Figure 4.3: (a) The distribution of T_{offset} from all of the 499 pixels in the camera of telescope 1 (b) Distribution of relative gain for all of the 499 pixels in the camera of telescope 1.

4.2.4 Absolute calibration

The main purpose of absolute calibration is to calculate a numeric factor that converts FADC digital counts to photo-electrons (p.e). The number of photo-electrons released from the PMT photo-cathode is directly proportional to the intensity of incident Cherenkov photons. Since the number of Cherenkov photons produced by an EAS is dependent upon the energy of the incident gamma-ray photons, the absolute calibration is a necessary step, required to accurately calculate the energy of the incident gamma-ray photon. To perform absolute calibration, single photoelectron (p.e.) measurements are made every few months by placing a plate with small holes in front of camera (see left side of Figure 4.4 [15]). The purpose of these holes is to attenuate the light from LED flasher reaching the PMTs and minimize the contamination of NSB. Under this low level of illumination for the majority of flashes, no photoelectron is released from PMT cathode. Occasionally, only 1 p.e. is released and very few times only 2 p.e.are released (see right side of Figure 4.4 [15]), and so on. Finally, from the positions of photoelectron peaks, the number of digital counts corresponding to a single photo-electron hitting the first dynode of PMT can be estimated (For more details see [5]). This estimation is performed for all four telescopes and the values obtained are given in Table 4.1.

Table 4.1: Relationship between photo-electrons (p.e.) to digital counts (DC)

Telescope No.	Conversion factor (1 p.e. to DC)
1	5.20 ± 0.18
2	5.12 ± 0.18
3	5.12 ± 0.24
4	5.54 ± 0.17

4.3 Flash-ADC trace summation/Charge in each pixel

The image of Cherenkov light from cosmic ray or γ ray shower is formed by recording the charge in each camera pixel. The charge is proportional to the number of

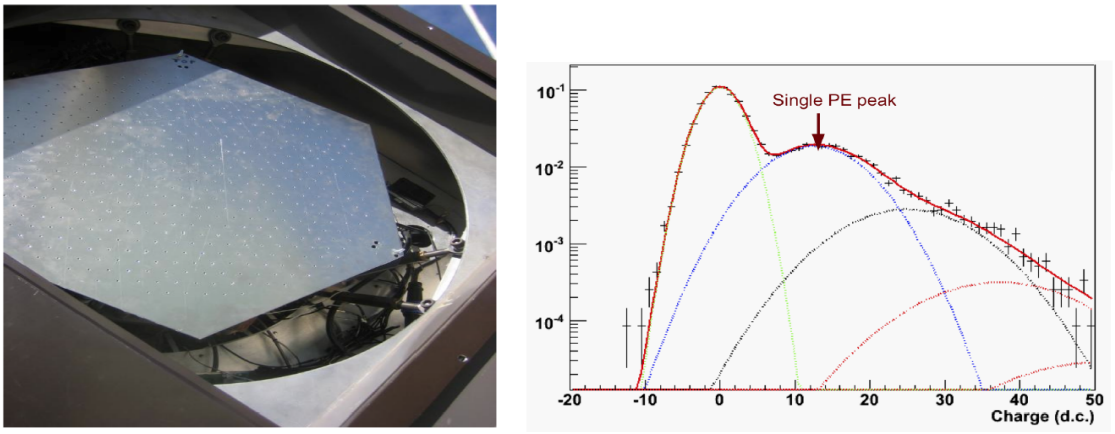

Figure 4.4: (left) "Holey plate" covering the camera of one of the VERITAS telescopes (right) Histogram showing peaks for pedestal, 1, 2 ,3 and 4 photoelectrons [15].

incident Cherenkov photons and estimated by integrating the recorded digital values of a Flash-ADC trace over a specified time window. After the integration, the charge is represented in units of digital counts (d.c.). With a sampling rate of 500 Mega-samples per second, a typical Flash-ADC trace consists of 16 samples, equivalent to a 32 ns time window (see Figure 4.7). Out of this 32 ns pulse, the real Cherenkov signal lasts for only $8-10$ ns, including time spread from the mirror and electronics. Therefore, if we integrate over the whole 32 ns window, we will also include charge from the NSB that will reduce the signal to noise ratio. In order to minimize the contamination of charge from NSB to the total charge, the pulse needs to be integrated over only that portion of trace where the Cherenkov pulse is present. This portion of the Flash ADC trace is called the signal window and it is calculated in the EventDisplay package using the *double pass method* [115]. The advantage of this method is that it takes into account the time gradient in the photon arrival times across a shower image recorded in the camera. This time gradient depends strongly on the distance between shower core and the telescope. At smaller core distances, Cherenkov photons emitted from the head of the shower arrive later than the photons emitted from the tail of the shower (negative sign of time gradient). In the case of large impact distance, the situation reverses and

the light from shower head arrives before the light from the shower tail (positive sign of time gradient). This can be understood using difference in the geometrical path lengths covered in two different scenario (see Figure 4.5).

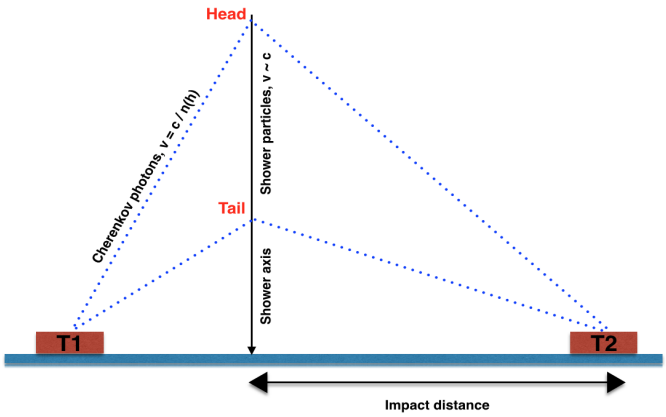

Figure 4.5: Figure 3.2 adopted from [16]. Illustration of geometrical path travelled by the emitted Cherenkov photons along the shower axis for telescope T1 and T2. For T1 (small impact parameter), Cherenkov photons from the head of the shower travel over long distance with reduced speed of $c/n(h)$, thus arrives later in camera than photons emitted from tail. For T2 (large impact parameter), photons emitted from the tail end of shower has to travel a longer geometrical path, thus they arrive later than the photons from the head of the shower.

Due to this time gradient, the start time of the integration window is different for different PMT channels lying along the image axis. In the first stage of the double pass method, a large integration window of 10 samples (20 ns) is used to calculate the charge. Besides charge, the T_{zero} value (the time at which pulse falls to half of its minimum value) is calculated. A straight line is then fit to the T_{zero} timings across all the channels in an event and, from the slope of this line, the time gradient of the event is measured (see Figure 4.6). In the second stage, a smaller integration window, with a size 6 samples (12 ns), is placed on every FADC trace. The starting position of each window is different for different channels and is determined from the time gradient calculated in first stage. Once the charge in digital counts is calculated for each pixel,

the mean pedestal value for that pixel, calculated using the same integration window, is subtracted. After this step, relative gains between pixels are applied to properly calibrate the charge in each pixel. This calibrated charge in digital counts is then used throughout the latter stages of analysis.

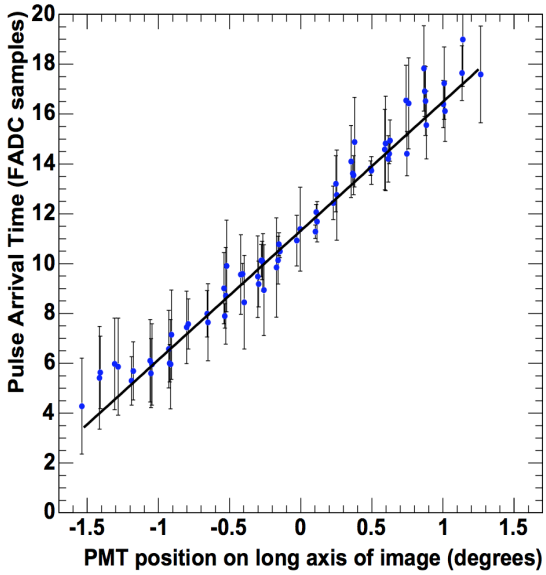

Figure 4.6: The Cherenkov photons pulse arrival time for PMTs that map the longitudinal axis of the shower (major axis of elliptical image).

4.4 Image cleaning and Parametrization

The next step of the analysis chain involves the cleaning of images, which is done independently for each telescope camera. After calculating the charge in every pixel, it is important to identify those pixels that contain Cherenkov light, while removing all other pixels where charge is dominated by night sky background fluctuations. It is also important to remove malfunctioning pixels. The image cleaning relies mainly on the "pedvar" value calculated in the calibration stage. In the first step, all pixels with a charge greater than 5 times their pedvar value are selected and branded as "image pixels". Secondly, any pixel adjacent to an "image pixel", but with a lower threshold condition (of charge greater than 2.5 times the pedvar value) is selected and labelled as

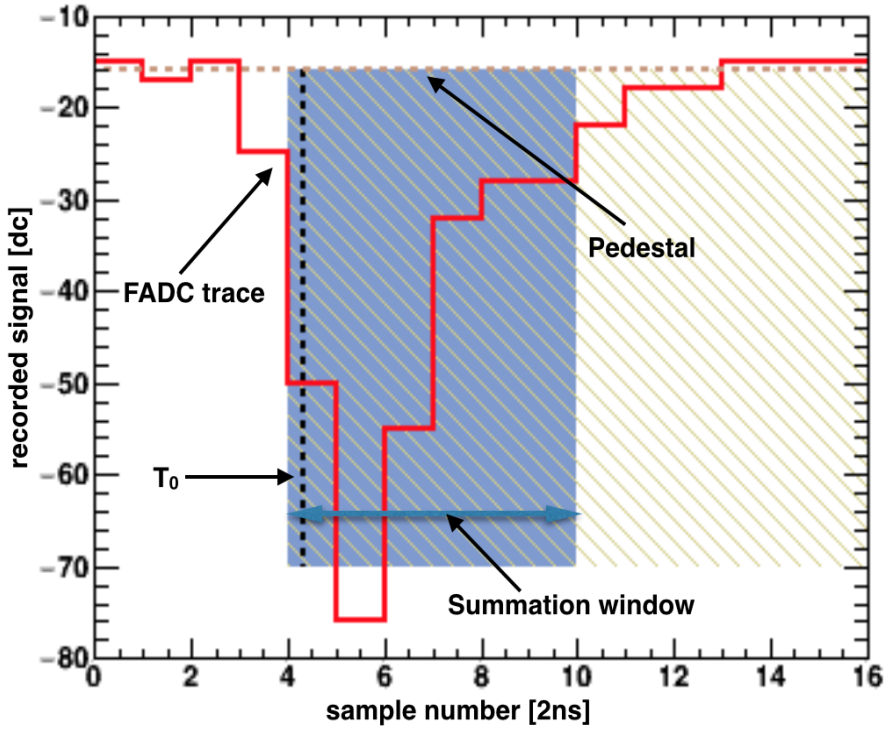

Figure 4.7: Time profile of a typical PMT pulse (FADC trace) digitized every 2 ns. The veritcal black dotted line represents the T_{zero} time, at which the pulse height reaches 50% of its minimum value. The light blue shaded region indicates the 12 ns summation window used to calculate the charge (in d.c.) in a pixel.

a "boundary pixel". If an image pixel is isolated, and does not have any neighbouring pixels, then it is removed from the image. The collection of all of the pixels which survive the above conditions of cleaning forms the final Cherenkov image.

After the images are cleaned, a moment analysis is performed on all of the surviving pixels to determine several parameters, such as width, length, size, distance etc. (see Figure 4.8 for their geometrical representation). Collectively, these parameters determine the position, orientation, shape and brightness of the images in the camera. Moments are based on the position of a pixel in the camera and its signal amplitude (in digital counts). The zeroth order moment is calculated as the sum of digital counts from all pixels that remains in the image after cleaning. The first order moment gives the centre of gravity of image in the focal plane of camera. Similarly, the second order moment describes the extent of image. The idea of representing the image in terms of a few parameters using moment analysis was first proposed by Hillas [103]. These parameters, in turn, are used for event discrimination and reconstruction. A description of all the relevant parameters which are used for analysis in this dissertation is given in Table 4.2.

4.5 Event reconstruction

After the parametrization of Cherenkov images in each telescope has been done using the Hillas method, the arrival direction and core location of each shower event is estimated using a stereoscopic imaging technique. This technique was first used by the HEGRA experiment, in which multiple telescope systems were used to image the same shower from different angles [116]. The basic principal of the stereoscopic observation is based on the idea that the major axis of the fitted ellipse maps the shower axis. When major axes from the multiple images are projected onto a common camera plane, their point of interaction gives the arrival direction of the shower. When N telescopes are used, there will be $N(N-1)/2$ intersection points, and it is important to find single intersection point from these multiple points. This is done by weighted averaging of all the intersection point; where the weights depend upon the sine of the angle between

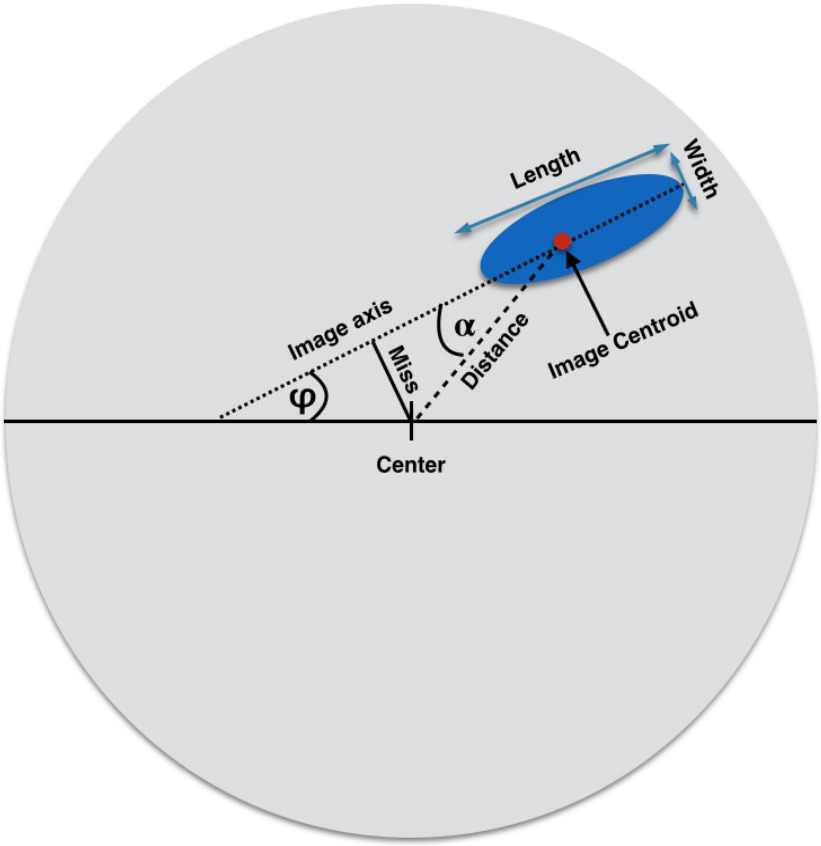

Figure 4.8: Shower image parameters for an ellipse fitted to Cherenkov image based on moment analysis. Each parameter is explained in the Table 4.2.

Table 4.2: Shower image parameter definition

Parameter	Definition
Size	Total light content of the image (in digital counts) calculated by summing charge in all of the pixels of an image
Size Second Max	The size of the second brightest image across all the telescopes that are triggered by an event
Distance	Distance from the center of camera to the center of gravity of the image
Width	RMS spread of the light along the minor axis of ellipse and represents lateral spread of shower
Length	RMS spread of the light along the major axis of ellipse and represents longitudinal spread of shower
Alpha	Angle between the major axis of the ellipse and the line joining center of gravity to the camera center
Asymmetry	Measure of the asymmetry of light distribution along the major axis of image. Gamma-ray images have their light distribution skewed towards the head
Miss	Perpendicular distance between the major axis of image and center of camera
Ntubes	Total number of photo-multiplier tubes that make the shower image; used for assessing quality of the image
Loss	The fraction of image size that is contained in the edge pixels; a measure of image containment

the image axes, the intensity (size) of the images and the ratio of width over length (elongation) for each image. The weighting is carried out to take into account the fact that image pairs with a large stereo angle provide better determination of the shower direction. Similarly, the shower core location (the point on ground where the gamma ray photon would hit if travelled directly to earth without being absorbed by the atmosphere) is determined by projecting multiple images in the shower plane coordinate system, and calculating the intersection point of the major axes. Figure 4.9 illustrates the method to calculate shower direction and core location.

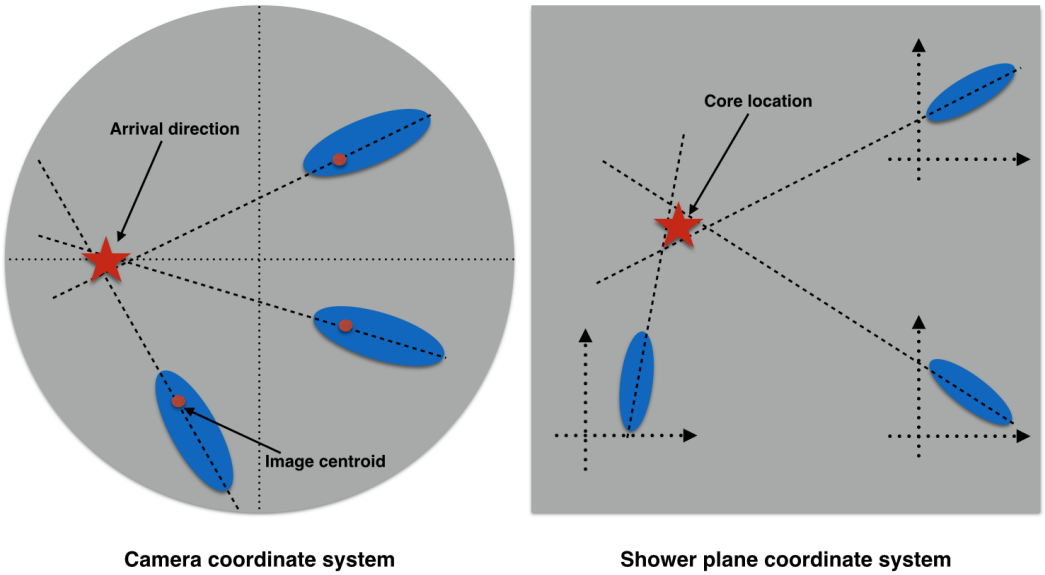

Figure 4.9: (left) Arrival direction of shower is calculated by superimposing multiple camera images into a single camera coordinate system (right) Shower core location is estimated in a similar fashion by superimposing images into shower plane coordinate system

4.6 Monte Carlo simulations and Look-up tables

It is not easy to determine certain physical quantities of interest from the data alone in ground- based gamma-ray astronomy. For example, the amount of Cherenkov light recorded in the camera scales with the energy of the primary particle initiating the shower. The amount of light recorded depends, however, upon other parameters,

such as impact distance (where the shower lands from the telescope), the amount of atmosphere it passes through, the zenith angle of observations, and the night sky background. Therefore, it is very hard to find a calibrator which can directly relate the energy of the primary particle with the Cherenkov light in a recorded image. To overcome this difficulty, it is essential to compare the real data with Monte Carlo (MC) gamma-ray simulations. The MC simulation for the VERITAS array is divided into three main steps.

In the first step, gamma-ray shower development is simulated using the CORSIKA package [8]. The showers are thrown over random azimuthal directions and uniformly cover a 750 m radius circular region on the ground. The center of the circle coincides with the center of the telescope array. Moreover, the showers are generated for different background noise levels and are divided into discrete zenith angle bins; 0°, 20°, 30°, 40° etc. The energies of gamma-ray showers are taken from a power-law distribution with a spectral index of -2. The properties of the atmosphere with which the Cherenkov photons interact is an important component of the simulations. The atmospheric transmission efficiency for Cherenkov photons is calculated based on the U.S. 1976 standard atmosphere model [1] and on local radiosonde measurements at the VERITAS site [117]. After passing through the atmosphere, the simulated Cherenkov photon information, such as impact point, arrival direction and wavelength, is recorded in a file.

In the second step, the Cherenkov photons are passed through a model of the VERITAS detector called *GrISUDet*[2] [118]. Firstly, the reflector response of the telescope is simulated by taking into account the wavelength dependent reflectively of the VERITAS mirrors, their optical alignment, optical PSF and the shadowing of the reflector by the quadrpod arms and camera housing. The camera response is simulated

[1] https://ccmc.gsfc.nasa.gov/modelweb/atmos/us_standard.html

[2] http://www.physics.utah.edu/gammaray/GrISU/

by taking into account the collection efficiency of the light cones, and the quantum efficiency of the photomultipier tubes. The complete readout chain, which includes PMT signal response, the amplifiers, the optical cables, trigger system and FADC readout, is also simulated in the detector model. Night sky background is modelled for various sky brightness levels which cover the range of noise from dark extragalactic fields to bright moonlight. Following the shower and detector simulation, the final data files are created which are identical in format to real data files. In the third step, the simulated data files are analyzed using the same software that is used to analyze the real data files.

In this analysis, the simulated gamma-ray showers are reconstructed and then parameterized by length, width, size and impact parameter. These values are used to fill lookup tables. From these lookup tables, the energy and scaled parameters (scaled width and length) for the real gamma-ray events can be calculated.

4.6.1 Simulations: Energy estimation

Energy estimation for a primary gamma-ray photon is an important step, since it allows us to perform spectral studies of a given gamma ray source. The energy of a primary gamma-ray photon is related to the amount of total charge contained in the telescope image (the size parameter), which, in turn, depends upon observing conditions such as NSB, impact distance and zenith angle for the observations. For each telescope image, the energy is estimated by using the lookup tables. Figure 4.10 shows an example of a lookup table for determining the energy from an image in telescope 3, taken at zenith angle of 20° and sky noise level of 469 photoelectrons $\mathrm{ns}^{-1}\ \mathrm{m}^{-2}\ \mathrm{sr}^{-1}$ (corresponding to a pedvar of 7.73 dc). From this, the event energy is estimated by the taking the weighted average of the energy estimates from N telescopes, where the weights are assigned according to the 90% width of the energy distribution in a particular bin of the lookup table. This results in the following formula for the

calculation of the energy of an event:

$$E_{event} = \frac{\sum_{i=1}^{N} \langle E_i \rangle / \langle \sigma_{Ei} \rangle^2}{\sum_{i=1}^{N} 1 / \langle \sigma_{Ei} \rangle^2} \tag{4.7}$$

where $\langle E_i \rangle$ is the median energy in a particular bin of the lookup table for telescope i and $\langle \sigma_{Ei} \rangle$ is 90% width in the energy distribution of that bin for telescope i.

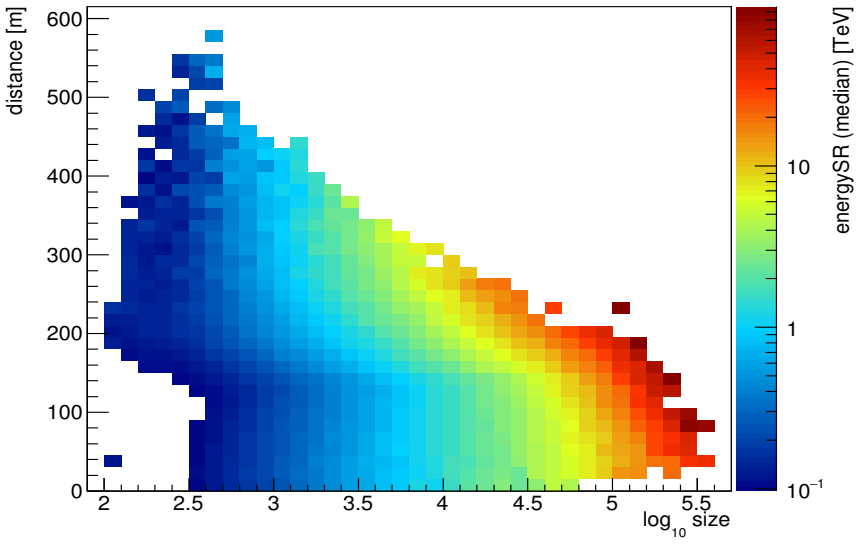

Figure 4.10: Example of a histogram in the lookup table file generated for a noise level 7.73 dc and zenith angle of 20°. This table is used to estimate the energy of an image in telescope 3. The estimation is dependent on the properties of the image parameters such as the impact distance, and the size of event (in this case). The color scale gives the estimated energy in units of Energy (TeV) in log scale.

4.6.2 Simulations: Mean scaled width and length estimation

As explained in section 2.2.1, there is an inherent difference between the image shape of a gamma-ray shower and the cosmic-ray background showers. Therefore, length and width parameters that define the image shape are very effective parameters to reject cosmic-ray background showers. However, the length and width of a shower image depends strongly on the energy of the shower, the impact distance of the core

from the telescope, the zenith angle at which observations are taking place and the night sky background (see Figure 4.11). In order to avoid this dependency, the actual length and width parameters are compared with the expected parameters stored in the lookup tables, and converted into new parameters called mean scaled width (MSCW) and mean scaled length (MSCL) which are calculated as:

$$
\begin{aligned}
MSCL &= \frac{1}{N}\sum_{i=1}^{N}\frac{length_i - \langle l(s,R,\Theta)\rangle}{\sigma_{length,MC}(s,R,\Theta)} \\
MSCW &= \frac{1}{N}\sum_{i=1}^{N}\frac{width_i - \langle w(s,R,\Theta)\rangle}{\sigma_{width,MC}(s,R,\Theta)}
\end{aligned}
\tag{4.8}
$$

where N is the number of telescopes taking part in the event reconstruction. The $length_i$ and $width_i$ are the length and width of the shower image in the ith telescope. The $\langle l(s,R,\Theta)\rangle$ (or $\langle w(s,R,\Theta)\rangle$) and $\sigma_{length,MC}(s,R,\Theta)$ (or $\sigma_{width,MC}(s,R,\Theta)$) are the expected length (width) median and length (width) standard deviation (at confidence level of 90%) calculated from the distribution of shower images stored in a particular bin of the lookup table.

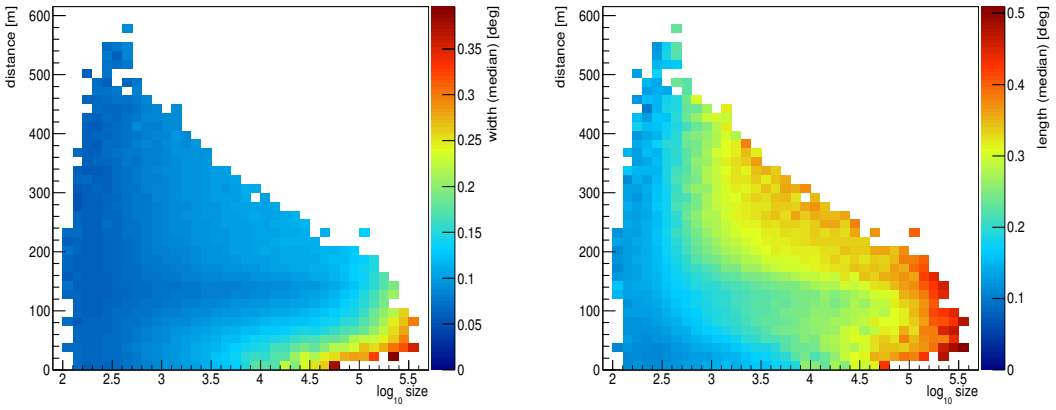

(a) (b)

Figure 4.11: (a) (b) Example of lookup tables for the Hillas parameter width (length) as a function of size and impact distance of shower from a telescope. The color scale indicates the median value for width (or length) which falls in a particular bin on the histogram .

4.7 Gamma/hadron separation

Until this step, all the events have been parameterized. For instance, with the use of the stereoscopic technique, the arrival direction and core location of an event is computed. The energy and mean scaled parameters (length and width) for every event are estimated by comparing the real events with the simulations stored in lookup tables. With all this information in hand, the remaining task to complete is the separation of gamma-ray like events from the cosmic-ray background events. Before applying the separation between gamma and hadronic showers, a set of quality cuts is applied to the images to ensure the least possible uncertainty in the parameter estimation. For example, only those images are selected that contain more than a certain value of total brightness. All the analysis done in this thesis has used a minimum Size Second Max (see Table 4.2 for definition) of 600 digital counts. Similarly, to ensure a better reconstruction of shower core and shower direction, only those showers are selected that have a signal in at least two telescopes after image cleaning. We also exclude those showers that have an impact parameter of more than 350 m (see Table 4.3).

After the quality of the images is assured, a set of standard cuts based on the shape of the shower are applied to reject the background events. As already explained in section 2.3, the width and length parameters of gamma-ray showers and cosmic-ray showers are very different. This is illustrated in Figure 4.12, in which, the mean scaled length and width parameter distribution for gamma-ray like events and background events are plotted. The distributions of mean scaled parameters for gamma-ray showers peak at zero, whereas the less compact and irregular background events are peaked at greater mean-scaled values. This allows us to define the cut values (see Table 4.3) on MSCL and MSCW (vertical green lines in Figure 4.12) parameters to reject the background showers.

4.8 Signal extraction and background estimation

Once the reconstructed events have passed the stereo quality and gamma/hadron separation cuts, they are binned into a 2D histogram, called a skymap. It is worth

Table 4.3: Quality cuts applied in the standard analysis

Cut Parameter	Value
Size Second Max	600 digital counts
N_{tel}	≥ 2
Core distance	≤ 350 m
MSCW	-1.2 to 0.5
MSCL	-1.2 to 0.7

mentioning here that not all of the binned events within the field of view come from the source of interest. Rather, a large proportion of these events are cosmic-ray showers, which arrive isotropically from the sky. These are wrongly reconstructed as gamma rays due to their resemblance with the real gamma-ray signal, i.e., their MSCW and MSCW parameters are similar to those of gamma-rays. In order to reduce these cosmic-ray background events, an ON region is defined around the putative source (location known *a prior*) using a parameter θ. θ denotes the angular distance between the arrival direction of the shower and the putative source location. The size of the ON region is determined by the θ^2 cut value. For standard point source analysis in VERITAS, the maximum allowed value for θ^2 is 0.008 deg^2. Although this θ^2 cut, in conjunction with the cuts defined in Table 4.3, greatly reduces the cosmic-ray background events, background events are still present in the ON region due to their isotropic nature (see θ^2 plot in Figure 4.13). Therefore, to extract a signal from this ON region, these background events need to be estimated. In the EventDisplay analysis package, this irreducible background is estimated by using two methods: reflected-region or ring-background method (For more details on estimating the background see [119]).

In the reflected region background estimation technique, a number of OFF regions, equidistant from the observation position, are taken. This technique is suitable if the source under investigation is a point source (or slightly extended) and the observations are taken in the "wobble mode". In wobble observations, the source is viewed at a slightly offset position with respect to camera center. For typical VERITAS observations, the wobble offset is set at 0.5° (or 0.7°) and the direction is alternated between

north, south, east and west directions. This method is based on the assumption that the cosmic ray distribution is azimuthally symmetric around the field of view (FOV), which allows us to determine the background from multiple symmetric locations with respect to the center of field of view (see left side of Figure 4.14). An exclusion region is also defined around the known gamma-ray sources in FOV to avoid the leakage of gamma-rays into the background regions. The number of events in the ON region is N_{on}. To estimate the background in the ON region, the total number of events in the OFF regions combined together, called N_{off}, are subtracted from the N_{on}. There is a normalization parameter, α, that needs to be multiplied with the N_{off} to take into account the relative area of ON and OFF regions. Since the area of OFF regions is always larger than the ON region, the value of $\alpha < 1$.

The ring background method uses an OFF region defined by an annulus around the ON region (see right side of Figure 4.14). The area of the ring is chosen such that the ratio of areas of OFF to ON regions is close to 10. The normalization in this case is given by the area ratio modified, by a weight factor to account for the radial camera acceptance correction. Such a radial acceptance curve is obtained by using gamma-ray like events from real data or Monte Carlo simulations (see Figure 4.15). Additionally, any part of the ring that overlaps with the known source or bright stars is also excluded from the background estimate.

4.9 Source detection

Once the background of gamma-ray like events has been estimated, the statistical significance for the presence of a gamma-ray source can be calculated. The most commonly used method to calculate the significance is derived by Li & Ma in 1983 [120] (equation 17 in paper).

$$S = \sqrt{2}\left\{ N_{on} \ln\left[\frac{1+\alpha}{\alpha}\left(\frac{N_{on}}{N_{on}+N_{off}}\right)\right] + N_{off} \ln\left[(1+\alpha)\left(\frac{N_{off}}{N_{on}+N_{off}}\right)\right]\right\}^{\frac{1}{2}} \quad (4.9)$$

where N_{on} is the number of photon counts in the signal region, N_{off} is the number of photon counts in the background regions and α is the normalization factor defined by ratio of area between ON region and OFF regions ($\alpha = A_{ON}/A_{OFF}$). Both the N_{off} and α parameters depend upon the background model used for estimating the background (i.e. reflected or ring background model).

In order to claim a significant source detection, a minimum value of $S \geq 5$ is generally required (denoted as 5σ) in the field of gamma-ray astronomy. This corresponds to a 99.9999997% probability that signal is not from a random fluctuation in the background.

4.10 Spectral analysis

After a source has been detected at a significance of more than 5σ in the source region, the differential energy spectrum can be calculated. The shape of the energy spectrum contains unique information about the population of the underlying particles (electrons or protons) producing gamma-rays. Calculation of the differential energy spectrum is dependent upon two quantities; the effective area of the instrument for detecting gamma-rays (A_{eff}) and the total live time (T_{live}). The live time is calculated by subtracting dead time from the actual observation time. Dead time is defined as the time during which telescope cannot register another event, since it is busy with the reading of the previous event (average readout time per event per VERITAS telescope is $\sim$ 400 μs [121]). The deadtime increases linearly with the array trigger rate. For most of the runs used in this thesis, the array trigger rate was $\sim 400 - 430$ Hz, giving a deadtime of 15-17 % of the total observation time.

4.10.1 Effective gamma-ray detection area

The effective area of a gamma-ray telescope depends upon the energy and the type of analysis cuts. To calculate it, gamma-ray showers between energies of 30 GeV

to 250 TeV are simulated over a radius of 750 m using the CORSIKA package. The effective area is then defined as:

$$A_{eff}(E) = A_{total}\frac{N_{sel}(E)}{N_{total}(E)} \tag{4.10}$$

where $N_{sel}(E)$ represents the number of simulated events passing the selection cuts for an energy E, $N_{total}(E)$ represents the total number of simulated gamma-ray showers for an energy E, and A_{total} is the total area over which simulated gamma-ray showers are thrown. It should be noted that effective area is not only a function of energy and analysis cuts. It is also a function of energy, zenith angle, offset angle between telescope pointing and source direction, azimuth angle and night sky background. Typical effective area values are plotted in Figure 4.16 for different zenith angles. Below 1 TeV (vertical line), the effective area decreases very sharply with a strong dependence on the zenith angle. This can also be interpreted as an increase in the detection threshold energy with an increase in the zenith angle. Thus, to increase the sensitivity of the instrument for low energy gamma-ray showers, it is important to observe the source at small zenith angle.

Observations at large zenith angle (LZA) have their own advantages. Comparison of effective areas above 1 TeV shows that as the zenith angle increases, the effective area also increases. This can be understood using the simple illustration in Figure 4.17. Most of the Cherenkov light from a gamma ray induced shower is emitted near the point of shower maximum. For a particular energy E, the distance between the point of shower maximum and the detector (D) depends upon the angle at which observations are taking place. At LZA, the total atmospheric depth increases considerably and the shower develops in the upper layers of the atmosphere, which leads to a larger geometrical distance between shower maximum and detector. This has a consequence of decreasing the intensity of Cherenkov light on ground. The decrease in the intensity of Cherenkov light for LZA observations results in a higher detection threshold, because low energy showers cannot trigger the telescope (the trigger depends upon the size of the image in camera i.e. the number of photoelectrons). At the same time, LZA

showers also generate a larger pool of Cherenkov light on the ground, thus increasing the effective area for high energy showers (high energy showers can still trigger the telescope easily because the photon intensity is still higher than the trigger threshold) [122, 123].

4.10.2 Differential flux Measurements

The differential energy spectrum is defined as the number of γ-ray photons observed per unit time, per unit area and per energy interval, and can be written as:

$$\frac{dN(E)}{dE} = \frac{N_{excess}(E)}{A_{eff}(E)T_{live}dE} \tag{4.11}$$

where $N_{excess} = N_{on} - \alpha N_{off}$ describes the excess number of events in the source region, A_{eff} describes the effective area of the instrument to detect γ-rays, T_{live} is the live time calculated from the observation time after applying the dead time corrections, and dE defines the width of the energy bin for which flux is being calculated. Generally, the data on a given γ-ray source is accumulated by multiple observations, where each observation last for 30 mins or 20 mins. Moreover, each observation is taken under different noise levels and zenith angles. By combining these multiple observations, a time averaged differential spectrum of a γ-ray source is calculated as:

$$\frac{dN(E)}{dE} = \frac{\sum_{i=0}^{n} N^i_{excess}(E)}{\sum_{i=0}^{n} A^i_{eff}(E)T^i_{live}dE} \tag{4.12}$$

where i denotes index of n observation runs.

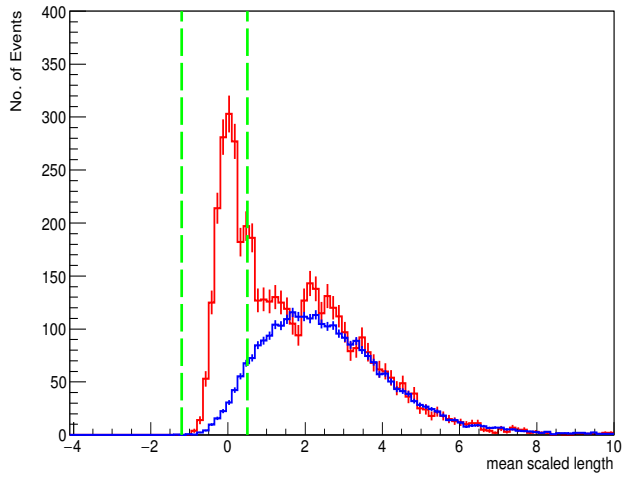

(a)

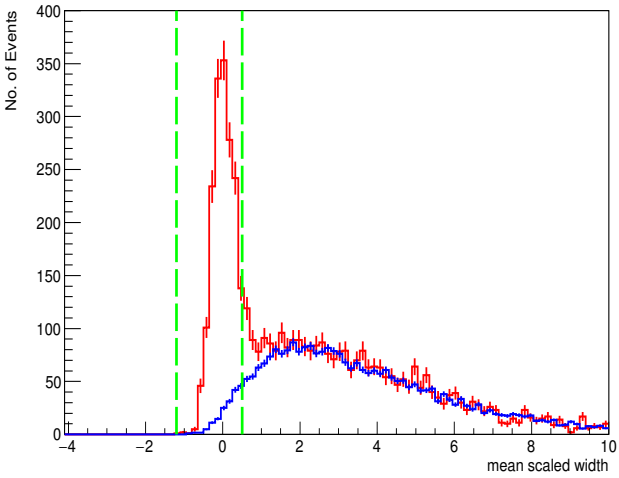

(b)

Figure 4.12: (a) The mean scale length distribution, (b) The mean scale width distributions. These distributions are obtained from one of the strongest sources of gamma-rays; Crab Nebula. In all plots, the red histogram represents the source regions (ON regions) and blue histogram represents the background regions (OFF regions). The vertical dashed green lines indicate the standard cut values for the parameters, given in Table 4.3. These cuts are used to suppress the background noise.

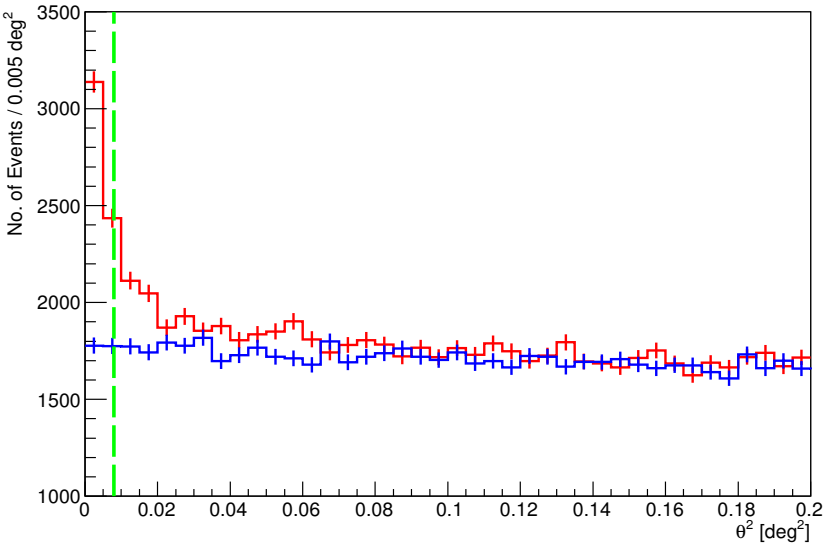

Figure 4.13: Plot of the distributions are obtained from one of the strongest sources of gamma-rays; Crab Nebula. In all plots, the red histogram represents the source regions (ON regions) and blue histogram represents the background regions (OFF regions). The vertical dashed green lines indicate the standard cut values for the parameters

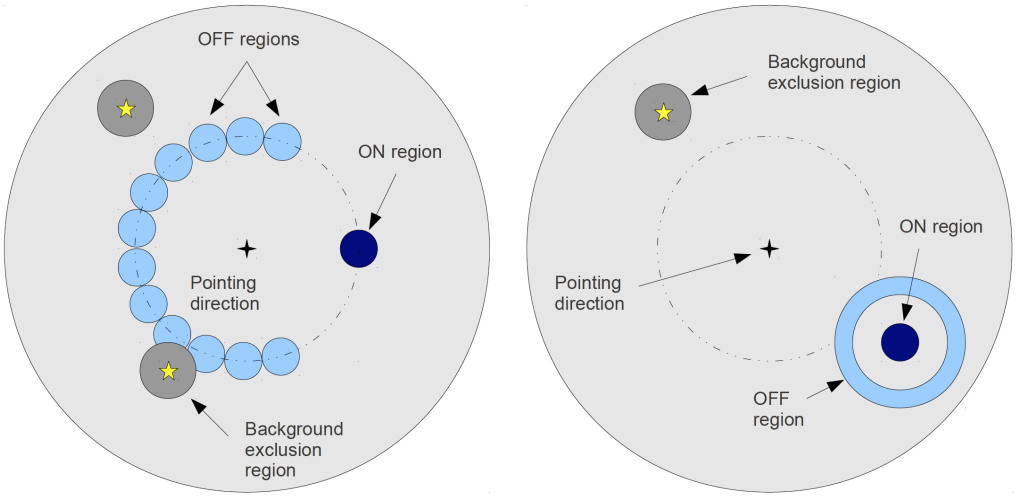

Figure 4.14: Figure 4.14 taken from [14]. (left) Reflected region background model, (right) Ring background model.

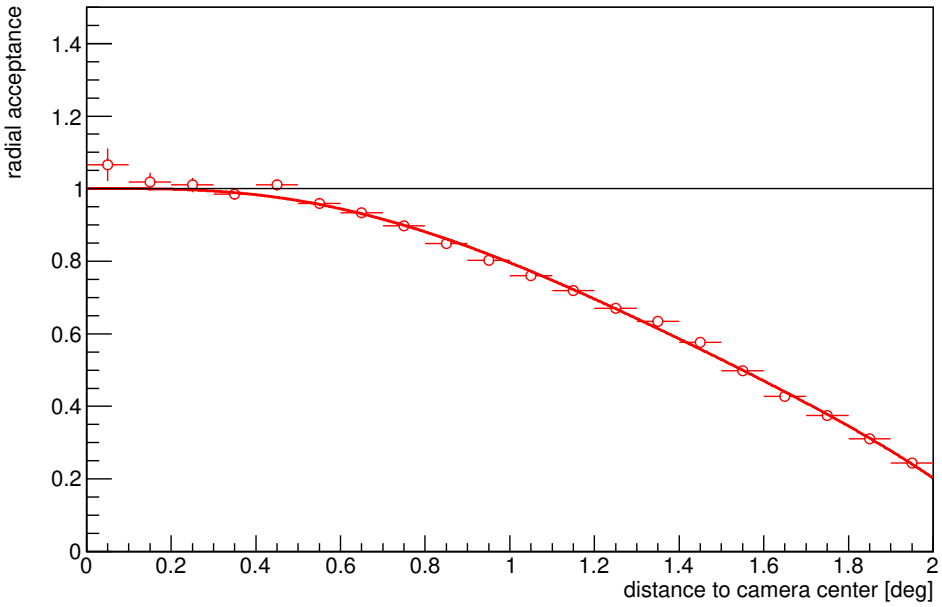

Figure 4.15: Radial Acceptance of gamma-ray like events in the camera as a function of distance from the camera center in degrees. The solid red line denotes the fit to the data and black line shows the level of full acceptance.

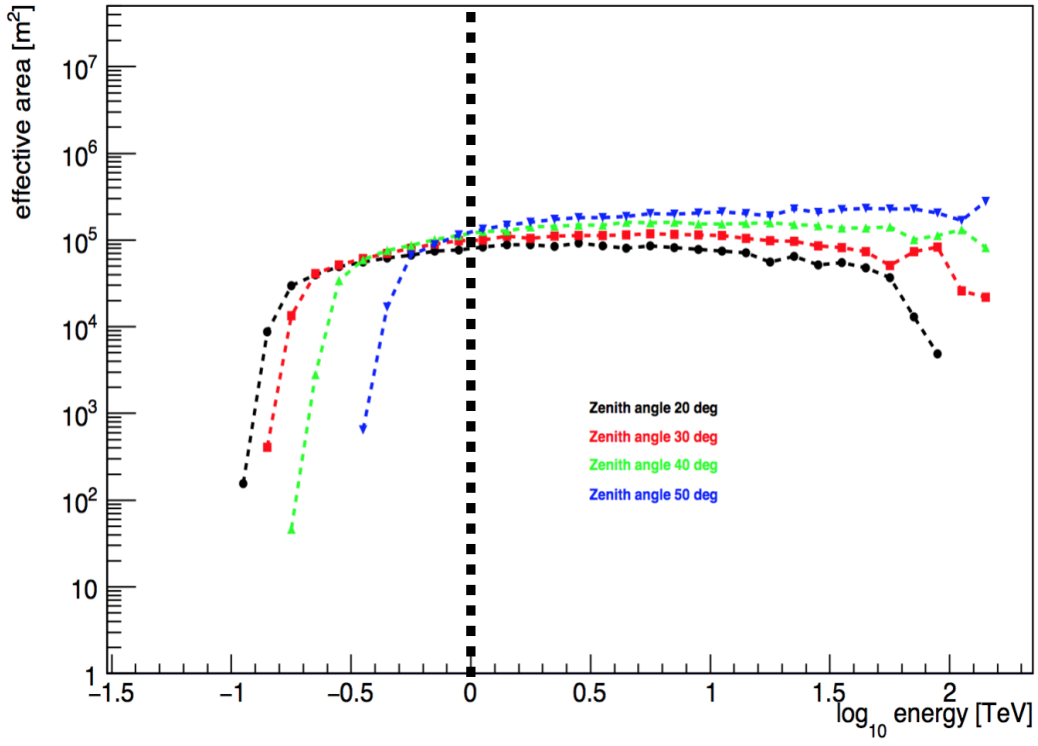

Figure 4.16: The plot of effective area of VERITAS as a function of energy at four different zenith angles.

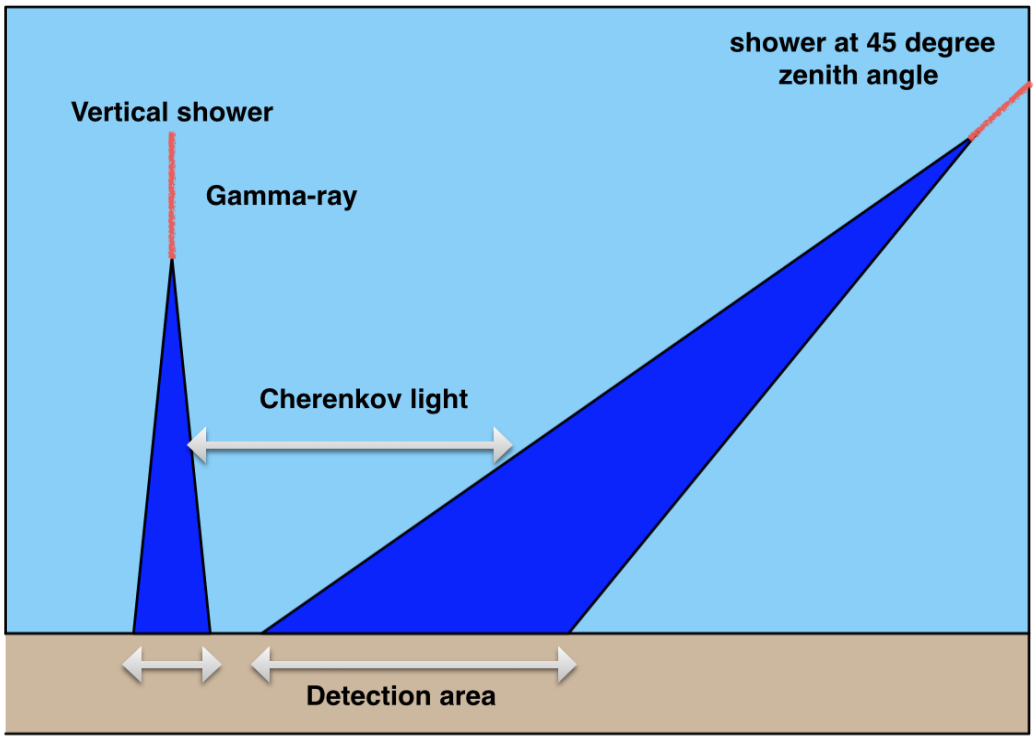

Figure 4.17: Comparison between the Cherenkov light pool area for a vertical shower and a shower at large angles. As the angle increase, the shower maximum develops higher up in the atmosphere and the Cherenkov light spreads out further, which results in illumination of larger area on ground.

Chapter 5

SUPERNOVA REMNANTS AT GEV-TEV ENERGIES

Supernova remnants (SNRs) are the remains of a star which underwent a supernova explosion at the end of its life. SNRs are important, since they play a key role to understand the evolutionary stages of the progenitor star prior to its explosion. In SNRs, we can observe the chemical elements that are synthesized in stars via the fusion process in the core of star. These elements are then dispersed into the interstellar medium (ISM) after the explosion of the star, leading to the chemical enrichment of galaxies. Moreover, the supernova types, especially type Ia supernovae, are an invaluable tool for measuring large distances in the Universe due to their high brightness [124]. This has profound implications for modern cosmology, as they have been used to demonstrate that the expansion of the Universe is accelerating.

Supernova explosions are known as one of the most energetic phenomena occurring in our Universe, in which kinetic energy on the order of 10^{51} erg is believed to be deposited into the ISM. Due to this huge kinetic energy, stellar matter is ejected at high speeds ($\sim$ 30000 km/s) into the dilute ISM (density $\sim$ 1 particle cm^{-3}). This interaction between high speed stellar material and the ISM forms a strong shock wave in front of the ejecta, and heats the ISM to a temperature of millions of kelvin. This high temperature material emits X-rays that have been observed with a number of satellite instruments, such as *Suzaku* and *Chandra*. Diffusive shock acceleration theory predicts that a significant fraction of the shock energy ($\sim$ 10%) is also used to accelerate highly relativistic particles (called cosmic rays). Observations in X-rays reveals that electrons are accelerated to an energy of 100 TeV in some SNRs [125]. However, whether protons, which account for 99% of the cosmic ray particles, are efficiently

accelerated or not in SNR, is still a puzzle. To solve this puzzle, observations of SNRs in GeV and TeV gamma rays are very important.

Understanding and interpreting GeV-TeV gamma-ray emission from SNRs requires knowledge about supernova explosion types, the overall dynamical evolution of SNRs, shock acceleration theory and radiative processes. In this chapter, we will review all these topics and connect them with the recent observational results at GeV-TeV energies.

5.1 Supernova and their classification

Supernova events are exploding stars. They are a rare phenomenon in our own Galaxy, if we consider the time span of human life. On average, 2 to 3 supernova explosions occur per century in the Milky Way [126], although many of them remain concealed due to Galactic dust and gas. For example, the supernova explosion of Cassiopeia A occurred around 1680 but was not recorded by anyone on Earth. Thick clouds of gas and dust might have absorbed the light from the explosion, making it optically invisible. The earliest recorded supernova explosion was that of the SN 185, witnessed in 185 A.D. by Chinese astronomers. This supernova was visible for eight months in the sky and was probably the supernova associated with young SNR RCW 86 [127]. Since that time, several other supernovae explosions have also been observed in sky in 1006, 1054, 1181, 1572. The most recent seen supernovae explosion in our Galaxy was that of SN 1604, observed by Johannes Kepler.

Conventionally speaking, supernova explosions (SNe) fall into two main categories; Type I and Type II. This is based primarily on the presence (Type II) or absence (Type I) of hydrogen lines in their spectra taken near maximum brightness. Type I SNe are further divided according to the presence or absence of silicon and helium lines in their spectra. If a silicon line at 615 nm is present near peak light, it is classified as Type Ia. If silicon is not present but He I at 587 nm is present, it is called Type Ib. However, if both silicon and helium lines are absent, it is classified as Type Ic

SNe. Figure 5.1 shows the classification scheme based on the spectral features (see this reference for details [128]).

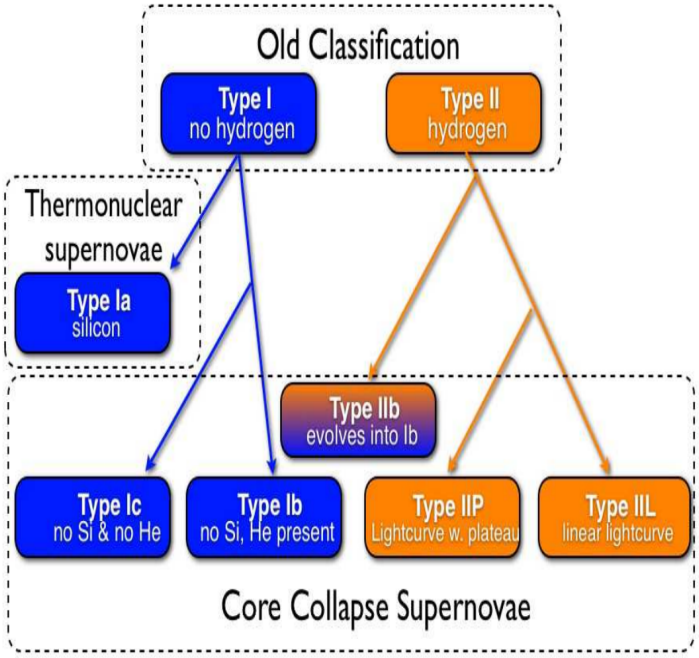

Figure 5.1: Figure 2 taken from [17]. Supernova explosion classification scheme based on spectroscopy and light curves.

Type Ia supernova are the result of the thermonuclear explosions of white dwarfs that are close to the Chandrasekhar mass limit ($M_{ch} \sim 1.38 M_{\odot}$). This type of explosions occur in a binary system - two stars orbiting each other. One of the stars in the binary system must be a white dwarf, a dense star about the size of our sun composed of carbon and oxygen. The other star can be anything from a giant star (single degenerate) to a compact white dwarf star (double degenerate). When the white dwarf approach Chandrasekhar mass after sufficient accumulation of mass from companion star or merger with another white dwarf, electron degeneracy pressure which supports the white dwarf against gravity, becomes unable to prevent the star from contraction. This contraction, in turn, raises the central temperature of star. Once the temperature

is larger than 10^9 K, ignition of carbon burning starts. These nuclear reactions create more energy than the gravitational binding energy which results in thermonuclear explosion of the star as a Type Ia supernova. The prototypical example of a Type Ia Supernova, confirmed from the optical spectrum obtained from a scattered light echo, is Tycho Brahe's supernova of 1572 (SN 1572) [129].

Contrary to Type Ia SNe, Type Ib, Type Ic and Type II supernovae result from the core-collapse of massive stars; i.e. stars with initial mass $> 8M_{\odot}$. During the course of stellar evolution, massive stars burn carbon as well as heavier elements in their core until the iron group is reached. Since the iron nucleus is tightest bound in the periodic table, the fusion reaction is exothermic in nature; meaning energy is required for the reaction to proceed. At this stage, nuclear reactions stop and the core starts to cool down. This leads to the loss of balance between gravity and the pressure force (due to core heating), resulting in the collapse of the core upon itself. Depending upon the mass of the progenitor star, the collapsing core can either become a neutron star or a black hole. The total gravitational energy released by the collapse of the core to a neutron star is given by:

$$\Delta E \simeq \frac{3}{5}\frac{GM_{NS}^2}{R_{NS}} - \frac{3}{5}\frac{GM_{NS}^2}{R_{core}} \simeq 10^{53} \text{ erg} \tag{5.1}$$

A large fraction of this energy is liberated in the form of thermal neutrinos in the $10-30$ MeV energy range. Observational evidence for this has also been confirmed with the detection of neutrinos from SN 1987A [130, 131]. Apart from compact stellar remnants such as neutron stars or black holes, there is the outer envelope of the star, which is ejected with a high kinetic energy, amounting to about $\sim 1\%(10^{51}$ erg) of the gravitational binding energy. This energy is released in the form of shock waves that heat the stellar envelope. Moreover, particles are believed to be accelerated to relativistic energy at these shocks.

Type II SNe are divided, based on optical spectroscopy and characteristics of their light curves, into three categories; Type IIP (plateau), Type IIL (linear) and Type IIb. A star in the red supergiant phase, when a substantial amount of hydrogen is still

present, explodes as a Type IIP supernova, and the light curve after the peak brighness shows a flat stretch known as plateau. Type IIL progenitors also explode in the red supergiant phase, but with a lower mass of hydrogen present, due to stellar wind mass loss or interaction with companion star. In Type IIL, the light curve shows a linear decline after the peak brightness. Type IIb shows mixed characteristics of Type II and Type Ib at different stages. Initially, their spectra resembles Type II, but at later times they evolve into spectra of Type Ib. This is due to the loss of a substantial amount of hydrogen rich envelope due to stellar wind loss. Recently, studies of Cassiopeia A based on light echoes shows that it is a remnant of a Type IIb SN [132].

5.2 Dynamical evolution of SNRs

When a supernova explosion occurs, stellar material, with a velocity of the order of 10^4 km/s, is ejected into the surrounding interstellar medium (ISM). Since the velocity of the ejecta is much higher than the local sound speed, a shock wave is created, the evolution of which may be an extremely complex phenomenon. This is due to the fact that, at the time of explosion, every star has a different spatial density profile of the ejecta and surrounding material. Still, a simplified analytical framework can be used to model the SNR evolution. The principal quantities that regulate the evolution of the SNR are the explosion energy, E_{SN}, total ejected mass ,M_{ej} and the density of the surrounding medium, ρ_{ISM}. In this standard picture, the evolution of SNRs is divided into four phases: the free expansion phase where ejecta mass dominates over the swept-up mass from the ISM, the Sedov-Taylor phase where swept-up mass starts to dominate but the SNR still evolves adiabatically, the radiative phase where radiative cooling becomes important, and finally the dissipative phase, in which the shock wave velocity becomes comparable to the surrounding material velocity and the SNR merges with the ISM.

5.2.1 First Phase: Free expansion

Initially, ejecta material expands almost freely at very high constant velocity; of the order of 10^4 km/s. Since the mass of the swept up matter from the circumstellar medium is very small compared with the mass of the ejecta, it is also called the ejecta-driven phase. This means that the evolution is mainly dependent on the initial properties of the explosion. If E_{SN} is the initial energy of SN the explosion then:

$$E_{SN} \sim \frac{1}{2} M_{ej} v_{ej}^2 \tag{5.2}$$

where M_{ej} is ejected mass and v_{ej} velocity of the ejected mass. This above equation can be written as:

$$v_{ej} \sim 10^4 \text{ km/s} \left(\frac{E_{SN}}{10^{51} \text{ erg}} \right)^{1/2} \left(\frac{M_{ej}}{M_\odot} \right)^{-1/2} \tag{5.3}$$

With such a high speed of the expansion of the ejecta in the forward direction, a strong shock is created in the ISM medium, called the forward shock. ISM medium is accumulated and heated behind this forward shock. The shocked ISM material is separated from the ejecta material by an imaginary boundary, called the contact discontinuity. Behind the contact discontinuity a reverse shock starts to form in the ejecta medium. Figure 5.2 shows the schematic representation of the evolution of a young supernova remnant.

Since the forward shock wave moves relatively freely through the surrounding medium, without any deceleration, the expansion radius R of the shock wave is given by $R = v_{ej}t$. Therefore, in the free expansion phase, the radius of the SNR increases linearly with time. As the shock wave sweeps-up more and more mass with time, its velocity starts to decrease. Generally speaking, when the swept-up mass becomes equal to the ejecta mass, it marks the transition between free expansion phase and Sedov-Taylor phase. At this stage, the swept-up mass is given by $\sim (4\pi/3) R_{trans}^3 \rho_{ISM} = M_{ej}$, defining R_{trans} as the radius of the remnant (or shock) at which the free expansion phase becomes the Sedov-Taylor phase. The interstellar density can be approximated as $\rho_{ISM} = m_H n_0 + m_{He} n_{He} = 1.4 m_H n_0$. Here we assume that $n_{He} = 0.1 n_0$, where n_0

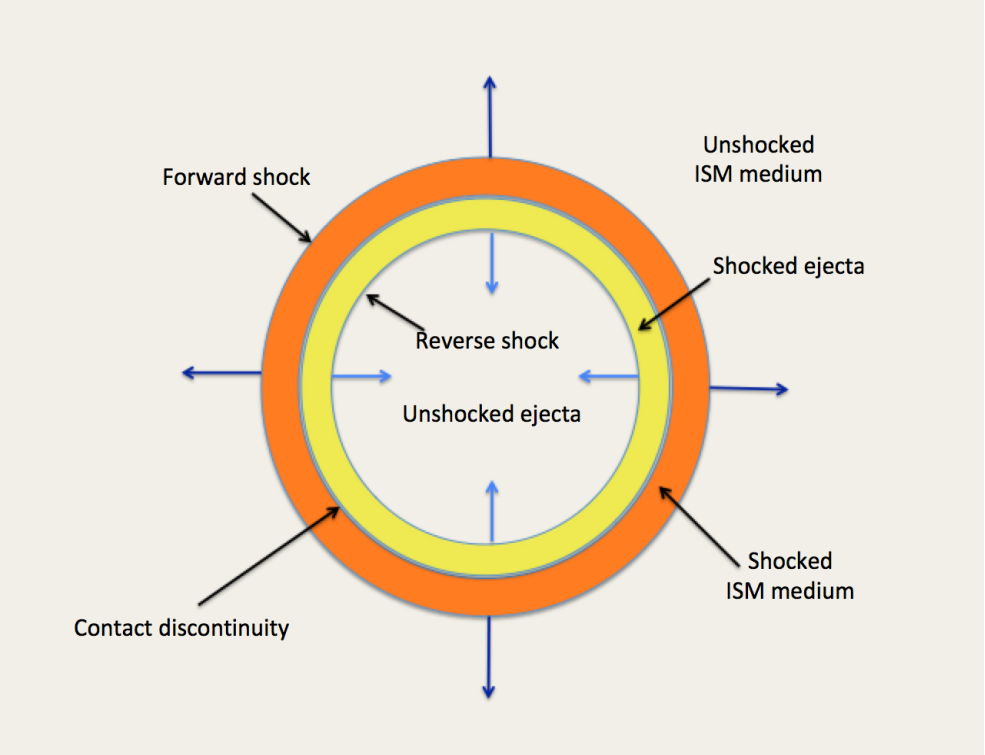

Figure 5.2: Schematic representation of the evolution of a young SNR. A forward shock is travel into the ISM medium, whereas the reverse shock travels back into the freely expanding supernova ejata.

is the unshocked proton number density . From this the radius is calculated as follows:

$$R_{trans} \sim \left(\frac{3}{4\pi}\frac{M_{ej}}{\rho_{ISM}}\right)^{1/3} \sim 2 \text{ pc}\left(\frac{M_{ej}}{M_{\odot}}\right)^{1/3}\left(\frac{n_0}{\text{cm}^{-3}}\right)^{-1/3} \tag{5.4}$$

From the radius, one can calculate the approximate time at which the free evolution phase ends as:

$$t_{trans} \sim \frac{R_{trans}}{v_{ej}} \sim 200 \text{ yr}\left(\frac{E_{SN}}{10^{51} \text{ erg}}\right)^{-1/2}\left(\frac{M_{ej}}{M_{\odot}}\right)^{5/6}\left(\frac{n_0}{\text{cm}^{-3}}\right)^{-1/3} \tag{5.5}$$

A more general expression for the variation of shock radius with time in the early stage evolution of SNRs is calculated by Chevalier [133]. This is required because the assumption of uniform interstellar matter density is not applicable for massive stars which, in their latter stages of evolution, modify their environment through strong stellar winds. In that case, the circumstellar density profile varies as R^{-s}, where s can take the value $s = 0$ (constant density medium) or $s = 2$ (Stellar wind density profile). Moreover, a freely expanding ejecta also has uniform inner core and an outer density profile which varies as R^{-n}. From the numerical modelling of SNe, a value of $n = 7$ describes Type Ia SNe and a value of $n = 9 - 12$ is a reasonable approximation for core collapse SNe. From these modifications, the radius of the SNR is described as:

$$R \propto t^{\beta} \tag{5.6}$$

where β is called the expansion parameter and given by:

$$\beta = \frac{n-3}{n-s} \tag{5.7}$$

For $s = 0$, $n = 7$, β becomes 0.57, and for $s = 2$, $n = 9$, β becomes 0.86. This shows that, in a realistic case, β varies from 0.57 to 0.86. This is different from the value of 1 ($R \propto t$) which we assume in the free expansion stage from the standard picture. This value of β is justified through observational study of the expansion of SN 1993J in the galaxy M81. The expansion parameter in this case is estimated at a value $\beta = 0.85 \pm 0.005$ [134].

5.2.2 Second phase: Sedov-Taylor

When the mass of ISM material swept-up by the forward shock becomes comparable and starts to dominate over the shocked ejecta mass, the Sedov-Taylor phase starts. The shock is still strong in this stage and the energy loss from the hot interior through radiation is negligible. This means that the remnant expands adiabatically and the evolution can be defined by the Sedov [135] and Taylor [136] self-similar solutions. In the Sedov-Taylor stage, the expansion radius is given by:

$$R = \left(\xi \frac{E_{SN}}{\rho_{ISM}}\right)^{1/5} t^{2/5} \tag{5.8}$$

where ξ is a dimensionless constant whose value depends upon the adiabatic index γ. For non-relativistic monoatomic gas ($\gamma = 5/3$), $\xi = 2.026$ [137].

From the observed SNR radius, the forward shock velocity is calculated as:

$$V = \frac{dR}{dt} = \frac{2}{5}\left(\xi \frac{E_{SN}}{\rho_{ISM}}\right)^{1/5} t^{-3/5} = \frac{2}{5}\frac{R}{t} \tag{5.9}$$

For a generalized case, where the circumstellar medium density profile varies as R^{-s}, the radius of the shock is written as $R \propto t^{\beta}$, with $\beta = 2/(5-s)$. Again, the value of β shows deviation from the standard value of $\beta = 2/5$ in the Sedov-Taylor phase. The case of the Cassiopeia A (Cas A) remnant is relevant here, since this is believed to be in the early Sedov phase and evolving in the wind of its progenitor star ($s = 2$). A value of $\beta = 0.63 \pm 0.02$ is calculated based on the expansion in X-rays [138], which is close to the value of 2/3 calculated from the analytical expression for β.

At the age of $\sim 10^4$ yr, the temperature of the shocked gas has fallen to less than one million K, and radiative loss starts to dominate the SNR evolution. This marks the end of the Sedov phase.

5.2.3 Third phase: Radiative or snowplow phase

In this phase, energy is no longer conserved. This is because, as the temperature falls, some ions start to recombine and radiate energy through emission lines in the optical waveband. The inner parts of the SNR are still expanding adiabatically and

exert an outward pressure on the outer shell. This expansion of the SNR is governed by momentum conservation, which can be written as:

$$\frac{d}{dt}[Mv] = \frac{d}{dt}\left[(\frac{4\pi}{3})\rho R^3 \dot{R}\right] = 0 \tag{5.10}$$

The radius of the SNR in this phase is approximated by Woltjer [139]:

$$R = R_{rad}\left[\frac{8}{5}\frac{t}{t_{rad}} - \frac{3}{5}\right]^{1/4} \tag{5.11}$$

where R_{rad}, t_{rad} refers to the value of radius and time at the transition from Sedov to radiative phase.

5.2.4 Fourth phase: Dissipative stage

In the final stage of the SNR, the decelerating forward shock eventually reaches a velocity which is comparable to the sound speed of the surrounding medium ($\sim$ 10 km/s). The SNR material dissipates and merges with the ISM. The full evolutionary time scale, from explosion to dissipation, takes about $10^5 - 10^6$ years.

5.3 Particle acceleration at SNR shocks

SNRs have long been considered as the prime candidates for the acceleration of Galactic cosmic-ray particles [140], at least to an energy of 10^{15} eV. The main reason for this connection is based on the argument that supernova explosions can supply the energy required to maintain the cosmic ray energy flux in our Galaxy. The inferred value of cosmic ray energy density is equal to $\sim 1 - 2$ eV cm^{-3} [141]. If these cosmic rays are confined in a Galactic volume (V_D) of $\sim 10^{67}$ cm^3 for a characteristic time (τ_R) of $\sim 10^7$ years, then the power required is calculated as $dE/dt = V_D\rho_E/\tau_R$ $\sim 5 \times 10^{40}$ erg/sec. This power requirement can be achieved if 10% of the total energy output of the supernova explosion (typically 10^{51} ergs), with a rate of 2-3 per 100 years, can be converted into CR energy.

Although supernova explosions fulfill the energy requirement for the acceleration of cosmic rays, the debate is still open about the mechanism which accelerates particles

to such a high energy. To explain this, diffusive shock acceleration (DSA) or first-order *Fermi* mechanism is widely accepted as the principal mechanism for the acceleration of the cosmic rays. The DSA theory naturally explains the experimental observations of a power law spectrum of cosmic rays, and further reinforces the energy-based argument of SNRs as the sources of cosmic rays. Within the DSA framework, the maximum number of particles are accelerated when the SNR evolves from the end of the free expansion phase to the Sedov-Taylor phase, typically $10^3 - 10^4$ years after the SN explosion [142]. After the Sedov phase, the shock speed slows down, which makes the DSA process inefficient for further particle acceleration.

5.3.1 First order Fermi acceleration (or diffusive shock acceleration (DSA))

It was Fermi [143] who first proposed that cosmic ray particles can be accelerated when they are deflected repeatedly by moving magnetized clouds. In this process, particles gain energy if they encounter the clouds "head-on" and lose energy if they hit the cloud "tail-on". However, this simplistic explanation is not always true. For example, the results derived by Gaisser [19] in his book (section 11.2.2 of the book) shows that it is not always true that the particles colliding head-on will always gain energy and overtaking particle collisions will always lose energy. But still, after many encounters, there is a net gain of energy. Later, it was proposed by various authors [144, 145, 146, 147, 148] that the particles can be accelerated more efficiently at collisionless shocks. When a particle bounces back and forth by crossing this shock, the collision is always head-on, thus the acceleration of the particle is much more efficient compared to the original idea proposed by Fermi. This process is known as first order Fermi acceleration. This type of acceleration takes place in the vicinity of strong shock waves, for example, those caused by supernova explosions and the jets of active galactic nuclei.

Let us assume that the shock front moves at a velocity of U from left to right. We denote the variables in the upstream region (unshocked region) by ρ_1, v_1, P_1 and in the downstream region (shocked region) by ρ_2, v_2, P_2. if we assume that the shock is adiabatic and that the gas is a monatomic ideal gas with a ratio of specfic heats

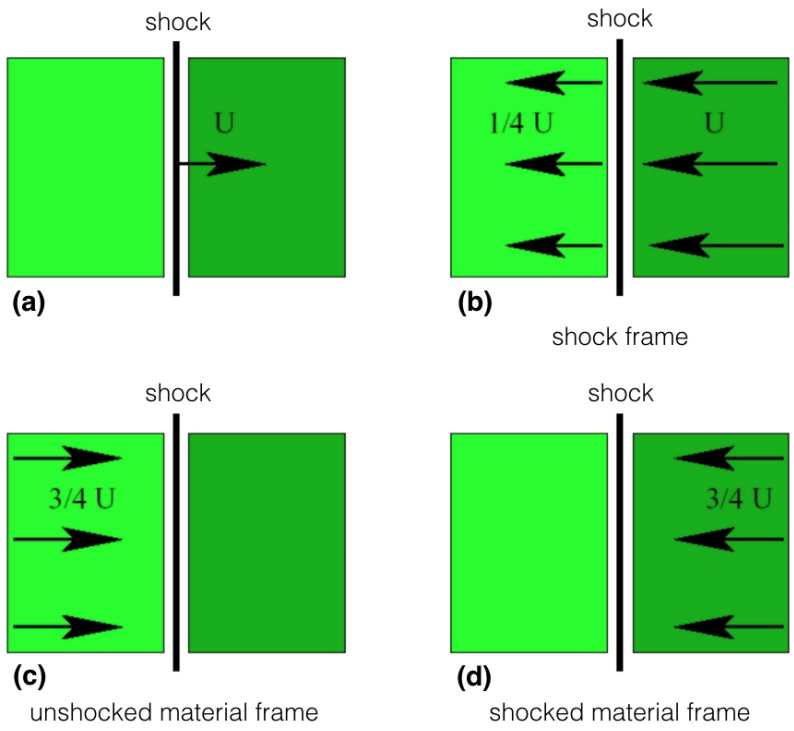

Figure 5.3: Illustration of first order Fermi mechanism

$\Gamma = \frac{5}{3}$, then using the *Rankine-Hugoniot* jump conditions, we can show that $\frac{\rho_2}{\rho_1} = 4$ and $\frac{v_1}{v_2} = 4$ [149]. In the frame of reference where the shock is at rest (Figure 5.3 (b)), the upstream gas moves into the shock with velocity $v_1 = U$, and leaves the shock with velocity $v_2 = U/4$. Viewed from the rest frame of the unshocked material (Figure 5.3 (c)), the shocked material moves towards the shock with a velocity of $v = 3U/4$. Similarly, if we go to the frame of reference of the shocked material (Figure 5.3 (d)), we see that unshocked material is moving at velocity $3U/4$ towards the shocked material. Let us now calculate the energy gain for a fast moving particle (from the tail of the Maxwell-Boltzmann distribution) crossing from the upstream side to the downstream side of the shock front. Let us consider the particle to be relativistic, such that its momentum is given by $p = E/c$, where E is the energy of particle and c is speed of light. The gas on the downstream side approaches the particle at a velocity of $v = 3U/4$.

If the particle that crosses the shock makes an angle θ with the shock normal, then the new energy of the particle can be evaluated using the Lorentz transformation:

$$E^{'} = \gamma(E + pv\cos\theta) \tag{5.12}$$

If the shock is nonrelativistic, then $\gamma \approx 1$, and this gives

$$\frac{\Delta E}{E} \approx \frac{v}{c}\cos\theta \tag{5.13}$$

The probability of the particle crossing the shock is proportional to $\sin\theta\cos\theta$.

$$p(\theta) = 2\sin\theta\cos\theta d\theta \tag{5.14}$$

Here we introduce a factor of 2 due to normalization so that the integral of the probability distribution over all of the particles approaching the shock is equal to unity. Therefore, the average energy gain on crossing the shock is

$$\frac{\Delta E}{E} = \frac{v}{c}\int_0^{\pi/2} 2\cos^2\theta\sin\theta d\theta = \frac{2}{3}\frac{v}{c} \tag{5.15}$$

If we consider the same process from the point of view of the downstream region, then we will get the same fractional gain in energy $\langle\frac{2}{3}\frac{v}{c}\rangle$ when a particle crosses the shock front from the downstream to the upstream region. Thus, with one round trip across the shock and back again, the average energy gain is given by

$$\langle\frac{\Delta E}{E}\rangle = \frac{4}{3}\frac{v}{c} \tag{5.16}$$

and the fractional gain per round is given by

$$\beta = \frac{E}{E_0} = 1 + \frac{4}{3}\frac{v}{c} \tag{5.17}$$

Thus, it is clear that particles passing back and forth through the shock front can attain very high energy and this energy is proportional to the first power of v/c. This is why it is called first order Fermi acceleration mechanism.

5.3.2 Particle Spectrum

From the first order fermi acceleration, we see that every time a particle crosses back and forth through the shock, its energy increases by a factor of $\beta = 1 + \frac{4}{3}\frac{v}{c}$ (Eq. 5.17). Therefore, after j crossings, a particle with an initial energy of E_0 will have an energy $E = E_0\beta^j$. It is also possible that the high energy particles leave the acceleration region after some crossings. Let us denote the probability of a particle to remain in the acceleration region by P. Then, after j crossings, the number of particles remaining in the acceleration region is given by $N = N_0P^j$, where N_0 is the original number of particles. We can eliminate j by writing

$$\frac{\log(N/N_0)}{\log(E/E_0)} = \frac{\log(P)}{\log(\beta)} \tag{5.18}$$

resulting in

$$\frac{N}{N_0} = \left(\frac{E}{E_0}\right)^{\log(P)/\log(\beta)} \tag{5.19}$$

In the differential form this leads to

$$N(E)dE = constant \times E^{(\log P/\log\beta)-1}dE \tag{5.20}$$

and this can be written as

$$N(E)dE = constant \times E^{-k}dE \tag{5.21}$$

where $k = 1-(\log P/\log\beta)$ is the power-law index. It is clear that we obtained a power law where the value of the index depends upon the value of P and β. To calculate the value of P we can proceed as follows: energetic particles have a finite probability to escape towards the downstream region. If the number density of particles in the upstream region is n, the flux of particles crossing the shock towards the downstream region becomes $nc/4$, due to density compression by a factor of 4 in the downstream region. In the downstream region, particles are swept away from the shock front by the

bulk flow velocity at the rate $nU/4$, where U is the shock velocity. Thus, the escape probability is given by:

$$P_{esp} = \frac{nU/4}{nc/4} = U/c \tag{5.22}$$

and the probability to remain in the shock is given by

$$P = 1 - P_{esp} = 1 - U/c \tag{5.23}$$

Now let us calulate $\log P$ and $\log \beta$.

$$\log P = \log(1 - U/c) \approx -U/c \tag{5.24}$$

and

$$\log \beta = \log(1 + \frac{4}{3}\frac{v}{c}) \approx \frac{4}{3}\frac{v}{c} = U/c \tag{5.25}$$

Inserting the values of $\log \beta$ and $\log P$ into Eq. 5.20 gives the differential energy spectrum of particles as:

$$N(E)dE \propto E^{-2}dE \tag{5.26}$$

Thus, the theory of diffusive shock acceleration predicts a universal E^{-2} spectrum for strong non-relativistic shocks. The above equation is derived under the assumptions that any process which causes the diffusion of the particles can lead to shock acceleration. However, it does not take into account the diffusion properties of the particles. For example, how the diffusion coefficient (D) changes with energy, or how the diffusion coefficient changes when particles go from the downstream to the upstream region. Therefore, it is not possible to calculate the maximum energy attained by a particle using the standard DSA theory.

5.3.3 Maximum achievable energy

In a standard picture of particle acceleration at SNR shocks, cosmic-ray particles can reach up to a energy of $\approx 10^{15}$ eV [150]. The maximum achievable energy is limited

by the time available for acceleration due to the finite age of the SNR, energy loss through radiative processes (mainly for electrons) and particle escape upstream due to a high diffusion coefficient above a certain energy. However, we will focus only on the acceleration of hadrons, for which radiation losses are not very important, and maximum energy is dependent on the age of the SNR. The acceleration time depends upon the scattering properties, in that, scattering determines the mean residence time a particle spends in the upstream and downstream region. Following the discussion from Gaisser [19] and Lagage and Cesarsky [150], the mean residence time over a complete cycle is given by

$$T_{cycle} = \frac{4}{c}\left(\frac{D_1}{v_1} + \frac{D_2}{v_2}\right) \tag{5.27}$$

where D_1 and D_2 is the diffusion coefficient in the upstream and downstream region respectively, and their value depends upon the particle energy and level of magnetic turbulence.

Now, the characteristic acceleration time is given by:

$$T_{acc} = \frac{E}{\langle \Delta E/\Delta T \rangle} = \frac{E}{\langle \Delta E \rangle} \times T_{cycle} \tag{5.28}$$

Using Eqs. 5.16 and 5.27:

$$T_{acc} = \frac{3}{v}\left(\frac{D_1}{v_1} + \frac{D_2}{v_2}\right) \tag{5.29}$$

If we assume that $D_1 \approx D_2$ and is equal to the Bohm diffusion coefficient (smallest possible diffusion coefficient) then

$$D_1 = D_2 = D_B = \frac{1}{3}\lambda_D c \tag{5.30}$$

where λ_D is the mean diffusion length and is given by E/ZeB, where E is the particle energy, and Z is the charge of particle. Therefore, the minimum acceleration time for a strong shock where $v_2 = v_1/4$ is given by:

$$T_{acc} = \frac{3}{v}\Big(\frac{D_1}{v_1} + \frac{D_2}{v_2}\Big) = \frac{D_B}{v}\Big(\frac{1}{v_1} + \frac{1}{v_2}\Big) = \frac{20 D_B}{v_1^2} \tag{5.31}$$

$$T_{acc}(min) \approx \frac{20}{3}\frac{E}{ZeBc}\Big(\frac{c}{v_1}\Big)^2 \tag{5.32}$$

Now, the maximum achievable energy can be calculated by equating $T_{acc}(E_{max}) = T_A$, where T_A is the age of the SNR.

The resulting estimate of the maximum energy is:

$$E_{max} \leq \frac{3}{20}\frac{v_1^2}{c} ZeBT_A \tag{5.33}$$

Although the acceleration mechanism continues for the entire lifetime of the SNR, most of the particle acceleration occurs before the blast wave starts to slow down. This happens when the swept up mass of the interstellar medium by the blast wave becomes comparable to the ejecta mass from the supernova explosion. Typically, this happens when age of SNR becomes $\sim$ 1000 yrs [150]. if we assume a magnetic field value of 3 μG [19] then Eq. 5.33 gives the upper limit to the energy of particle:

$$E_{max} \leq Z \times 3 \times 10^{13} \text{ eV} \tag{5.34}$$

Clearly, for protons ($Z = 1$), the linear theory is not able to explain how the maximum energy of protons can reach to E_{knee} ($\sim 10^{15}$ eV). Therefore, some non-linear effects (e.g. magnetic field amplification) need to be taken into account if we believe that the SNRs accelerate the cosmic rays to E_{knee}.

5.3.4 Non-linear DSA theory

In the previous section, we derived the basic test particle DSA theory, which shows that cosmic-ray particles can be accelerated in SNR shocks. This theory is valid,

provided that the non-thermal particles do not have an effect on the shock structure, which is true only if the energy transferred from the shock to the non-thermal particles is a negligible fraction of the plasma kinetic motion. However, this assumption can not be true based on several arguments. For example, if SNRs are the main sources which populate the Galactic cosmic-ray pool, then a fraction $\sim 10\%$ of their kinetic energy needs to be transferred to cosmic rays [151]. This means that particles will have a dynamical effect on the shock and the correct description of the acceleration process can only be achieved within the framework of non-linear diffusive shock acceleration. A great deal of work has been done to build the non-linear DSA (NLDS) theory in the past (see references for review [152], [153], [154], [155], [156], [157]). The main features of NLDS includes the back-reaction of accelerated particles on the shock, and magnetic field amplification.

Figure 5.4 shows the qualitative description of the effect of the back-reaction of particles on the shock. The pressure in the accelerated particles slows down the incoming upstream plasma and creates a "precursor". This leads to a compression factor which depends on the location upstream of the shock. If we assume that the diffusion of particles is dependent on the energy of the particle, then high energy particles can scatter farther ahead of the shock and will see a higher compression ratio (compression ratio is defined as $r = \frac{v_1}{v_2}$, where v_1 and v_2 are upstream and downstream particle velocities w.r.t shock). This leads to a locally harder spectrum for high energy particles. On the other hand, low energy particles can not go very far in the upstream region and feel a lower compression ratio, which leads to a softer spectrum. Thus, we would expect a curved particle distribution rather than power law distribution (see Figure 5.4).

The second effect that concerns the NLDS is the magnetic field amplification (MFA) induced by the accelerated particles. When the accelerated particles stream ahead of the shock they produce an instability (*resonant streaming instability* [158], [146]) in the plasma which leads to MFA. The actual physical description of this phenomenon is very complex (see reviews [155, 156, 157]). However, there are direct

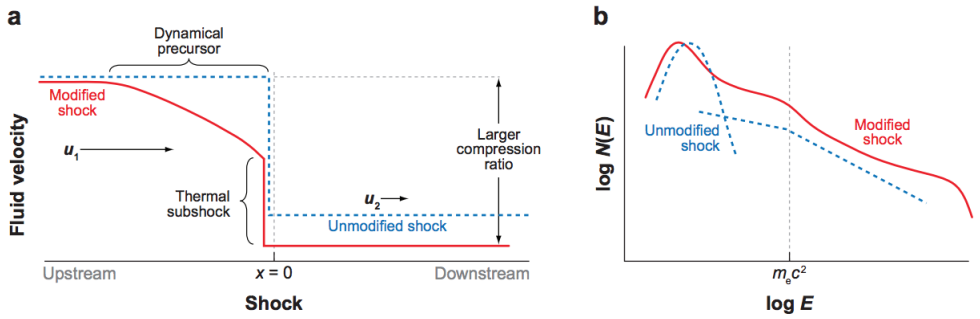

Figure 5.4: Figure 4.4 taken from [18] (a) Schematic shock profile. Dotted blue line, unmodified shock; solid red line, shock modified by accelerated particles. (b) corresponding schematic particle energy distribution form unmodified shock (dotted blue line) and modified shock (solid red line)

observational results which show that this phenomenon is occurring in SNRs. For example, narrow X-ray rims of non-thermal emission are observed in most of the young SNRs such as Tycho, Cas A, SN 1006 and RCW86 (see [17], [159] for more details), which implies that high energy electrons cool down very fast behind the shock. This fast cooling constraint suggests a relatively large magnetic field behind the shocks ($\sim 100\ \mu\text{G} - 600\ \mu\text{G}$) [160, 161]. Another observational result, the fast time variability of X-ray emission in SNR RX J1713-3946, has also led to inference of amplified magnetic field ($100\ \mu\text{G} - 1$ mG) [162]. Another important consequence of the amplified magnetic field is that, if this MFA takes place in the SNR, it may facilitate cosmic-ray acceleration to the knee (few PeV energies) (see Eq 5.33). However, the magnetic field amplification should occur both at upstream and downstream of the shock, otherwise particles can leave the acceleration region from either side of shock, and can not reach the knee energy. Deeper Chandra observations show the observational evidence for particles accelerated to knee energies in Tycho SNR, which most likely is the result of the magnetic field of few hundred μG [163, 164].

5.4 Gamma Ray Production Mechanisms

Cosmic rays mainly consists of charged particles (i.e protons, electrons). Due to this charged nature, their original direction is altered by interaction with magnetic fields in the interstellar medium. Thus, it is very difficult to trace back their point of origin, and hence to determine their source. However, these cosmic rays do interact near their source of origin and produce gamma rays. These gamma rays are neutral photons and their paths are not deflected by the magnetic field. Therefore, gamma rays can be used as an indirect tool to detect and study the sources of very high energy cosmic rays. There are three main radiative processes that are capable of producing gamma-rays from the MeV to TeV energy range. Two are leptonic in nature: non-thermal Bremsstrahlung and Inverse Compton (IC). The third process is hadronic in nature: π^0 decay. Here, we discuss the basic properties of these three processes in the context of SNRs.

5.4.1 Non thermal Bremsstrahlung

When a charged particle, for example, an electron, decelerates in the Coulomb field of a nucleus, it emits photons. This process is known as bremsstrahlung (German name for "braking radiation"). The rate of photon production, $dn_\gamma(E_e, E_\gamma)/dE_\gamma dt$, in the energy interval between E_γ and $E_\gamma + dE_\gamma$ by an electron of kinetic energy E_e is given by (See Equation 27 in Baring et al. 1999 [165])

$$\frac{dn_\gamma(E_e, E_\gamma)}{dE_\gamma dt} = v_e[(n_H + 4n_{He})\sigma_{e-p}(E_e, E_\gamma) + n_e\sigma_{e-e}(E_e, E_\gamma)] \text{ photons erg}^{-1}\text{ s}^{-1} \quad (5.35)$$

where v_e is the electron speed (relative speed in the bremsstrahlung collisions), n_e, n_{He} and n_H are the densities of the ambient electrons, helium and protons respectively, σ_{e-p} is the electron-ion cross section (Bethe-Heitler cross section), σ_{e-e} is the electron-electron cross section. Analytical expressions for σ_{e-e} are given in the appendix of Baring et al. 1999 ([165]). In the relativistic regime, the e-e and e-p cross sections are similar and contribute comparably to the emission. However, in the non-relativistic

regime, electrons-ions contribution dominates the emission. If we approximate the non thermal electron spectrum by $N_e = dN/dE_e = N_0 E^{-\alpha}$ electrons erg^{-1}, then the photon emissivity can be obtained by integrating equation 5.35 over the electron spectrum. A rough calculation is done by Gaisser, Protheroe and Stanev (see [166]) to give an estimate of the bremsstrahlung luminosity when electrons interact with a medium with proton density n_H cm^{-3}

$$\frac{dn_\gamma}{dE_\gamma dt dV} \sim 7 \times 10^{-16} n_H N_e \text{ photons erg}^{-1}\text{ s}^{-1}\text{ cm}^{-3} \tag{5.36}$$

One thing to note here is that the power law spectrum of bremsstrahlung photons produced by the electrons has the same slope as the slope of the electron energy distribution [18].

5.4.2 Inverse Compton Scattering

The collision between a relativistic electron with Lorentz factor γ and a low energy photon can up-scatter the low energy photon to higher energies. This process is called inverse Compton scattering and the gain of energy by this process is proportional to γ^2. For example, if the electron has a Lorentz factor of 10^3, photons of radio waves can be up-scattered into the ultraviolet and optical photons can be up-scattered into the gamma-ray regime. Production of gamma-rays through this process is very efficient and it occurs in many astrophysical environments such as pulsars, AGN, supernova remnants and clusters of galaxies. The cross-section for IC scattering is given ([167]):

$$\sigma_{IC} = \frac{3}{8}\sigma_T \frac{1}{x}\left[\left(1 - \frac{2}{x} - \frac{2}{x^2}\right)\ln(1+2x) + \frac{1}{2} + \frac{4}{x} - \frac{1}{2(2x+1)^2}\right] \tag{5.37}$$

where x is the energy of the incident photon in units of the electron rest mass energy, $x = h\nu/m_e c^2$. In the frame where the electron is at rest, if the energy of the incoming photon is smaller than $m_e c^2$, i.e. $x \ll 1$, the above expression reduces to $\sigma_{IC} \approx \sigma_T$, and we are in the *Thomson* regime. On the other hand, if $x \gg 1$, then Eq 5.37 can be approximated as $\sigma_{IC} \approx \frac{3}{8}\sigma_T \frac{1}{x}[\ln(2x) + \frac{1}{2}]$. This is called the *Klein-Nishina* regime.

In the case of an isotropic incident photon field $dn_\gamma(E_{\gamma i})/dV$ photons cm^{-3} erg^{-1}, scattered by a single electron of energy $E = \gamma mc^2$, the spectrum of outgoing photons is calculate by Jones ([18])

$$\frac{dn_{\gamma,e}}{dE_\gamma dt} = \frac{3}{4}\frac{\sigma_T c}{\gamma^2}\frac{m_e c^2}{E_{\gamma i}}\frac{dn_\gamma(E_{\gamma i})}{dV}dE_{\gamma i}\left[2q\ln q + (1+2q)(1-q) + \frac{\Gamma_{K-N}^2 q^2(1-q)}{2(1+\Gamma_{K-N})q}\right] \quad (5.38)$$

where $q = \frac{E_\gamma}{4E_{\gamma i}\gamma(\gamma - E_\gamma/m_e c^2)}$ and $\Gamma_{K-N} = 4\gamma E_{\gamma i}/m_e c^2$.

For the electron spectrum, i.e. the number of electrons with Lorentz factors between γ and $\gamma + d\gamma$, $dN_e/d\gamma \propto \gamma^{-\Gamma}$, the resulting gamma-ray emission spectrum in the non-relativistic regime ($\Gamma_{K-N} \ll 1$) has a power law form $n_\gamma \propto E_\gamma^{-(1+\Gamma)/2}$. In the Klein-Nishina regime, the gamma-ray spectrum becomes steeper, with an index of $(\Gamma + 1)$ [168]. Therefore, a power-law spectrum of the electron distribution produces a break in the gamma-ray emission with the onset of the Klein-Nishina regime.

5.4.3 Neutral Pion decay

Non-thermal bremsstrahlung and inverse Compton scattering are two very effective means of producing high energy gamma-rays and give us a direct hint that electrons are being accelerated to high energies. This statement is further strengthened by the observational facts. For example, the detection of thin rims in number of SNRs such as Tycho, CasA, in the X-ray energy band as previously discussed. However, the question of the acceleration of protons by SNR shocks still needs a conclusive answer. The process that provides unique information about the acceleration of the hadronic component of cosmic rays is the production of gamma-rays through the interaction of high energy protons with ambient gas. For example, when high energy protons collide inelastically with the interstellar gas, they produces three types of pions ($\pi^\pm$, π^0) with equal probability. This implies that π^0's account for roughly one-third of the total reaction products. To produce a neutral pion with a rest mass of about $m_\pi = 135$ MeV, the kinetic energy of the protons should be close to 280 MeV. Since the decay time of neutral pions is $\sim 10^{-17}$ s, it decays almost immediately into two γ-rays photons. In

the center of mass frame, where the neutral pion is at rest, each photon from the pion decay has an energy of $E_{\gamma*} = m_{\pi^0}/2 \approx 70$ MeV. The photon energy in the laboratory frame is given by the Lorentz transformation:

$$E_{Lab} = \gamma(E_{\gamma*} + \beta p^* \cos\theta^*) = \frac{m_{\pi^0}\gamma}{2}(1 + \beta\cos\theta^*) \tag{5.39}$$

where θ^* is the angle between the pion direction and the gamma-ray photon in the center of mass frame.

The photons emitted in the direction of motion of the pions have a maximum energy in the laboratory frame equal to $E_{Lab}(max) = \frac{m_{\pi^0}\gamma}{2}(1+\beta)$. Photons emitted opposite to the direction of motion of the pion have the minimum energy, equal to $E_{Lab}(min) = \frac{m_{\pi^0}\gamma}{2}(1-\beta)$. As the spin of the neutral pion is zero, pions decay into photons isotropically in their rest frame, meaning:

$$dN = \frac{1}{4\pi}d\Omega = \frac{1}{2}d(\cos\theta^*) \tag{5.40}$$

The value of $d(\cos\theta^*)$ is calculated from Eq 5.39, and is equal to $dE_{Lab}/\beta\gamma p^*$. Putting the value of $d(\cos\theta^*)$ into Eq 5.40 gives:

$$\frac{dN}{dE_{Lab}} = \frac{1}{\gamma\beta m_{\pi^0}} = constant \tag{5.41}$$

We have seen that the distribution of gamma-rays is constant between E_{min} to E_{max} for mono-energetic pions. For an arbitrary distribution of pions, the gamma-ray spectrum will be represented by a superposition of rectangles around $m_{\pi^0}/2$. Clearly this gives a spectral maximum at the position of $m_{\pi^0}/2$, irrespective of the spectral shape of the parent pion population. This is also called the "pion bump" as shown in Fig 5.5.

5.5 Detection of Supernova remnants at VHE gamma rays

In the previous two sections, I have explained the mechanism for particle acceleration at SNR shocks and the associated gamma ray production when protons or

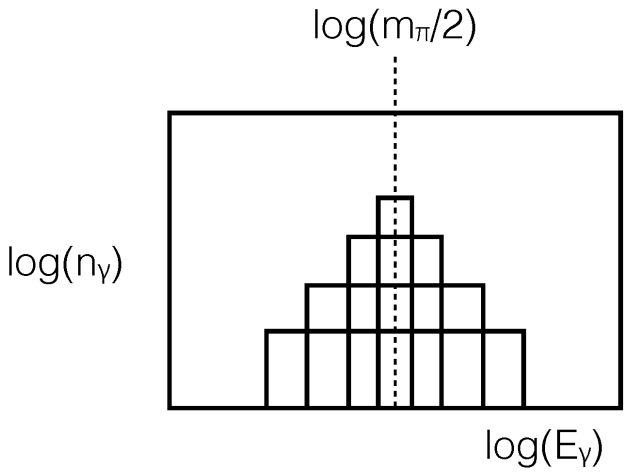

Figure 5.5: Figure 10.1 taken from [19]. Rough skectch of spectral energy distribution of gamma rays resulting from the decay of neutral pions having a power law distribution.

electrons interact with ambient matter or radiation. Every SNR evolves in a different environment, ranging from a relatively clean environment for Type Ia SNe to a very complex environment for Type II explosions of massive stars. This has an implication for the evolution of SNRs, which in turn affects the timing and efficiency of the CR production. Evidence for this is visible in the gamma-ray observations of SNRs, where diversity is observed in the luminosity and spectral shapes.

In general, if we assume that gamma-ray emission results from π^0 decay, then Drury [169] estimated the gamma-ray flux from an SNR at a distance of d from earth as:

$$F(\geq 100 \text{ MeV}) \approx 4.4 \times 10^{-7} \theta \left(\frac{E_{SN}}{10^{51} \text{ erg}} \right) \left(\frac{d}{1 \text{ kpc}} \right)^{-2} \left(\frac{n}{1 \text{ cm}^{-3}} \right) \text{ cm}^{-2} \text{ s}^{-1} \quad (5.42)$$

where n is the ambient density and θ is the fraction of total supernova explosion energy E_{SN}, converted to cosmic-ray energy. The value of θ varies from a few percent to as high as 10% [170]. If we assume a differential energy spectrum of protons at the SNR

shock $\propto E^{-2.1}$, then the flux in the TeV region is given by [19]:

$$F(\geq E) \approx 9 \times 10^{-11}\theta\left(\frac{E}{1\ \mathrm{TeV}}\right)^{-1.1}\left(\frac{E_{SN}}{10^{51}\ \mathrm{erg}}\right)\left(\frac{d}{1\ \mathrm{kpc}}\right)^{-2}\left(\frac{n}{1\ \mathrm{cm}^{-3}}\right)\ \mathrm{cm}^{-2}\,\mathrm{s}^{-1} \tag{5.43}$$

It is clear from the above equation that at $E \geq 0.1$ TeV, $n = 0.1\ \mathrm{cm}^{-3}$, $d = 3$ kpc and $\theta = 0.1$, the integral flux can exceed 10^{-11} photons $\mathrm{cm}^{-2}\,\mathrm{s}^{-1}$. This flux is detectable with the current generation and with the future generations of VHE telescopes. In this section, I will review some of the SNRs from which gamma rays are observed by different ground-based observatories, such as VERITAS, H.E.S.S. and MAGIC.

5.5.1 Young shell-type SNRs

A supernova remnant is considered as young if, in the course of its evolution, it is in the Sedov-Taylor or earlier phase, i.e., when the shock speed is high ($\geq 2000\ \mathrm{km\,s}^{-1}$). If diffusive shock acceleration is a viable mechanism for particle acceleration within SNR shocks, strong gamma-ray emission with a hard photon index (~ 2) is expected. In fact, five such SNRs: RX J1713-345 [171], RX J0852.0-4622 [172], SN 1006 [173], RCW 86 [174] and HESS J1731-347 [175], have been detected by the H.E.S.S. collaboration, where clear shell type morphology coincident with the forward shock of the SNR is detected in VHE gamma-rays (see Figure 5.6). Moreover, there are other young shell-type SNRs, such as Cassiopeia A [28] and Tycho [176], which are also producing VHE gamma rays. These have not been resolved yet, because of the limited angular resolution of VHE telescopes ($\sim$ 5 arcminute). From this VHE emission, it is clear that particles are accelerated at the shock front of these SNRs. In addition to VHE gamma rays, non-thermal X-ray emission is firmly detected in these SNRs, which is interpreted as the synchrotron emission of very high energy electrons. For example, X-ray observations of SN 1006, made by ASCA satellite, indicate that electrons up to an energy of 100 TeV are accelerated in the shock front of this remnant [177]. Although it is clear that high energy electrons are producing the X-ray synchrotron emission,

the critical issue regarding the nature of particles producing gamma rays is still unresolved. In some cases, like RX J1713.7-3946, Cassiopeia A and Tycho, evidence for an amplified magnetic field in range of hundreds of micro gauss, restricts the contribution of electrons in producing the TeV gamma rays, and thus favors a hadronic model.

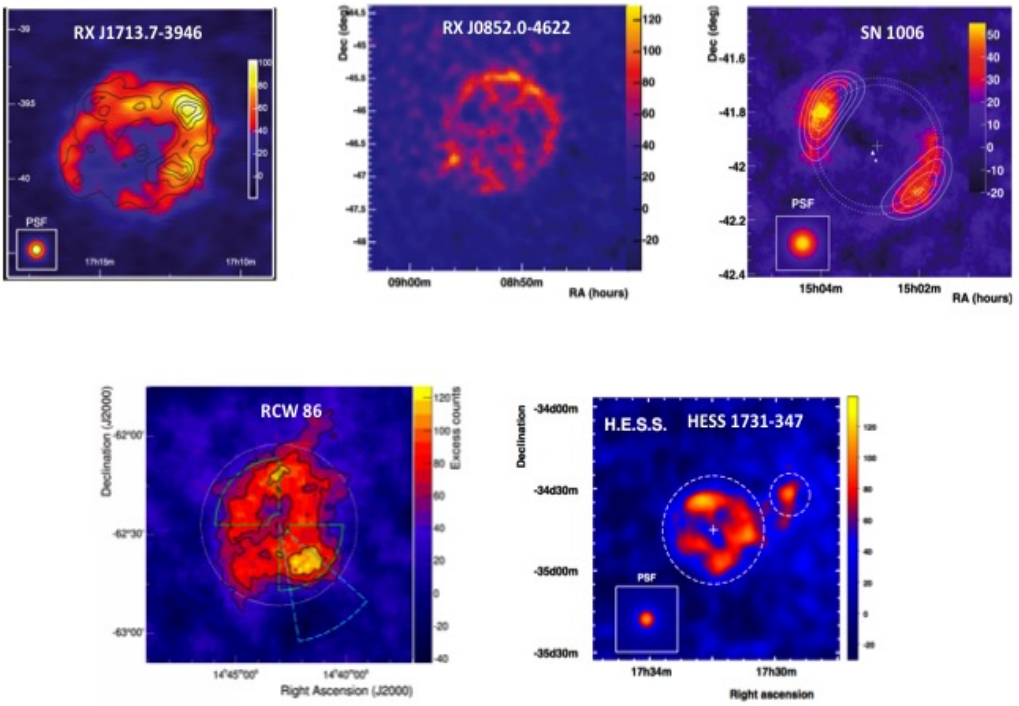

Figure 5.6: Young SNRs with shell morphology

For **RX J1713.7-3946**, observations of non-thermal X-rays and TeV gamma rays gives a strong observational evidence for the acceleration of particles to multi TeV energies. The morphology of both TeV and X-ray emission correlates well with each other, although a recent paper from the H.E.S.S. collaboration found some differences in some parts of SNR [20]. In addition, in some regions, the SNR extends to a larger radius in gamma rays than in X-rays (see Figure 5.7). This can be interpreted as very

high energy particles leaking out from the shock acceleration region, which gives the first observational evidence for escape of particles from the shock region [20]. The X-ray emission is undoubtedly produced by the high energy electrons through synchrotron radiation, the emission in the GeV-TeV range is still debatable. Different interpretations are put forward to explain the nature of gamma-ray emission using the modelling of multiwavelength data, thus making hadronic origin of emission a controversial issue.

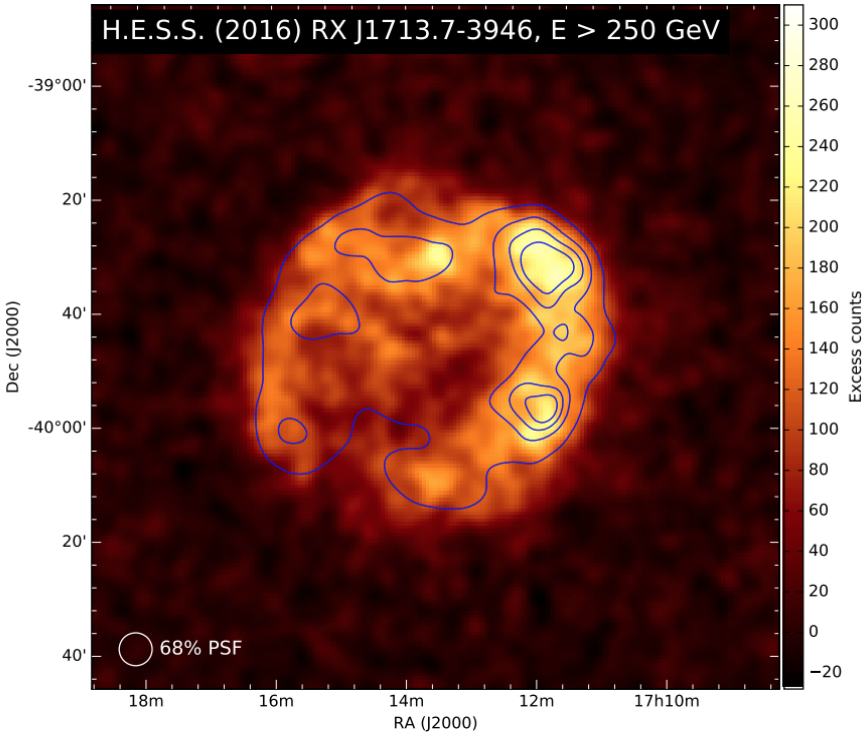

Figure 5.7: Figure B.1 taken from [20]. H.E.S.S. gamma-ray excess image of RX J1713.7-3946 with overlaid *XMM-Newton* contours (1-10 keV).

The arguments against the hadronic origin of gamma-ray emission are backed by some interesting observations. For example, the lack of thermal X-ray emission puts an upper limit on the shocked ambient medium density at ≤ 0.3 cm$^{-3}(d_{kpc}/6)^{-1/2}$ [178]. For the estimated distance of ~ 1 kpc [179], the number density of the ambient matter becomes ≤ 0.7 cm^{-3}. As the gamma ray emission scales with the target density of matter, the contribution from the hadronic channel ($p-p$ collision) cannot explain

the gamma-ray observations in RX J1713.7-3946. In order to explain the gamma-ray observations with a hadronic model, detailed calculations have been performed by Ellison [180]. They found that, for small shocked gas density, one needs extremely efficient acceleration of cosmic rays, such that all the shock energy goes into the cosmic rays. This automatically makes the contribution of shock to thermal energy negligible, thus explaining the lack of thermal X-rays.

The spectral shape of gamma-ray emission from RX J1713.7-3946 is the second most popular argument against the hadronic origin of the emission. A very hard power-law shape with a photon index of $\Gamma = 1.5 \pm 0.1$ in the energy range from 500 MeV $-$ 400 GeV can be explained by invoking the inverse Compton model for emission [181]. However, for inverse Compton emission to be viable, a weak magnetic field at the SNR shocks is required (~ 10 μG), which is in contradiction to the magnetic field measured ($0.1 - 1$ mG) in thin filaments by X-ray observations [162]. From these arguments, it is clear that the origin of gamma ray emission is not yet established. A recent paper by the CTA team, based on 50 hrs of simulated data shows that it might be possible to identify the dominant gamma-ray emission component from morphological studies of the SNR [182].

5.5.2 Middle aged SNRs interacting with molecular clouds

In the previous section, arguments were given based on spectral shape and low ambient density that the gamma-ray emission from RX J1713-3946 favors a leptonic model. This does not mean that protons are not accelerated in this SNR. It is quite possible that, due to low ambient density, the γ-ray flux is largely dominated by the inverse Compton component of radiation, which makes it difficult to identify the hadronic component. However, if molecular clouds are located at or near the site of the SNR shock, gamma-ray emission by the hadronic channel can be enhanced, due to the high target densities in the molecular clouds [183]. Thus, the best cases to identify SNRs as sources of CRs are those sites where SNRs interact with molecular clouds. In fact, several SNRs interacting with molecular clouds are detected at GeV/TeV gamma-ray

energies. The famous ones are: IC 443 [21, 22, 23], W28 [184, 185], W44 [186] (yet to be detected at TeV energy), and W49 [187, 188]. In general, these SNRs are much brighter at GeV than at TeV energies, due to a steeping of the spectral index around a few GeV. In the case of IC 443 and W44 (see Figure 5.8), the pion decay signature (spectra steeply rising below 200 MeV) is uniquely identified by Fermi-LAT collaboration using broadband spectral modelling [21]. This detection provides strong evidence that protons are accelerated at SNR shocks in IC 443 and W44.

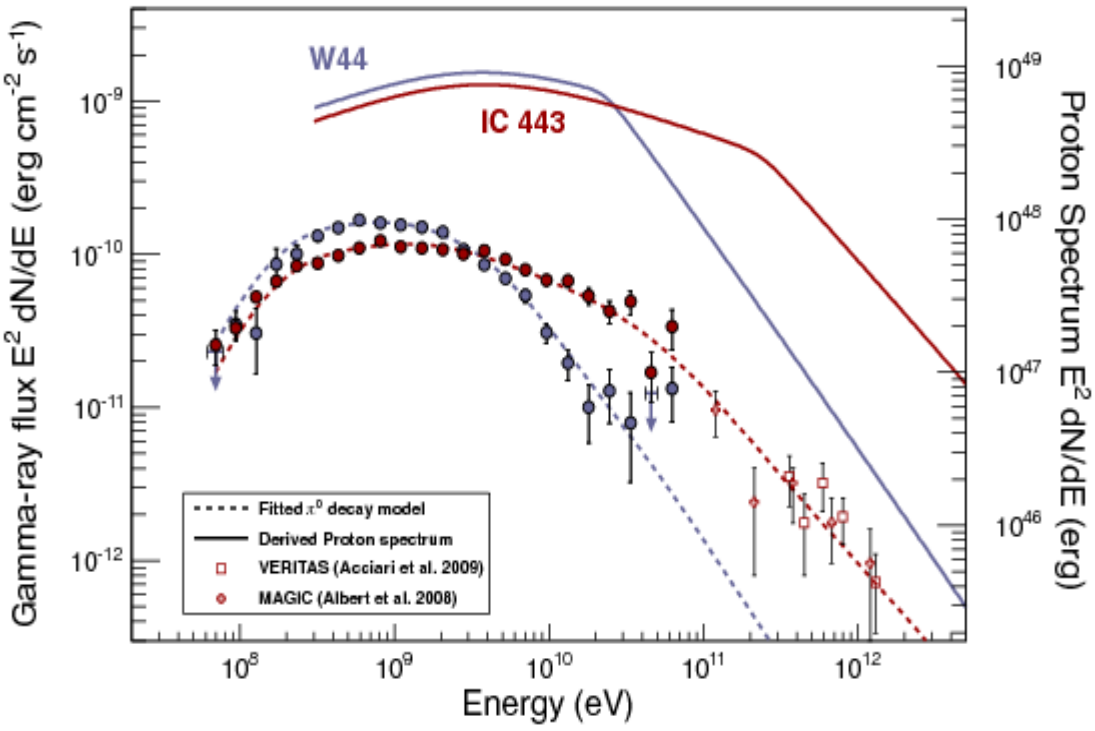

Figure 5.8: Figure taken from [21]. Proton and gamma-ray spectrum for IC 443 and W44. Also, showing spectral points from Fermi-LAT at GeV energies and from VERITAS [22] and MAGIC [23] at TeV energies.

Two kind of models are prevalent to explain the hadronic gamma-ray emission from SNRs interacting with molecular clouds. Both the scenarios are depicted in Figure 5.9. In the first case, called the "Runaway CRs" model [189], it is assumed that gamma-ray emission results from the interaction of escaping CRs (CRs that left the acceleration region) with the molecular clouds lying outside the shell of the SNR.

Such a scenario has been suggested for SNR W28 [184, 185], in which some gamma-ray emission is detected outside of the SNR shell and is spatially coincident with the position of MCs. An alternative model is the "Crushed cloud" model [190], in which the SNR shock wave is driven into a molecular cloud. In this shocked cloud, CRs are compressed and accelerated, resulting in enhanced gamma-ray emission. Moreover, this model naturally predicts the observed synchrotron radiation in SNRs, W51C [191], W44 [192] and IC 443 [193], which is largely contributed by secondary electrons and positrons generated by $p - p$ interactions [190].

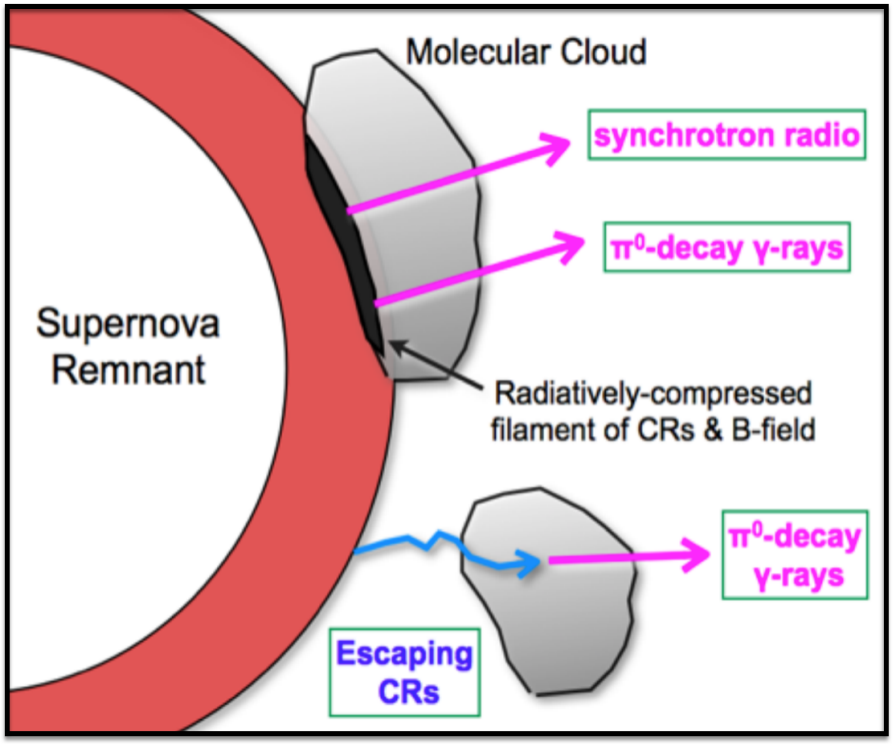

Figure 5.9: Gamma ray production sites: Gamma ray can be produced through the interaction of shocked cloud and accelerated cosmic rays or can be produced by the escaping cosmic rays that left the acceleration region.

Chapter 6

DEEP STUDY OF γ-RAY EMISSION FROM CASSIOPEIA A USING FERMI-LAT AND VERITAS

The shell-type remnant Cassiopeia A (Cas A) is one of the youngest and closest supernova remnants in our Galaxy. No historical records are available for observing any light from the supernova explosion associated with Cas A, likely due to the absorption of light by interstellar clouds of molecular gas along the line of sight [194]. However, the explosion can be linked to an event observed by John Flamsteed in A.D. 1680 [195], who catalogued it as "3 Cassiopeiae", quite close to the present position of Cas A. Using optical observations, the age of the remnant is derived by observing many fast expanding knots that lie ahead of the SNR forward shock. The date at which these knots converge is estimated at A.D. 1671.3 ± 0.9, assuming no knot deceleration [196]. The lack of direct information about the explosion means that there does not exist any light curve to determine the true nature of its progenitor star. Nonetheless, in 2008, the detection of infrared light echoes with the *Spitzer* Space Telescope showed that the remnant resulted from a type IIb core-collapse supernova explosion [132]. The progenitors of such explosions are believed to be red supergiants, which have lost most of their hydrogen envelope through strong stellar winds before the supernova occurred [197]. The loss of these outer layers of mass before the explosion might be an another reason for not sighting the explosion, even though it was relatively close by; the clouds of ejected material might have occulted the light from the explosion. Based on the proper motion of the optical filaments, the distance to this supernova remnant is estimated to be $3.4^{+0.3}_{-0.1}$ kpc [198], suggesting a physical size of 2.5 pc. As one of the youngest and closest SNRs, it has been observed extensively over a broad spectral range from radio through X-ray, and up to gamma-ray wavelengths.

6.1 Multi-wavelength observational properties of Cas A

Cassiopeia A was detected for the first time in 1948 by Ryle & Smith as an intense source of radio waves [199]. As the radio astronomy was still in its early stages, the source was not resolved at that time (the resolving power was ~ 6 minutes of arc). Since its discovery, it has been observed continuously at radio wavelengths [200, 201, 202, 203] with much improved radio telescopes that use the interferometry technique. This results in highly-resolved images of the remnant of Cas A at a scale of 1 arcsecond. Left Figure 6.1 shows the total intensity radio image of Cas A at 6 cm taken with the Very Large Array (VLA) radio telescope and shows a complex morphology. The main fraction of the radio emission comes from a circular bright ring at a radius of 100 arcsecond, which in general is marked as the location where ejecta interact with the reverse shock. Fainter radio emission can be seen in the outer radio-plateau region up to a radius of 150 arcseconds. The bright radio emission can be interpreted as synchrotron radiation of relativistic electrons spiralling around magnetic fields (see standard textbooks for more details [204, 205]). The population of these radio emitting electrons follows a non-thermal power law distribution with a spectral index of -0.77 [201]. Apart from mapping the large scale radio structure, strong radio emission is also observed over smaller and more compact regions having spatial scale ranges from 11 to 80 arcsecconds. This implies that, in addition to enhanced magnetic field in these compact regions, a population of relativistic electrons is also present. Interestingly, the radio spectrum in these compact regions also showed spectral index variations from -0.64 to -0.92 [25], which shows strong support for local variations in the acceleration of particles in Cas A [206]. These results also have important implications for the relation between conditions in various parts of the SNR and the relativistic particle distribution [25].

Optically, the emission from Cas A consists of a faint nebula that is not illuminated uniformly across a spherical surface (see right side of Figure 6.1), implying that the SNR is evolving in a non-uniform circumstellar medium (CSM). The optical emission can be divided into two main components; fast moving knots (FMKs) and

quasi-stationary flocculi (QSFs). The observations of FMKs, which have spatial velocities of 5000 km s^{-1} for the bulk of the emission, shows emission lines from O, S, Ar, Ca and very little H, He and nitrogen emission lines [207, 208]. These FMKs represent emission from ejecta and are produced by deeper layers of the star (oxygen burning products; Si, Ar, Ca). Although the FMKs are mostly associated with the bright ring, some FMKs, having velocity up to 12000 km s^{-1}, are also found beyond the main ring in the northeast jet region [209].

The slow moving knots, also called QSFs, have a space velocity of about 200 km s^{-1} and emit emission lines of Hα and nitrogen [207]. The absence of hydrogen lines from the ejecta suggests that the progenitor of Cas A may have been a Wolf-Rayet star that has undergone substantial mass loss due to strong stellar winds before exploding [210].

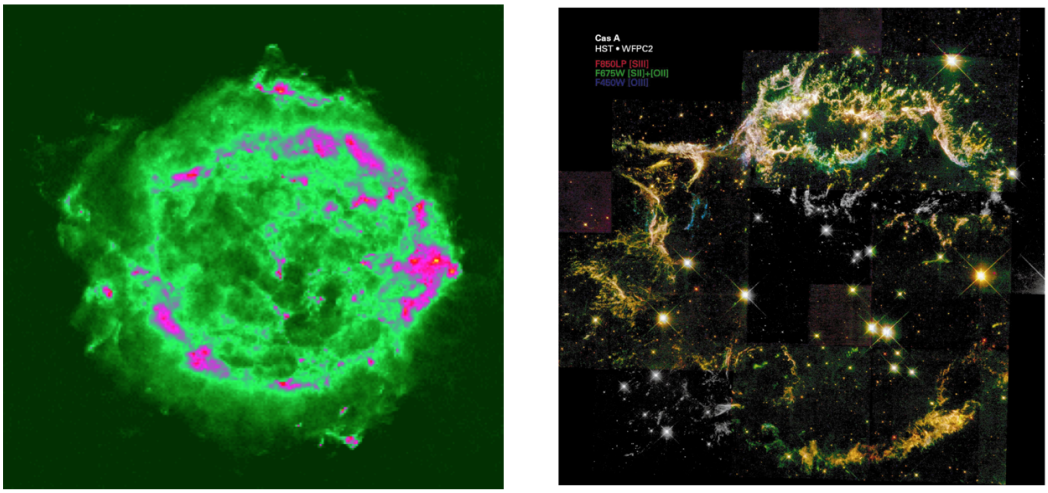

Figure 6.1: (Left) Radio 6 cm Very Large Array (VLA) image, (Right) Three color composite image showing line emission.

Synchrotron emission from Cas A is not limited to the radio waveband, it is also detected in the near-infrared at 2.2 μm (K-band) [211, 24, 212] and extends up to hard X-rays [213]. The dominant feature at near-IR wavelengths is diffuse emission that forms a complete ring and correlates very well with the radio emission (see Figure 6.2). Furthermore, when broadband spectral index measurements are performed, by

combining radio and IR flux points, a significant curvature is seen in the spectrum, indicating that shock might have been modified by the back reaction of cosmic rays onto the shock itself (non-linear modifications to first order Fermi acceleration)[24].

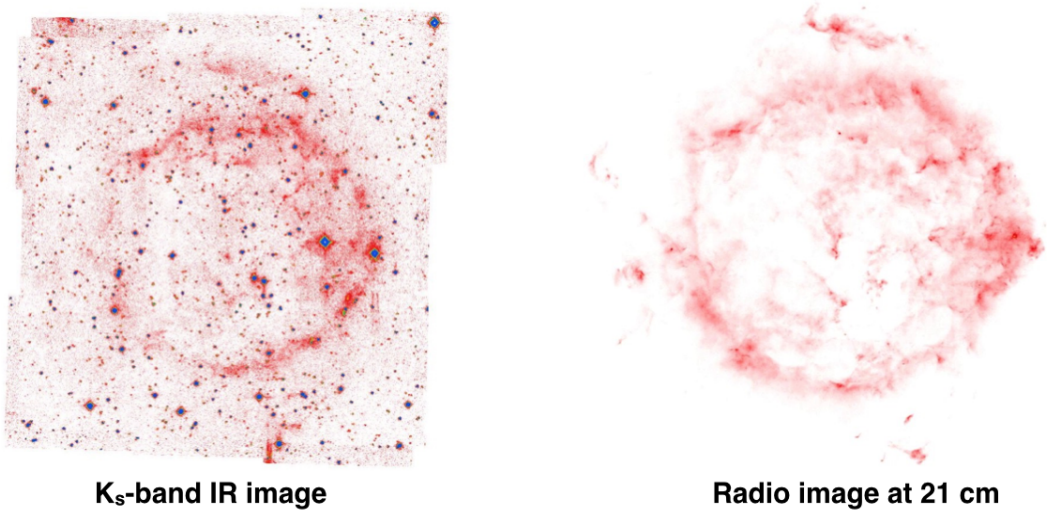

Figure 6.2: Left: Near-IR emission in the K_s band [24], Right: 21 cm radio image of Cas A [25].

In the X-ray regime, the high resolution *Chandra* observatory has detected non-thermal X-ray emission from both the forward and reverse shocks (see Figure 6.3), implying that electrons are accelerated to at least a few tens of TeV [26, 214]. Recently, X-ray observations from *NuSTAR* resolve the remnant above 15 KeV and find that the emission is produced not only by forward and reverse shocks, but also by knots located in the interior of the remnant [27]. The ten years of observations published by *INTEGRAL* [32] detected non-thermal X-ray continuum emission which can be fit by a smooth power-law with no cutoff up to 220 KeV. They invoke an asymmetrical supernova explosion scenario to explain this. Besides the non-thermal X-ray emission, there is also a strong thermal X-ray component, dominated mainly by line emission from the plasma of the shocked metal-rich ejecta [215]. Diffuse thermal emission is studied by Lee [216] using the X-ray *Chandra* observations, where they suggested that the thermal emission is coming from the shocked circumstellar gas and is consistent

with the model of SNR interacting with the red super giant (RSG) wind.

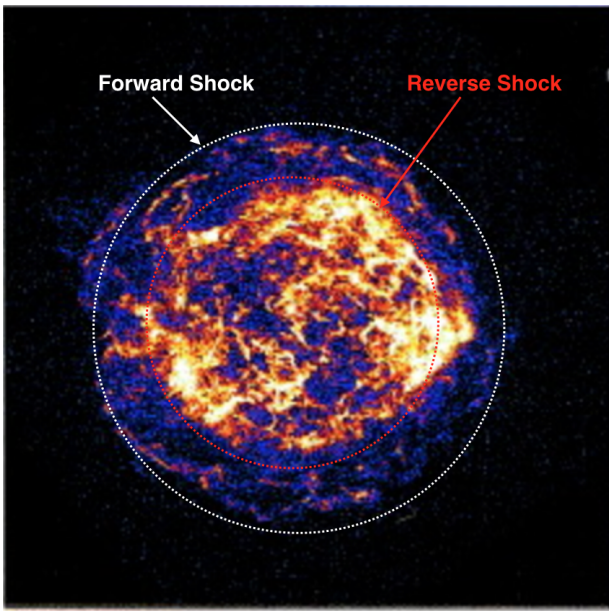

Figure 6.3: High-energy X-ray continuum emission map of Cas A between 4 and 6 keV [26]. White and red circle roughly shows the position of forward and reverse shock respectively.

While non-thermal X-ray observations constrain the properties of the relativistic electron population, γ-ray observations can play an important role in determining the efficiency of proton acceleration at the shocks. Early γ-ray observations provided only upper limits on the flux from Cas A, due to the limited sensitivity of both space-based [50, 217] and ground-based [218, 219] observatories. At TeV energies, the first detection of Cas A was made by the HEGRA stereoscopic Cherenkov telescope system [220], requiring an exceptionally deep exposure of 232 hours. The differential photon spectrum measured between 1 TeV and 10 TeV was consistent with a power law with an index of $-2.5 \pm 0.4_{stat} \pm 0.1_{syst}$ and the derived integral flux above 1 TeV was $(5.8 \pm 1.2_{stat} \pm 1.2_{stat}) \times 10^{-13}$ cm^{-2} s^{-1}. These results were later confirmed by MAGIC [221] and VERITAS [28]. In the case of MAGIC, the source was detected above 250 GeV at 5.2 standard deviations (σ) with 47 hours of data. The power-law spectrum was measured to have an index of $2.3 \pm 0.2_{stat} \pm 0.2_{syst}$ and an integral flux above 1 TeV of

$(7.3 \pm 0.7_{stat} \pm 2.2_{stat}) \times 10^{-13}$ cm^{-2} s^{-1}.

Initial VERITAS observations detected the source above 200 GeV at the 8.2σ level with 22 hours of data. The power law index and integral flux was consistent with the MAGIC and HEGRA results, with $\Gamma = 2.61 \pm 0.24_{stat} \pm 0.2_{syst}$ and Flux(> 1 TeV) $= (7.76 \pm 0.11_{stat}) \times 10^{-13}$ cm^{-2} s^{-1}. In 2017, MAGIC Collaboration shows a clear cutoff (at 4.6σ level) in the spectral measurements at $3.5^{+1.6}_{-1.0}$ TeV. At the lower end of γ-ray energies, *Fermi*-LAT, after one year of observations, reported the first detection of GeV γ-ray emission from Cas A [222] at a significance level of 12.2σ above 500 MeV. Following this, 3.6 years of LAT data were analysed above 100 MeV by [29], which revealed a low-energy break in the spectrum at $1.72^{+1.35}_{-0.89}$ GeV. Similar results were found from a recent 8.3 years of "Pass 8" data analysis by [223]. Both of these results suggest a preference for hadronic emission in the MeV-GeV range.

In terms of morphology, the source has not been resolved at high energies because of the limited resolution of gamma-ray instruments as compared to the angular size of the SNR. However, the centroid for the peak of the gamma-ray emission is reported by various space based and ground based instruments. At GeV energies, *Fermi-LAT* reported the best fit source position as RA(J2000)$= 350.853^\circ \pm 0.01^\circ_{stat} \pm 0.005^\circ_{sys}$ and Dec(J2000)$= +58.825^\circ \pm 0.01^\circ_{stat} \pm 0.005^\circ_{sys}$ [29]. In the TeV range, VERITAS gives the centroid location as RA(J2000)$= 350.825^\circ \pm 0.01^\circ_{stat} \pm 0.02^\circ_{sys}$ and Dec(J2000)$= +58.802^\circ \pm 0.01^\circ_{stat} \pm 0.02^\circ_{sys}$ [28]. If both the systematic and statistical errors are taken into account, then the positions given by *Fermi* and VERITAS are consistent with each other.

In this work, we describe further observations of Cas A with two instruments; VERITAS and *Fermi*-LAT. The main focus will be on presenting the results from observations of Cas A with VERITAS data taken between 2007 and 2013, which amount to more than 60 hours. This represents almost three times the previously published exposure by VERITAS, and significantly reduces the statistical errors on the flux and spectral index. We also discuss emission models in the framework of both leptonic and hadronic scenarios, and compare these to the multi-wavelength data.

6.2 High energy observations with Fermi-LAT

6.2.1 Fermi-LAT instrument

The LAT instrument on board the *Fermi* satellite is a pair conversion γ-ray detector that detects photons in the energy range between 20 MeV to $>$ 500 GeV. The main components consist of a converter (to convert photons into electrons and positrons), silicon-strip detectors (to track the path of the electrons and positrons and subsequently determine the direction of the incoming photon), a cesium iodide calorimeter (to measure the energy of the photon) and an anti-coincidence shield (to suppress the unwanted background due to charged particles). The LAT has a field of view of $\sim$2.4 sr, an effective area of $\sim$ 8200 cm^2 on-axis above 1 GeV and an angular resolution of $\sim$ 0.8 degree at 1 GeV. Full details about the LAT instrument can be found in [59]. In 2015, the *Fermi*-LAT collaboration achieved major improvement in the event reconstruction with the release Pass 8 data. This new Pass 8 data provides better sensitivity over a wider energy range over its predecessor Pass 7 data by combining a gain in the effective area, better angular reconstruction and energy resolution [224].

6.2.2 Data selection and analysis

In the present work, we analyzed publicly available eight years of Pass 8 LAT data, from 2008 August 4 to 2016 July 15. This period corresponds to the Mission elapsed time (the number of seconds since midnight at the beginning of January 1, 2001) from 239557417- 490233604. We used the Fermipy[1] python package that automates the analysis of Pass 8 data in conjuction with the standard Fermi Science Tools v10r0p5[2]. We select events from a $20^\circ \times 20^\circ$ region centered on the position of Cas A in the energy range from 100 MeV to 500 GeV. In order to minimize the contamination from cosmic rays mis-classified as gamma rays, we select events belonging to the "UltraCleanVeto" Class ($evclass$ = 1024). Data is filtered further by selecting only

[1] http://fermipy.readthedocs.org/en/latest/

[2] https://fermi.gsfc.nasa.gov/ssc/data/analysis/software/

PSF2 and PSF3 ($evtype = 16$ and 32) event types that give the best angular resolution at a particular energy. For details about the event classes and event types see the *Fermi* web pages[3]. Once this data selection is made, we applied another cut to select the good time intervals by using (`DATA_QUAL`) > 0 && (`LAT_CONFIG` $== 1$). In order to avoid the contamination from photons produced by cosmic-ray interactions in the upper atmosphere, we applied a zenith angle cut of $< 90°$. The remaining photons are binned using *gtbin* tool into a spatial bin size of $0.1° \times 0.1°$ and into 22 equal logarithmically-spaced energy bins.

We apply the likelihood technique to find the parameters of the source of interest, where likelihood is defined as the probability of data given the model (see this [225] for detailed explanation of likelihood analysis). A joint likelihood function is defined in this work by taking product of the likelihood function of PSF2 and PSF3 type events. The maximization of this likelihood function provides the parameters of the input model. The input model file used in the binned likelihood analysis is created by including all of the background sources within 20 degrees from the center of the region of interest (ROI) from the 3FGL catalogue [60]. In addition to that, two background diffuse models; Galactic (gll-iem-v06.fits)and extragalactic (iso-P8R2-ULTRACLEANVETO-V6-PSF3-v06.txt) are also included in the input model, and the normalization is set free for these two models. During the maximum likelihood fitting of data with *gtlike*, the normalization and spectral parameters of sources within 5 degrees from the center of the ROI were set free. The parameters for other sources, located outside of the 5 degree radius, are fixed and set at their catalogue values. The instrument response function (IRF) used in our analysis is "P8R2-ULTRACLEANVETO-V6"

6.2.3 Source localization

For source localization in the HE band, we selected the "P8 SOURCE" class with "front" plus "back" type γ-ray events in the energy range from 10 GeV $\leq E_\gamma \leq$

[3] https://fermi.gsfc.nasa.gov/ssc/data/analysis/documentation/Cicerone/Cicerone_Data/LAT_DP.html

500 GeV. Such a selection provides a good instrument PSF ($\sim 0.1^\circ$) and less contamination from Galactic diffuse emission, thus results in less source confusion. Figure 6.4 shows a Fermi-LAT counts map of > 10 GeV. In this energy range, source is detected with high significance, at a test-statistic (TS) value of ~ 870. The best-fit source position is obtained by the *source localization* method in the *Fermipy* package.

In this method, we selected a sky region of $1^\circ \times 1^\circ$ centered on Cas A. With a bin size of $0.1^\circ \times 0.1^\circ$, this square region contains 100 bins. In the first step, a maximum likelihood test statistic (TS) value is calculated at each spatial bin of $1^\circ \times 1^\circ$ region. A TS is defined as twice the difference in log-likelihood between a null hypothesis[4] and a test source[5] hypothesis; $TS = 2(\ln L_{test} - \ln L_{null})$, where L_{test} and L_{null} denotes the likelihood function between models with and without the test source respectively. A location with a maximum value of TS in the map gives the best fit position of the source of interest.

Following this, the source position is further refined by performing a full likelihood fit in the vicinity of best-fit position found in the first step. During this step, fitting is performed by freeing the normalization of the galactic diffuse model and isotropic template and the sources within 2° radius of source of interest while fixing the parameters of all other sources to their nominal values. The result of this localization analysis gives a best fit position at $l = 111.744^\circ$, $b = -2.128^\circ$, with a statistical uncertainty of 0.007° at 68% confidence level. This new position is offset from the previous position by 0.002° [29]. The systematic error in the position of source is estimated at 0.005° (adopted from 3FGL analysis paper [60]).

Next, the extension on the source size is computed by likelihood ratio test with respect to the point source hypothesis and a radial Gaussian model for extension. Since

[4] The null hypothesis contains all the sources from 3FGL catalogue plus the diffuse background models. The parameters of the null hypothesis are fixed to their default value in 3FGL catalogue

[5] A test source is defined as point source with a powerlaw spectrum and fixed photon index of $\Gamma = 2$

the TS value for extension is −0.009, we report only an upper limit on extension at 95% confidence level estimated at 2.74′. This size is larger than the size of the SNR (2.5′), which means that currently we can not resolve this source with the Fermi-LAT.

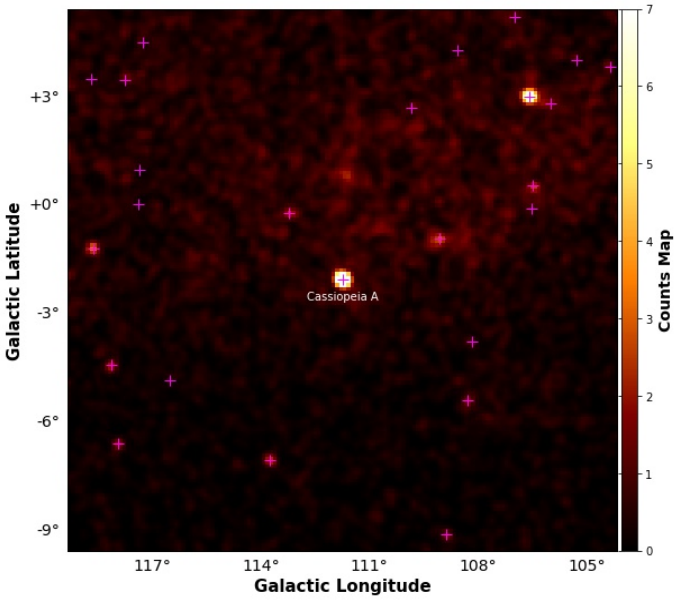

Figure 6.4: *Fermi*-LAT counts map of the region of interest surrounding Cas A ($20° \times 20°$) from 10 GeV to 500 GeV. Sources from 3FGL catalog are marked by the magenta crosses.

6.2.4 Spectral analysis

Spectral analysis is performed over the full energy range from $0.1 - 500$ GeV using *gtlike*. The spectral shape of Cas A is assumed to be a log-parabola function (see Equation 6.1 for the mathematical form), as given in the 3FGL catalogue. From the binned analysis, best fit parameters are shown in Table 6.1

$$\frac{dN}{dE} = N_0 \left(\frac{E}{E_0} \right)^{-(\alpha + \beta log(E/E_0))} \tag{6.1}$$

where N_0 is a normalization parameter and E_0 is a scaling parameter fixed at a value of 1 GeV.

We also evaluated the possibility of a spectral break in the LAT energy range by fitting the Cas A spectrum with a smoothly-broken power-law (SBPL; see Equation 6.2 for mathematical form) model.

$$\frac{dN}{dE} = N_0 \left(\frac{E}{E_0}\right)^{\gamma_1} \left(1 + \left(\frac{E}{E_b}\right)^{\frac{\gamma_1-\gamma_2}{\beta}}\right)^{-\beta} \tag{6.2}$$

where N_0 is a normalization parameter, E_0 is scale parameter fixed at a value of 1 GeV, E_b is represents the break energy in the spectrum, γ_1 and γ_2 are the photon indexes before and after the break, and β represents the smoothness of the break, and is fixed at value of 0.1. Parameters from the binned analysis are shown in this case also (see Table 6.1).

Following the parameter estimation, the preference of a smoothly-broken power-law over log parabola (LPL) is estimated using a likelihood ratio test as: $TS_{break} = 2(\ln L_{SBPL} - \ln L_{LPL}) = 16$, where L_{SBPL} and L_{LPL} is the likelihood of the smoothly-broken power-law model and log-parabola model respectively. From the TS value, a smoothly-broken power-law is preferred over the log-parabola at the 4σ level, thus we adopt a smooth broken power law as the spectral model for Cas A.

Table 6.1: Comparison between LPL and SBPL model parameters

Spectral shape	Parameter values	loglikelihood
LPL	n = 8.303e-13 ± 3.64e-14 $\mathrm{cm^{-2}s^{-1}MeV^{-1}}$	-24270
	α = 1.85 ± 0.03	
	β = 0.107 ± 0.01	
	E_0 (GeV) = 3	
	TS = 2419	
SBPL	N_0 = 6.05e-12 ± 7.37e-13 $\mathrm{cm^{-2}s^{-1}MeV^{-1}}$	-24262
	γ_1 = -1.2 ± 0.19	
	γ_2 = -2.11 ± 0.051	
	E_b (GeV) = 1.49 ± 0.3	
	β = 0.1	
	E_0 (GeV) = 1	
	TS = 2434	

For calculating the spectral energy distribution (SED), the energy range from $0.1 - 500$ GeV is divided into 22 logarithmically spaced bins. We used the *sed* method in the *Fermipy* package, where a likelihood analysis is performed in each energy bin independently. The spectral shape of Cas A in each energy bin is assumed to be a power-law with an index fixed at a value of 2. The normalization of the Galactic diffuse model and all sources within 2 degrees from the source of interest are allowed to vary. See Table 6.2 for differential flux points in all the bins. In addition to statistical errors, systematic errors are also calculated on the LAT spectral data. The major contribution to the systematic errors in the spectral points comes from the uncertainty in the modeling of Galactic diffuse emission. To estimate this error, we calculated the discrepancy between the best-fit model and data at different locations close to the position of Cas A and away from all known sources (similar to the procedure adopted in [226]). The difference between the best-fit model and data is found to be $\sim 5\%$. In order to estimate the systematic error, we change the normalization of the Galactic diffuse model artificially by $\pm 5\%$ from the best-fit values. Figure 6.5 shows the Cas A SED from Fermi-LAT data with systematic and statistical errors.

6.3 Very high energy observations with VERITAS

6.3.1 Data set

VERITAS observations of Cas A, taken using all four telescopes and under dark sky conditions, are summarized in Table 6.3. These observations, which amount to a total time of 65 hours, were accumulated in the period from 2007 to 2015. Data set I was taken between September 2007 and November 2007 with the original array configuration (see blue lines in Figure 6.6) and, after data quality selection cuts, consists of 18 hours of observations. After 2007, the VERITAS array underwent two major upgrades. The first happened in summer 2009 when telescope 1 was relocated to a different position to make the array more symmetric (see red lines in Figure 6.6). This increased the sensitivity of the telescope array by 30% [227]. Two hours of data was taken after this first upgrade, labelled as Data set II in Table 6.3.

Table 6.2: SED points from Fermi-LAT data in energy range $0.1 - 500$ GeV

Energy (GeV)	Band (GeV)	$E^2dN(E)/dE$ (10^{-9} GeV^1 cm^{-2} s^{-1})	TS
0.12	0.10-0.15	$3.60^{+0.92}_{-0.91}$	16
0.18	0.15-0.22	2.90 (upper limit)	3
0.26	0.22-0.32	$1.51^{+0.75}_{-0.74}$	4
0.39	0.32-0.47	$3.03^{+0.68}_{-0.67}$	22
0.57	0.47-0.69	$3.01^{+0.58}_{-0.57}$	31
0.84	0.69-1.02	$5.12^{+0.58}_{-0.56}$	112
1.24	1.02-1.50	$7.74^{+0.61}_{-0.59}$	301
1.82	1.50-2.21	$6.75^{+0.61}_{-0.58}$	269
2.69	2.21-3.26	$6.77^{+0.67}_{-0.62}$	296
3.96	3.26-4.80	$9.51^{+0.88}_{-0.83}$	466
5.83	4.80-7.07	$7.66^{+0.97}_{-0.90}$	260
8.58	7.07-10.41	$4.24^{+0.89}_{-0.77}$	119
12.64	10.41-15.34	$6.75^{+1.31}_{-1.16}$	180
18.61	15.34-22.59	$7.12^{+1.62}_{-1.42}$	146
27.41	22.59-33.27	$4.28^{+1.55}_{-1.29}$	59
40.37	33.27-49.00	$4.11^{+1.85}_{-1.50}$	42
59.46	49.00-72.16	$5.80^{+2.61}_{-2.11}$	49
87.57	72.16-106.27	$5.85^{+3.40}_{-2.50}$	34
128.97	106.27-156.52	$2.24^{+2.94}_{-1.65}$	7
189.95	156.52-230.52	$6.82^{+6.00}_{-3.98}$	13
279.75	230.52-339.50	$11.19^{+9.54}_{-6.34}$	22
412.01	339.50-500.00	$8.62^{+10.85}_{-6.54}$	11

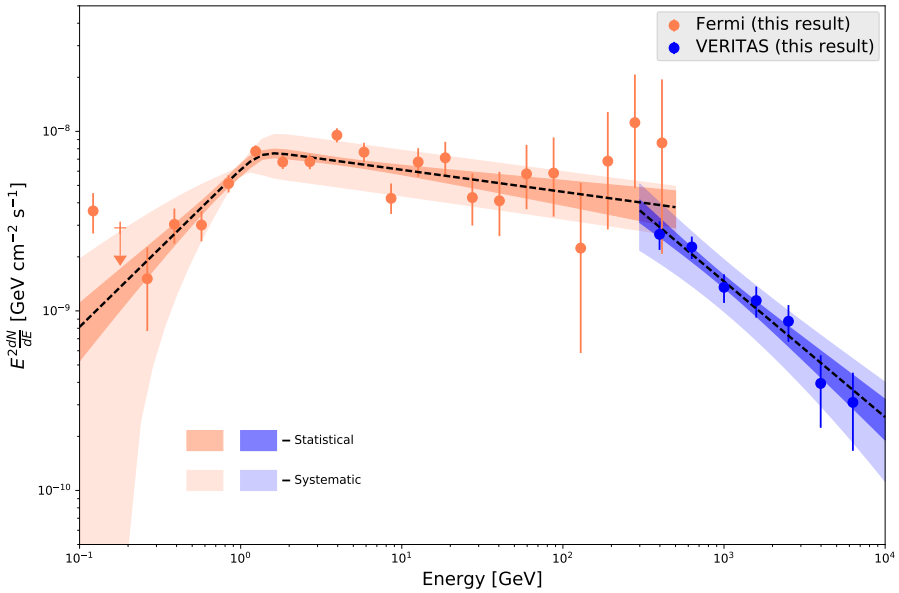

Figure 6.5: Broad-band spectral energy distribution of Cas A using *Fermi*-LAT and VERITAS points. Coral (blue) shaded region represents the 1σ statistical error band on the spectral fit of *Fermi*-LAT (VERITAS). Similarly, the light-coral (light-blue) shaded region represents 1σ systematic errors for *Fermi*-LAT (VERITAS). *Fermi*-LAT points (coral) are fitted with a smoothly-broken power-law (SBPL) from $0.1 - 500$ GeV and VERITAS points (blue) are fitted with a simple power-law from $300 - 10000$ GeV.

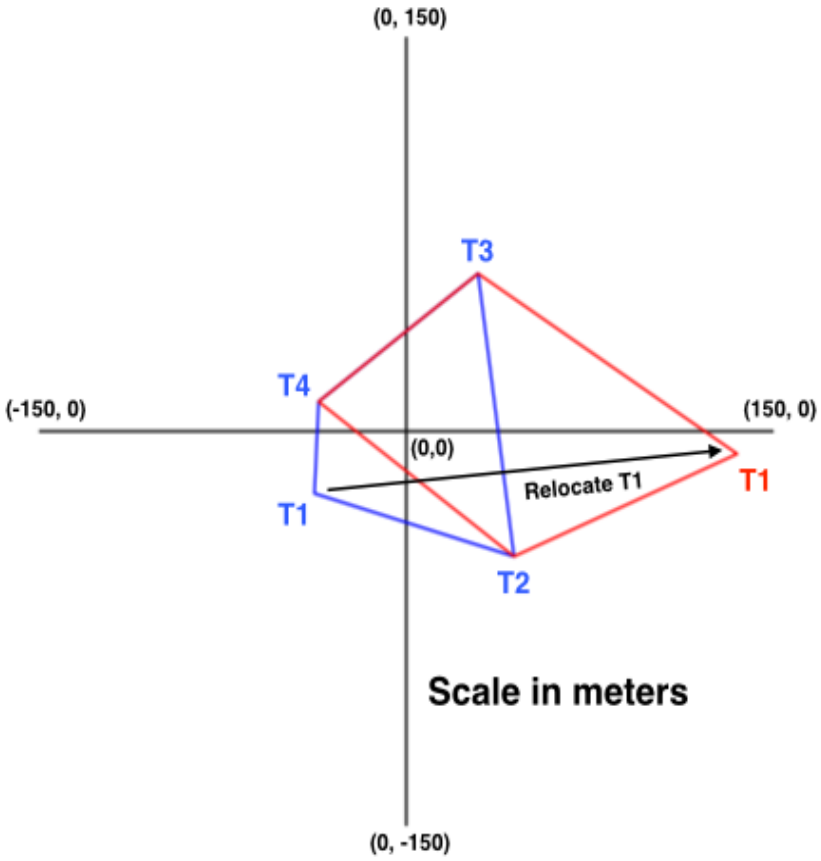

Figure 6.6: Comparison of telescopes position between the original VERITAS configuration and the first upgrade configuration.

In the summer of 2012, a second upgrade occured when VERITAS replaced the old Photonics XP2970 PMTs of the camera in each telescope with new super-bialkali PMTs (see section 3.2.1 for more details). These PMTs with their higher quantum efficiency and shorter pulse profile helps to lower the energy threshold of the VERITAS telescope from 100 GeV to 70 GeV and improve the overall sensitivity of instrument. The total amount of quality data taken after the camera upgrade (data sets III & IV) is 43 hours.

All data were taken in wobble mode, in which a source is offset by 0.5° from the center of the field of view of the camera. This allows other regions which do not contain the source, at the same radial distance from the camera center, to be used for estimating the background level. Data taken between September 2012 and December 2013 were divided in two parts; observations taken at small zenith angle (SZA; data set III) and large zenith angle (LZA; data set IV), with an average zenith angle of 31° and 55° respectively. Observations at large angles to the zenith result in a higher energy threshold, but with a larger effective collection area, allowing to measure the highest energy part of the source spectrum [122]

Table 6.3: Details of VERITAS observations of Cas A.

Data Set	Date	Number of Telescopes	Mean Zenith Angle (deg)	Exposure Time (Hours)	Previously Published ?
I	09/07 - 11/07	4	34	21	Yes
II	12/11 - 12/11	4	38	1.3	No
III	09/12 - 12/13	4	31	20	No
IV	09/12 - 12/13	4	55	23	No

6.3.2 Analysis and cut selection

VERITAS data analysis is performed using EventDisplay analysis package [112]. The details of the analysis have already been described in Chapter 4. To summarize, after the calibration and cleaning of shower images, images are parameterzied using the Hillas criteria [103]. From the Hillas parameters (see Table 4.2), arrival direction and

core location of a shower is estimated using the stereoscopic technique [104]. After the reconstruction of each event, the background is removed from the sample of gamma-ray events. This is done using the cuts on various shower parameters of the image. In the analysis of Cas A data, we used cuts defined in Table 6.4.

Table 6.4: Cuts used in the analysis of Cas A data

Parameter name	Cut value		
	V4	V5	V6 I and V6 II
Size[6]	> 400 *d.c.*	> 400 *d.c.*	> 600 *d.c.*
N_{tel} (Exclude)	≥ 2 T1T3, T1T4 and T2T4	≥ 2 T1T4 and T2T3	≥ 2 T1T4 and T2T3
θ^2	$< 0.008°$	$< 0.008°$	$< 0.008°$
MSCW	$[-1.2, 0.5]$	$[-1.2, 0.5]$	$[-1.2, 0.5]$
MSCL	$[-1.2, 0.7]$	$[-1.2, 0.7]$	$[-1.2, 0.7]$
Core position (m)	350	350	350
Emission height (km)	> 6	> 6	> 6

6.3.3 Source detection and skymap

After the above mentioned cuts are applied to the data, all the remaining events are used to produce the skymaps. In the standard analysis, two kinds of skymaps, correlated and uncorrelated, are produced. To produce uncorrelated map, $4° \times 4°$ sky region is divided into 6400 bins, where the size of each bin is $0.05°$ on each side. From the reconstructed shower direction of each γ-like event that survive after the cuts, a two dimensional histogram of skymap is filled (or ON map). The next step is the calculation of background within this region of skymap, which is estimated using the reflected background model [119]. While estimating the background, all the regions in the field-of-view containing bright stars (brighter than magnitude 7) as well as a region around Cas A are excluded (called "exclusion regions"). This results in an OFF map. The final step is the subtraction of OFF events from the ON events to yield the uncorrelated excess map (see Figure 6.7).

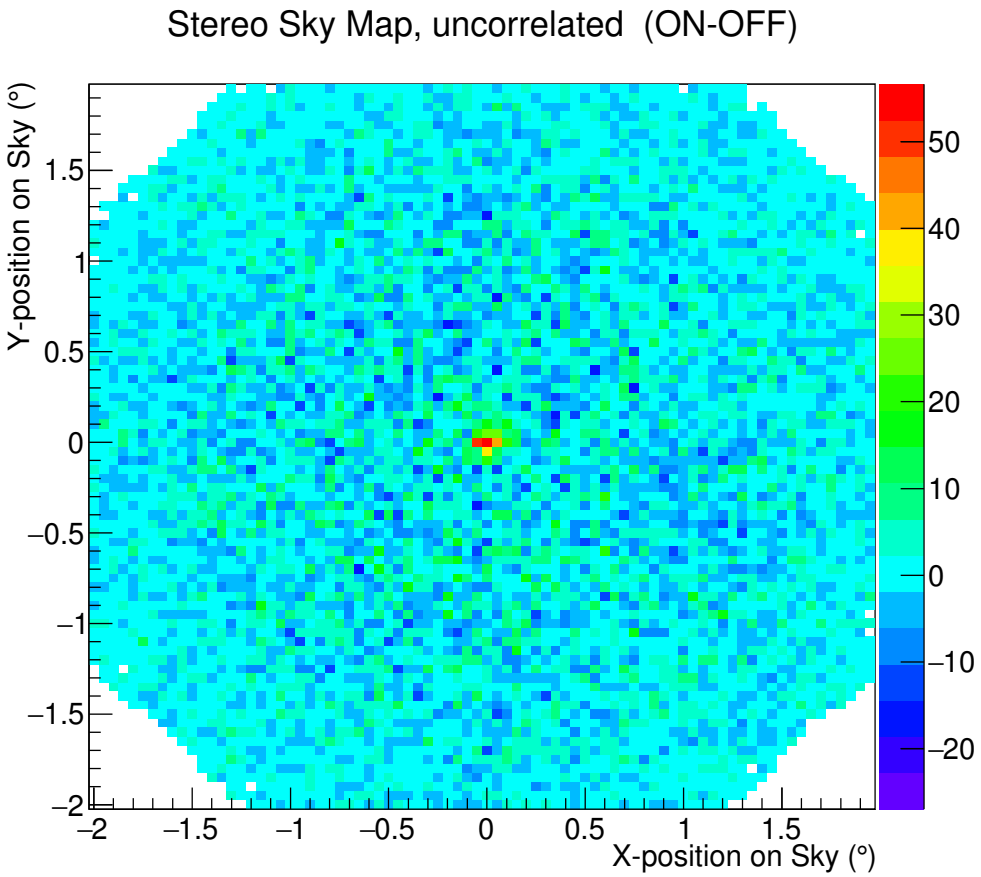

Figure 6.7: Uncorrelated excess map for Cas A. This map was produced using 20 hours of VERITAS observations from 2012 (with the upgraded camera and at small zenith angles).

Since the VERITAS detector has a finite angular resolution (PSF of $\sim 0.1^{\circ}$), signal events can spill over to the adjacent bins. Therefore, in order to define the excess of gamma rays from a source, it is interesting to define a ON signal for a given bin in the sky by summing the values from its neighbouring bins that lie inside a circle of radius equal to value of square root of the θ^2 cut. In our case, we use a radius of 0.09°. After that the background is calculated again according to reflected background model. Finally, we apply the Li and Ma equation [120] to obtain a map of significance of excesses in each bin on the skymap.

It is also useful to plot the distribution of the significance, to see if the background calculation is correct or not. The general rule is that, if we exclude "exclusion regions" (magenta circles in Figure 6.8), the background distribution follows a Gaussian distribution with a mean of 0 and width of 1. Figure 6.9 shows the distribution of significances for the bins of the skymap shown in Figure 6.8 for Cas A.

A summary of Cas A analysis results using the techniques described here, separately by data sets, are shown in Table 6.5. In the same table, we also show the analysis result from the combined data set of total exposure time ~ 65 hours. A clear detection of gamma-ray signal is present with an excess of ~ 500 events at the position of Cas A. This corresponds to a statistical significance of 13.1σ, calculated using Li and Ma formula [120].

6.3.4 Position fitting

The best-fit position of the emission of centroid at TeV energies from Cas A is measured by performing maximum likelihood two dimensional (2D) morphology fitting using the Sherpa package [228]. In order to achieve the best angular resolution, only small zenith angle (SZA) data taken between 2012-13 is selected (Data set III in Table 6.3). This also helps to minimize the systematic error on direction determination since adding large zenith angle data and data from old array will further deteriorate the systematic errors. For the fitting, uncorrelated sky images of ON map (2D histogram of γ-ray like events those survive after the cuts) and OFF map (consists of background

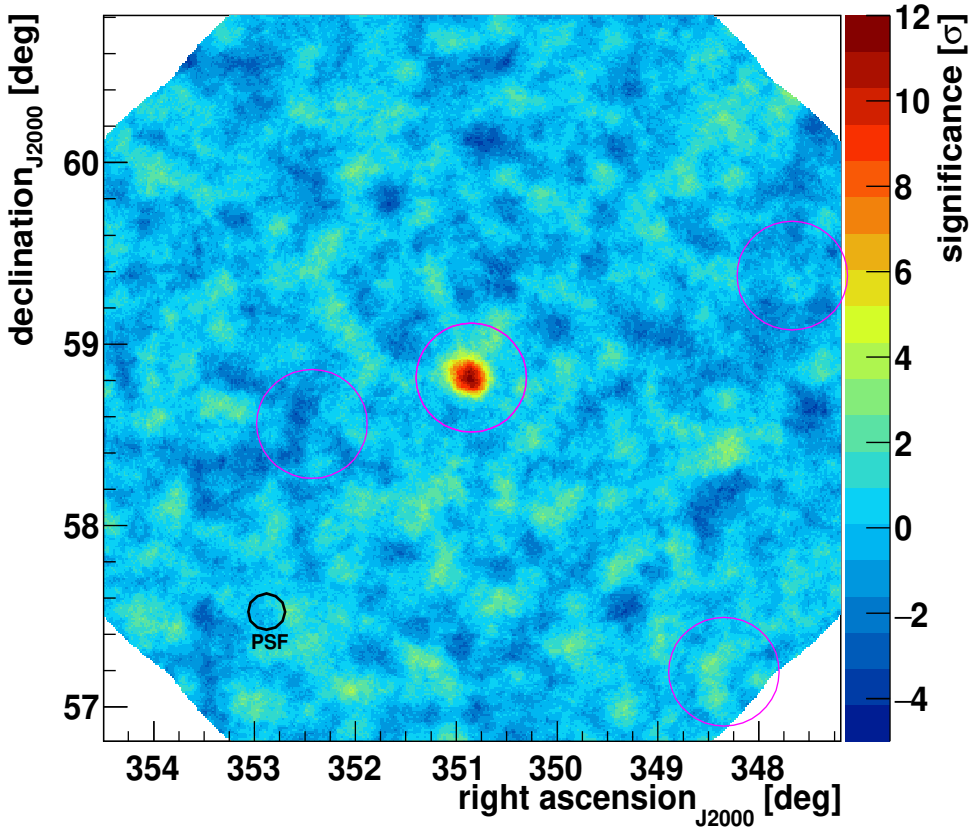

Figure 6.8: Significance map from the region of Cas A. This map was produced using 20 hours of VERITAS observations from 2012 (with the upgraded camera and at small zenith angles). Magneta circles denotes those regions which are excluded while estimating the background. The black circle indicates the size of VERITAS point spread function

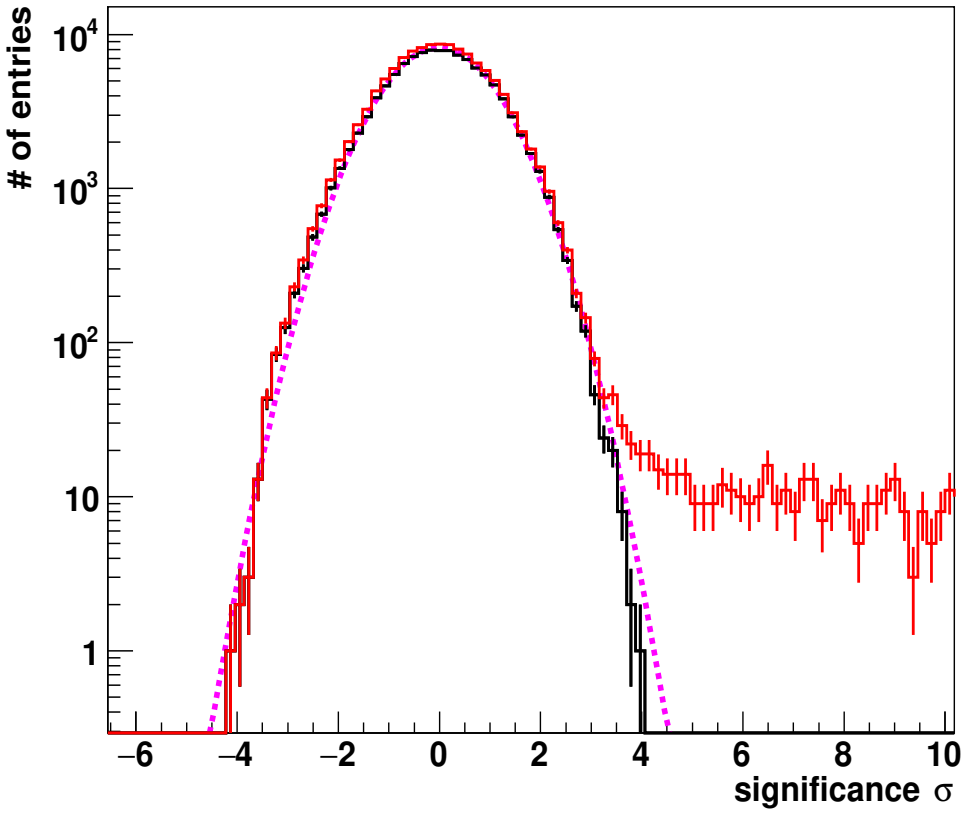

Figure 6.9: Significance distributions from the significance map shown in Figure 6.8 using reflected background model. The black curve shows the significance distributions for the bins which do not include the "exclusion regions" (magenta circles in Figure 6.8). They are well-fitted by a Gaussian distribution of mean 0 and standard deviation 1. The red curve denotes the significance distribution for all the bins in the skymap.

Table 6.5: Results of the Cas A data analysis

Data set	Time (hours)	N_{on}	N_{off}	Excess	Significance	Gamma-ray rate (min^{-1})	Background rate (min^{-1})
V4 + V5	22.13	482	369.67	112	5.1	0.085 ± 0.018	0.278
V6 I (SZA)	19.55	733	435.83	297.17	11.8	0.253 ± 0.024	0.371
V6 II (LZA)	23.91	320	234.67	85.33	4.8	0.059 ± 0.013	0.164
Total	65.6	1535	1040.17	494.83	13.1	0.126 ± 0.010	0.264

events) are used. The background is modelled using a 2D constant function, whereas the signal is modelled using a 2D symmetric Gaussian function. Moreover, modeling is limited only to the $\pm 0.3^{\circ}$ around the position of Cas A. This is because the acceptance of γ-ray like events in the camera stays constant until $\pm 0.3^{\circ}$ and starts to decreases after that (See Figure 4.15 in Chapter 4).

In the first step, a constant 2D model is fit on the OFF map. This gives an estimate of the background level. In the second step, the ON map (containing signal plus background events) is modelled by adding a constant 2D background function to a 2D symmetric Gaussian source function. During the fit in the second step, the parameters for the background model are frozen to the value calculated from the first step, while xpos, ypos and standard deviation (σ) parameters of the Gaussian source model are allowed to vary. From this analysis, we find the best-fit source position, in equatorial coordinates at RA(J2000)= $350.842^{\circ} \pm 0.013^{\circ}_{stat}$ and Dec(J2000)= $+58.816^{\circ} \pm 0.006^{\circ}_{stat}$. The systematic error in this position due to the VERITAS pointing accuracy is 0.006°. The comparison of this measured TeV centroid position with the GeV centroid, and with the previous measurements shows that they are consistent within errors. The centroid is consistent with a location in the center of the remnant (see Figure 6.10). It should be noted that the errors on the position includes both statistical and systemic errors added in quadrature.

In order to study the angular extent of the TeV emission from Cas A, the source 1ES 1959+650 has been chosen for comparison. This is a blazar at a redshift of $z = 0.048$, which acts as a point-like source for VERITAS. It can therefore be used to derive the point spread function (PSF) of the VERITAS array. Only data on 1ES1959+650 taken under conditions similar to Cas A (same zenith angle, same array configuration) has been selected. The PSF (68% containment radius) can be estimated from the standard deviation parameter (σ) of the 2D gaussian function ($68\% = 1.36\sigma$ for 2D Gaussian function). Similar steps are followed to estimate the sigma parameter as discussed in the position fitting procedure. The value of the PSF is measurable to be $6' \pm 0.3'$. When the same function is fitted on the Cas A source, the 68% containment

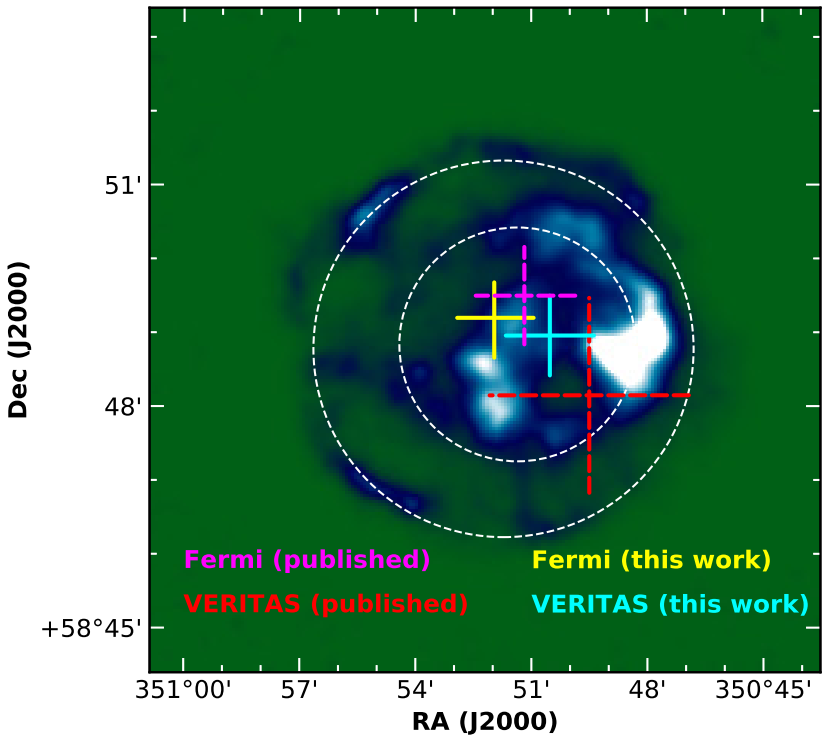

Figure 6.10: Comparison of GeV and TeV centroid positions. The background image shows the NuSTAR $15 - 20$ keV hard X-ray emission from Cas A [27]. VERITAS (for photons above 200 GeV energy) and Fermi-LAT (for photons above 10 GeV energy) centroid positions are denoted by cyan and yellow crosses. The size of the crosses represents the 1σ statistical errors added in quadrature with the systematic errors (at 68% confidence level). The two white circles denote the positions of forward and reverse shocks [26]. Also shown here are the best-fit positions from the previous VERITAS [28] and Fermi-LAT observations [29] in red and magneta crosses, respectively.

radius is estimated at a value of $4.8' \pm 0.4'$. This showed the emission region of Cas A is is consistent with a point source in the TeV range above an energy threshold of 200 GeV.

6.3.5 Gamma-ray energy spectrum

To derive the energy spectrum of Cas A, the entire data set is used. γ rays are selected from a region of radius 0.09° around Cas A position. After removing the background from this region, 495 excess γ-ray events are detected at a significance level of 13.1σ. These γ-ray events are then distributed in 9 equal bins in logarithmic energy space from an energy of 200 GeV to $\sim$ 12 TeV (see Table 6.6). The differential energy spectrum (see Figure 6.5) is derived above 200 GeV and is well-described by a power-law model:

$$\frac{dN}{dE} = (1.45 \pm 0.11) \times 10^{-12} (E/\mathrm{TeV})^{-2.75 \pm 0.10_{stat} \pm 0.20_{sys}} \ \mathrm{cm}^{-2}\ \mathrm{s}^{-1}\ \mathrm{TeV}^{-1}\,. \qquad (6.3)$$

This power-law fit to the data points gives a χ^2 of 2.22 for 5 degrees of freedom, resulting in a good fit probability of 81%. This result is in good agreement with the previously published HEGRA [220], VERITAS [28] and MAGIC [221] spectral measurements, if both statistical and systematic errors are taken into account. Based on the analysis of present data-set, the statistical errors on the spectral index are reduced by $\sim 60\%$ as compared to the published VERITAS index [28].

6.3.6 Joint spectral energy distribution using Fermi and VERITAS points

Figure 6.11 shows the joint fitting of *Fermi*-LAT (above the spectral break only, i.e. > 1.5 GeV) and VERITAS spectral points using three different models: a single power-law (PL), a power-law with exponential cut-off (PLE) and a smoothly-broken power-law (SBPL). See Table 6.7 for the formulae of each spectral model. The PL fit yields a χ^2 fit probability of 2.2×10^{-6}, whereas the PLE and SBPL yield χ^2 fit probabilities of 0.05 and 0.09, respectively. The PLE and SBPL models are therefore favored over the PL model at $> 5.0\sigma$ level. However, this is true only if we take into

Table 6.6: SED points from VERITAS data in energy range 200 − 10000 GeV

Energy (GeV)	Band (GeV)	$E^2dN(E)/dE$ (10^{-9} GeV^1 cm^{-2} s^{-1})	TS
251	200-316	9.49 (upper limit)	0
398	316-501	$2.67^{+0.49}_{-0.48}$	37
631	501-794	$2.27^{+0.33}_{-0.32}$	66
1000	794-1259	$1.35^{+0.25}_{-0.24}$	40
1585	1259-1995	$1.14^{+0.23}_{-0.22}$	35
2512	1995-3162	$0.88^{+0.21}_{-0.19}$	28
3981	3162-5012	$0.39^{+0.18}_{-0.16}$	7
6310	5012-7943	$0.31^{+0.16}_{-0.13}$	8
10000	7943-12589	0.23 (upper limit)	1

account just the statistical errors on the data points. Adding a systematic error of 0.1_{sys} [29] in the Fermi spectral index and 0.2_{sys} [229] on the VERITAS spectral index, reduces the significance of the PLE and SBPL over PL to the $\sim 4.0\sigma$ level. Since both PLE and SBPL show the same significance, and PLE has fewer parameters than SBPL, the PLE can be used as the best-fit model for our data-set. The energy of the cut-off is measured to be 2.5 ± 0.58 TeV. This value is consistent with the MAGIC results, that measured a cutoff energy at $3.5^{+1.6}_{-1.0}$ TeV [223].

6.4 Modeling and interpretation

Before starting the modeling section, I would like to mention that modeling work is performed in collaboration with two theoretical scientists in the VERITAS collaboration. In October 2015, I received iPROGRESS scholarship award from Helmholz Alliance for Astroparticle Physics. This award supported a 4-week travel to work at DESY, a national research center in Germany. During that period, I collaborated with Martin Pohl and his graduate student Alina Wilhelm to understand the origin of gamma-ray emission from Cas A.

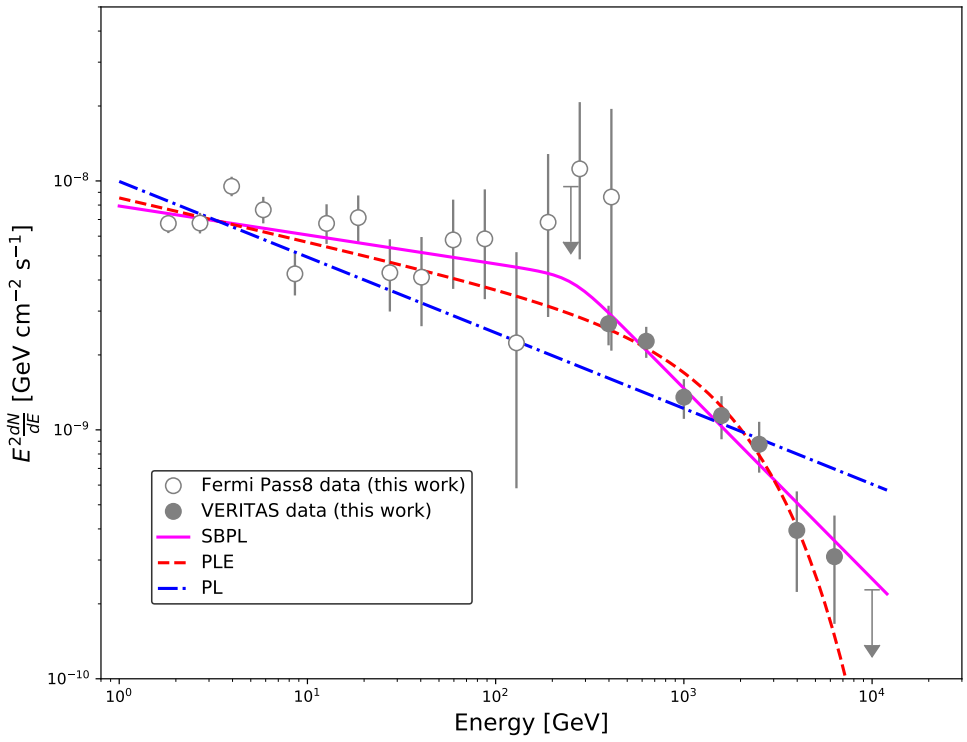

Figure 6.11: *Fermi* and VERITAS spectra of Cas A with statistical errors only. Only those *Fermi* points are shown which lie above the low energy break (i.e. above 1.5 GeV). Three different power-laws are fitted to the entire range from GeV to TeV energies. A smoothly-broken power-law or a power-law with an exponential cut-off are favored over the simple power-law fit, at more than 5σ level.

Table 6.7: Comparison of different spectral models

Spectral Model	Formula	Parameter values	χ^2 / ndf
PL	$N_0(E/E_0)^{-\gamma}$	$\gamma = 2.30 \pm 0.01$	63/20
PLE	$N_0(E/E_0)^{-\gamma}\exp(E/E_c)$	$\gamma = 2.18 \pm 0.02$ E_c (TeV) $= 2.5 \pm 0.58$	30/19
SBPL	$N_0(E/E_0)^{\gamma_1}(1+(E/E_b)^{\frac{\gamma_1-\gamma_2}{\beta}})^{-\beta}$	$\gamma_1 = -2.12 \pm 0.05$ $\gamma_2 = -2.77 \pm 0.11$ E_b (TeV) $= 0.25 \pm 0.1$	26/18

6.4.1 Model assumptions

To constrain the nature of gamma-ray emission from Cas A, multi-wavelength data at GeV (*Fermi*-LAT; this work), TeV (VERITAS; this work), radio [30] and X-ray [31, 32] energies are used. For simplicity, we consider a one-zone model, which assumes that all the non-thermal emission, including radio, X-ray and gamma rays, is coming from the same emission region (i.e. forward shock). Furthermore, the number density ($n_{\rm H}$) and the magnetic field (B) in the emission region are considered as constant parameters. The particle spectra for electrons and protons are assumed to follow a power-law with an exponential cut-off:

$$N(p) = N_0\, p^{-s} \exp\left(-\frac{p}{p_{cut}}\right) . \tag{6.4}$$

Here p denotes the electron (proton) momentum normalized by its mass scale, $m_{e(p)}\, c$. The cut-off momentum, p_{cut}, and the power-law index of the spectra, s, are free parameters. The normalization, N_0, in principle reflects the injection efficiency of each particle species.

The gamma-ray emission, in general, can be explained by hadronic model (protons; neutral pion decay) or leptonic model (electrons; inverse Compton and non-thermal bremsstrahlung). In the context of multi-wavelength emission, it is assumed that same population of relativistic electrons, which produce inverse Compton (IC) and non-thermal bremsstrahlung (NTB), can also produce synchrotron emission. We computed electron contribution to the syncrotron, IC and NTB emission following [230, 231]. For the inverse Compton (IC) interactions, we consider two target photon fields: the cosmic microwave background and the infrared background with temperature $\sim 100\,\mathrm{K}$ and energy density $2\,\mathrm{eV\,cm^{-3}}$ [232]. Additionally, thermal bremsstrahlung contribution from plasma electrons is included assuming local thermodynamic equilibrium [233].

The γ-ray yield from protons assumed to produce γ-photons via neutral neutral-pion decay is computed using the procedure of [234]. Summarizing, with the hydrogen number density and the magnetic field strength we have in total nine independent parameters of our global model that we list in Table 6.8.

6.4.2 Hadronic dominated model

In this case, we assume that gamma rays are predominately produced by accelerated protons through their interaction with ambient gas (through neutral pions), with a small electron contribution from the NTB and IC components. The electron power-law index, $\mathrm{s_e} \approx 2.5$, is entirely fixed by the radio data [30], and the cutoff is constrained by synchrotron X-ray flux [31]. A minor discrepancy occurs above 100 keV where the INTEGRAL spectral data [32] suggest a spectral hardening, which might reflect an asymmetric explosion [32] and thus can not be included in our modeling. An alternative explanation might involve weakly relativistic electrons emitting non-thermal bremsstrahlung.

Following the most recent result of [216], we take for the upstream gas density $n_\mathrm{H} \approx 1.0\,\mathrm{cm^{-3}}$. The magnetic field in the downstream region, $B \approx 450\,\mu\mathrm{G}$, is chosen to suppress the IC component. This is the minimal value required to establish the

hadron-dominated case. Additionally, the derived magnetic-field strength $\sim 450\,\mu$G is compatible with the results of [160], [214] and [235] who argue that, for Cas A, $B \sim 0.5 - 1\,$mG.

The entire spectral energy distribution (SED) is presented in Figure 6.12, and the corresponding model parameters are summarized in Table 6.8 (Model I). Besides hadronic component (green line), marginal IC and NTB components are also present. The electron temperature, T_e, is chosen according to [31], and the thermal emission provides a moderate contribution to the X-ray flux. The main reason for the rather insignificant thermal and non-thermal bremsstrahlung contributions is a relatively low plasma density in the downstream region[7]

6.4.3 Leptonic dominated model

In this section we investigate the possibility of a lepton-dominated model for the observed γ-spectrum of Cas A. The lowermost *Fermi*-LAT point at ∼100 MeV suggests the presence of additional emission besides the pion bump, such as non-thermal bremsstrahlung. Cas A has been considered for a long time as the best candidate for detecting non-thermal bremsstrahlung [236]. Non-thermal bremsstrahlung at a few hundred MeV is emitted by the same electrons that produce radio synchrotron emission at a few hundred MHz, and so a flux comparison between the radio data and the Fermi points at ∼100 MeV, $(F_{1\,\mathrm{GHz}}/F_{100\,\mathrm{MeV}})$, determines the relation between the average gas density and the minimal magnetic-field strength:

$$B \gtrsim 120\ \mu\mathrm{G}\ \left(\frac{n_\mathrm{H}}{\mathrm{cm}^{-3}}\right)^{\frac{2}{1+s_e}}\ . \tag{6.5}$$

It is important to note that Equation 6.5 constrains the magnetic field in the downstream region and the gas density in the upstream region of the shock.

With the upstream density $n_\mathrm{H} \approx 1.0\,\mathrm{cm}^{-3}$ [216], we obtain for the minimal magnetic-field strength, $B_{min} \approx 120\,\mu G$. If the magnetic field is decreased below

[7] The dependency on the downstream number density, $n_\mathrm{H,down}$, is linear ($\propto n_\mathrm{H,down}$) for the non-thermal and quadratic ($\propto n^2_\mathrm{H,down}$) for the thermal-bremsstrahlung intensities.

$B_{min} \approx 120\,\mu G$, then the IC contribution in the TeV domain overshoots the cut-off provided by the VERITAS data. Therefore, both IC and NTB provide the same lower limit for the magnetic-field value, $\sim 120\mu$G. The final SED for lepto-dominated model is shown in Figure 6.13. Furthermore, the Table 6.8 presents the parameters for the global lepto-dominated model (Model II). Although the IC contribution can explain the TeV data when we use a minimum magnetic field of $120\,\mu G$, the GeV emission can not be explained without invoking the pion decay model. Therefore, according to our observations, we conclude that a purely leptonic model is very unlikely. However, an advantage of the lepto-hadronic model is a possible explanation for the hardening of the X-ray spectrum above 100 keV observed with INTEGRAL [32] by emission from non-relativistic electrons radiating NTB.

6.4.4 Discussion

The total cosmic-ray energy from our hadro-dominated model is $\sim 2 \cdot 10^{49}$ erg, which accounts for only 1% of the explosion energy, $E_{\rm SN} = 2 \cdot 10^{51}$ erg, of Cas A [237].

The observed radio spectrum constrains the spectral index of the electrons to be $s_e \approx 2.5$, and also the γ-ray data favor a softer proton spectrum, $s_p \approx 2.16$, than predicted by DSA. One possible explanation involves effects arising from turbulence growth and damping [238, 239]. Alternatively, quasi-perpendicular shocks in young SNRs can steepen the spectral index [240]. Moreover, the complex hydro-dynamical structure of the progenitor wind zone and acceleration at the reverse shock in young core-collapse SNRs can significantly modify the particle spectra [241, 242]. In the case of Cas A, particle acceleration at the reverse shock is suggested by observations of X-ray synchrotron emission from the region of the reverse shock [243], but newer data indicate that essentially all of the $>$ 15-keV synchrotron flux is produced in small knots located in the 3D interior of the remnant, rather than a surface like the reverse shock [27]. Finally, stochastic re-acceleration of electrons behind the forward shock may be able to soften the total particle spectra over a certain range in energy [231]. In the present work, we presented a simple procedure to derive the most important

conclusions. However, it is likely that a more sophisticated model is needed to further differentiate between competing scenarios concerning particle acceleration in SNRs.

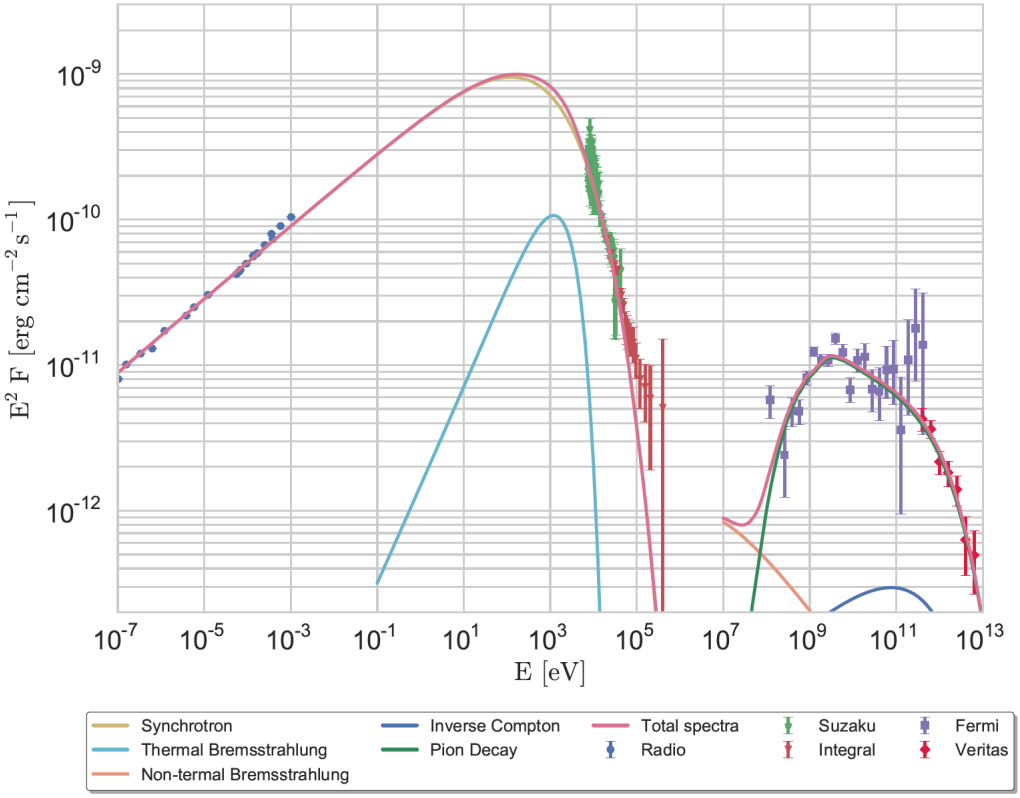

Figure 6.12: Model I: Hadronic dominated model with downstream magnetic field $B \approx 450\,\mu$G and upstream gas density $n_H = 1\,\mathrm{cm}^{-3}$. The radio data is taken from [30], X-ray from [31] and [32].

6.5 Conclusions

We have presented a detailed study of the supernova remnant Cas A using 8 years of *Fermi*-LAT and 65 hours of VERITAS data. The centroid positions from *Fermi*-LAT and VERITAS measurements are consistent, within errors, and lie inside of the remnant. Since the size of the remnant is comparable to the PSF of Fermi-LAT and VERITAS instruments, it is difficult to locate the position of emission from this SNR. A spectral break is detected at 1.48 ± 0.3 GeV with the Fermi-LAT, which is

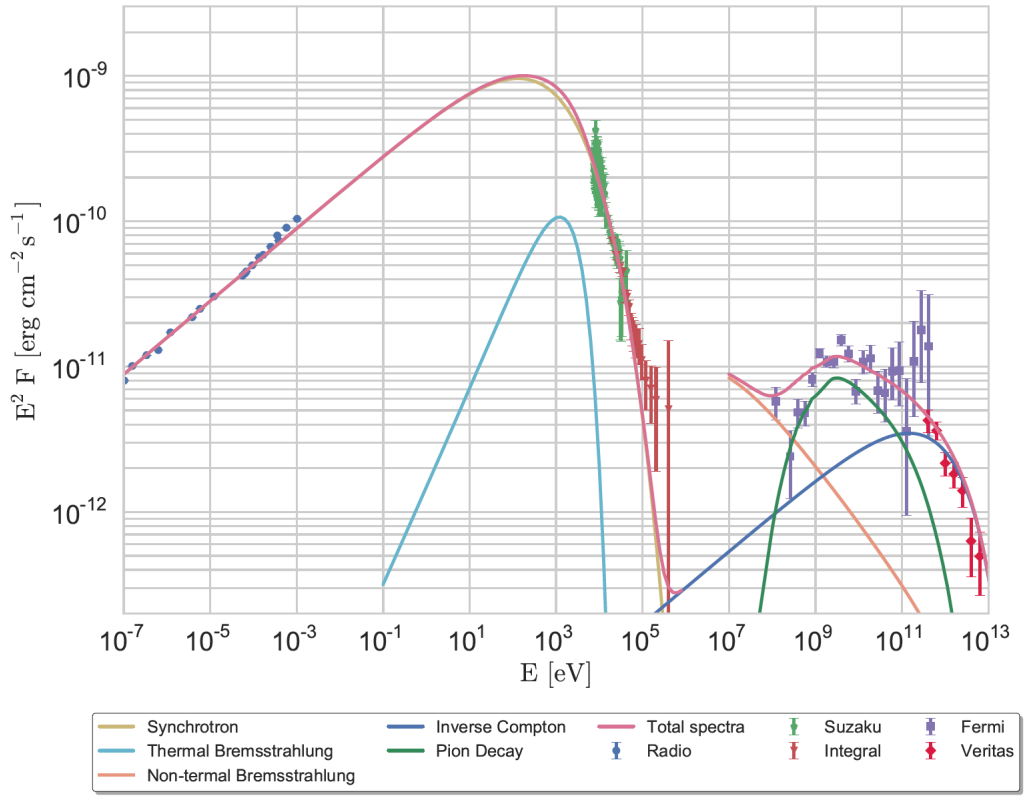

Figure 6.13: Model II: Leptonic dominated model with an absolutely minimal magnetic field (in the downstream region) $B \approx 120\,\mu$G and upstream gas density $n_H = 1\,\mathrm{cm}^{-3}$. The radio data is taken from [30], X-ray from [31] and [32].

Table 6.8: Parameters for theoretical models. The hydrogen number density, n_{H}, corresponds to the upstream while further quantities to the downstream regions.

Model	n_{H} (cm^{-3})	B (μG)	T_e (10^7K)	$N_{0,e}$ ($\mathrm{cm}^{-3}/(\mathrm{m_e c})$)	s_e	$p_{cut,e}$ ($\mathrm{m_e c}$)	$N_{0,p}$ ($\mathrm{cm}^{-3}/(\mathrm{m_p c})$)	s_p	$p_{cut,p}$ ($\mathrm{m_p c}$)
I	1.0	450	1.8	$6.1 \cdot 10^{-3}$	2.5	$9.0 \cdot 10^{6}$	$1.1 \cdot 10^{-5}$	2.16	$1.9 \cdot 10^{4}$
II	1.0	120	1.8	$6.1 \cdot 10^{-2}$	2.5	$1.8 \cdot 10^{7}$	$8.4 \cdot 10^{-6}$	2.16	$3.0 \cdot 10^{3}$

consistent with the previous observations [29], and can be explained by γ-ray emission produced through neutral-pion decay. In addition, a joint spectral fit of Fermi-LAT and VERITAS spectral data from 2 GeV to 10 TeV prefer an exponential cutoff power-law to a single power-law model. The cutoff energy found using Fermi-LAT and VERITAS data is estimated at 2.52 ± 0.58 TeV. This is compatible with the cutoff energy found by the MAGIC collaboration using only MAGIC data [223]. This shows that the Cas A SNR is unlikely to be a source of PeV cosmic rays.

In the theoretical part of this work, we have performed a broadband spectral fit by taking gamma-ray data from *Fermi*-LAT and VERITAS. We also took into account data from radio and X-ray observations. Under the assumption of global one-zone model, two different scenarios for the origin of gamma-ray emission are considered: a leptonic dominated and a hadron dominated case. If the lowest energy point in the MeV range (around 100 MeV) is not taken into account, due to large systematic errors (see Figure 6.5), then the hadronic dominated scenario is strongly favored. However, if the systematics errors on flux points are ignored, then it is difficult to distinguish between hadronic dominated and leptonic dominated models. Furthermore, a purely leptonic model is excluded, and we conclude that proton acceleration up to TeV energies is clearly evident. Despite the efficient hadron acceleration, only 1% of the explosion energy is converted into cosmic rays, according to our estimates.

Furthermore, assuming a NTB flux in Cas A, we set an absolute minimal value for the magnetic-field strength inside the remnant, $B_{min} \approx 120\,\mu$G. Additionally, this value is independently confirmed by the IC peak. Therefore, it is evident that an efficient magnetic-field amplification occurs in Cassiopeia A.

Summarizing, the most important results of our measurements are:

1. A confirmation of the pion bump in the Cas A SNR
2. Clear evidence for acceleration of protons in Cas A up to TeV for any scenario
3. A cut off is seen in the TeV domain, which clearly indicates that Cas A is unlikely to be a Pevatron at present time
4. If the contribution of NTB is significant for the gamma-ray emission, then a lower limit for the magnetic field $B_{\rm min} \approx 120\ \mu$G can be derived

Chapter 7

RESOLVED SPECTRAL AND MORPHOLOGICAL STUDY OF TEV SNR IC 443 WITH VERITAS

In the constellation of Gemini, IC 443 (G189.1+3.0) is a middle-aged SNR, with an angular size of 50 arc minute, located in the direction of the Galactic anticenter. It shows a prominent shell-like structure in the radio and optical bands, while its appearance in X-rays is centrally filled [33, 244, 245, 42]. These morphological features imply that this remnant belongs to the class of mixed morphology SNR [246]. The distance to this source is uncertain and lies in the range $0.7 - 1.5$ kpc [247]. However, the assumption of the remnant's shock interaction with an HI cloud (associated with H II region sharpless 249) leads to a distance of $1.5 - 2.0$ kpc [248]. The remnant is believed to have resulted from a supernova explosion which happened $\sim$ 3000 years ago [245]. This explosion date is derived if the velocity of the shock is adopted from X-ray observations. However, if the velocity is derived from the optical filaments, then the explosion date changes by an order of magnitude to $\sim$ 30000 years ago [249]. A neutron star is also found in IC 443 in radio and X-ray observations, suggesting a core-collapse origin of the remnant, though no pulsations are detected from this neutron star [34]. The velocity of the neutron star ($V_{NS} = 250 \pm 50$ km s^{-1}) provides an alternative estimate of the age of the SNR of about 30000 years [34]. A possible association of the neutron star with the IC 443 remnant is argued on the basis of detection of very hard X-ray emission in the southern edge of the remnant. This emission can be interpreted as a wind nebula powered by neutron star physically associated with IC 443[34, 250]. However, Leahy (using radio observations) and Asaoka and Aschenbach (using X-ray observations) questioned the association of the pulsar with IC 443. Instead, they

advocate the association of the pulsar with a fainter, older SNR, G189.1+3.3, lying in front of IC 443 [251, 252].

IC 443 has always been a very interesting target for γ-ray observations using space-based and ground-based telescopes. It belongs to a class of SNRs which shows ample proof of supernova shock interaction with molecular clouds [253, 39, 254, 36, 43]. Since the molecular cloud provides dense target material for the accelerated cosmic rays, the resultant gamma-ray emission is expected to be prominent [255, 256, 257]. In this regard, IC 443 provides an opportunity to study the connection between SNRs, molecular clouds, non-thermal particle acceleration and gamma-ray emission.

7.1 An overview of the morphology of IC 443

Studying radio to X-ray data reveals a complex morphological picture of the IC 443 remnant, owing to its evolution in a very inhomogeous environment. Despite the complexity, the overall picture of IC 443 is simplified by Braun & Strom [33]. It consists of two shells (A and B) with different radii as depicted in Figure 7.1. Shell A lies in the northeast (NE) direction and appears to be confined by the encounter of the shock with a neutral HI cloud [258]. It includes bright optical [248], radio [259, 260, 35], and infrared filaments [36]. Shell B represents the shock front in the south-west direction where the surrounding medium is more homogeneous and rarefied [261]. This results in greater radial extent and dimmer surface brightness for shell B than shell A. In addition to the A and B shells, a third larger and fainter shell C is also proposed to be associated with IC 443. However, Asaoka & Aschenbach proposed that the shell C is a part of another SNR, G189.1+3.3 [251].

Optical filaments in the NE region are interpreted as the recombined neutral gas behind the shock front. Spectrophotometry of these filaments performed by Fesen & Kirshner indicate a gas temperature of the order of 10^4 K and an electron density in the range of less than 100 up to 500 cm^{-3} [244]. Comparison of these observations with the shock-wave model of Raymond suggests that a 65 to 100 kms^{-1} shock is propagating through preshock H I cloud of density $10 - 20$ cm^{-3} [262]. However, from the infrared

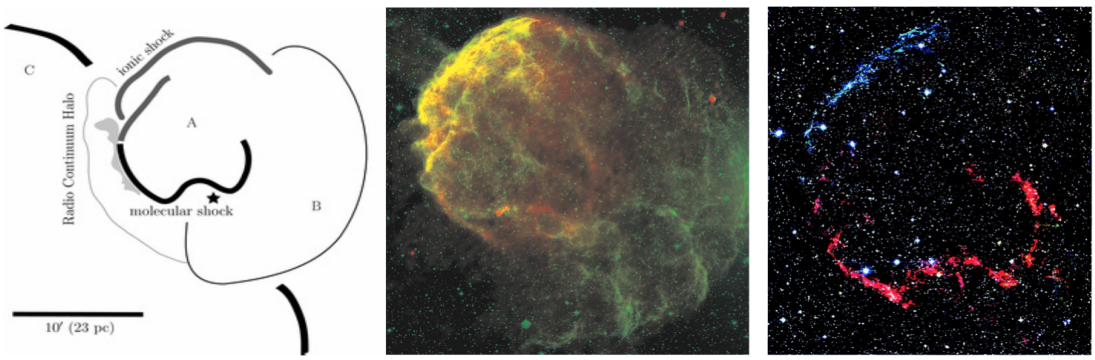

Figure 7.1: (left)Schematic showing the overall morphology of IC 443. The shell nomenclature is adopted from Braun & Strom [33]. The star indicates the position of the neutron star [34]. (middle) Radio at 330 MHz (red) and optical(green) emission from IC 443. The yellow color indicates the regions where radio and optical emission overlaps [35]. (right) A color representation of near infrared emission observed with 2MASS in J (blue), H(green) and K (red) band [36]. It is worth mentioning here that the red color in the K band is mostly emission from H_2 lines.

emission in the NE region, coming mainly from atomic lines, Rho deduces a preshock density of $10-1000$ cm^{-3} [36]. When the NE region is observed in the radio waveband (at 1420 MHz by Lee et al. [37], 74 MHz and 330 MHz by Castelletti et al. [35]), bright filaments are observed, which show a strong correlation with the optical filaments. The observed radio emission in IC 443 is interpreted as the synchrotron radiation of very high-energy electrons gyrating in the magnetic field of the shell of the remnant. Moreover, a spatial resolved radio spectral studies in IC 443 revealed a spectral index variation across the remnant [35]. The brightest parts of the remnant along the eastern border and the parts interacting with the molecular clouds shows a flat spectrum ($\alpha < 0.25$). This flat spectrum is signature of Fermi shock acceleration occurring at the sites where SNR blast wave interact with the dense material. This confirms that SNR is accelerating particles at the sites of strong interaction with surrounding medium.

In the soft X-ray band ($\sim 0.5-3.0$ keV), observations were carried out with

the Einstein Observatory [245], ROSAT [251] and XMM-Newton [42], which shows that the emission is primarily thermal ($\sim 10^7$ K) in nature and arises primarily from swept-up interstellar gas. Unlike the radio/optical shell structure, the emission in X-rays is seen predominately from the interior of the remnant towards the NE quadrant. Contrary to this, the morphology of very soft X-ray emission ($0.3-0.5$ keV) correlates well with the optical and radio shell in the NE region [42]. The position of the brightest X-ray emission is confined behind the brightest optical filaments. This is consistent with a shock front that encounters asymmetries in the density of ISM gas, with higher density located in the outward regions. In addition to soft X-rays, a hard component is also detected up to 20 keV using Ginga, which was believed to be thermal in nature [263]. However, *Chandra* data revealed that the hard emission is non-thermal in nature (synchrotron emission) and results from a pulsar wind nebula (PWN) powered by a neutron star (age 3×10^4 yr) [34]. This statement is further supported by radio observations that show significant polarization and flat radio spectrum from the PWN [34].

Apart from the atomic cloud in the NE region, with a total estimated mass of 730 solar masses (500 solar masses shocked mass) [37], IC 443 is also known for its association with a molecular cloud. This cloud, which divides the remnant into shell A and B, appears to be lying diagonally in front of the SNR, from the the north-west to south-east direction, and absorbs most of the optical emission [264, 253]. CO observations are used to estimate the mass of the entire molecular cloud associated with IC 443 at 9.24×10^3 solar masses [265]. One of the interesting features of IC 443 is its interaction with the molecular cloud, the first evidence for which was given by DeNoyer, who detected high-velocity HI emission, and subsequently detected emission and absorption lines of CO and OH molecules [258, 38, 266]. This detection was later confirmed by the detection of several OH masers from the southern boundary of shell A [43]. The interaction produces the shocked gas whose distribution was mapped by Dickmann in CO and HCO+ [39] and by Xu in CO[265]. The emission from the shocked gas is bright along the southern boundary of shell A. Dickmann [39] and Huang [41],

identified smaller and brighter emission regions along this boundary and called these regions shocked clumps (named B-H, see Figure 7.2). From this, the total mass of perturbed gas is estimated at $500 - 2000$ solar masses [39]. Furthermore, the Two Micron All Sky Survey image shows strong shocked H_2 emission lines not only along the southern sinuous ridge (W-shaped see Figure 7.1) but also from the inner part of the northeastern rim [36]. These lines results from the interaction of slow moving shock (velocity of 30 km s^{-1}) with a molecular gas of density $\geq 10^4$ cm^{-3} [36].

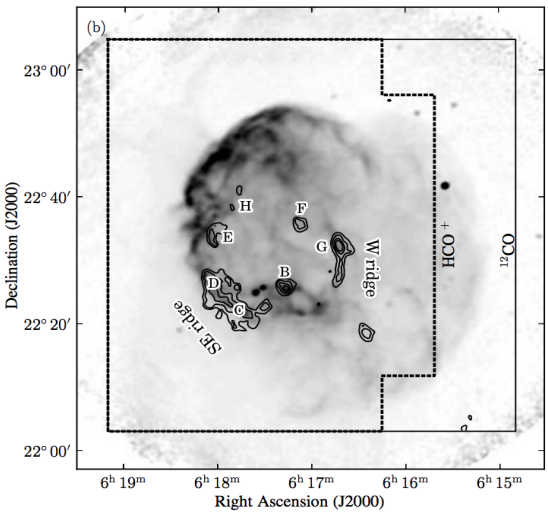

Figure 7.2: The contours are distribution of shocked 12CO overlaid on 21 cm radio continuum image taken from [37]. The shock clumps (BH) identified by Denoyer [38] and Dickman et al. [39] are indicated..

7.2 Previous high-energy and very high-energy gamma-ray observations

The dense molecular environment around IC 443 provides a reasonable site for the production of gamma rays through its interaction with accelerated cosmic rays. In fact, a detection of these gamma-rays at GeV energies by EGRET [217], Fermi-LAT [40, 21], AGILE [267] and at TeV energies by MAGIC [23] and VERITAS [22], has already been established. The measured locations of the gamma-ray emission at GeV and TeV energies correlates with shocked clump regions (for clump definition, see

previous section) [40]. Figure 7.3 shows that GeV emission is peaked towards the center of remnant and TeV emission is located near the position of shocked clump G. Moreover, the emission at GeV and TeV energies is displaced from the known pulsar wind nebula by 0.26° and 0.15° respectively. Interestingly, gamma-ray emission anticorrelates with radio, optical and X-ray emissions which are mainly concentrated towards the rim of the remnant (NE). Two different models have been proposed to explain the gamma-ray emission. In the first case, the gamma-ray emission can be produced by the direct interaction between the accelerated particles and shocked molecular gas [190, 249, 268]. Alternatively, high energy protons can escape from the acceleration region and collide with the unshocked molecular cloud ahead of the SNR shock. In both cases, gamma-ray emission can be produced through p-p interaction [269, 189]. The TeV emission can also be explained with inverse Compton scattering off electrons accelerated from the PWN. However, the emission at GeV seems inconsistent with PWN scenario due to large displacement between the PWN and the Fermi source (the PWN is 11 times away from the localization error of the centroid of the Fermi emission, i.e. 0.26 degree away [40].

The gamma-ray observations from IC 443 and their interpretation described in the previous section were established prior to the work I will present in this chapter. Since the first detection of IC 443 by VERITAS, we continued to observe this source and accumulated approximately 153 hours of livetime data in total. With an angular resolution better than 0.1° at 1 TeV, combined with a long exposure, we have been able to resolve IC 443 for the first time at TeV energies. In this chapter of thesis, I will report the results from the entire data set taken by VERITAS on IC 443.

7.3 Summary of observations

The IC 443 observations used in this thesis were conducted between February 2007 and March 2015. This period can be divided into three epochs, where each epoch defined a progression of VERITAS array towards better sensitivity. During the period of three epochs, the VERITAS array underwent two major upgrades (see section

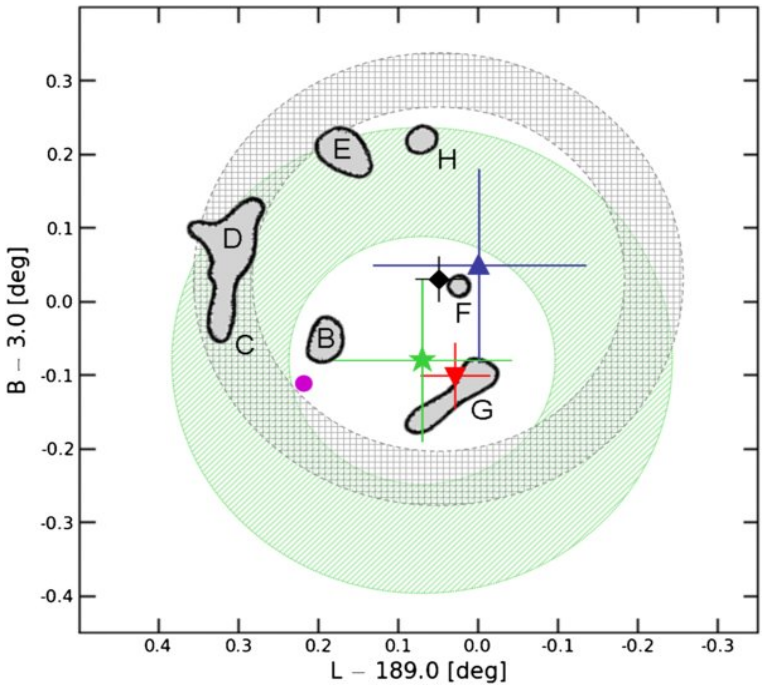

Figure 7.3: (Figure 5 from [40]) Locations of centroids of gamma-ray sources detected by four instruments: EGRET ($\triangle$), Fermi-LAT ($\diamond$), MAGIC ($\bigtriangledown$), VERITAS ($\star$).The PWN location is shown as a magenta dot. Contours are the locations and shapes of the local shocked molecular clouds [41]. Cross-hatched and striped green bands represent the best-fit extension measurements (in degrees) from Fermi-LAT ($0.27\pm0.01(stat)\pm0.03(sys)$) and VERITAS ($0.24 \pm 0.05(stat) \pm 0.06(sys)$) respectively.

6.3.1 for explanation). Most of the observations are taken in wobble mode in which telescopes are pointed to a position 0.7° from the source position. In the first epoch (Data set I), 54 hours of data were taken, which corresponds to a live time of 46 hours after applying data quality cuts and dead time correction. These data were taken before the relocation of the prototype telescope to a more optimal position. Based on these data, the VERITAS collaboration announced the discovery of IC 443 [22]. The second epoch (Data set II) starts when the array became more sensitive due to better positioning of all four telescopes. A total of 44 hours of data was accumulated during the second epoch, corresponding to 38 hours of livetime. The third epoch (Data set III) corresponds to the date when all PMTs from the four cameras were replaced with new high quantum efficiency PMTs. An additional 82 hours of data were recorded in the third epoch, corresponding to 69 hours of livetime data. Combining all three epochs, after selecting quality data, yields a dead-time corrected live time of 153 hours.

7.4 Data analysis procedure

The first two steps in the data analysis pipeline related to image cleaning and parametrization follows the standard procedure (see Chapter 4 for details). To separate gamma-ray events from background events, standard *moderate cuts* are used, where only those events were selected which triggered at least three telescopes. Moreover, a minimum number of 120 (and 80) photo-electrons are required in each recorded image, depending upon the epoch. The remaining background, after the application of analysis cuts, is estimated using the reflected region model [119]. In the case of IC 443 data analysis, we require morphological and spatially-resolved spectral studies. A different value of θ^2 cut is used for morphological and spectral studies. For morphological studies, the best angular resolution is desirable, which is obtained by using a tighter cut on $\theta^2 < 0.008\,\mathrm{deg}^2$. On the other hand, spectral studies were performed using a larger angular integration radius. Larger integration radius is required to take into account the gamma rays from the entire remnant. For the whole remnant, θ^2 cut value of $0.12\,\mathrm{deg}^2$ was used. Since the remnant is extended in gamma-ray regime [22], it is

also possible to obtain spatially-resolved spectral measurements. To do that, the whole remnant was divided into four sub-regions and excess gamma-ray events were obtained from each region using θ^2 cut value of $< 0.0169\,\mathrm{deg}^2$. A summary of analysis cuts are illustrated in Table 7.1. These cuts results in an energy threshold of ~ 200 GeV.

7.5 Source Morphology using new VERITAS data

Figure 7.4 shows the background subtracted excess gamma-ray count map in a $2^\circ \times 2^\circ$ region surrounding IC 443. The number of counts in each bin (size $0.01^\circ \times 0.01^\circ$) of the skymap is calculated using an integration radius of 0.09°, corresponds to a $\theta^2 < 0.008\,\mathrm{deg}^2$. This map is produced by analyzing 153 hours of usable data using standard Hillas paramterzation criterion (see Chapter 4) and analysis cuts described in the first row of Table 7.1.

7.5.1 Comparing GeV and TeV morphology

For comparison of GeV emission with TeV emission, an updated *Fermi*-LAT analysis of IC 443, using 83 months of Pass 8 data, is performed [270]. During the morphology study, only PSF2 and PSF3 type events having energy greater than 5 GeV are used. This event selection criterion allows the GeV analysis to achieve an angular resolution comparable to the TeV analysis. Figure 7.5 shows the counts map of gamma-ray photons associated with IC 443. In addition, TeV contours from VERITAS at the 3, 6, 9, and 12σ level are overlaid over the Fermi counts map. The high degree of resemblance between the GeV and TeV morphology suggests that the morphology is energy independent, and the gamma-ray emission may be originating from a single population of cosmic rays interacting with shocked gas.

7.5.2 Comparison with other wavelengths

Figure 7.6 shows the morphological comparison of radio, optical and X-ray emission with the gamma-ray emission. Radio and optical images show similar emission in the north east region, where the gamma-ray emission is the weakest. In the NE region, only atomic gas is detected, and ionization and recombination of gas after the

Table 7.1: Cuts used in the analysis of IC 443 data

Analysis type	Parameter value						
	size (digital counts)	θ^2	N_{tel}	MSCW	MSCL	Emission height	Core position
Morphological studies	> 400 (V4 & V5) > 600 (V6)	$< 0.008°$	≥ 3	$[-1.2, 0.5]$	$[-1.2, 0.7]$	> 6 km	350 m
Spectral studies	> 400 > 600 (V6)	$< 0.0169°$ (sub-regions) $< 0.12°$ (entire remnant)	≥ 3	$[-1.2, 0.5]$	$[-1.2, 0.7]$	> 6 km	350 m

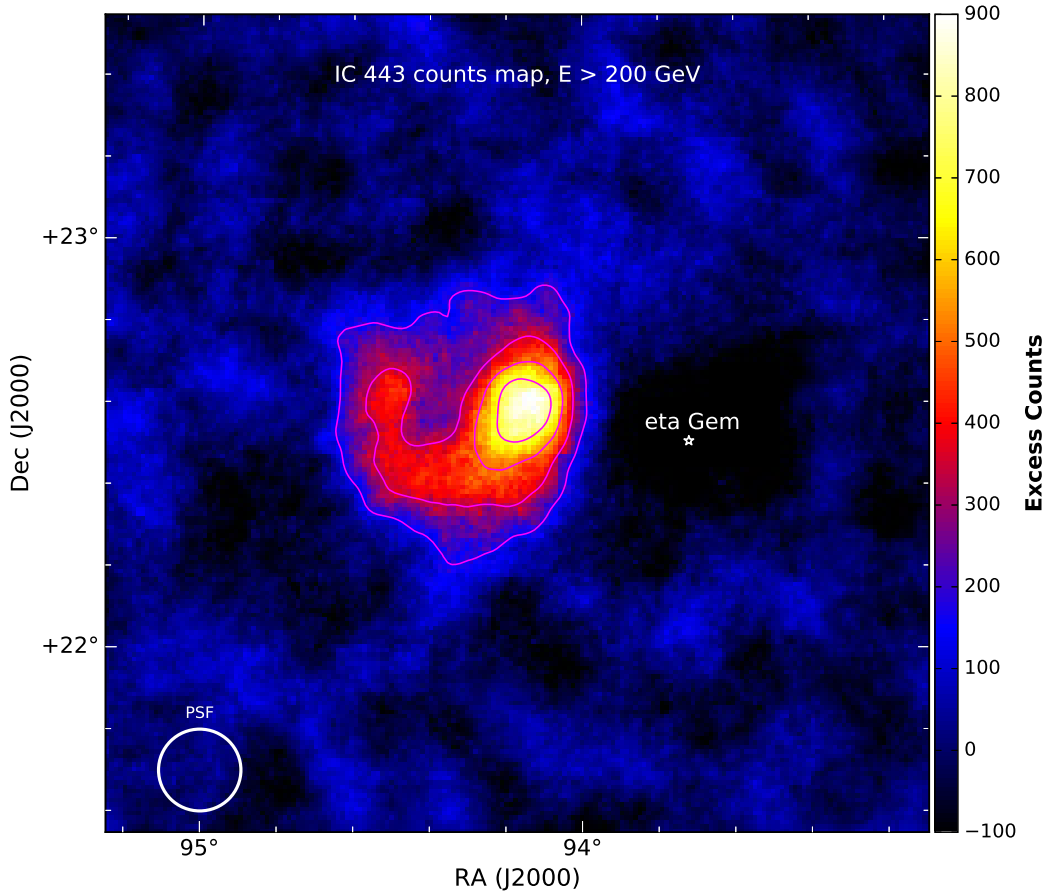

Figure 7.4: VERITAS IC 443 background corrected gamma-ray excess map made using $\sim$ 153 hours of livetime data. All gamma-rays in this image have energy $>$ 200 GeV, as set by the analysis threshold. Magenta contours indicates VERITAS signal from IC 443 at the 3, 6, 9 and 12σ levels. The white star shows the position of a bright star (magnitude of 4.91) close to IC 443. The color indicates the number of gamma ray events per bin calculated using an integration radius of 0.09°. The white circle in the lower left corner indicates the VERITAS PSF (68% containment radius) of 0.1°.

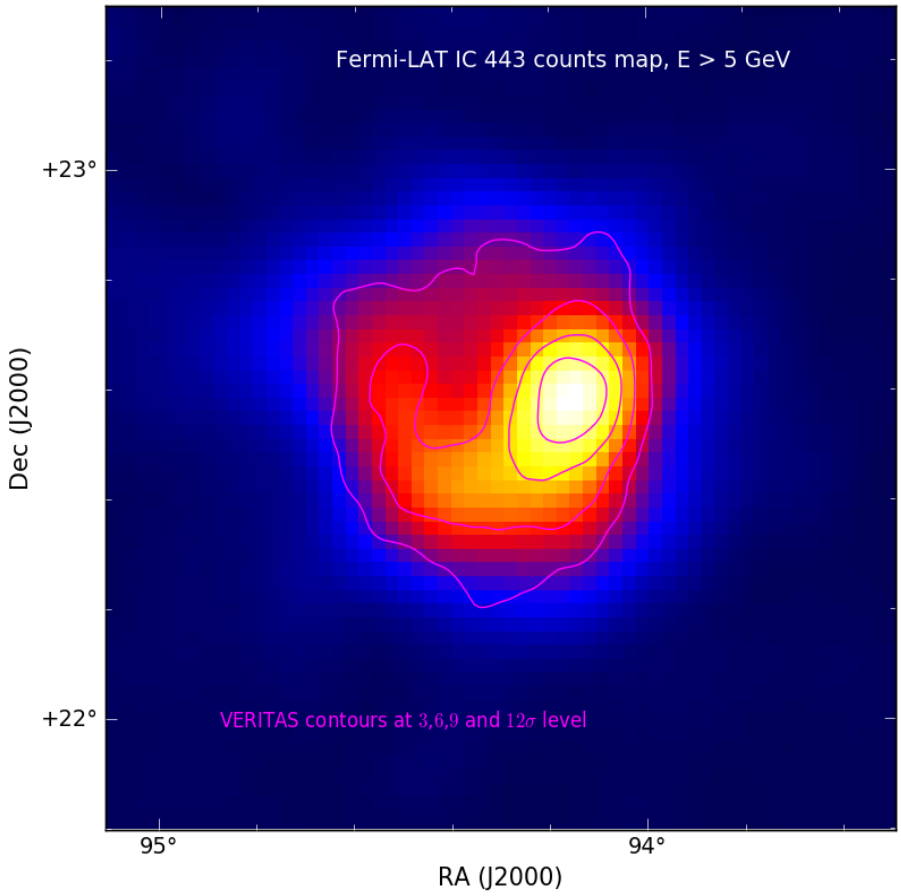

Figure 7.5: Fermi-LAT counts map of Pass 8 gamma-ray events from $5 - 500$ GeV. In order to match with the resolution of VERITAS events, only PSF2 and PSF3 type events are used in Fermi analysis. The overlaid magenta contours are taken from the VERITAS significance map at 3, 6, 9 and 12σ level.

passage of the shock dominates the emission mechanism. The extinction of the radio and optical emission from the NW to SE region is due to the tilted molecular cloud lying in front of the remnant. In X-rays, the strongest emission lies in the northen region, while weak diffuse emission is seen all over the remnant.

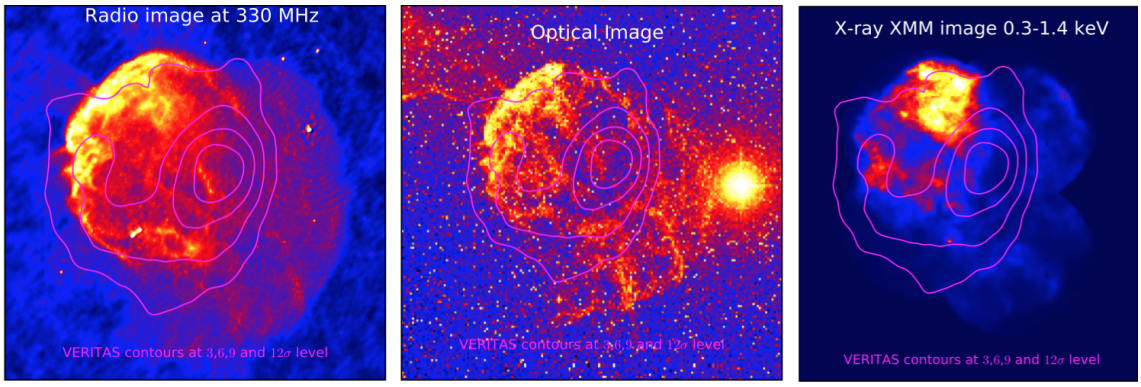

Figure 7.6: (left) Radio Image at 330 MHz [35], (middle) Optical image from Digital sky survey, and (right) XMM X-ray image in $0.3-1.4$ keV [42]. Magenta contours overlaid on every image are taken from VERITAS at 3, 6 ,9 and 12σ significance level. These images shows a weak correlation of radio, optical and X-ray emission with the gamma-ray emission at GeV/ TeV energy.

A comparison of the shocked gas, traced by HCO+, CO and maser emission, with the gamma-ray emission at GeV and TeV energies, shows a remarkable degree of correlation. It should be noted that the region of the strongest gamma-ray emission lies close to clump G as shown in Figure 7.7(a). This could be explained using the Chevalier model [249] (see Figure 7.7(b)) which suggests that gamma-ray emission could result from the interaction of the SNR shock with molecular clumps.

7.6 Energy spectrum at TeV energies

The increased data set for IC 443 results in a resolved morphology, which in turn allows us to do a spatially-resolved spectral analysis. For this, we divide the entire remnant into four regions and study the properties of gamma-ray emission from each region separately. Figure 7.8(a) shows the selected four regions from which the

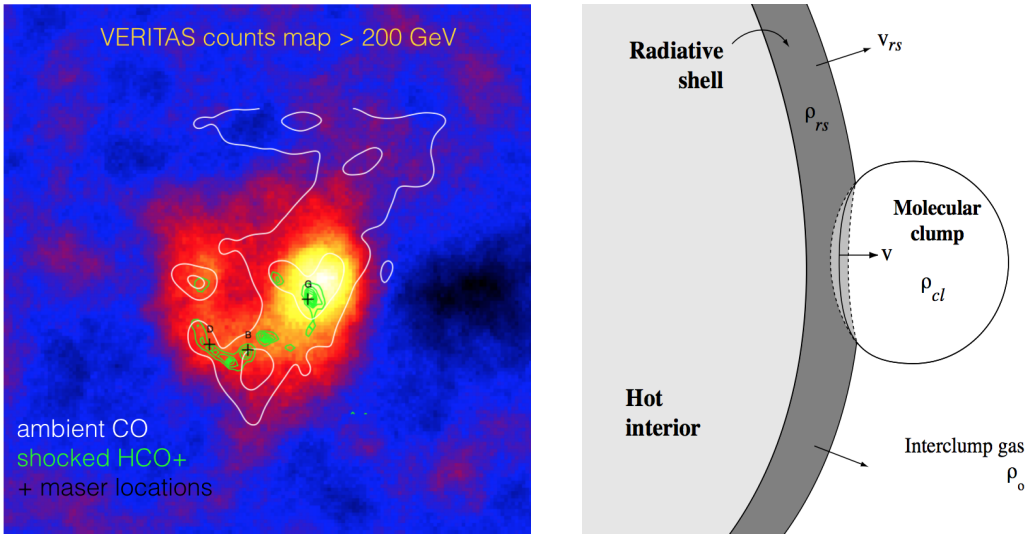

(a) (b)

Figure 7.7: (a) VERITAS excess map above an energy of 200 GeV overlaid with ^{12}CO contours (white) and shcoked HCO+ contours. Black crosses on the image shows the positions of three maser emission detected [43].(b) Schematic figure of the interaction of radiative shell, moving at velocity some velocity v, with the molecular clump.

spectrum is extracted and fitted with power-law function as shown in Figure 7.8(b). Similarly, the spectrum is extracted from the entire remnant. Table 7.2 shows the values of parameters calculated from fitting the power-law function. All the five regions show a soft spectral index near $\Gamma \sim -3$, and there is no statistically significant evidence for any spectral variations between four regions. The previous studies at TeV energies [23, 22] measured similar soft spectral index, however previous studies could not resolve the source, and the amount of data was much less as compared to the data taken in this thesis.

7.6.1 Broadband spectrum combining GeV and TeV data

For broadband spectral studies, we took GeV − TeV spectral points from the entire IC 443 SNR (integration radius of 0.35°). The resulting spectrum is shown in Figure 7.9. The broadband spectrum shown here is fit with three different power law

Table 7.2: Results of power-law fits to spectral points extracted from four regions and entire remnant

Region	Radius (degree)	Position (Ra, Dec)	Integral flux (> 200 GeV) $1/(\text{cm}^2\,\text{s}^1) \times 10^{-12}$	Index	χ^2/ndf
Entire remnant	0.35	(94.31, 22.62)	11.05 ± 0.65	2.96 ± 0.09	4.02/6
Region 1	0.13	(94.15, 22.58)	4.57 ± 0.32	3.14 ± 0.09	17.08/5
Region 2	0.13	(94.36, 22.41)	2.34 ± 0.28	2.72 ± 0.12	2.32/7
Region 3	0.13	(94.51, 22.63)	1.91 ± 0.28	2.74 ± 0.02	3.12/3
Region 4	0.13	(94.30, 22.81)	0.38 ± 0.27	2.33 ± 0.60	0.94/1

functions. A broken power-law or power-law with exponential cutoff is preferred over a pure power-law model at the 7.8 and 7.4 σ level, as can be seen in Table 7.3. This significance calculation is performed by taking difference of the χ^2 values of two models in question ($\chi^2_{diff} = \chi^2_{model1} - \chi^2_{model2}$) and also by taking the difference of the degree of freedom ($df_{diff} = df_{model1} - df_{model2}$). From χ^2_{diff} value and df_{diff} degree of freedom value, the significance of preference of one model over the other can be estimated using χ^2 table.

From the fit statistics, it is reasonable to assume that the broadband spectrum can be explained with a broken power law, where the break energy is estimated at $E_{break} = 43 \pm 14$ GeV. This energy is slightly higher than the break energy of ~ 20 GeV already calculated by [21]. Here, we can say that the broadband spectrum smoothly connects from GeV to TeV energies, and suggests that the same particle population is responsible for the production of gamma-ray emission. In the next section, I will try to explain the origin of gamma-ray emission using both hadronic and leptonic scenarios.

7.7 SED modeling

The modeling of the gamma-ray emission from IC 443 is not carried out in a detailed fashion as we have performed in the case of Cas A in the previous chapter. Rather, I have used a publicly available code *naima* [271], a python-based package. This code allows the computation of non-thermal radiation from relativistic population of particles. To find the best-fit parameters of radiation models, it uses Markov-Chain

Table 7.3: Spectral model formulas for IC 443

model	formula	parameters to vary	χ^2/df
PL	$N_0(E/E_0)^{-\Gamma}$	N_0, Γ	98/19
BPL	$N_0(E/E_b)^{-\Gamma_1} for E < E_b$ $N_0(E/E_b)^{-\Gamma_2} for E > E_b$	$N_0, \Gamma_1, \Gamma_2, E_b$	32/17
ECPL	$N_0(E/E_0)^{-\Gamma} \exp(E/E_c)$	N_0, Γ, E_c	42/18

Monte Carlo emcee sampling [272]. To make the modelling simpler, we are using only the gamma-ray spectrum extracted from the entire remnant. Furthermore, we also assume that particles are accelerating in the shell A of the remnant IC 443.

We know that the gamma-ray emission can be produced either by the electron population through the inverse Compton or bremsstrahlung or by proton population through the p-p interaction. From the morphological studies in the previous sections, we have a strong case for rejecting inverse compton and bremsstrahlung hypothesis for the origin of gamma-ray emission. This is because, the electrons which produce gamma-ray emission, should also produce radio and X-ray synchrotron emission. However, this is clearly not the case here since the radio emission is concentrated towards the rim of remnant, whereas gamma-ray emission is mainly coming from the south of shell A. The second argument against the electrons is already established by the *Fermi*-LAT team by detecting a low energy break around 200 MeV, which can only be explained using the hadronic models as due to a pion bump. Therefore, we will consider only hadronic model to explain the gamma-ray emission from IC 443.

The code *naima* [271] calculates the gamma-ray spectrum arising from the interaction of high energy protons with target protons using the parametrization of neutral pion decay [273]. A user-defined parent particle distribution function is fitted with the observed gamma-ray spectrum using Markov Chain Monte Carlo (MCMC) fitting

routines. From the fitting, the parameters of the parent particle population can be derived. Since the gamma-ray spectrum of IC 443 can be best fit with a broken power (see Section 7.6.1), we will use a distribution of parent particle as a broken power law, also. This is justified, since the gamma-ray spectral shape mimics the proton spectral shape above 1 GeV [168].

As discussed in section 7.5.2, the most prominent site for gamma-ray emission is concentrated near the shocked gas (See Figure 7.7(a)). The total mass of this shocked gas is estimated at about 1000 solar masses. If we assume that the emission is only coming from shell A containing shock accelerated cosmic rays, then the effective number density for the target material can be calculated as $M_{shocked}/V_{shell}$, at a value of 20 cm^{-3} [21]. The result of hadronic model fitting is shown in Figure 7.10 and the parameters of the model can be seen in Table 7.4. It should be noted that, for a target density of $n_H = 20$ cm^{-3}, an energy of $W_p = (2.82 \pm 0.19) \times 10^{49}$ erg above 1 GeV is required to produce the measured gamma-ray flux from IC 443. From the estimates of the total energy of the supernova explosion of IC 443, i.e. 10^{51} ergs, it is clear that about 3% of the total energy is transferred to protons at this current age. However, the large uncertainties in the density of material at the location of gamma-ray emission prevents us from drawing a firm conclusions about the conversion efficiency of total energy of SN explosion to the energy in protons.

Table 7.4: Hadronic model parameter for IC 443

Parameter name	value
Γ_1	2.37 ± 0.04
Γ_2	2.93 ± 0.07
E_{break}(GeV)	413 ± 137
$W_p(> 1$ GeV)	$(2.82 \pm 0.19) \times 10^{49}$ erg

7.8 Summary and conclusions

In this work, we have studied very high energy gamma-ray emission from the IC 443 supernova remnant using deep VERITAS observations of more than 150 hours. The four-fold increase in the exposure, compared to the previously published results [22], has provided a significant improvement in the morphological and spectral studies. With an angular resolution of better than 0.1° above a γ-ray energy of 1 TeV provided by VERITAS, the VHE gamma-ray emission from IC 443 has been resolved for the first time on the arc-minute scale. To constrain the origin of the observed gamma rays from IC 443, we have collected morphological information in other wavebands including radio, optical and X-rays. The apparent morphological mismatch between the strongest VHE gamma-ray emission region and the non-thermal radio and X-rays does not support high energy electrons as the source of the VHE gamma-ray emission. Similar conclusions, which emphasize electrons can not be the source of gamma-ray emission, were also derived in [21]. Conversely, the observations of shocked gas tracers establish that a strong spatial correlation exists between the TeV emission region and the molecular cloud-shock interaction regions. This suggests that the TeV emission results from the interaction of high energy protons with the shocked gas. Additionally, the GeV and TeV map of IC 443 produced from *Fermi*-LAT and VERITAS data respectively shows that the morphology does not depend upon the energy of gamma-ray photons. A high degree of correlation between GeV and TeV morphology suggests that the same population of particles, mainly protons, are producing both the GeV and TeV emission.

A spatially resolved spectral analysis is also performed by dividing the whole IC 443 remnant into four regions, where each region represents different environmental conditions around the remnant. The spectral fit on three regions and the entire remnant can be described using a simple power law with a soft index $\sim \Gamma = 3$. The fourth region, which displays the faintest VHE emission, shows a somewhat harder spectral index, of 2.33 ± 0.60. This is still consistent, within the large statistical errors, with the other regions, and we conclude that there is no evidence forthe spectral variation

across the remnant.This lack of spectral variation suggests that the same population of particles are producing the gamma-ray emission throughout the remnant. Secondly, it also indicates that the shock acceleration is independent of the properties of the shock and the ambient medium.

To model the gamma-ray emission, we only discuss the hadronic scenario (the leptonic scenario is already ruled out based on morphological analysis), in which we assume that protons are the parent particles that produce the observed gamma-ray flux from IC 443. The broadband emission spectra in the GeV and TeV energies, extracted from the entire remnant, is used to derive the present age proton spectra. A low-energy break in the gamma-ray spectrum, resulting from π^0-decay, is already established by [21]. This is strong evidence for the hadronic origin of the gamma-ray emission. In the present work, we have established a second break in the photon spectrum around 43 ± 14 GeV by joint fitting the Fermi-LAT (GeV) and VERITAS (TeV) spectrum. The break in the energy spectrum can be interpreted as two different populations of particles producing GeV and TeV emission. However, this scenario of different populations seems highly unlikely due to energy independent morphology found in GeV and TeV band.

Although it is difficult to find a definitive explanation for the spectral break in the high energy part of the gamma-ray spectrum of IC 443, there are a few possible explanations available in the literature. For example, using the case of SNR W44, Malkov [238] suggested a mechanism for the spectral break in the cosmic ray proton spectrum. This break happens due to a modification of shock acceleration when the shock interacts with the surrounding molecular clouds, possibly by neutral ion damping. Another possibility to explain the gamma-ray emission and the spectral break is given by simple reacceleration of the existing cosmic rays in the shocks in molecular clouds, as suggested by Uchiyama [190].

The joint fit of the GeV and TeV emission can also be explained with an exponential cut-off power law, which suggests that high energy particles may have already left the shock region. This is expected from middle-aged SNR like IC 443. Since IC

443 is in the radiative phase, with a low shock speed, it is hard for the SNR shock to contain the highest energy particles. The existence of a cut-off in the energy spectrum also provides an evidence that IC 443 can not be considered as a Pevatron at the present time.

At present, given the large uncertainties in the environmental parameters and limitation in the modelling of the data, the interpretation of the gamma-ray emission from IC 443 remnant is still an open issue. In future, more detailed modelling of gamma-ray emission from the different parts of the remnant may provide further insight into the relation between the shock acceleration and the environment in which the shock is moving. Furthermore, measurements with Cherenkov Telescope Array (CTA), having a better sensitivity and angular resolution, may reveal more detailed morphological features that will allow us to better constrain the particle acceleration mechanism in IC 443.

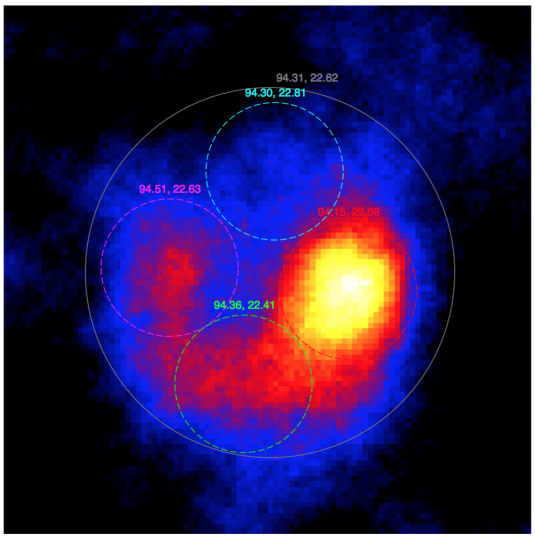

(a)

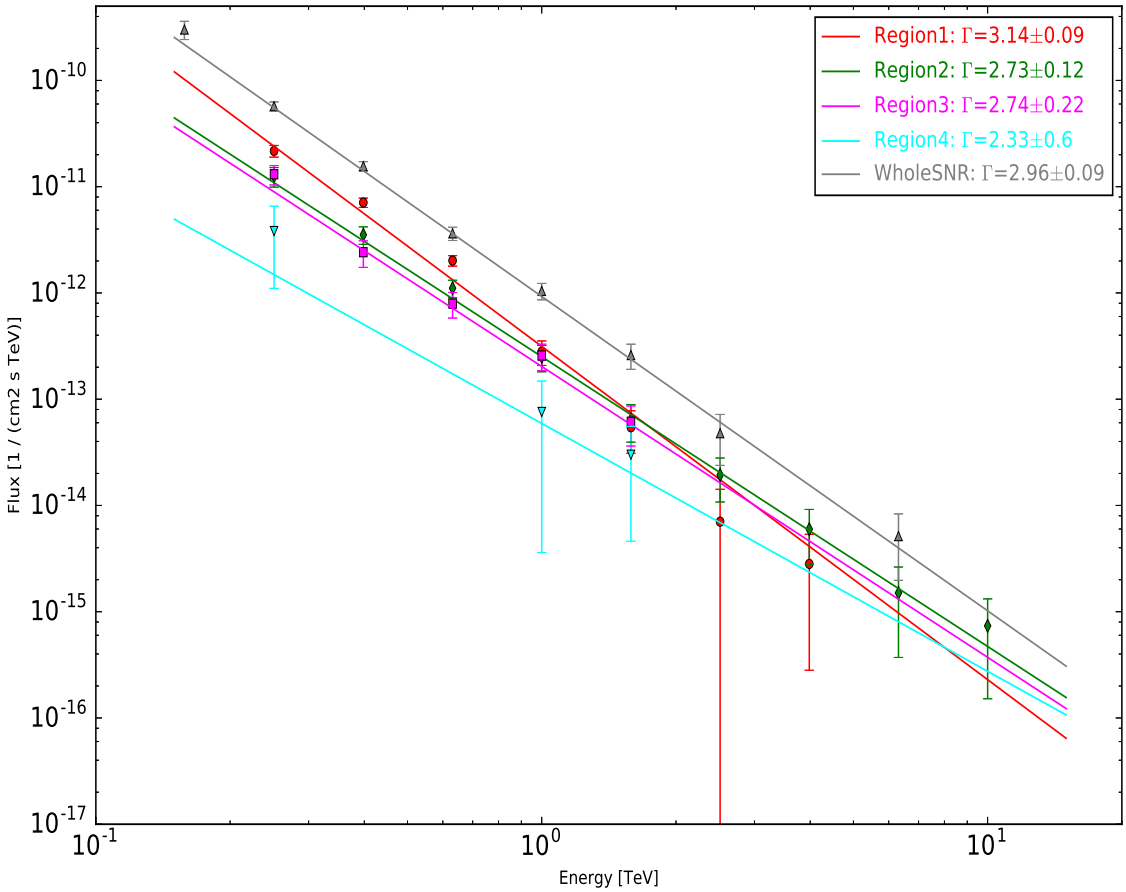

(b)

Figure 7.8: (a) This shows four regions from which VERITAS spectrum is extracted. In addition to four smaller regions, spectrum is extracted from the whole SNR shown by grey circle. (b) Power-law spectral fit on all five regions along with their spectral index.

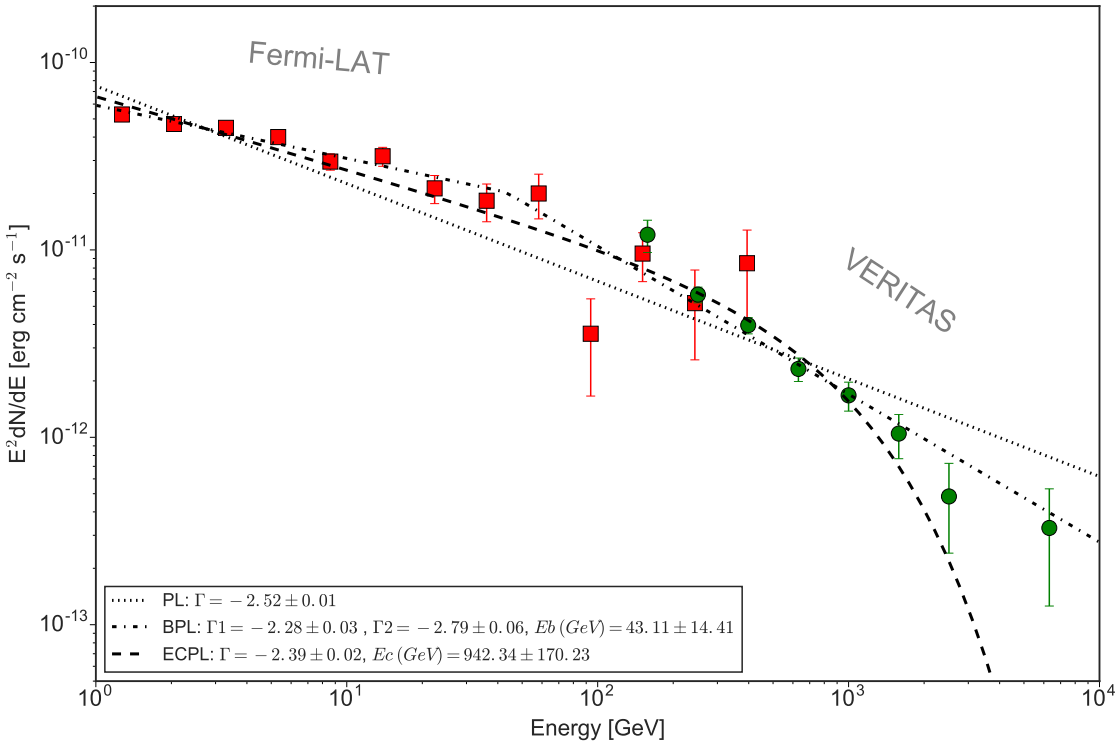

Figure 7.9: Broadband spectral fit using gamma-ray emission from whole SNR. Three power-law function are fitted on the data. From the fitting statistics broen power law is preferred over pure power law fit.

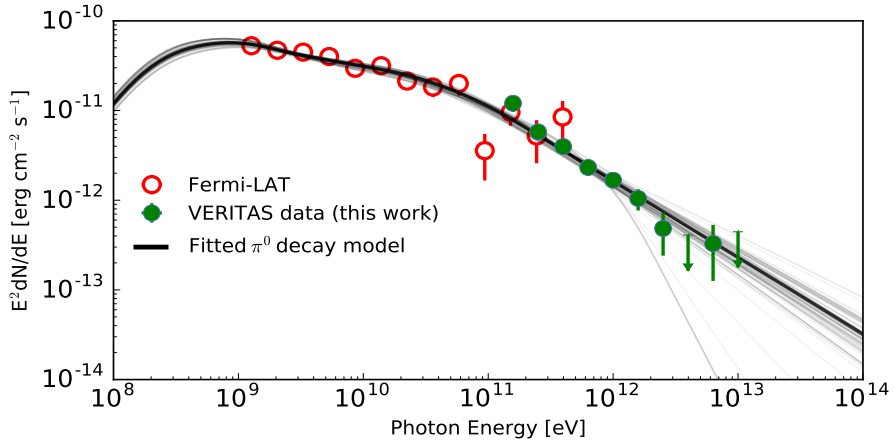

(a)

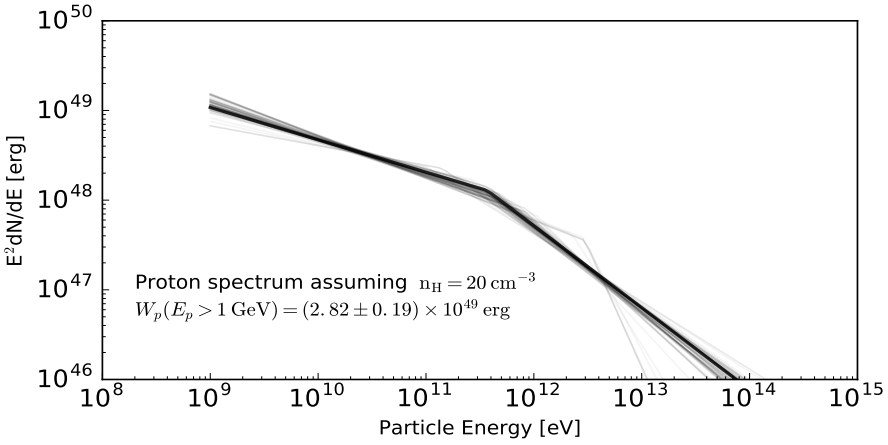

(b)

Figure 7.10: (a) Broadband spectral fitting on Fermi-LAT and VERITAS data using Pion decay model. (b) Distribution of proton population responsible for producing the gamma-ray spectrum of IC 443.

BIBLIOGRAPHY

[1] T. Weekes, editor. *Very High Energy Gamma-Ray Astronomy*, volume 11 of *Wiley Praxis Series in Astronomy and Astrophysics*, April 2003.

[2] S. P. Wakely and D. Horan. TeVCat: An online catalog for Very High Energy Gamma-Ray Astronomy. *International Cosmic Ray Conference*, 3:1341–1344, 2008.

[3] W. Heitler. *Quantum theory of radiation*. 1954.

[4] F. Aharonian, J. Buckley, T. Kifune, and G. Sinnis. High energy astrophysics with ground-based gamma ray detectors. *Reports on Progress in Physics*, 71(9):096901, September 2008.

[5] Andrew McCann. *Discovery of Emission above 100 GeV from the Crab Pulsar With VERITAS*. PhD thesis, McGill University, 2011.

[6] Ester Aliu Fuste. *VHE -ray observations of Northern sky pulsar wind nebulae with the MAGIC Telescope*. PhD thesis, Universitat Aut'onoma de Barcelona, 2007.

[7] J. Holder. Atmospheric Cherenkov Gamma-ray Telescopes. *ArXiv e-prints*, October 2015.

[8] D. Heck, J. Knapp, J. N. Capdevielle, G. Schatz, and T. Thouw. *CORSIKA: a Monte Carlo code to simulate extensive air showers.* February 1998.

[9] M. Spurio. *Particles and Astrophysics*. 2015.

[10] F. Krennrich et al. Veritas: the very energetic radiation imaging telescope array system. *New Astronomy Reviews*, 48(56):345 – 349, 2004. 2nd {VERITAS} Symposium on the Astrophysics of Extragalactic Sources.

[11] E. Roache, R. Irvin, J. S. Perkins, K. Harris, A. Falcone, J. Finley, and T. Weeks. Mirror Facets for the VERITAS Telescopes. *International Cosmic Ray Conference*, 3:1397–1400, 2008.

[12] A. McCann, D. Hanna, J. Kildea, and M. McCutcheon. A new mirror alignment system for the VERITAS telescopes. *Astroparticle Physics*, 32:325–329, January 2010.

[13] A. Nepomuk Otte and for the VERITAS Collaboration. The Upgrade of VERITAS with High Efficiency Photomultipliers. *ArXiv e-prints*, October 2011.

[14] Heike Prokoph. *Observations and modeling of the active galactic nucleus B2 1215+30 together with performance studies of the ground-based gamma-ray observatories VERITAS and CTA*. PhD thesis, Humboldt-Universitt zu Berlin, 2013.

[15] Gayle Ratliff. *The VERY ENERGETIC RADIATION IMAGING TELESCOPE ARRAY SYSTEM OBSERVATIONS OF THE STARBURST GALAXY M82*. PhD thesis, Illinois Institute of Technology, 2015.

[16] Heike Prokoph. Investigations on gamma-hadron separation for imaging cherenkov telescopes exploiting the time develpoment of particle cascades. Master's thesis, Universität Leipzig, 2009.

[17] J. Vink. Supernova remnants: the X-ray perspective. *Astronomy and Astrophysics Reviews*, 20:49, December 2012.

[18] S. P. Reynolds. Supernova Remnants at High Energy. *Annual Review of Astronomy and Astrophysics*, 46:89–126, September 2008.

[19] T. K. Gaisser. *Cosmic rays and particle physics*. 1990.

[20] H. E. S. S. Collaboration, :, H. Abdalla, et al. H.E.S.S. observations of RX J1713.7-3946 with improved angular and spectral resolution; evidence for gamma-ray emission extending beyond the X-ray emitting shell. *ArXiv e-prints*, September 2016.

[21] M. Ackermann et al. Detection of the Characteristic Pion-Decay Signature in Supernova Remnants. *Science*, 339:807–811, February 2013.

[22] V. A. Acciari et al. Observation of Extended Very High Energy Emission from the Supernova Remnant IC 443 with VERITAS. *The Astrophysical Journal, Letters*, 698:L133–L137, June 2009.

[23] J. Albert et al. Discovery of Very High Energy Gamma Radiation from IC 443 with the MAGIC Telescope. *The Astrophysical Journal, Letters*, 664:L87–L90, August 2007.

[24] J. Rho, S. P. Reynolds, W. T. Reach, T. H. Jarrett, G. E. Allen, and J. C. Wilson. Near-Infrared Synchrotron Emission from Cassiopeia A. *The Astrophysical Journal*, 592:299–310, July 2003.

[25] M. Anderson, L. Rudnick, P. Leppik, R. Perley, and R. Braun. Relativistic electron populations in Cassiopeia A. *The Astrophysical Journal*, 373:146–157, May 1991.

[26] E. V. Gotthelf, B. Koralesky, L. Rudnick, T. W. Jones, U. Hwang, and R. Petre. Chandra Detection of the Forward and Reverse Shocks in Cassiopeia A. *The Astrophysical Journal, Letters*, 552:L39–L43, May 2001.

[27] B. W. Grefenstette et al. *ApJ*, 802:15, March 2015.

[28] V. A. Acciari et al. Observations of the Shell-type Supernova Remnant Cassiopeia A at TeV Energies with VERITAS. *The Astrophysical Journal*, 714:163–169, May 2010.

[29] Y. Yuan, S. Funk, G. Jóhannesson, J. Lande, L. Tibaldo, and Y. Uchiyama. Fermi Large Area Telescope Detection of a Break in the Gamma-Ray Spectrum of the Supernova Remnant Cassiopeia A. *The Astrophysical Journal*, 779:117, December 2013.

[30] E. N. Vinyaikin. Frequency dependence of the evolution of the radio emission of the supernova remnant Cas A. *Astronomy Reports*, 58:626–639, September 2014.

[31] Y. Maeda et al. Suzaku X-Ray Imaging and Spectroscopy of Cassiopeia A. *Publ. Astron. Soc. Jap.*, 61:1217, 2009.

[32] W. Wang and Z. Li. Hard X-Ray Emissions from Cassiopeia A Observed by INTEGRAL. *The Astrophysical Journal*, 825:102, July 2016.

[33] R. Braun and R. G. Strom. The structure and dynamics of evolved supernova remnants - The IC 443 complex. *Astronomy and Astrophysics*, 164:193–207, August 1986.

[34] C. M. Olbert, C. R. Clearfield, N. E. Williams, J. W. Keohane, and D. A. Frail. A Bow Shock Nebula around a Compact X-Ray Source in the Supernova Remnant IC 443. *The Astrophysical Journal, Letters*, 554:L205–L208, June 2001.

[35] G. Castelletti, G. Dubner, T. Clarke, and N. E. Kassim. High-resolution radio study of SNR IC 443 at low radio frequencies. *Astronomy and Astrophysics*, 534:A21, October 2011.

[36] J. Rho, T. H. Jarrett, R. M. Cutri, and W. T. Reach. Near-Infrared Imaging and [O I] Spectroscopy of IC 443 using Two Micron All Sky Survey and Infrared Space Observatory. *The Astrophysical Journal*, 547:885–898, February 2001.

[37] J.-J. Lee, B.-C. Koo, M. S. Yun, S. Stanimirović, C. Heiles, and M. Heyer. A 21 cm Spectral and Continuum Study of IC 443 Using the Very Large Array and the Arecibo Telescope. *The Astronomical Journal*, 135:796–808, March 2008.

[38] L. K. Denoyer. Discovery of shocked CO within a supernova remnant. *The Astrophysical Journal, Letters*, 232:L165–L168, September 1979.

[39] R. L. Dickman, R. L. Snell, L. M. Ziurys, and Y.-L. Huang. Structure and kinematics of dense gas associated with the supernova remnant IC 443. *The Astrophysical Journal*, 400:203–213, November 1992.

[40] A. A. Abdo et al. Observation of supernova remnant ic443 with the fermi large area telescope. *The Astrophysical Journal*, 712(1):459, 2010.

[41] Y.-L. Huang, R. L. Dickman, and R. L. Snell. IRAS sources associated with shocked gas regions in IC 443. *The Astrophysical Journal, Letters*, 302:L63–L66, March 1986.

[42] E. Troja, F. Bocchino, and F. Reale. XMM-Newton Observations of the Supernova Remnant IC 443. I. Soft X-Ray Emission from Shocked Interstellar Medium. *The Astrophysical Journal*, 649:258–267, September 2006.

[43] J. W. Hewitt, F. Yusef-Zadeh, M. Wardle, D. A. Roberts, and N. E. Kassim. Green Bank Telescope Observations of IC 443: The Nature of OH (1720 MHz) Masers and OH Absorption. *The Astrophysical Journal*, 652:1288–1296, December 2006.

[44] Allan Chapman. A new perceived reality: Thomas harriot's moon maps. *Astronomy & Geophysics*, 50(1):1.27–1.33, 2009.

[45] Victor F. Hess. ber Beobachtungen der durchdringenden Strahlung bei sieben Freiballonfahrten. *Phys. Z.*, 13:1084–1091, 1912.

[46] Kenneth Greisen. End to the cosmic-ray spectrum? *Phys. Rev. Lett.*, 16:748–750, Apr 1966.

[47] W. Kraushaar, G. W. Clark, G. Garmire, H. Helmken, P. Higbie, and M. Agogino. Explorer XI Experiment on Cosmic Gamma Rays. *The Astrophysical Journal*, 141:845, April 1965.

[48] W. L. Kraushaar, G. W. Clark, G. P. Garmire, R. Borken, P. Higbie, V. Leong, and T. Thorsos. High-Energy Cosmic Gamma-Ray Observations from the OSO-3 Satellite. *The Astrophysical Journal*, 177:341, November 1972.

[49] R. Browning, D. Ramsden, and P. J. Wright. Detection of Pulsed Gamma Radiation from the Crab Nebula. *Nature Physical Science*, 232:99–101, August 1971.

[50] C. E. Fichtel, R. C. Hartman, D. A. Kniffen, D. J. Thompson, H. Ogelman, M. E. Ozel, T. Tumer, and G. F. Bignami. High-energy gamma-ray results from the second small astronomy satellite. *The Astrophysical Journal*, 198:163–182, May 1975.

[51] D. J. Thompson, C. E. Fichtel, D. A. Kniffen, and H. B. Ogelman. SAS-2 high-energy gamma-ray observations of the VELA pulsar. *The Astrophysical Journal, Letters*, 200:L79–L82, September 1975.

[52] B. N. Swanenburg, K. Bennett, G. F. Bignami, R. Buccheri, P. Caraveo, W. Hermsen, G. Kanbach, G. G. Lichti, J. L. Masnou, H. A. Mayer-Hasselwander, J. A. Paul, B. Sacco, L. Scarsi, and R. D. Wills. Second COS B catalog of high-energy gamma-ray sources. *The Astrophysical Journal, Letters*, 243:L69–L73, January 1981.

[53] G. Kanbach, D. L. Bertsch, C. E. Fichtel, R. C. Hartman, S. D. Hunter, D. A. Kniffen, B. W. Hughlock, A. Favale, R. Hofstadter, and E. B. Hughes. The project EGRET (Energetic Gamma-Ray Experiment Telescope) on NASA's Gamma-Ray Observatory (GRO). *Space Science Reviews*, 49:69–84, 1988.

[54] E. B. Hughes, R. Hofstadter, J. Rolfe, A. Johansson, D. L. Bertsch, W. J. Cruickshank, C. H. Ehrmann, C. E. Fichtel, R. C. Hartman, and D. A. Kniffen. Characteristics of the telescope for high energy gamma-ray astronomy selected for definition studies on the Gamma Ray Observatory. *IEEE Transactions on Nuclear Science*, 27:364–369, February 1980.

[55] R. C. Hartman, D. L. Bertsch, C. E. Fichtel, S. D. Hunter, G. Kanbach, D. A. Kniffen, P. W. Kwok, Y. C. Lin, J. R. Mattox, H. A. Mayer-Hasselwander, P. F. Michelson, C. von Montigny, H. I. Nel, P. L. Nolan, K. Pinkau, H. Rothermel, E. Schneid, M. Sommer, P. Sreekumar, and D. J. Thompson. Detection of high-energy gamma radiation from quasar 3C 279 by the EGRET telescope on the Compton Gamma Ray Observatory. *The Astrophysical Journal, Letters*, 385:L1–L4, January 1992.

[56] D. J. Thompson. Space detectors for gamma rays (100 MeV-100 GeV): From EGRET to Fermi LAT. *Comptes Rendus Physique*, 16:600–609, August 2015.

[57] R. C. Hartman, D. L. Bertsch, S. D. Bloom, A. W. Chen, P. Deines-Jones, J. A. Esposito, C. E. Fichtel, D. P. Friedlander, S. D. Hunter, L. M. McDonald, P. Sreekumar, D. J. Thompson, B. B. Jones, Y. C. Lin, P. F. Michelson, P. L. Nolan, W. F. Tompkins, G. Kanbach, H. A. Mayer-Hasselwander, A. Mücke, M. Pohl, O. Reimer, D. A. Kniffen, E. J. Schneid, C. von Montigny, R. Mukherjee, and B. L. Dingus. The Third EGRET Catalog of High-Energy Gamma-Ray Sources. *The Astrophysical Journal, Supplement*, 123:79–202, July 1999.

[58] J.-M. Casandjian and I. A. Grenier. A revised catalogue of EGRET γ-ray sources. *Astronomy and Astrophysics*, 489:849–883, October 2008.

[59] W. B. Atwood, A. A. Abdo, M. Ackermann, W. Althouse, B. Anderson, M. Axelsson, L. Baldini, J. Ballet, D. L. Band, G. Barbiellini, and et al. The Large Area

Telescope on the Fermi Gamma-Ray Space Telescope Mission. *The Astrophysical Journal*, 697:1071–1102, June 2009.

[60] F. Acero et al. Fermi Large Area Telescope Third Source Catalog. *The Astrophysical Journal, Supplement*, 218:23, June 2015.

[61] M. Tavani et al. The AGILE Mission. *Astronomy and Astrophysics*, 502:995–1013, August 2009.

[62] T. Hassan, L. Arrabito, K. Bernlöhr, J. Bregeon, J. Cortina, P. Cumani, F. Di Pierro, D. Falceta-Goncalves, R. G. Lang, J. Hinton, T. Jogler, G. Maier, A. Moralejo, A. Morselli, C. J. Todero Peixoto, and M. Wood. Monte Carlo performance studies for the site selection of the Cherenkov Telescope Array. *Astroparticle Physics*, 93:76–85, July 2017.

[63] F. Aharonian et al. Observations of the Crab nebula with HESS. *Astronomy and Astrophysics*, 457:899–915, October 2006.

[64] S. R. Kelner and F. A. Aharonian. Energy spectra of gamma rays, electrons, and neutrinos produced at interactions of relativistic protons with low energy radiation. *Physical Review D*, 78(3):034013, August 2008.

[65] J. A. Hinton and W. Hofmann. Teraelectronvolt Astronomy. *Annual Review of Astronomy and Astrophysics*, 47:523–565, September 2009.

[66] T. C. Weekes, M. F. Cawley, D. J. Fegan, K. G. Gibbs, A. M. Hillas, P. W. Kowk, R. C. Lamb, D. A. Lewis, D. Macomb, N. A. Porter, P. T. Reynolds, and G. Vacanti. Observation of TeV gamma rays from the Crab nebula using the atmospheric Cerenkov imaging technique. *The Astrophysical Journal*, 342:379–395, July 1989.

[67] D. Ferenc and MAGIC Collaboration. The MAGIC gamma-ray observatory. *Nuclear Instruments and Methods in Physics Research A*, 553:274–281, November 2005.

[68] D. B. Tridon, T. Schweizer, F. Goebel, R. Mirzoyan, M. Teshima, and MAGIC Collaboration. The MAGIC-II gamma-ray stereoscopic telescope system. *Nuclear Instruments and Methods in Physics Research A*, 623:437–439, November 2010.

[69] T. C. Weekes, H. Badran, S. D. Biller, I. Bond, S. Bradbury, J. Buckley, D. Carter-Lewis, M. Catanese, S. Criswell, W. Cui, P. Dowkontt, C. Duke, D. J. Fegan, J. Finley, L. Fortson, J. Gaidos, G. H. Gillanders, J. Grindlay, T. A. Hall, K. Harris, A. M. Hillas, P. Kaaret, M. Kertzman, D. Kieda, F. Krennrich, M. J. Lang, S. LeBohec, R. Lessard, J. Lloyd-Evans, J. Knapp, B. McKernan, J. McEnery, P. Moriarty, D. Muller, P. Ogden, R. Ong, D. Petry, J. Quinn, N. W. Reay, P. T. Reynolds, J. Rose, M. Salamon, G. Sembroski, R. Sidwell, P. Slane,

N. Stanton, S. P. Swordy, V. V. Vassiliev, and S. P. Wakely. VERITAS: the Very Energetic Radiation Imaging Telescope Array System. *Astroparticle Physics*, 17:221–243, May 2002.

[70] T. C. Weekes and the VERITAS Collaboration. Veritas: Status c. 2009. *ArXiv e-prints*, January 2010.

[71] K. Bernlöhr, O. Carrol, R. Cornils, S. Elfahem, P. Espigat, S. Gillessen, G. Heinzelmann, G. Hermann, W. Hofmann, D. Horns, I. Jung, R. Kankanyan, A. Katona, B. Khelifi, H. Krawczynski, M. Panter, M. Punch, S. Rayner, G. Rowell, M. Tluczykont, and R. van Staa. The optical system of the H.E.S.S. imaging atmospheric Cherenkov telescopes. Part I: layout and components of the system. *Astroparticle Physics*, 20:111–128, November 2003.

[72] R. Cornils, S. Gillessen, I. Jung, W. Hofmann, M. Beilicke, K. Bernlöhr, O. Carrol, S. Elfahem, G. Heinzelmann, G. Hermann, D. Horns, R. Kankanyan, A. Katona, H. Krawczynski, M. Panter, S. Rayner, G. Rowell, M. Tluczykont, and R. van Staa. The optical system of the H.E.S.S. imaging atmospheric Cherenkov telescopes. Part II: mirror alignment and point spread function. *Astroparticle Physics*, 20:129–143, November 2003.

[73] M. Holler, D. Berge, C. van Eldik, J.-P. Lenain, V. Marandon, T. Murach, M. de Naurois, R. D. Parsons, H. Prokoph, D. Zaborov, and for the H. E. S. S. collaboration. Observations of the Crab Nebula with H.E.S.S. Phase II. *ArXiv e-prints*, September 2015.

[74] J. Aleksić et al. The major upgrade of the MAGIC telescopes, Part II: A performance study using observations of the Crab Nebula. *Astroparticle Physics*, 72:76–94, January 2016.

[75] N. Park et al. Performance of the VERITAS experiment. In *34th International Cosmic Ray Conference (ICRC2015)*, volume 34 of *International Cosmic Ray Conference*, page 771, July 2015.

[76] Gus Sinnis for the Milagro Collaboration. Cosmic-ray physics with the milagro gamma-ray observatory. *Journal of the Physical Society of Japan*, 78(Suppl.A):84–87, 2009.

[77] J. Pretz. Highlights from the High Altitude Water Cherenkov Observatory. In *34th International Cosmic Ray Conference (ICRC2015)*, volume 34 of *International Cosmic Ray Conference*, page 25, July 2015.

[78] B. Bartoli et al. Crab Nebula: Five-year Observation with ARGO-YBJ. *The Astrophysical Journal*, 798:119, January 2015.

[79] M. Amenomori, Z. Cao, L. K. Ding, Z. Y. Feng, K. Hibino, N. Hotta, Q. Huang, A. X. Huo, H. Y. Jia, and G. Z. Jiang. Search for steady emission of 10-TeV gamma rays from the Crab Nebula, Cygnus X-3, and Hercules X-1 using the Tibet Air Shower Array. *Physical Review Letters*, 69:2468–2471, October 1992.

[80] A. U. Abeysekara et al. Observation of the Crab Nebula with the HAWC Gamma-Ray Observatory. *The Astrophysical Journal*, 843:39, July 2017.

[81] F. Aharonian et al. Discovery of the binary pulsar PSR B1259-63 in very-high-energy gamma rays around periastron with HESS. *Astronomy and Astrophysics*, 442:1–10, October 2005.

[82] F. Aharonian et al. Discovery of Very High Energy Gamma Rays Associated with an X-ray Binary. *Science*, 309:746–749, July 2005.

[83] J. Albert et al. Variable Very-High-Energy Gamma-Ray Emission from the Microquasar LS I +61 303. *Science*, 312:1771–1773, June 2006.

[84] V. A. Acciari et al. VERITAS Observations of the γ-Ray Binary LS I +61 303. *The Astrophysical Journal*, 679:1427–1432, June 2008.

[85] J. Aleksić et al. Detection of VHE γ-Rays from HESS J0632+057 during the 2011 February X-Ray Outburst with the MAGIC Telescopes. *The Astrophysical Journal, Letters*, 754:L10, July 2012.

[86] R. Bird and for the VERITAS Collaboration. PSR J2032+4127, the counterpart of TeV J2032+4130? Multiwavelength Monitoring of the Approach to Periastron. *ArXiv e-prints*, August 2017.

[87] Wodek Bednarek, Piotr Banasiski, and Julian Sitarek. Gamma-rays from the binary system containing psr j2032+4127 during its periastron passage. *Journal of Physics G: Nuclear and Particle Physics*, 45(1):015201, 2018.

[88] H. Krawczynski and E. Treister. Active galactic nuclei-the physics of individual sources and the cosmic history of formation and evolution. *Frontiers of Physics*, 8:609–629, December 2013.

[89] Grzegorz (Greg) Madejski and Marek Sikora. Gamma-ray observations of active galactic nuclei. *Annual Review of Astronomy and Astrophysics*, 54(1):725–760, 2016.

[90] C. M. Urry and P. Padovani. Unified Schemes for Radio-Loud Active Galactic Nuclei. *Publications of the Astronomical Society of the Pacific*, 107:803, September 1995.

[91] VERITAS Collaboration, V. A. Acciari, et al. A connection between star formation activity and cosmic rays in the starburst galaxy M82. *Nature*, 462:770–772, December 2009.

[92] F. Acero et al. Detection of Gamma Rays from a Starburst Galaxy. *Science*, 326:1080, November 2009.

[93] A. U. Abeysekara et al. Sensitivity of the high altitude water Cherenkov detector to sources of multi-TeV gamma rays. *Astroparticle Physics*, 50:26–32, December 2013.

[94] W. Galbraith and J. V. Jelley. Light Pulses from the Night Sky associated with Cosmic Rays. *Nature*, 171:349–350, February 1953.

[95] P. M. S. Blackett. A possible contribution to the night sky from the Cerenkov radiation emitted by cosmic rays. In *The Emission Spectra of the Night Sky and Aurorae*, page 34, 1948.

[96] J. Matthews. A heitler model of extensive air showers. *Astroparticle Physics*, 22(5):387 – 397, 2005.

[97] A M Hillas. Angular and energy distributions of charged particles in electron-photon cascades in air. *Journal of Physics G: Nuclear Physics*, 8(10):1461, 1982.

[98] W.-M. Yao et al. Review of Particle Physics. *Journal of Physics G Nuclear Physics*, 33:1–1232, July 2006.

[99] P. K. F. Grieder. *Extensive Air Showers: High Energy Phenomena and Astrophysical Aspects - A Tutorial, Reference Manual and Data Book*. 2010.

[100] Oliver Heaviside. Xxxix. on the electromagnetic effects due to the motion of electrification through a dielectric. *The London, Edinburgh, and Dublin Philosophical Magazine and Journal of Science*, 27(167):324–339, 1889.

[101] P. A. Cherenkov. Visible emission of clean liquids by action of gamma radiation. *Doklady Akademii Nauk SSSR*, 2:451+, 1934.

[102] I.E. Tamm and I.E. Frank. Coherent radiation of fast electrons in a medium. *Doklady Akademii Nauk SSSR*, pages 14,107, 1937.

[103] A. M. Hillas. Cerenkov light images of EAS produced by primary gamma. *International Cosmic Ray Conference*, 3, August 1985.

[104] HEGRA Collaboration, A. Konopelko, et al. Performance of the stereoscopic system of the HEGRA imaging air Čerenkov telescopes: Monte Carlo simulations and observations. *Astroparticle Physics*, 10:275–289, May 1999.

[105] John M. Davies and Eugene S. Cotton. Design of the quartermaster solar furnace. *Solar Energy*, 1(2):16 – 22, 1957.

[106] J. Holder et al. The first VERITAS telescope. *Astroparticle Physics*, 25:391–401, July 2006.

[107] VERITAS website. https://veritas.sao.arizona.edu/.

[108] H.E.S.S. website. https://www.mpi-hd.mpg.de/hfm/hess/.

[109] MAGIC website. https://magic.mpp.mpg.de/.

[110] J. Hall, V. V. Vassiliev, D. B. Kieda, J. Moses, T. Nagai, and J. Smith. Veritas CFDs. *International Cosmic Ray Conference*, 5:2851, July 2003.

[111] B. Zitzer and for the VERITAS Collaboration. The VERITAS Upgraded Telescope-Level Trigger Systems: Technical Details and Performance Characterization. *ArXiv e-prints*, July 2013.

[112] G. Maier and J. Holder. Eventdisplay: An Analysis and Reconstruction Package for Ground-based Gamma-ray Astronomy. *ArXiv e-prints*, August 2017.

[113] P. Cogan. VEGAS, the VERITAS Gamma-ray Analysis Suite. *International Cosmic Ray Conference*, 3:1385–1388, 2008.

[114] D. Hanna, A. McCann, M. McCutcheon, and L. Nikkinen. An LED-based flasher system for VERITAS. *Nuclear Instruments and Methods in Physics Research A*, 612:278–287, January 2010.

[115] J. Holder. Exploiting VERITAS Timing Information. *International Cosmic Ray Conference*, 5:383, 2005.

[116] A. Kohnle et al. Stereoscopic imaging of air showers with the first two HEGRA Cherenkov telescopes. *Astroparticle Physics*, 5:119–131, August 1996.

[117] M. K. Daniel. The VERITAS standard data analysis. *International Cosmic Ray Conference*, 3:1325–1328, 2008.

[118] G. Maier. Monte Carlo studies of the VERITAS array of Cherenkov telescopes. *International Cosmic Ray Conference*, 3:1413–1416, 2008.

[119] D. Berge, S. Funk, and J. Hinton. Background modelling in very-high-energy γ-ray astronomy. *Astronomy and Astrophysics*, 466:1219–1229, May 2007.

[120] T.-P. Li and Y.-Q. Ma. Analysis methods for results in gamma-ray astronomy. *The Astrophysical Journal*, 272:317–324, September 1983.

[121] A. Weinstein. The VERITAS Trigger System. *International Cosmic Ray Conference*, 3:1539–1542, 2008.

[122] P. Sommers and J. W. Elbert. Ultra-high-energy gamma-ray astronomy using atmospheric Cerenkov detectors at large zenith angles. *Journal of Physics G Nuclear Physics*, 13:553–566, April 1987.

[123] A. Konopelko, F. Aharonian, M. Hemberger, W. Hofmann, J. Kettler, G. Pühlhofer, and H. J. Völk. Effectiveness of TeV γ-ray observations at large zenith angles with a stereoscopic system of imaging atmospheric Cerenkov telescopes. *Journal of Physics G Nuclear Physics*, 25:1989–2000, September 1999.

[124] A. G. Riess et al. New Hubble Space Telescope Discoveries of Type Ia Supernovae at z $\geq$ 1: Narrowing Constraints on the Early Behavior of Dark Energy. *The Astrophysical Journal*, 659:98–121, April 2007.

[125] J. S. Warren, J. P. Hughes, C. Badenes, P. Ghavamian, C. F. McKee, D. Moffett, P. P. Plucinsky, C. Rakowski, E. Reynoso, and P. Slane. Cosmic-Ray Acceleration at the Forward Shock in Tycho's Supernova Remnant: Evidence from Chandra X-Ray Observations. *The Astrophysical Journal*, 634:376–389, November 2005.

[126] W. Li, R. Chornock, J. Leaman, A. V. Filippenko, D. Poznanski, X. Wang, M. Ganeshalingam, and F. Mannucci. Nearby supernova rates from the Lick Observatory Supernova Search - III. The rate-size relation, and the rates as a function of galaxy Hubble type and colour. *Monthly Notices of the Royal Astronomical Society*, 412:1473–1507, April 2011.

[127] B. J. Williams, W. P. Blair, J. M. Blondin, K. J. Borkowski, P. Ghavamian, K. S. Long, J. C. Raymond, S. P. Reynolds, J. Rho, and P. F. Winkler. RCW 86: A Type Ia Supernova in a Wind-blown Bubble. *The Astrophysical Journal*, 741:96, November 2011.

[128] L. A. L. Da Silva. The classification of supernovae. *Astrophysics and Space Science*, 202(2):215–236, 1993.

[129] O. Krause, M. Tanaka, T. Usuda, T. Hattori, M. Goto, S. Birkmann, and K. Nomoto. Tycho Brahe's 1572 supernova as a standard typeIa as revealed by its light-echo spectrum. *Nature*, 456:617–619, December 2008.

[130] K. Hirata, T. Kajita, M. Koshiba, M. Nakahata, and Y. Oyama. Observation of a neutrino burst from the supernova SN1987A. *Physical Review Letters*, 58:1490–1493, April 1987.

[131] R. M. Bionta, G. Blewitt, C. B. Bratton, D. Casper, and A. Ciocio. Observation of a neutrino burst in coincidence with supernova 1987A in the Large Magellanic Cloud. *Physical Review Letters*, 58:1494–1496, April 1987.

[132] O. Krause, S. M. Birkmann, T. Usuda, T. Hattori, M. Goto, G. H. Rieke, and K. A. Misselt. The Cassiopeia A Supernova Was of Type IIb. *Science*, 320:1195–, May 2008.

[133] R. A. Chevalier. Self-similar solutions for the interaction of stellar ejecta with an external medium. *The Astrophysical Journal*, 258:790–797, July 1982.

[134] J. M. Marcaide et al. A decade of SN 1993J: discovery of radio wavelength effects in the expansion rate. *Astronomy and Astrophysics*, 505:927–945, October 2009.

[135] L. I. Sedov. *Similarity and Dimensional Methods in Mechanics*. 1959.

[136] G. Taylor. The Formation of a Blast Wave by a Very Intense Explosion. I. Theoretical Discussion. *Proceedings of the Royal Society of London Series A*, 201:159–174, March 1950.

[137] F. H. Shu. *The physics of astrophysics. Volume II: Gas dynamics.* 1992.

[138] J. Vink, H. Bloemen, J. S. Kaastra, and J. A. M. Bleeker. The expansion of Cassiopeia A as seen in X-rays. *Astronomy and Astrophysics*, 339:201–207, November 1998.

[139] L. Woltjer. Supernova Remnants. *Annual Review of Astronomy and Astrophysics*, 10:129, 1972.

[140] V. L. Ginzburg and S. I. Syrovatskii. *The origin of cosmic rays*. 1969.

[141] W. R. Webber. A New Estimate of the Local Interstellar Energy Density and Ionization Rate of Galactic Cosmic Cosmic Rays. *The Astrophysical Journal*, 506:329–334, October 1998.

[142] E. G. Berezhko and H. J. Völk. Kinetic theory of cosmic rays and gamma rays in supernova remnants. I. Uniform interstellar medium. *Astroparticle Physics*, 7:183–202, August 1997.

[143] E. Fermi. On the Origin of the Cosmic Radiation. *Physical Review*, 75:1169–1174, April 1949.

[144] G. F. Krymskii. A regular mechanism for the acceleration of charged particles on the front of a shock wave. *Akademiia Nauk SSSR Doklady*, 234:1306–1308, June 1977.

[145] W. I. Axford, E. Leer, and G. Skadron. The acceleration of cosmic rays by shock waves. *International Cosmic Ray Conference*, 11:132–137, 1977.

[146] A. R. Bell. The acceleration of cosmic rays in shock fronts. I. *Monthly Notices of the Royal Astronomical Society*, 182:147–156, January 1978.

[147] A. R. Bell. The acceleration of cosmic rays in shock fronts. II. *Monthly Notices of the Royal Astronomical Society*, 182:443–455, February 1978.

[148] R. D. Blandford and J. P. Ostriker. Particle acceleration by astrophysical shocks. *The Astrophysical Journal, Letters*, 221:L29–L32, April 1978.

[149] M. S. Longair. *High Energy Astrophysics*. February 2011.

[150] P. O. Lagage and C. J. Cesarsky. The maximum energy of cosmic rays accelerated by supernova shocks. *Astronomy and Astrophysics*, 125:249–257, September 1983.

[151] V. L. Ginzburg and S. I. Syrovatsky. Origin of Cosmic Rays. *Progress of Theoretical Physics Supplement*, 20:1–83, 1961.

[152] L. O. Drury and J. H. Voelk. Hydromagnetic shock structure in the presence of cosmic rays. *The Astrophysical Journal*, 248:344–351, August 1981.

[153] D. C. Ellison and D. Eichler. Monte Carlo shock-like solutions to the Boltzmann equation with collective scattering. *The Astrophysical Journal*, 286:691–701, November 1984.

[154] M. A. Malkov and L. O. Drury. Nonlinear theory of diffusive acceleration of particles by shock waves. *Reports on Progress in Physics*, 64:429–481, April 2001.

[155] P. Blasi. The origin of galactic cosmic rays. *Astronomy and Astrophysics Reviews*, 21:70, November 2013.

[156] E. Amato. The origin of galactic cosmic rays. *International Journal of Modern Physics D*, 23:1430013, May 2014.

[157] D. Caprioli. Hybrid Simulations of Particle Acceleration at Shocks. *Nuclear Physics B Proceedings Supplements*, 256:48–55, November 2014.

[158] J. Skilling. Cosmic ray streaming. II - Effect of particles on Alfven waves. *Monthly Notices of the Royal Astronomical Society*, 173:245–254, November 1975.

[159] J. Ballet. X-ray synchrotron emission from supernova remnants. *Advances in Space Research*, 37:1902–1908, 2006.

[160] J. Vink and J. M. Laming. On the Magnetic Fields and Particle Acceleration in Cassiopeia A. *The Astrophysical Journal*, 584:758–769, February 2003.

[161] E. G. Berezhko, L. T. Ksenofontov, and H. J. Völk. Confirmation of strong magnetic field amplification and nuclear cosmic ray acceleration in SN 1006. *Astronomy and Astrophysics*, 412:L11–L14, December 2003.

[162] Y. Uchiyama, F. A. Aharonian, T. Tanaka, T. Takahashi, and Y. Maeda. Extremely fast acceleration of cosmic rays in a supernova remnant. *Nature*, 449:576–578, October 2007.

[163] K. A. Eriksen, J. P. Hughes, C. Badenes, R. Fesen, P. Ghavamian, D. Moffett, P. P. Plucinksy, C. E. Rakowski, E. M. Reynoso, and P. Slane. Evidence for Particle Acceleration to the Knee of the Cosmic Ray Spectrum in Tycho's Supernova Remnant. *The Astrophysical Journal, Letters*, 728:L28, February 2011.

[164] A. M. Bykov, D. C. Ellison, S. M. Osipov, G. G. Pavlov, and Y. A. Uvarov. X-ray Stripes in Tycho's Supernova Remnant: Synchrotron Footprints of a Nonlinear Cosmic-ray-driven Instability. *The Astrophysical Journal, Letters*, 735:L40, July 2011.

[165] M. G. Baring, D. C. Ellison, S. P. Reynolds, I. A. Grenier, and P. Goret. Radio to Gamma-Ray Emission from Shell-Type Supernova Remnants: Predictions from Nonlinear Shock Acceleration Models. *The Astrophysical Journal*, 513:311–338, March 1999.

[166] T. K. Gaisser, R. J. Protheroe, and T. Stanev. Gamma-Ray Production in Supernova Remnants. *The Astrophysical Journal*, 492:219–227, January 1998.

[167] P. S. Coppi and R. D. Blandford. Reaction rates and energy distributions for elementary processes in relativistic pair plasmas. *Monthly Notices of the Royal Astronomical Society*, 245:453–507, August 1990.

[168] F. A. Aharonian. *Very high energy cosmic gamma radiation : a crucial window on the extreme Universe*. 2004.

[169] L. O. Drury, F. A. Aharonian, and H. J. Voelk. The gamma-ray visibility of supernova remnants. A test of cosmic ray origin. *Astronomy and Astrophysics*, 287:959–971, July 1994.

[170] L. O. Drury, W. J. Markiewicz, and H. J. Voelk. Simplified models for the evolution of supernova remnants including particle acceleration. *Astronomy and Astrophysics*, 225:179–191, November 1989.

[171] F. Aharonian et al. Primary particle acceleration above 100 TeV in the shell-type supernova remnant ¡ASTROBJ¿RX J1713.7-3946¡/ASTROBJ¿ with deep HESS observations. *Astronomy and Astrophysics*, 464:235–243, March 2007.

[172] F. Aharonian et al. H.E.S.S. Observations of the Supernova Remnant RX J0852.0-4622: Shell-Type Morphology and Spectrum of a Widely Extended Very High Energy Gamma-Ray Source. *The Astrophysical Journal*, 661:236–249, May 2007.

[173] F. Acero et al. First detection of VHE γ-rays from SN 1006 by HESS. *Astronomy and Astrophysics*, 516:A62, June 2010.

[174] H. E. S. S. Collaboration, A. Abramowski, F. Aharonian, F. Ait Benkhali, A. G. Akhperjanian, E. O. Angüner, M. Backes, A. Balzer, Y. Becherini, J. Becker Tjus, and et al. Detailed spectral and morphological analysis of the shell type SNR RCW 86. *ArXiv e-prints*, January 2016.

[175] H.E.S.S. Collaboration, A. Abramowski, et al. A new SNR with TeV shell-type morphology: HESS J1731-347. *Astronomy and Astrophysics*, 531:A81, July 2011.

[176] VERITAS Collaboration, S. Archambault, et al. Gamma-ray observations of Tycho's SNR with VERITAS and Fermi. *ArXiv e-prints*, January 2017.

[177] K. Koyama, R. Petre, E. V. Gotthelf, U. Hwang, M. Matsuura, M. Ozaki, and S. S. Holt. Evidence for shock acceleration of high-energy electrons in the supernova remnant SN1006. *Nature*, 378:255–258, November 1995.

[178] P. Slane, B. M. Gaensler, T. M. Dame, J. P. Hughes, P. P. Plucinsky, and A. Green. Nonthermal X-Ray Emission from the Shell-Type Supernova Remnant G347.3-0.5. *The Astrophysical Journal*, 525:357–367, November 1999.

[179] Y. Fukui, Y. Moriguchi, K. Tamura, H. Yamamoto, Y. Tawara, N. Mizuno, T. Onishi, A. Mizuno, Y. Uchiyama, J. Hiraga, T. Takahashi, K. Yamashita, and S. Ikeuchi. Discovery of Interacting Molecular Gas toward the TeV Gamma-Ray Peak of the SNR G 347.3–0.5. *Publications of the Astronomical Society of Japan*, 55:L61–L64, October 2003.

[180] D. C. Ellison, D. J. Patnaude, P. Slane, and J. Raymond. Efficient Cosmic Ray Acceleration, Hydrodynamics, and Self-Consistent Thermal X-Ray Emission Applied to Supernova Remnant RX J1713.7-3946. *The Astrophysical Journal*, 712:287–293, March 2010.

[181] A. A. Abdo et al. Observations of the Young Supernova Remnant RX J1713.7-3946 with the Fermi Large Area Telescope. *The Astrophysical Journal*, 734:28, June 2011.

[182] T. CTA Consortium, :, F. Acero, R. Aloisio, J. Amans, E. Amato, L. A. Antonelli, C. Aramo, T. Armstrong, F. Arqueros, and et al. Prospects for CTA observations of the young SNR RX J1713.7-3946. *ArXiv e-prints*, April 2017.

[183] F. A. Aharonian and A. M. Atoyan. On the emissivity of $\pi\hat{}0\hat{}$-decay gamma radiation in the vicinity of accelerators of galactic cosmic rays. *Astronomy and Astrophysics*, 309:917–928, May 1996.

[184] A. A. Abdo et al. Fermi Large Area Telescope Observations of the Supernova Remnant W28 (G6.4-0.1). *The Astrophysical Journal*, 718:348–356, July 2010.

[185] F. Aharonian et al. Discovery of very high energy gamma-ray emission coincident with molecular clouds in the W 28 (G6.4-0.1) field. *Astronomy and Astrophysics*, 481:401–410, April 2008.

[186] A. A. Abdo et al. Gamma-Ray Emission from the Shell of Supernova Remnant W44 Revealed by the Fermi LAT. *Science*, 327:1103, February 2010.

[187] A. A. Abdo et al. Fermi-LAT Study of Gamma-ray Emission in the Direction of Supernova Remnant W49B. *The Astrophysical Journal*, 722:1303–1311, October 2010.

[188] F. Brun, M. de Naurois, W. Hofmann, S. Carrigan, A. Djannati-Ataï, S. Ohm, and for the H. E. S. S. Collaboration. Discovery of VHE gamma-ray emission from the W49 region with H.E.S.S. *ArXiv e-prints*, April 2011.

[189] Y. Ohira, K. Murase, and R. Yamazaki. Gamma-rays from molecular clouds illuminated by cosmic rays escaping from interacting supernova remnants. *Monthly Notices of the Royal Astronomical Society*, 410:1577–1582, January 2011.

[190] Y. Uchiyama, R. D. Blandford, S. Funk, H. Tajima, and T. Tanaka. Gamma-ray Emission from Crushed Clouds in Supernova Remnants. *The Astrophysical Journal, Letters*, 723:L122–L126, November 2010.

[191] D.-S. Moon and B.-C. Koo. Thermal and Non-Thermal Radio Continuum Sources in the W51 Complex. *Journal of Korean Astronomical Society*, 27:81–102, April 1994.

[192] G. Castelletti, G. Dubner, C. Brogan, and N. E. Kassim. The low-frequency radio emission and spectrum of the extended SNR ¡ASTROBJ¿W44¡/ASTROBJ¿: new VLA observations at 74 and 324 MHz. *Astronomy and Astrophysics*, 471:537–549, August 2007.

[193] W. C. Erickson and M. J. Mahoney. Clark Lake observations of IC 443 and Puppis A. *The Astrophysical Journal*, 290:596–601, March 1985.

[194] T. L. Wilson, R. Mauersberger, D. Muders, A. Przewodnik, and C. A. Olano. The molecular gas toward Cassiopeia A. *Astronomy and Astrophysics*, 280:221–230, December 1993.

[195] D. W. Hughes. Did Flamsteed see the Cassiopeia A supernova? *Nature*, 285:132–133, May 1980.

[196] J. R. Thorstensen, R. A. Fesen, and S. van den Bergh. The Expansion Center and Dynamical Age of the Galactic Supernova Remnant Cassiopeia A. *The Astronomical Journal*, 122:297–307, July 2001.

[197] R. A. Chevalier and J. Oishi. Cassiopeia A and Its Clumpy Presupernova Wind. *The Astrophysical Journal, Letters*, 593:L23–L26, August 2003.

[198] J. E. Reed, J. J. Hester, A. C. Fabian, and P. F. Winkler. The Three-dimensional Structure of the Cassiopeia A Supernova Remnant. I. The Spherical Shell. *The Astrophysical Journal*, 440:706, February 1995.

[199] M. Ryle and F. G. Smith. A New Intense Source of Radio-Frequency Radiation in the Constellation of Cassiopeia. *Nature*, 162:462–463, September 1948.

[200] A. R. Bell, S. F. Gull, and S. Kenderdine. New radio map of Cassiopeia A at 5 GHz. *Nature*, 257:463–465, October 1975.

[201] J. W. M. Baars, R. Genzel, I. I. K. Pauliny-Toth, and A. Witzel. The absolute spectrum of CAS A - an accurate flux density scale and a set of secondary calibrators. *Astronomy and Astrophysics*, 61:99–106, October 1977.

[202] R. Braun, S. F. Gull, and R. A. Perley. Physical process which shapes Cassiopeia A. *Nature*, 327:395–398, June 1987.

[203] N. E. Kassim, R. A. Perley, K. S. Dwarakanath, and W. C. Erickson. Evidence for Thermal Absorption inside Cassiopeia A. *The Astrophysical Journal, Letters*, 455:L59, December 1995.

[204] I. S. Shklovskii. *Radioastronomiia.* 1953.

[205] A. G. Pacholczyk. *Radio astrophysics. Nonthermal processes in galactic and extragalactic sources.* 1970.

[206] M. Wright, J. Dickel, B. Koralesky, and L. Rudnick. The Supernova Remnant Cassiopeia A at Millimeter Wavelengths. *The Astrophysical Journal*, 518:284–297, June 1999.

[207] R. A. Chevalier and R. P. Kirshner. Spectra of Cassiopeia A. II - Interpretation. *The Astrophysical Journal*, 219:931–941, February 1978.

[208] R. A. Chevalier and R. P. Kirshner. Abundance inhomogeneities in the Cassiopeia A supernova remnant. *The Astrophysical Journal*, 233:154–162, October 1979.

[209] R. A. Fesen, J. A. Morse, R. A. Chevalier, K. J. Borkowski, C. L. Gerardy, S. S. Lawrence, and S. van den Bergh. Hubble Space Telescope WFPC2 Imaging of Cassiopeia A. *The Astronomical Journal*, 122:2644–2661, November 2001.

[210] S. E. Woosley, N. Langer, and T. A. Weaver. The evolution of massive stars including mass loss - Presupernova models and explosion. *The Astrophysical Journal*, 411:823–839, July 1993.

[211] C. L. Gerardy and R. A. Fesen. Near-Infrared Spectroscopy of the Cassiopeia A and Kepler Supernova Remnants. *The Astronomical Journal*, 121:2781–2791, May 2001.

[212] T. J. Jones, L. Rudnick, T. DeLaney, and J. Bowden. The Identification of Infrared Synchrotron Radiation from Cassiopeia A. *The Astrophysical Journal*, 587:227–234, April 2003.

[213] G. E. Allen, J. W. Keohane, E. V. Gotthelf, R. Petre, K. Jahoda, R. E. Rothschild, R. E. Lingenfelter, W. A. Heindl, D. Marsden, D. E. Gruber, M. R. Pelling, and P. R. Blanco. Evidence of X-Ray Synchrotron Emission from Electrons Accelerated to 40 TeV in the Supernova Remnant Cassiopeia A. *The Astrophysical Journal, Letters*, 487:L97–L100, September 1997.

[214] Y. Uchiyama and F. A. Aharonian. Fast Variability of Nonthermal X-Ray Emission in Cassiopeia A: Probing Electron Acceleration in Reverse-Shocked Ejecta. *The Astrophysical Journal, Letters*, 677:L105–L108, April 2008.

[215] S. S. Holt, E. V. Gotthelf, H. Tsunemi, and H. Negoro. ASCA observations of Cassiopeia A. *Publications of the Astronomical Society of Japan*, 46:L151–L155, August 1994.

[216] J.-J. Lee, S. Park, J. P. Hughes, and P. O. Slane. X-Ray Observation of the Shocked Red Supergiant Wind of Cassiopeia A. *The Astrophysical Journal*, 789:7, July 2014.

[217] J. A. Esposito, S. D. Hunter, G. Kanbach, and P. Sreekumar. EGRET Observations of Radio-bright Supernova Remnants. *The Astrophysical Journal*, 461:820, April 1996.

[218] R. Lessard. Search for TeV Gamma-Rays from Shell-Type Supernova Remnants. *International Cosmic Ray Conference*, 3:488, August 1999.

[219] P. Goret, C. Gouiffes, E. Nuss, and D. C. Ellison. Search for $\geq=$ 400 GeV gamma-rays from the SNR Cas A. *ArXiv Astrophysics e-prints*, June 1999.

[220] F. Aharonian et al. Evidence for TeV gamma ray emission from Cassiopeia A. *Astronomy and Astrophysics*, 370:112–120, April 2001.

[221] J. Albert et al. Observation of VHE γ-rays from Cassiopeia A with the MAGIC telescope. *Astronomy and Astrophysics*, 474:937–940, November 2007.

[222] A. A. Abdo et al. Fermi-Lat Discovery of GeV Gamma-Ray Emission from the Young Supernova Remnant Cassiopeia A. *The Astrophysical Journal, Letters*, 710:L92–L97, February 2010.

[223] M. L. Ahnen et al. A cut-off in the TeV gamma-ray spectrum of the SNR Cassiopeia A. *Monthly Notices of the Royal Astronomical Society*, 472:2956–2962, December 2017.

[224] W. Atwood, A. Albert, L. Baldini, M. Tinivella, J. Bregeon, M. Pesce-Rollins, C. Sgrò, P. Bruel, E. Charles, A. Drlica-Wagner, A. Franckowiak, T. Jogler, L. Rochester, T. Usher, M. Wood, J. Cohen-Tanugi, and S. Zimmer for the Fermi-LAT Collaboration. Pass 8: Toward the Full Realization of the Fermi-LAT Scientific Potential. *ArXiv e-prints*, March 2013.

[225] J. R. Mattox, D. L. Bertsch, J. Chiang, B. L. Dingus, S. W. Digel, J. A. Esposito, J. M. Fierro, R. C. Hartman, S. D. Hunter, G. Kanbach, D. A. Kniffen, Y. C. Lin, D. J. Macomb, H. A. Mayer-Hasselwander, P. F. Michelson, C. von Montigny, R. Mukherjee, P. L. Nolan, P. V. Ramanamurthy, E. Schneid, P. Sreekumar,

D. J. Thompson, and T. D. Willis. The Likelihood Analysis of EGRET Data. *The Astrophysical Journal*, 461:396, April 1996.

[226] A. A. Abdo et al. Fermi LAT Discovery of Extended Gamma-Ray Emission in the Direction of Supernova Remnant W51C. *The Astrophysical Journal, Letters*, 706:L1–L6, November 2009.

[227] J. S. Perkins, G. Maier, and The VERITAS Collaboration. VERITAS Telescope 1 Relocation: Details and Improvements. *ArXiv e-prints*, December 2009.

[228] P. Freeman, S. Doe, and A. Siemiginowska. Sherpa: a mission-independent data analysis application. In J.-L. Starck and F. D. Murtagh, editors, *Astronomical Data Analysis*, volume 4477 of *Proceedings of SPIE*, pages 76–87, November 2001.

[229] Arun Madhavan. *The VHE gamma-ray spectra of several hard-spectrum blazars from long-term observations with the VERITAS telescope array.* PhD thesis, Iowa State University, 2013.

[230] G. R. Blumenthal and R. J. Gould. Bremsstrahlung, synchrotron radiation, and compton scattering of high-energy electrons traversing dilute gases. *Rev. Mod. Phys.*, 42:237–270, 1970.

[231] M. Pohl, A. Wilhelm, and I. Telezhinsky. Reacceleration of electrons in supernova remnants. *Astron. Astrophys.*, 574:A43, 2015.

[232] P. G. Mezger, R. J. Tuffs, R. Chini, E. Kreysa, and H.-P. Gemuend. Maps of Cassiopeia A and the Crab Nebula at lambda 1.2 MM. *Astronomy and Astrophysics*, 167:145–150, October 1986.

[233] B. Hnatyk and O. Petruk. Evolution of supernova remnants in the interstellar medium with a large scale density gradient. I. general properties of the morphological evolution and x-ray emission. *Astron. Astrophys.*, 344:295, 1999.

[234] C.-Y. Huang, S.-E. Park, M. Pohl, and C. D. Daniels. Gamma-rays produced in cosmic-ray interactions and the TeV-band spectrum of RX J1713.7-3946. *Astroparticle Physics*, 27:429–439, June 2007.

[235] T. Sato, S. Katsuda, M. Morii, A. Bamba, J. P. Hughes, Y. Maeda, M. Ishida, and F. Fraschetti. X-ray Measurements of the Particle Acceleration Properties at Inward Shocks in Cassiopeia A. *ArXiv e-prints*, October 2017.

[236] Ramanath Cowsik and Subir Sarkar. A lower limit to the magnetic field in Cassiopeia-A. *Mon. Not. Roy. Astron. Soc.*, 191:855–861, 1980.

[237] J. Martin Laming and Una Hwang. On the determination of ejecta structure and explosion asymmetry from the x-ray knots of cassiopeia a. *The Astrophysical Journal*, 597(1):347, 2003.

[238] M. A. Malkov, P. H. Diamond, and R. Z. Sagdeev. Mechanism for spectral break in cosmic ray proton spectrum of supernova remnant W44. *Nature Communications*, 2:194, February 2011.

[239] R. Brose, I. Telezhinsky, and M. Pohl. Transport of magnetic turbulence in supernova remnants. *Astronomy and Astrophysics*, 593:A20, August 2016.

[240] A. R. Bell, K. M. Schure, and B. Reville. Cosmic ray acceleration at oblique shocks. *Monthly Notices of the Royal Astronomical Society*, 418:1208–1216, December 2011.

[241] A. M. Atoyan, F. A. Aharonian, R. J. Tuffs, and H. J. Völk. On the gamma-ray fluxes expected from Cassiopeia A. *Astronomy and Astrophysics*, 355:211–220, March 2000.

[242] I. Telezhinsky, V. V. Dwarkadas, and M. Pohl. Acceleration of cosmic rays by young core-collapse supernova remnants. *Astronomy and Astrophysics*, 552:A102, April 2013.

[243] E. A. Helder and J. Vink. Characterizing the Nonthermal Emission of Cassiopeia A. *The Astrophysical Journal*, 686:1094–1102, October 2008.

[244] R. A. Fesen and R. P. Kirshner. Spectrophotometry of the supernova remnant IC 443. *The Astrophysical Journal*, 242:1023–1040, December 1980.

[245] R. Petre, A. E. Szymkowiak, F. D. Seward, and R. Willingale. A comprehensive study of the X-ray structure and spectrum of IC 443. *The Astrophysical Journal*, 335:215–238, December 1988.

[246] J. Rho and R. Petre. Mixed-Morphology Supernova Remnants. *The Astrophysical Journal, Letters*, 503:L167–L170, August 1998.

[247] T. A. Lozinskaya. The radio brightness-diameter relation for supernova remnants - Some new distance calibrators. *Soviet Astronomy Letters*, 7:29–32, February 1981.

[248] R. A. Fesen. The nature of the filaments northeast of the supernova remnant IC 443. *The Astrophysical Journal*, 281:658–664, June 1984.

[249] R. A. Chevalier. Supernova Remnants in Molecular Clouds. *The Astrophysical Journal*, 511:798–811, February 1999.

[250] B. M. Gaensler, S. Chatterjee, P. O. Slane, E. van der Swaluw, F. Camilo, and J. P. Hughes. The X-Ray Structure of the Pulsar Bow Shock G189.22+2.90 in the Supernova Remnant IC 443. *The Astrophysical Journal*, 648:1037–1042, September 2006.

[251] I. Asaoka and B. Aschenbach. An X-ray study of IC443 and the discovery of a new supernova remnant by ROSAT. *Astronomy and Astrophysics*, 284:573–582, April 1994.

[252] D. A. Leahy. 1420 and 408 MHz Continuum Observations of the IC 443/G189.6+3.3 Region. *The Astronomical Journal*, 127:2277–2283, April 2004.

[253] M. G. Burton, T. R. Geballe, P. W. J. L. Brand, and A. S. Webster. Shocked molecular hydrogen in the supernova remnant IC 443. *Monthly Notices of the Royal Astronomical Society*, 231:617–634, April 1988.

[254] E. F. van Dishoeck, D. J. Jansen, and T. G. Phillips. Submillimeter observations of the shocked molecular gas associated with the supernova remnant IC 443. *Astronomy and Astrophysics*, 279:541–566, November 1993.

[255] F. A. Aharonian. Gamma Rays From Molecular Clouds. *Space Science Reviews*, 99:187–196, October 2001.

[256] S. Gabici, F. A. Aharonian, and P. Blasi. Gamma rays from molecular clouds. *Astrophysics and Space Science*, 309:365–371, June 2007.

[257] S. Gabici, F. A. Aharonian, and S. Casanova. Broad-band non-thermal emission from molecular clouds illuminated by cosmic rays from nearby supernova remnants. *Monthly Notices of the Royal Astronomical Society*, 396:1629–1639, July 2009.

[258] L. K. Denoyer. Observations of negative velocity hydrogen in IC 443. *Monthly Notices of the Royal Astronomical Society*, 183:187–193, April 1978.

[259] S. L. Mufson, M. L. McCollough, J. R. Dickel, R. Petre, R. White, and R. Chevalier. A multiwavelength investigation of the supernova remnant IC 443. *The Astronomical Journal*, 92:1349–1357, December 1986.

[260] R. M. Duin and H. van der Laan. The radio structure of the supernova remnant IC 443. *Astronomy and Astrophysics*, 40:111–122, April 1975.

[261] E. Troja, F. Bocchino, M. Miceli, and F. Reale. XMM-Newton observations of the supernova remnant IC 443. II. Evidence of stellar ejecta in the inner regions. *Astronomy and Astrophysics*, 485:777–785, July 2008.

[262] J. C. Raymond. Shock waves in the interstellar medium. *The Astrophysical Journal, Supplement*, 39:1–27, January 1979.

[263] Z. R. Wang, I. Asaoka, S. Hayakawa, and K. Koyama. Hard X-rays from the supernova remnant IC 443. *Publications of the Astronomical Society of Japan*, 44:303–308, June 1992.

[264] R. H. Cornett, G. Chin, and G. R. Knapp. Observations of CO emission from a dense cloud associated with the supernova remnant IC 443. *Astronomy and Astrophysics*, 54:889–894, February 1977.

[265] J.-L. Xu, J.-J. Wang, and M. Miller. Star Formation Associated with the Supernova Remnant IC443. *The Astrophysical Journal*, 727:81, February 2011.

[266] L. K. Denoyer. Shocked OH within a supernova remnant. *The Astrophysical Journal, Letters*, 228:L41–L43, February 1979.

[267] M. Tavani et al. Direct evidence for hadronic cosmic-ray acceleration in the supernova remnant ic 443. *The Astrophysical Journal Letters*, 710(2):L151, 2010.

[268] J. Fang and L. Zhang. Hadronic gamma-ray emission from molecular clouds overtaken by supernova remnants. *New Astronomy*, 18:35–41, January 2013.

[269] D. F. Torres, A. Y. R. Marrero, and E. de Cea Del Pozo. The GeV to TeV connection in the environment of SNR IC 443. *Monthly Notices of the Royal Astronomical Society*, 408:1257–1266, October 2010.

[270] J. W. Hewitt, E. A. Hays, H. Tajima, J. Schmid, and V. C. LAT Collaboration. Resolving the hadronic accelerator IC 443 with Fermi-LAT and VERITAS. In *American Astronomical Society Meeting Abstracts*, volume 227 of *American Astronomical Society Meeting Abstracts*, page 238.10, January 2016.

[271] V. Zabalza. Naima: a Python package for inference of particle distribution properties from nonthermal spectra. In *34th International Cosmic Ray Conference (ICRC2015)*, volume 34 of *International Cosmic Ray Conference*, page 922, July 2015.

[272] D. Foreman-Mackey, D. W. Hogg, D. Lang, and J. Goodman. emcee: The MCMC Hammer. *Publications of the Astronomical Society of the Pacific*, 125:306, March 2013.

[273] E. Kafexhiu, F. Aharonian, A. M. Taylor, and G. S. Vila. Parametrization of gamma-ray production cross sections for p p interactions in a broad proton energy range from the kinematic threshold to PeV energies. *Physical Review D*, 90(12):123014, December 2014.